

---

TOWARDS ION-LATTICE QUANTUM PROCESSORS  
WITH SURFACE TRAP ARRAYS

---

**Dissertation**

by

**Philip Christoph Holz**

Submitted to the Faculty of  
Mathematics, Computer Science and Physics  
of the University of Innsbruck

Carried out under the supervision of Univ. Prof. Dr. Rainer Blatt  
at the Quantum Optics and Spectroscopy group



Institute for Experimental Physics  
University of Innsbruck

November 2019



# Abstract

Trapped-ions are one of the most successful platforms for quantum information processing to date, with high gate fidelities and long coherence times. The established technology can be extended to potentially hundreds and thousands of qubits using microfabricated trap arrays. This thesis explores the path towards an ion-lattice quantum processor, based on two-dimensional arrays of microfabricated surface traps. Different technical elements are thereby investigated: electrode design and trap fabrication, suitable trap materials and electrical operation. The studies of electrode design are focused on two-dimensional point trap arrays and linear trap arrays, where ion-shuttling operations are used to dynamically reconfigure the ion lattice in terms of lattice connectivity and ion-spacing. The latter enables tunable interactions between ions in adjacent lattice sites. Extensive trap simulations show the feasibility of this approach for a two-dimensional linear trap array with 18 trapping sites. The simulated trapping potentials facilitate interaction strengths between ions in adjacent sites in the kHz range, while maintaining a moderate ion-surface separation  $d \approx 100 \mu\text{m}$  to keep the electric field noise low. For point trap arrays, a weakness is revealed in terms of a greatly diminished trap depth in lattice configurations with reduced ion spacing. First instances of a point trap array and a linear trap array have been fabricated using multilayer microfabrication methods. Voltage tests are used to investigate aging effects of the dielectric insulation layer as well as the origin of dielectric breakdown of the trap structures. Trapping of a lattice of ions in a linear trap array is demonstrated. With regard to electrical operation, the generation of radio-frequency (RF) fields that are differentially tunable on different trap electrodes is studied with an electrical resonator prototype. The performance of this prototype should be sufficient to realize RF-controlled ion-shuttling over many tens of  $\mu\text{m}$  in realistic trap geometries. In addition, the resonator remains tunable at cryogenic temperatures of 10 K, where extremely good vacuum conditions can be achieved as required for the operation of large ion lattices. Lastly, a high-temperature superconductor is investigated as a novel trap material in a linear surface trap. The ion heating rate above a superconducting trap surface is measured, with a low value on the order of  $\Gamma_h \sim 1$  phonon/s at an ion-surface separation of  $d = 225 \mu\text{m}$ . Furthermore, it is shown that superconducting electrode leads can offer better RF grounding of trap electrodes and a lower level of electric field noise compared to standard trap materials such as aluminium or gold.



# Zusammenfassung

Gespeicherte Ionen sind eine der am weitesten fortgeschrittenen Plattformen für die Quanteninformationsverarbeitung und ermöglichen Gatteroperationen hoher Güte und lange Kohärenzzeiten. Die etablierte Technologie kann durch die Verwendung von mikrofabrizierten Oberflächenfallen auf Quantenregister von einigen hundert bis möglicherweise sogar tausend Qubits erweitert werden. Ziel dieser Arbeit ist es, einen neuartigen Ionengitter-Prozessor zu erforschen, der auf zweidimensionalen Anordnungen von Oberflächenfallen basiert. Dabei werden unterschiedliche technische Aspekte dieses Ansatzes untersucht: Elektrodendesign und Fabrikation, geeignete Fallenmaterialien sowie die elektrische Ansteuerung der Fallen. Die Studien zum Elektrodendesign konzentrieren sich auf zweidimensionale Anordnungen von Punktfallen und linearen Fallen, welche eine dynamische Rekonfiguration der Konnektivität des Ionengitters sowie des Ionenabstands erlauben. Durch Letzteres werden Wechselwirkungen mit einstellbarer Stärke zwischen Ionen in benachbarten Gitterplätzen möglich. Die Durchführbarkeit dieses Ansatzes in einer zweidimensionalen Anordnung linearer Fallen mit 18 Gitterplätzen wird durch umfassende Fallensimulationen gezeigt. Die realisierbaren Wechselwirkungsstärken zwischen benachbarten Ionen sind dabei im kHz-Bereich, während gleichzeitig ein moderater Abstand  $d \approx 100 \mu\text{m}$  zwischen den Ionen und der Fallenoberfläche gewährleistet wird, um das elektrische Feldrauschen gering zu halten. Des Weiteren legen die Simulationen eine Schwäche von Anordnungen von Punktfallen offen, die durch eine stark verminderte Fallentiefe in Gitterkonfiguration mit reduziertem Ionenabstand gegeben ist. Auf experimenteller Seite wird die Herstellung verschiedener Versionen von Mikrochips mit Anordnungen von Punktfallen und linearen Fallen mittels Mehrschicht-Mikrofabrikationsmethoden beschrieben. Elektrische Spannungstest werden eingesetzt, um Alterungseffekte in dielektrischen Isolationsschichten zu untersuchen, sowie die Ursache für das Versagen des Dielektrikums in den Fallenchips zu identifizieren. Das Laden eines Ionengitters in einer Anordnung linearer Fallen wird demonstriert. Im Bezug auf elektrische Ansteuerung der Fallen wird die Erzeugung von Radiofrequenz- (RF-) Feldern untersucht, die differentiell auf unterschiedlichen Elektroden eingestellt werden können. Diese Schlüsseltechnologie für das dynamische Einstellen des Ionenabstands im Gitter wird in einem Prototyp eines durchstimmbaren RF-Resonators untersucht. Die demonstrierte elektrische Verstimrbarkeit des Prototyps

sollte ausreichen, um Ionentransport über mehrere Dutzend  $\mu\text{m}$  in typischen Fallengeometrien zu gewährleisten. Zudem lässt sich der Prototyp bei kryogenen Temperaturen von 10 K betreiben, welche für die Erzeugung des für große Ionengitter wichtigen, extrem hohen Vakuums unerlässlich sind. Schließlich wird in einem weiteren Experiment ein Hochtemperatursupraleiter auf seine Verwendbarkeit als neues Fallenmaterial hin überprüft. Die Messung der Heizrate eines einzelnen gefangenen Ions oberhalb der supraleitenden Fallenoberfläche ergibt niedrige Werte von  $\Gamma_h \sim 1$  Phonon/s bei einem Abstand  $d = 225 \mu\text{m}$  zwischen Ion und Fallenchip. Des Weiteren wird gezeigt, dass supraleitende Elektrodenzuleitungen in Bezug auf elektrisches Feldrauschen sowie Erdung von parasitären RF-Spannungen gegenüber gebräuchlicheren Fallenmaterialien wie Gold oder Aluminium von Vorteil sein können.

# Acknowledgements

The work described in this thesis would not have been possible without the contributions and help of many others, whom I would like to thank at this point. Specifically I would like to mention Rainer Blatt, Mike Brownutt and Yves Colombe for their supervision, support and guidance. Further, I thank the former and present members of the cryolab team, Kirill Lakhmanskiy, Muir Kumph, Michi Niedermayr, Ben Ames, Kirsten Langer, Martin Meraner, Alexander Erhard, Dominic Schärfl, Gerald Stocker, Silke Auchter and Marco Valentini for their help, assistance and support. A great thanks also goes to the collaboration partners in the group of Johannes Edlinger at FHV, Stefan Partel, Stephan Kasemann and Volha Matylitskaya, as well as Clemens Rössler and all other partners at Infineon, for their efforts in fabricating the trap chips described in this thesis and for the fruitful collaboration. I wish to thank all other members of the Blatt group for the warm-hearted, helpful and creative atmosphere, for the generous sharing of expertise as well as for the enlightening discussions and advice, here in particular Philipp Schindler, Thomas Monz and Christian Roos. I also thank Armin Sailer and the team from the mechanical workshop, as well as Wolfgang Kratz and Wolfgang Kuen from the electrical workshop for their assistance and advice. Furthermore, Patricia Moser, Christine Götsch-Obmascher, Verena Tanzer, Renate Rupprechter and all other administrative staff for their support. I am grateful to Martin van Mourik, Gabriel Araneda, Pavel Hrmo and Martin Ringbauer for their critical comments to the thesis. And I owe special thanks to all the colleagues and friends for making the life in Innsbruck a real pleasure. Lastly and most-importantly, I would like to thank my family, foremost my wife Alexandra, for her patience, encouragement and unconditional support. And thanks to my two sons Stefan and Benjamin for always being there to brighten my days.



# Contents

|                                                       |              |
|-------------------------------------------------------|--------------|
| <b>Abstract / Zusammenfassung</b>                     | <b>i</b>     |
| <b>Acknowledgements</b>                               | <b>v</b>     |
| <b>List of Figures</b>                                | <b>xiv</b>   |
| <b>List of Tables</b>                                 | <b>xv</b>    |
| <b>List of Acronyms</b>                               | <b>xviii</b> |
| <b>1. Introduction</b>                                | <b>1</b>     |
| <b>2. Ion storage and quantum state manipulation</b>  | <b>5</b>     |
| 2.1. Paul trap basics . . . . .                       | 5            |
| 2.1.1. Electrode configurations . . . . .             | 6            |
| 2.1.2. Mathieu equations and trap stability . . . . . | 8            |
| 2.1.3. Pseudopotential approximation . . . . .        | 10           |
| 2.1.4. Trap depth . . . . .                           | 11           |
| 2.2. Laser-ion interaction . . . . .                  | 11           |
| 2.2.1. The $^{40}\text{Ca}^+$ ion . . . . .           | 12           |
| 2.2.2. Free two-level ion . . . . .                   | 13           |
| 2.2.3. Harmonically confined ion . . . . .            | 15           |
| 2.3. Quantum optics toolbox . . . . .                 | 17           |
| 2.3.1. Laser cooling . . . . .                        | 18           |
| 2.3.2. Qubit manipulation . . . . .                   | 20           |
| 2.3.3. Trap characterization . . . . .                | 21           |
| <b>3. Surface trap arrays</b>                         | <b>25</b>    |
| 3.1. General considerations . . . . .                 | 26           |
| 3.1.1. Electrode arrangement . . . . .                | 26           |
| 3.1.2. Laser access . . . . .                         | 27           |
| 3.1.3. Array operation . . . . .                      | 28           |

|                                                                           |           |
|---------------------------------------------------------------------------|-----------|
| 3.2. Tunable well-to-well interactions . . . . .                          | 29        |
| 3.2.1. Interaction mechanism . . . . .                                    | 29        |
| 3.2.2. Ion shuttling for enhanced interaction strength . . . . .          | 30        |
| 3.2.3. Outline of an entangling scheme . . . . .                          | 32        |
| 3.3. Motional heating . . . . .                                           | 33        |
| 3.3.1. Sources of electric field noise . . . . .                          | 34        |
| 3.3.2. Noise mitigation . . . . .                                         | 36        |
| <b>4. Experimental setup</b>                                              | <b>37</b> |
| 4.1. Cryogenic vacuum vessel . . . . .                                    | 37        |
| 4.1.1. General setup . . . . .                                            | 37        |
| 4.1.2. Cryogenic electronics . . . . .                                    | 39        |
| 4.2. Optical setup . . . . .                                              | 41        |
| 4.2.1. General setup . . . . .                                            | 41        |
| 4.2.2. Laser sheet for Doppler cooling . . . . .                          | 43        |
| 4.3. Experiment control . . . . .                                         | 45        |
| <b>5. 2 D point trap array “Ziegelstadl”</b>                              | <b>47</b> |
| 5.1. Trap design and fabrication . . . . .                                | 47        |
| 5.1.1. Electrode layout . . . . .                                         | 47        |
| 5.1.2. RF-controlled shuttling operations . . . . .                       | 48        |
| 5.1.3. Fabrication . . . . .                                              | 49        |
| 5.2. Electrical characterization . . . . .                                | 52        |
| 5.3. Ion-loading attempts . . . . .                                       | 56        |
| 5.4. Failure analysis and suggested improvements . . . . .                | 59        |
| 5.4.1. Dielectric layer . . . . .                                         | 59        |
| 5.4.2. Surface topology . . . . .                                         | 60        |
| 5.4.3. Pseudo potential barrier . . . . .                                 | 60        |
| <b>6. Tunable RF fields in cryogenic traps</b>                            | <b>63</b> |
| 6.1. Requirements on tunable RF circuits . . . . .                        | 64        |
| 6.1.1. Capacitive networks . . . . .                                      | 65        |
| 6.1.2. Multiple resonators . . . . .                                      | 69        |
| 6.2. Operation of a tunable resonator at cryogenic temperatures . . . . . | 74        |
| 6.2.1. Resonator setup . . . . .                                          | 74        |
| 6.2.2. Experimental results . . . . .                                     | 78        |
| 6.3. Discussion and outlook . . . . .                                     | 81        |

|                                                                                      |            |
|--------------------------------------------------------------------------------------|------------|
| <b>7. Superconducting surface traps</b>                                              | <b>85</b>  |
| 7.1. Trap design                                                                     | 86         |
| 7.1.1. Electrode layout and fabrication                                              | 86         |
| 7.1.2. Trap setup and operation                                                      | 88         |
| 7.2. Superconducting electrode leads                                                 | 90         |
| 7.3. Experimental results                                                            | 95         |
| 7.3.1. RF pickup study                                                               | 95         |
| 7.3.2. Heating rate measurements                                                     | 97         |
| 7.4. Discussion                                                                      | 101        |
| <b>8. 2D linear trap array “Bucket-brigade”</b>                                      | <b>105</b> |
| 8.1. Objectives                                                                      | 106        |
| 8.1.1. Next-neighbor interactions and ion-surface separation                         | 106        |
| 8.1.2. Lattice reconfiguration                                                       | 109        |
| 8.2. Trap design and simulation                                                      | 111        |
| 8.2.1. RF confinement in collinear twin traps                                        | 111        |
| 8.2.2. Axial multiwell confinement                                                   | 119        |
| 8.2.3. Lattice reconfiguration                                                       | 124        |
| 8.2.4. RF shuttling                                                                  | 129        |
| 8.2.5. Axial interaction zone                                                        | 133        |
| 8.2.6. Comparison of the designs with $d = 120 \mu\text{m}$ and $d = 80 \mu\text{m}$ | 138        |
| 8.3. Fabrication                                                                     | 139        |
| 8.3.1. Multilayer structure                                                          | 139        |
| 8.3.2. Electrical characterization                                                   | 143        |
| 8.4. Future experiments                                                              | 146        |
| <b>9. Summary and outlook</b>                                                        | <b>149</b> |
| <b>A. Appendix to the superconducting traps</b>                                      | <b>153</b> |
| A.1. Thermal insulation and temperature calibration                                  | 153        |
| A.2. DC voltage sets                                                                 | 154        |
| A.3. Details of the RF pickup model                                                  | 155        |
| A.3.1. Estimates for the parasitic capacitances $C_p, C_0$                           | 158        |
| A.3.2. Estimates for the connection line impedance $Z_{\text{line}}$                 | 158        |
| A.3.3. Low pass filter components                                                    | 160        |
| A.4. Sources of electric field noise                                                 | 161        |
| A.4.1. Johnson noise from the YBCO meander leads                                     | 161        |
| A.4.2. Exclusion of Johnson noise for the experiments in chip B                      | 162        |
| A.4.3. Exclusion of external technical noise                                         | 166        |

*Contents*

|                                                                              |            |
|------------------------------------------------------------------------------|------------|
| A.4.4. Surface noise contribution from the exposed YBCO surface . . . .      | 168        |
| <b>B. Appendix to the 2 D linear trap array</b>                              | <b>171</b> |
| B.1. Voltage sets . . . . .                                                  | 171        |
| B.2. Bucket-brigade shuttling with meander-shaped DC electrodes . . . . .    | 173        |
| B.3. Shuttling out of the axial interaction configuration . . . . .          | 175        |
| B.4. Finite element simulations of trap capacitances . . . . .               | 176        |
| B.5. Simulation of a trap array with $10 \times 10$ trapping sites . . . . . | 178        |
| <b>Bibliography</b>                                                          | <b>185</b> |

# List of Figures

|      |                                                                                                                                         |    |
|------|-----------------------------------------------------------------------------------------------------------------------------------------|----|
| 1.1. | Illustration of a two-dimensional ion lattice with next neighbor interactions.                                                          | 3  |
| 2.1. | Realization of an electric quadrupole field in a macroscopic trap and in a surface trap. . . . .                                        | 6  |
| 2.2. | Electrode configurations in surface point traps and linear traps. . . . .                                                               | 7  |
| 2.3. | $^{40}\text{Ca}^+$ level diagram. . . . .                                                                                               | 12 |
| 2.4. | Experimental data showing Rabi oscillations on the $4S_{1/2} \leftrightarrow 3D_{5/2}$ qubit transition of $^{40}\text{Ca}^+$ . . . . . | 15 |
| 2.5. | Experimental data showing resolved sideband spectroscopy on the $4S_{1/2} \leftrightarrow 3D_{5/2}$ qubit transition. . . . .           | 17 |
| 2.6. | Illustration of the sideband cooling process. . . . .                                                                                   | 19 |
| 3.1. | Surface trap realizations of ion lattices. . . . .                                                                                      | 26 |
| 3.2. | Illustration of motional coupling between ions in adjacent trapping sites.                                                              | 29 |
| 3.3. | Illustration of local ion-shuttling operations in surface trap arrays. . . .                                                            | 31 |
| 4.1. | Cryogenic vacuum system. . . . .                                                                                                        | 38 |
| 4.2. | Photograph of a mounted trap chip with cryogenic electronics PCBs. . . .                                                                | 39 |
| 4.3. | Schematics of the cryogenic electronics. . . . .                                                                                        | 40 |
| 4.4. | Optical setup for the realization of a laser sheet for Doppler cooling. . . .                                                           | 44 |
| 4.5. | Experimental sequence for a measurement of Rabi oscillations on the micromotion sideband. . . . .                                       | 46 |
| 4.6. | Experimental sequence for a heating rate measurement. . . . .                                                                           | 46 |
| 5.1. | Electrode layout of the Ziegelstadl trap array. . . . .                                                                                 | 48 |
| 5.2. | Illustration of RF-controlled shuttling operations. . . . .                                                                             | 49 |
| 5.3. | Schematic cross section of the multilayer structure of the Ziegelstadl chip.                                                            | 50 |
| 5.4. | Microscope images of the Ziegelstadl trap array. . . . .                                                                                | 51 |
| 5.5. | Degradation of the dielectric $\text{SiO}_2$ layer due to drifts in the coating parameters. . . . .                                     | 52 |
| 5.6. | Setup for DC breakdown tests. . . . .                                                                                                   | 52 |
| 5.7. | Microscope images of traps after unsuccessful removal of electrical shorts.                                                             | 53 |
| 5.8. | Typical test data of DC breakdown tests. . . . .                                                                                        | 54 |

List of Figures

|                                                                                                                        |     |
|------------------------------------------------------------------------------------------------------------------------|-----|
| 5.9. Data showing aging effects of the dielectric layer. . . . .                                                       | 55  |
| 5.10. Microscope images of structural damage due to micro discharge events. . . . .                                    | 56  |
| 5.11. Setup for ion loading in the Ziegelstadl trap. . . . .                                                           | 57  |
| 5.12. Schematic of the resonator circuit for ion loading in the Ziegelstadl trap. . . . .                              | 58  |
| 5.13. Simulations of the potential barrier during RF shuttling processes in point trap and linear trap arrays. . . . . | 61  |
| 6.1. Schematic of an electrically tunable load capacitance in an RF circuit. . . . .                                   | 64  |
| 6.2. Schematic circuit of capacitive networks for tunable RF fields. . . . .                                           | 66  |
| 6.3. Requirements on capacitance tunability in capacitive networks. . . . .                                            | 67  |
| 6.4. Schematic circuit of two RF resonators used for tunable RF fields. . . . .                                        | 69  |
| 6.5. Concept of active mode suppression in tunable, capacitively coupled resonators. . . . .                           | 72  |
| 6.6. Requirements on capacitance tunability in tunable resonators. . . . .                                             | 73  |
| 6.7. Schematic circuit of an electrically tunable resonator prototype. . . . .                                         | 75  |
| 6.8. Photographs of an electrically tunable resonator prototype. . . . .                                               | 76  |
| 6.9. Typical data showing resonator tunability. . . . .                                                                | 79  |
| 6.10. Characterization of the resonator tunability and quality factor using different varactor diode models. . . . .   | 80  |
| 6.11. Realization of tunable RF fields by amplitude and phase control of the RF drive fields. . . . .                  | 83  |
| 7.1. Electrode layout of the YBCO traps. . . . .                                                                       | 87  |
| 7.2. SEM images of the YBCO electrodes. . . . .                                                                        | 88  |
| 7.3. Photographs of a mounted YBCO trap chip. . . . .                                                                  | 89  |
| 7.4. Schematic illustration of Johnson noise and RF pickup fields due to high-resistance electrode leads. . . . .      | 91  |
| 7.5. Estimated excess micromotion for two temperatures $T > T_c$ and $T < T_c$ . . . . .                               | 94  |
| 7.6. Typical Rabi oscillation data on the carrier and micromotion sideband. . . . .                                    | 95  |
| 7.7. Measured excess micromotion for two temperatures $T > T_c$ and $T < T_c$ . . . . .                                | 96  |
| 7.8. Typical heating rate data. . . . .                                                                                | 97  |
| 7.9. Heating rate spectra in chip B with and without superconducting electrode leads. . . . .                          | 99  |
| 7.10. Temperature scaling of the heating rate in trap chips A and B. . . . .                                           | 99  |
| 7.11. Temperature dependence of the heating rate in chip B. . . . .                                                    | 100 |
| 8.1. Schematic illustration of entangling operations in a linear trap array. . . . .                                   | 108 |
| 8.2. Schematic illustration of a lattice reconfiguration. . . . .                                                      | 109 |
| 8.3. Concept of bucket-brigade shuttling. . . . .                                                                      | 110 |

|                                                                                                                                    |     |
|------------------------------------------------------------------------------------------------------------------------------------|-----|
| 8.4. Electrode geometry for the study of RF confinement in collinear surface traps. . . . .                                        | 112 |
| 8.5. Qualitative equivalence between geometry change and RF shuttling in a twin-trap. . . . .                                      | 113 |
| 8.6. Universal scaling of the pseudopotential barrier. . . . .                                                                     | 115 |
| 8.7. Optimization of the electrode geometry – Step 1. . . . .                                                                      | 117 |
| 8.8. Optimization of the electrode geometry – Step 2. . . . .                                                                      | 118 |
| 8.9. Electrode geometry of the Bucket-brigade traps. . . . .                                                                       | 119 |
| 8.10. Set of DC electrodes for bucket-brigade shuttling. . . . .                                                                   | 121 |
| 8.11. Trap confinement in the home configuration. . . . .                                                                          | 122 |
| 8.12. Simulation of bucket-brigade shuttling. . . . .                                                                              | 126 |
| 8.13. Trap confinement for a shift of the right multiwell. . . . .                                                                 | 128 |
| 8.14. Simulation of the RF shuttling process. . . . .                                                                              | 130 |
| 8.15. Trap confinement in the configuration with reduced RF voltage. . . . .                                                       | 131 |
| 8.16. Set of DC electrodes used for confinement in the axial interaction zone. . . . .                                             | 134 |
| 8.17. Trap confinement in the axial interaction configuration. . . . .                                                             | 135 |
| 8.18. Shuttling sequence from the axial interaction configuration into the home configuration. . . . .                             | 137 |
| 8.19. SEM images of the trap’s multilayer structure. . . . .                                                                       | 140 |
| 8.20. Microscope images of the Bucket-brigade traps. . . . .                                                                       | 142 |
| 8.21. Photograph of four ions trapped in a square lattice configuration. . . . .                                                   | 147 |
| 8.22. Illustration of future array geometries. . . . .                                                                             | 148 |
|                                                                                                                                    |     |
| A.1. Thermal decoupling and temperature calibration of the YBCO traps. . . . .                                                     | 154 |
| A.2. Schematic view of the YBCO trap electrodes. . . . .                                                                           | 155 |
| A.3. Amplitudes of the axial components of RF pickup fields. . . . .                                                               | 157 |
| A.4. Illustration of the calculation of JN from electrode CC. . . . .                                                              | 163 |
| A.5. Schematic circuits for the measurement of the transfer function of the low-pass filters. . . . .                              | 167 |
| A.6. Measured transfer function of the low-pass filters. . . . .                                                                   | 168 |
|                                                                                                                                    |     |
| B.1. Electrode set for confinement and micromotion compensation in the axial interaction zone of the bucket-brigade traps. . . . . | 173 |
| B.2. Electrode set for bucket-brigade shuttling using meander-shaped DC electrodes. . . . .                                        | 173 |
| B.3. Characterization of the bucket-brigade shuttling process using meander-shaped DC electrodes. . . . .                          | 174 |
| B.4. Schematic view of the simplified trap structure simulated with COMSOL. . . . .                                                | 177 |

*List of Figures*

|                                                                                                                  |     |
|------------------------------------------------------------------------------------------------------------------|-----|
| B.5. Electrode geometry of a linear trap array with $10 \times 10$ trapping sites. . .                           | 179 |
| B.6. Trap confinement in an array with $10 \times 10$ trapping sites. . . . .                                    | 180 |
| B.7. Trap confinement in an array with $10 \times 10$ trapping sites in the reduced<br>RF configuration. . . . . | 182 |

# List of Tables

|                                                                                                         |     |
|---------------------------------------------------------------------------------------------------------|-----|
| 2.1. Electric field properties of Paul traps with point-like and line-like RF null.                     | 10  |
| 5.1. Specifications of the wafer fabrication runs of the Ziegelstadl trap. . . .                        | 50  |
| 6.1. Room-temperature specifications of semiconductor diodes with tunable junction capacitance. . . . . | 69  |
| 6.2. Room-temperature specifications of varactor diodes used as capacitive tuning elements. . . . .     | 77  |
| 7.1. Properties of the YBCO trap chips. . . . .                                                         | 87  |
| 7.2. Estimated RF pickup ratios on trap electrodes C1, C2 and CC. . . . .                               | 93  |
| 7.3. Measured heating rates in chip A. . . . .                                                          | 98  |
| 8.1. Geometric parameters of the Bucket-brigade trap designs. . . . .                                   | 120 |
| 8.2. Trap parameters in the home configuration. . . . .                                                 | 122 |
| 8.3. Trap parameters in the configuration with reduced RF voltage. . . . .                              | 132 |
| 8.4. Trap parameters in the axial interaction configuration. . . . .                                    | 136 |
| 8.5. Multilayer structure of the Bucket-brigade traps. . . . .                                          | 140 |
| 8.6. Measured layer resistivities and via resistances. . . . .                                          | 143 |
| 8.7. Measured and simulated values of electrode capacitances. . . . .                                   | 146 |
| A.1. DC voltage sets for the operation of the YBCO traps. . . . .                                       | 155 |
| A.2. Estimates for JN-induced electric field noise from each trap electrode. .                          | 164 |
| B.1. Voltage sets for the home configuration of the bucket-brigade traps. . .                           | 171 |
| B.2. Voltage sets for the configuration with reduced RF voltage. . . . .                                | 172 |
| B.3. Voltage sets for trapping in the axial interaction zone. . . . .                                   | 172 |
| B.4. Trap parameters of a $10 \times 10$ linear trap array. . . . .                                     | 181 |
| B.5. Trap parameters of a $10 \times 10$ linear trap array in the reduced RF configuration. . . . .     | 183 |



# List of Acronyms

**AC** alternating current

**AOM** acousto-optical modulator

**BB** bucket-brigade

**CCD** charge-coupled device

**DC** direct current, static (when used for voltages)

**EPR** equivalent parallel resistance

**ESR** equivalent series resistance

**FHV** Fachhochschule Vorarlberg (University of Applied Sciences Vorarlberg)

**GND** electric ground

**ITO** indium tin oxide

**JN** Johnson-Nyquist noise

**PCB** printed circuit board

**PCI** peripheral component interconnect

**PDH** Pound-Drever-Hall

**PEEK** polyether ether ketone

**PI** photoionization

**PM** polarization-maintaining

**PMT** photo-multiplier tube

**PTFE** polytetrafluoroethylene (Teflon)

**QCCD** quantum charge-coupled device

*List of Tables*

**qubit** quantum binary digit

**RF** radio-frequency

**RIE** reactive ion etching

**SM** single-mode

**TTL** transistor-transistor logic

**UHV** ultra-high vacuum

**YBCO**  $\text{YBa}_2\text{Cu}_3\text{O}_7$

# 1. Introduction

Within the last decades, impressive advancements in the detection and manipulation of quantum objects have been made. Emergent quantum technologies are now on the threshold to maturity, initiating what is called a “second quantum revolution” [1]. The promises of these new technologies are far-reaching and encompass testing the foundations of physics with unprecedented precision, enhancing sensing applications, most prominently gravitational wave detection, relativistic geodesy or earthquake detection, and also breakthroughs in information technologies. First applications have already been commercialized, such as quantum-encrypted communication or quantum random number generation. Others still require academic research, such as quantum information processing.

## **The limits of classical computation**

Given the success of classical computers and the fact that they are ubiquitous in our daily life, one might ask what quantum information processors may additionally offer. First, further progress in modern classical computers is facing major technological challenges, for instance the rising energy consumption and power dissipation within the processor, which cannot be minimized beyond a fundamental limit described by Landauer’s principle [2]. Even if the future development of classical computers can keep up with the past improvements of microprocessors, there exist problems to which a quantum computer can find the solution faster and more efficiently. Prime examples are Shor’s factorization algorithm [3] and Grover’s search algorithm [4]. However, the power of quantum information processing extends far beyond the small number of known quantum algorithms, where a significant speedup compared to classical computers can be mathematically proven. Taking up the seminal idea of Feynman [5], a quantum processor can efficiently simulate the behavior of another quantum system, whereas classical computers often struggle [6]. For instance, simply storing the quantum state of 80 spin-1/2 particles would require a classical memory for  $2^{80}$  numbers, or about  $5 \times 10^{12}$  TB, a factor ten thousand more information than what was globally stored in 2007 [6]. There are numerous examples of simulation problems, that are difficult to solve with a classical computer, but whose solution would be of significant scientific and even economical relevance: quantum chemical problems such as nitrogen

## 1. Introduction

or carbon dioxide fixation [7], condensed-matter physics, like quantum phase transitions or high- $T_c$  superconductivity [6], and transport problems such as photosynthetic energy transfer [8], just to name a few. Several physical systems are currently being explored as platforms for quantum information processing: trapped-ions [9], superconducting circuits [10], cold atoms [11], photons [12], nuclear spin ensembles [13] and defect centers in solid state systems [14] fulfill most of the fundamental requirements, listed in the Di Vincenzo criteria [15].

### Quantum information processing with trapped ions

The fundamental unit of quantum information is the quantum binary digit (qubit). In the case of trapped ions, the qubit is encoded in the electronic states of an atomic ion and can be manipulated using laser or microwave radiation [16]. A big advantage of trapped-ions as platform for quantum computers is the fact that ions are charged particles. As such, ions can be stored for days in a confining electric potential [17], where they are well isolated from the environment to keep the fragile quantum information protected. Furthermore, the repulsive Coulomb forces between multiple ions within the same trap pushes them apart, such that they build crystalline structures. This enables optical addressing of single ions with laser beams for individual state manipulation. At the same time, the Coulomb interaction gives rise to a practically immediate coupling of the ion motion within an ion crystal. This leads to a collective motion which can be used to realize entangling operations between different ions. State-of-the-art trapped-ion quantum computers are operating with several tens of ions stored in a common confining potential [18–20]. A universal set of gate operations, comprised of single qubit rotations and entangling operations, is available, and can be realized with high precision [21–23]. Typical gate durations of a few to a few tens of  $\mu\text{s}$  are significantly lower than the coherence times, which can be up to several minutes [24]. With the universal gate set at hand, arbitrary quantum algorithms can be performed, as demonstrated for example for Grover’s and Shor’s algorithms [25, 26]. Basic quantum error correction has been implemented as well [27–29], showing the prospect of fault-tolerant quantum computing [30]. Trapped-ion quantum processors have also been successfully employed as quantum simulators, for instance for the observation of many-body dynamical phase transitions [31, 32], the simulation of particle-antiparticle generation in lattice gauge theories [33] or to calculate molecular ground state energies of simple molecules [34].

### Two-dimensional arrangements of ions

Currently, the biggest challenge for trapped-ion quantum processors is to scale-up the number of qubits. Problems are for instance the growing density of motional modes

in frequency space and the reduction in the speed of motional sideband operations upon increase of the ion number. Several approaches have been suggested, to solve this scalability issue: mediating the entangling operations by Rydberg interactions [35], replacing the common electric confinement by an optical lattice [36], or to modularize future processors [16, 37, 38], which is also the approach followed in this thesis. The core idea behind the modularization is to distribute the quantum register over several trapping potentials, each of which contains a small number of qubits that can be manipulated with high fidelity. In such a distributed register, quantum information between different trapping potentials can be exchanged by splitting, shuttling and merging of ions strings, known as quantum quantum charge-coupled device (QCCD) [39]. The individual processes required for a QCCD have been demonstrated in various proof-of-principle experiments, e. g. Refs. [40–49]. Multiple of such QCCD units could eventually be linked using probabilistic entanglement schemes with photons [50, 51].

Complementary to the QCCD architecture, microfabricated ion trap arrays can be used to realize two-dimensional ion lattices on a microchip [52–55]. In this approach, the ions remain in their individual trapping sites and may be coupled and entangled utilizing adiabatic well-to-well interactions [56–58] or, as recently proposed, broadband pulse sequences with high-power lasers [59]. An illustration of such an ion lattice is shown in Fig. 1.1. Due to their inherent two-dimensional connectivity, ion lattices should be

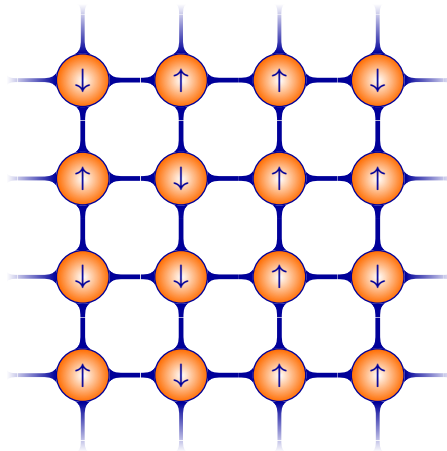


**Figure 1.1.** Illustration of a two-dimensional ion lattice with next neighbor interactions. The qubit state of the ions is depicted as a spin with orientations  $|\uparrow\rangle$  and  $|\downarrow\rangle$ .

well suited to implement topological error correction [60], which is considered a key technology for scaling up trapped ion quantum computers [16, 37]. With the ability to entangle next neighbors and thereby create so-called cluster states, a universal ion-lattice processor could also be implemented using the principle of measurement-based quantum computing [61]. Furthermore, ion lattices with next neighbor interactions are

## 1. Introduction

well suited for quantum simulation of spin models [62], for instance, magnetism [63] or quantum Hall physics [64]. Moderate lattice sizes of around  $7 \times 7$  sites are conjectured to be sufficient to outperform a classical computer [6].

### Outline of the thesis

The purpose of this thesis is to develop and assess new surface trap arrays, capable of storing an ion lattice, as well as to investigate and improve technologies related to their operation. The structure of the thesis is as follows. The general working principle of a trapped-ion quantum processor is explained in chapter 2. In chapter 3, the concept of surface trap arrays is introduced, and techniques as well as requirements specific to their operation are discussed. The general experimental setup is described in chapter 4. The subsequent chapters form the main body of the thesis. Chapter 5 introduces the two-dimensional point trap array “Ziegelstadl”. The electrical characterization of the trap chips is described and the reasons for the unsuccessful trap operation are analyzed. In chapter 6, different techniques for the generation of tunable radio-frequency trapping fields are compared. The implementation of such techniques is crucial to enhance the well-to-well interaction between neighboring ions in an ion-lattice. The development and test of a prototype circuit for the implementation of such tunable fields is described. The topic of chapter 7 is the study of a surface trap made from a high-temperature superconductor. The investigations focus on the performance of ultra-low resistance electrodes and signal leads, which will become important for the further advancement of surface traps. In addition, the impact of the high-temperature superconducting trap material on the electric field noise experienced by a single trapped ion are investigated. Additional information on the operation of this trap is summarized in appendix A. In chapter 8, the development of a two-dimensional linear trap array with a reconfigurable ion lattice geometry, referred-to as “Bucket-brigade” trap, is described. Detailed trap simulations are presented, an overview of the fabrication process is given, and the electrical characterization of the fabricated trap chips is discussed. Furthermore, first results of simultaneous trapping of ions in multiple lattice sites are shown. Additional information on the Bucket-brigade trap are given in appendix B. The findings of this thesis are summarized in chapter 9 and an outlook on future experiments is given.

## 2. Ion storage and quantum state manipulation

Charged particles such as atomic ions can be trapped in a combination of static electric and magnetic fields (Penning traps) or by using oscillating electric fields (Paul traps). The big advantage of Paul traps is that the ion positions in an ion crystal are fixed in space and time, which greatly simplifies laser addressing of single ions and groups of ions. Interaction with laser light plays a central role for cooling of the ion motion and for controlling their quantum state. Laser light can be used to manipulate the internal, electronic degrees of freedom, but it also allows one to couple the internal levels to the motional degrees of freedom in the trap. This is the basis for entangling operation between different ions.

In this chapter, the key concepts of a trapped-ion quantum processor are described. The first section explains how particle confinement arises in a Paul trap. In particular, the electrode configuration in surface traps is considered, which are the building blocks of the surface trap arrays described in the later chapters. In the second section, the interaction between stored ions and laser light is explained at the example of the  $^{40}\text{Ca}^+$  ion. The last section provides an introduction to the basic quantum optics toolbox, which allows one to manipulate the quantum state of trapped ions. The discussion focuses on the techniques relevant for this thesis.

### 2.1. Paul trap basics

The purpose of an ion trap is to confine charged particles in all three spatial dimensions. Ideally, for harmonic confinement, one would like to use a static potential of the form

$$\varphi_s = \alpha_x x^2 + \alpha_y y^2 + \alpha_z z^2. \quad (2.1)$$

However, at least one of the coefficients  $\alpha_x, \alpha_y, \alpha_z$  needs to be negative to fulfill Laplace's equation,  $\Delta\varphi = 0$ , such that a static electric potential cannot provide confinement in all directions simultaneously [65]. In Paul traps this problem is overcome by using an oscillating electric quadrupole field to confine ions *dynamically*. The mathematical description and basic operation parameters of a Paul trap are presented in this section.

## 2. Ion storage and quantum state manipulation

### 2.1.1. Electrode configurations

The dynamic confinement of charged particles in Paul traps arises from using a time-varying electric quadrupole potential of the form [66]

$$\varphi_d(t) = \frac{\kappa_d U_{\text{RF}}}{2d^2} (x^2 - z^2) \cos(\Omega_{\text{RF}}t). \quad (2.2)$$

For atomic ions, the field's oscillation frequency  $\Omega_{\text{RF}}$  is on the order of a few tens of MHz, i. e. within the radio-frequency (RF) band. For an ion with positive charge  $Q > 0$  and located at the origin at time  $t = 0$ , this gives an energy potential  $Q\varphi_d(t)$  which is confining along the  $x$ -direction and anti-confining along the  $z$ -direction. At a later time  $t = \pi/\Omega_{\text{RF}}$ , the situation of confining and anti-confining directions is reversed. In this way, ions can be trapped dynamically for an appropriate value of the frequency  $\Omega_{\text{RF}}$  and voltage  $U_{\text{RF}}$ . An important parameter is the dimensionless trap efficiency  $\kappa_d$ , which only depends on the electrode geometry and quantifies the strength of the electric quadrupole at a fixed ion-electrode distance  $d$  and for a given applied voltage  $U_{\text{RF}}$ . In other words,  $\kappa_d$  is a measure of the curvature  $\partial_x^2\varphi_d$  and  $\partial_z^2\varphi_d$  of the quadrupole potential per Volt. Fig. 2.1 shows two examples of electrode geometries that produce an electric quadrupole field<sup>1</sup>. The RF voltage  $U_{\text{RF}}$  is applied to electrodes colored in

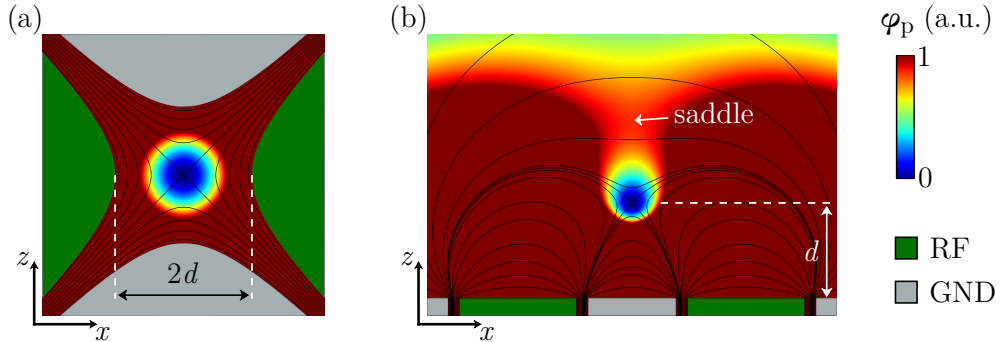


**Figure 2.1.** Realization of an electric quadrupole field in, (a), a macroscopic trap and in, (b), a surface trap. The gray and green areas are the RF and GND electrodes, respectively. The black lines show the simulated equipotential lines forming a quadrupole at the trap center. The pseudopotential  $\varphi_p$ , introduced in section 2.1.3, is displayed as color code with a potential minimum (blue) at the trap center. The color scale is cut off at large values of  $\varphi_p$  for better visibility of the minimum at the trap center. The pseudopotential saddle occurring in surface traps is marked with an arrow.

green. Gray electrodes are connected to the electric ground (GND). For hyperbolically shaped electrodes placed on all four sides around the trap center, as shown in (a), the trap efficiency is optimal with  $\kappa_d = 1$  [66]. Such an electrode arrangement is, however,

<sup>1</sup> Simulations of the electric fields and resulting pseudopotential were done with COMSOL, version 5.3a.

not suited for quantum optics experiments since it severely restricts the optical access for laser beams and ion imaging. This restriction can be lifted by using a blade-like electrode shape [20]. An alternative configuration with sufficient optical access is shown in Fig. 2.1 (b), where all electrodes are arranged in a plane to form a surface trap. The trap efficiency  $\kappa_d$  in a surface trap depends on the exact electrode geometry and is typically significantly less than one, a disadvantage which needs to be compensated by higher RF voltages. For instance, a value  $\kappa_d \approx 0.24$  can be reached for an optimized surface electrode structure [67].

Ion confinement in all three spatial directions can be achieved by revolving the electrode cross sections in Fig. 2.1 around the  $z$ -axis. The result is a point trap with radial symmetry in the  $xy$ -plane as shown in Fig. 2.2 (a) for a surface trap. The quadrupole

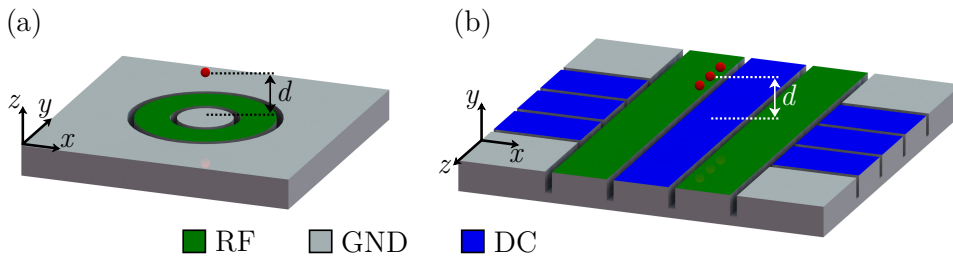


**Figure 2.2.** Electrode configurations in surface traps. (a) An RF voltage applied to a ring-like electrode creates a point trap for a single ion (red sphere) at a distance  $d$  above the electrode plane. (b) Two parallel RF rails create a quadrupole field with translational symmetry, allowing one to trap strings of ions. The ions are confined along the  $z$ -axis by additional static fields provided by the DC electrodes (blue). Note that the  $z$ -axis usually points along the direction of weakest confinement, leading to different conventions for the coordinate systems in (a) and (b).

potential in a point trap is given by the generalization of Eq. (2.2) to three dimensions [66],

$$\varphi_d^{(\text{pt})}(t) = \frac{\kappa_d U_{\text{RF}}}{2d^2} (x^2 + y^2 - 2z^2) \cos(\Omega_{\text{RF}} t). \quad (2.3)$$

In a point trap, the RF potential vanishes in a single point in space, the so-called RF null at  $(x, y, z) = (0, 0, 0)$ . Alternatively, one can achieve a line-like RF null by extruding the cross section along the third dimension, as shown in Fig. 2.2 (b). The result is called a linear trap. By convention, the axis of translational symmetry – the trap axis – is set along the  $z$ -direction. Confinement along the trap axis is achieved by superimposing a static electric field  $\varphi_s$  with positive curvature along  $z$  onto the RF field  $\varphi_d(t)$ . The total electric field applied in a linear trap is thus

$$\varphi^{(\text{lt})}(t) = \frac{\kappa_d U_{\text{RF}}}{2d^2} (x^2 - y^2) \cos(\Omega_{\text{RF}} t) + \frac{\kappa_s U_{\text{DC}}}{2d^2} (z^2 - \alpha_x x^2 - \alpha_y y^2), \quad (2.4)$$

## 2. Ion storage and quantum state manipulation

with  $\alpha_x + \alpha_y = 1$ . The axial confinement in a surface linear trap is typically realized by applying static voltages (DC) to a dedicated set of DC electrodes. The voltage  $U_{\text{DC}}$  can then be seen as a global scaling factor for all individual DC voltages. The dimensionless efficiency parameter  $\kappa_s$  characterizes the strength of the axial confinement per applied DC voltage  $U_{\text{DC}}$ , in analogy to  $\kappa_d$ . Both,  $\kappa_s$  and  $\kappa_d$ , are entirely dependent on the geometry of the trap electrodes [67, 68].

The electric potentials for a point trap, Eq. (2.3), and a linear trap, Eq. (2.4), can be written in a generalized form as [69]

$$\begin{aligned}\varphi(t) &= \varphi_d(t) + \varphi_s \\ &= \frac{\kappa_d U_{\text{RF}}}{2d^2} \cos(\Omega_{\text{RF}} t) \left( \alpha'_x x^2 + \alpha'_y y^2 + \alpha'_z z^2 \right) + \frac{\kappa_s U_{\text{DC}}}{2d^2} \left( \alpha_x x^2 + \alpha_y y^2 + \alpha_z z^2 \right),\end{aligned}\tag{2.5}$$

with coefficients  $\alpha'_x + \alpha'_y + \alpha'_z = 0$  and  $\alpha_x + \alpha_y + \alpha_z = 0$ , that independently fulfill Laplace's equation. The classical ion motion in the general potential of Eq. (2.5) is described by a set of uncoupled differential equations,

$$\left\{ \frac{d^2}{dt^2} + \frac{Q}{Md^2} \left[ \alpha_x \kappa_s U_{\text{DC}} + \alpha'_x \kappa_d U_{\text{RF}} \cos(\Omega_{\text{RF}} t) \right] \right\} x = 0,\tag{2.6a}$$

$$\left\{ \frac{d^2}{dt^2} + \frac{Q}{Md^2} \left[ \alpha_y \kappa_s U_{\text{DC}} + \alpha'_y \kappa_d U_{\text{RF}} \cos(\Omega_{\text{RF}} t) \right] \right\} y = 0,\tag{2.6b}$$

$$\left\{ \frac{d^2}{dt^2} + \frac{Q}{Md^2} \left[ \alpha_z \kappa_s U_{\text{DC}} + \alpha'_z \kappa_d U_{\text{RF}} \cos(\Omega_{\text{RF}} t) \right] \right\} z = 0,\tag{2.6c}$$

where  $Q$  and  $M$  are the ion's charge and mass, respectively.

### 2.1.2. Mathieu equations and trap stability

The three equations of motion, Eq. (2.6), describing the time-evolution of the ion trajectory are each formally identical to the Mathieu equation [66]

$$\left\{ \frac{d^2}{d\xi^2} + \left[ a - 2q \cos(2\xi) \right] \right\} u = 0,\tag{2.7}$$

using the substitutions  $\xi = \Omega_{\text{RF}} t / 2$  and

$$a_i = \frac{4Q\alpha_i \kappa_s U_{\text{DC}}}{Md^2 \Omega_{\text{RF}}^2}, \quad q_i = -\frac{2Q\alpha'_i \kappa_d U_{\text{RF}}}{Md^2 \Omega_{\text{RF}}^2}, \quad \text{for } i \in \{x, y, z\}.\tag{2.8}$$

The general solution of the Mathieu equation (2.7) is bounded as  $\xi \rightarrow \infty$  if the  $a$  and  $q$  parameters are within specific regions of the  $a$ - $q$ -parameter space [66, 70]. Such solutions

are called stable. The stability regions are symmetric upon a sign change  $q \rightarrow -q$  and in practice only positive values of  $q$  are considered [66]. Ion traps in quantum optics experiments are typically operated at small stability values,  $|a_i|, q_i^2 \ll 1$ , in the so-called lowest stability region [69]. In the limit  $|a_i| \ll q_i$ , this region is defined by  $0 \leq q_i \leq 0.908$ . In imperfect Paul traps, the trapping potential can have higher order terms beyond the quadrupole-moment, leading to discrete instabilities at higher  $q$ -values [71]. In practice, stability parameters  $q \lesssim 0.5$  are therefore used. Stable trapping of ions is realized if the stability requirements are met for all spatial dimensions,  $x, y, z$ , simultaneously.

In the limit  $|a_i|, q_i^2 \ll 1$ , the components  $u_i$  of the ion motion are well approximated by [69]

$$u_i(t) \approx A_i \cos(\omega_i t) \left[ 1 + \frac{q_i}{2} \cos(\Omega_{\text{RF}} t) \right], \text{ for } i \in \{x, y, z\}, \quad (2.9)$$

where the secular frequency

$$\omega_i = \frac{\sqrt{a_i + q_i^2/2}}{2} \Omega_{\text{RF}} \quad (2.10)$$

has been introduced. The ion motion described by Eq. (2.9) corresponds to a harmonic oscillation at the secular frequency  $\omega_i$  with amplitude  $A_i$  – the so-called secular motion – which is modulated by a fast oscillation at the drive frequency  $\Omega_{\text{RF}}$ . This fast oscillation is called micromotion since its amplitude  $A_i q_i/2$  is much smaller than that of the secular motion. For the application of ion traps in quantum optics experiments, it is often required to keep the micromotion amplitude at the minimal level given by Eq. (2.9). In realistic trapping situations, however, the micromotion amplitude can be significantly above the minimum, for instance due to stray electric fields pushing the ion away from the RF null [72]. A micromotion amplitude exceeding the ideal minimum of  $A_i q_i/2$  is called excess micromotion and can in many cases be reduced by applying control fields, that move the ions back into the RF null. This process is called micromotion compensation.

The properties of the confining electric fields for point traps and linear traps are summarized in Tab. 2.1. In a point trap, no static fields are required for confinement. With respect to Eq. (2.5), this corresponds to all static field coefficients  $\alpha_i$  being zero, and consequently  $a_i = 0$  for  $i \in \{x, y, z\}$ . The radial symmetry of the RF potential then leads to a degeneracy of the radial modes (the motion along  $x$  and  $y$ ), with secular frequency  $\omega_r \equiv \omega_x = \omega_y = q_y \Omega_{\text{RF}} / \sqrt{8}$ . For the axial mode, it holds that  $\omega_z = q_z \Omega_{\text{RF}} / \sqrt{8} = 2\omega_r$ , since  $\alpha'_x = \alpha'_y = -\alpha'_z/2$ . Typical secular frequencies in quantum optics experiments are on the order of a few MHz. An axial frequency  $\omega_z = 2\pi \times 2.0$  MHz, for instance, can be realized with an RF drive frequency  $\Omega_{\text{RF}} = 2\pi \times$

## 2. Ion storage and quantum state manipulation

20.0 MHz at a stability factor  $q_z \approx 0.3$ . Additional static fields are in practice often superimposed onto the RF field to lift the degeneracy of the radial modes or to fine tune the frequency values. In linear traps, there is no RF confinement along the trap axis,  $q_z = 0$ , and the axial frequency is imposed by a static potential with  $\alpha_z = 1$ , such that  $\omega_z = \sqrt{a_z} \Omega_{\text{RF}}/2 = \sqrt{Q\kappa_s U_{\text{DC}}/(Md^2)}$ . The static field shifts the radial mode frequencies according to Eq. (2.10). In the general case that  $a_x \neq a_y$ , the radial mode degeneracy is lifted. For storage of ion strings, the axial frequency is required to be smaller than the radial frequencies,  $\omega_z < \omega_x, \omega_y$ . Typical operating parameters are axial frequencies  $\omega_z \sim 2\pi \times 1.0$  MHz and radial frequencies  $\omega_r \sim 2\pi \times (2 - 5)$  MHz.

**Table 2.1.** Electric field properties of Paul traps with point-like and line-like RF null. Common values for the stability parameters are  $0.1 \leq q_i \leq 0.5$ ,  $a_i \ll q_i$ . The typical secular frequencies are on the order of a few MHz.

|             | field coefficients                                                                      | stability parameters                         | secular frequencies                    |
|-------------|-----------------------------------------------------------------------------------------|----------------------------------------------|----------------------------------------|
| point trap  | $\alpha'_x = \alpha'_y = 1, \alpha'_z = -2$<br>$\alpha_x = \alpha_y = \alpha_z = 0$     | $q_x = q_y = q_z/2$<br>$a_x = a_y = a_z = 0$ | $\omega_x = \omega_y = \omega_z/2$     |
| linear trap | $\alpha'_x = -\alpha'_y = 1, \alpha'_z = 0$<br>$\alpha_x + \alpha_y = -1, \alpha_z = 1$ | $q_x = q_y, q_z = 0$<br>$a_x + a_y = -a_z$   | $\omega_x \approx \omega_y > \omega_z$ |

### 2.1.3. Pseudopotential approximation

The approximate solution, Eq. (2.9), of the Mathieu equation suggests that the confining effect of the RF field can be described by a ponderomotive pseudopotential [71]

$$\varphi_{\text{p}} = \frac{Q^2}{4M\Omega_{\text{RF}}^2} |E_{\text{RF}}(\mathbf{r})|^2 = \frac{Q^2 \kappa_{\text{d}}^2 U_{\text{RF}}^2}{4M\Omega_{\text{RF}}^2 d^4} \left( \alpha_x'^2 x^2 + \alpha_y'^2 y^2 + \alpha_z'^2 z^2 \right), \quad (2.11)$$

where in the last step the RF electric field amplitude  $E_{\text{RF}}(\mathbf{r})$  corresponding to the RF potential  $\varphi_{\text{d}}$  in Eq. (2.5) was inserted. It is important to note, that the RF pseudopotential in Eq. (2.11) is confining in all three spatial directions, in contrast to the electrostatic potential, Eq. (2.1). The RF pseudopotential is most useful for trap simulations, since it relates the dynamic confinement within a Paul trap to amplitudes of the RF field, which can be efficiently simulated quasi-statically. In Fig. 2.1, the simulated pseudopotential  $\varphi_{\text{p}}$  for the given electrode geometries is displayed as a color code. Within the pseudopotential approximation, the total confining electric potential  $\Phi$  is simply given by the sum of the pseudopotential and additional static potentials,  $\Phi = \varphi_{\text{p}} + \varphi_{\text{s}}$ . Adopting the form of the static potential from Eq. (2.5), one can then express the energy potential  $U_{\text{pot}}$  of a trapped ion in the pseudopotential approximation

as

$$U_{\text{pot}} = Q\Phi = \frac{M}{2} \left( \omega_x^2 x^2 + \omega_y^2 y^2 + \omega_z^2 z^2 \right), \quad (2.12)$$

where the frequencies  $\omega_i$  with  $i \in x, y, z$  are the secular frequencies defined in Eq. (2.10). It is important to add, that the quantization of the harmonic oscillator energy potential given by Eq. (2.12) offers a valid description of the quantum motion in Paul traps [69]. This will be used in section 2.2 to describe the laser-ion interactions.

#### 2.1.4. Trap depth

Within the pseudopotential approximation, the trap depth  $U_0$  can be defined as the minimum energy that a particle, initially at rest and located at the trap center, is required to gain in order to leave the trap. For an ideal trap, as displayed in Fig. 2.1 (a), the trap depth corresponds to the pseudopotential difference between the trap center and the closest electrode,  $U_0 = Q^2 U_{\text{RF}}^2 / (4M \Omega_{\text{RF}}^2 d^2)$ . For instance, for a  $^{40}\text{Ca}^+$  ion in an ideal point trap configuration with ion-electrode separation  $d = 250 \mu\text{m}$ , RF drive frequency  $\Omega_{\text{RF}} = 2\pi \times 30 \text{ MHz}$  and amplitude  $U_{\text{RF}} = 100 \text{ V}$  ( $q_z = 0.43$ ), the trap depth is  $U_0 \approx 2.7 \text{ eV}$ . This is very deep in comparison to the thermal energy of background gas atoms at room-temperature,  $E_{\text{therm}}^{300 \text{ K}} \approx 40 \text{ meV}$ , which may be transferred to a trapped ion in a collision event. In surface traps, the pseudopotential exhibits a saddle point, as seen in Fig. 2.1 (b). The existence of this saddle severely reduces the trap depth. Considering an ideal surface point trap with  $\kappa_d \approx 0.24$  [67], and adjusting  $\Omega_{\text{RF}} = 2\pi \times 15 \text{ MHz}$  to yield a similar stability factor  $q_z = 0.41$  at otherwise identical parameters, one finds that  $U_0 \approx 0.21 \text{ eV}$ . This strong reduction shows the importance of optimizing the electrode geometry in a surface trap with respect to the trap depth.

## 2.2. Laser-ion interaction

Single trapped ions are elementary quantum systems with electronic and motional degrees of freedom, which can be coherently manipulated using the interaction with light fields. The mathematical description of laser-atom interactions is well documented in the literature. The description in this section follows Ref. [69] and is structured as follows: after introducing the  $^{40}\text{Ca}^+$  level scheme, the atom-light interaction is first explained for a free particle. Subsequently, the quantized motion in a harmonic trapping potential is added.

## 2. Ion storage and quantum state manipulation

### 2.2.1. The $^{40}\text{Ca}^+$ ion

Several atomic ion species are suited as qubits in trapped-ion quantum information processors [73, 74]. Desirable characteristics for an ion qubit are a simple level structure that is compatible with established laser cooling techniques and an electronic transition with a long-lived excited state suited to encode and manipulate a qubit state. For the trapped-ion experiments described in this thesis,  $^{40}\text{Ca}^+$  ions were used, whose level scheme is shown in Fig. 2.3 (a). The transitions relevant for Doppler cooling and resolved sideband operations, both further explained in section 2.3, are described in the following. The electronic ground state of  $^{40}\text{Ca}^+$  is the  $4S_{1/2}$  state. The  $4S_{1/2} \leftrightarrow 4P_{1/2}$  transition at 397 nm is used for Doppler cooling, where the short lifetime of the excited  $4P_{1/2}$  state of  $\tau \approx 7.1$  ns, corresponding to a natural linewidth of  $\gamma = 1/\tau \approx 2\pi \times 22.4$  MHz, gives rise to a maximal photon scattering rate of about  $1 \times 10^7$  per second. The  $4P_{1/2}$  state relaxes with a probability of around 6% to the metastable  $3D_{3/2}$  state. Population lost in this channel is restored to the Doppler cooling cycle by driving the  $3D_{3/2} \leftrightarrow 4P_{1/2}$  transition with an 866 nm repump laser. The  $4P_{1/2}$  state also relaxes with a probability of around 1% to the  $3D_{5/2}$  state. The  $3D_{5/2}$  state is metastable with a lifetime of  $\tau = 1.2$  s. The  $3D_{5/2} \leftrightarrow 4P_{1/2}$  transition is driven by an 854 nm laser (6% branching fraction). The  $3D_{3/2} \leftrightarrow 4S_{1/2}$  transition is driven by a 729 nm laser. The  $3D_{5/2} \leftrightarrow 4S_{1/2}$  transition is driven by a 732 nm laser.

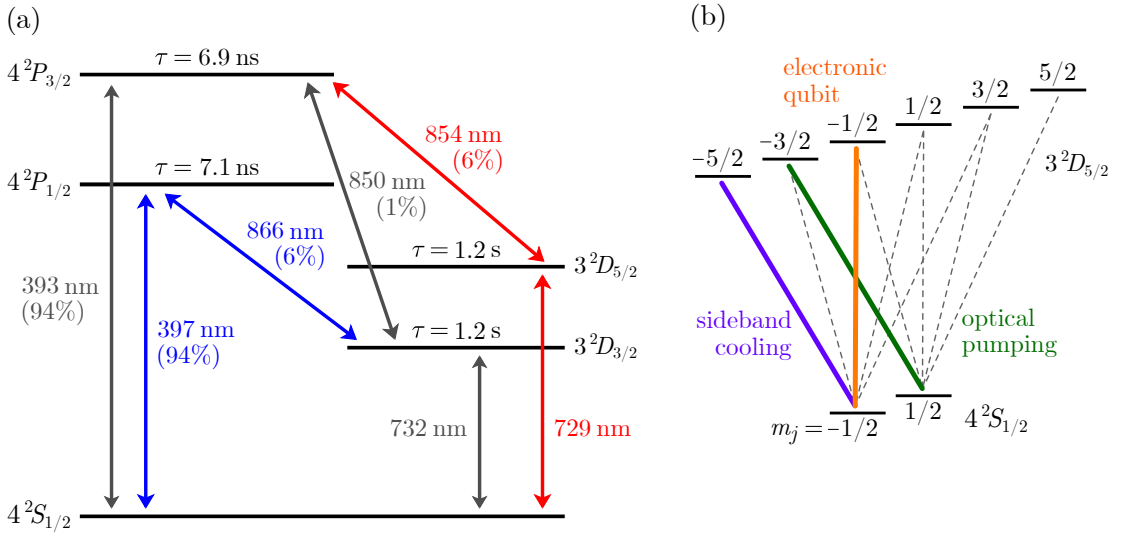


**Figure 2.3.**  $^{40}\text{Ca}^+$  level diagram. (a) Overview of the ground state and first excited states. The transitions used for Doppler cooling and qubit manipulations are highlighted blue and red, respectively. The lifetimes  $\tau$  and branching fractions for spontaneous decay (in parentheses) are taken from Refs. [75, 76] and Refs. [77, 78]. (b) Zeeman manifold of the  $4^2S_{1/2}$  and  $3^2D_{5/2}$  levels. The three quadrupole transitions used in the experiments are highlighted.

The quadrupole transition,  $4S_{1/2} \leftrightarrow 3D_{5/2}$ , with its change of the angular momentum quantum number by  $\Delta l = 2$ , is forbidden by the dipole transition selection rules. The  $3D_{5/2}$  state is therefore metastable with a lifetime of  $\tau = 1.2$  s. The correspondingly narrow natural linewidth of  $\gamma \approx 2\pi \times 0.13$  Hz makes this transition well suited

for resolved sideband spectroscopy with a laser at 729 nm. The long lifetime of the  $3D_{5/2}$  state can be quenched by applying a laser at 854 nm, which pumps the population to the short-lived  $4P_{3/2}$  state, from where it rapidly decays to the ground state. The Zeeman sublevel structure of the  $4S_{1/2}$  and  $3D_{5/2}$  states is shown in Fig. 2.3 (b). The sublevels of the  $4S_{1/2}$  ground state have a splitting of 2.8 MHz/G, the  $3D_{5/2}$  levels are split by 1.7 MHz/G [79]. At an applied magnetic field of a few Gauss, all ten quadrupole-allowed transition can be resolved. For the experiments described in this thesis, three transition are used for specific purposes. The electronic qubit is encoded on the transition  $|1\rangle \equiv 4S_{1/2}(m_j = -1/2) \leftrightarrow 3D_{5/2}(m_j = -1/2) \equiv |0\rangle$ , which is to first order insensitive to magnetic field variations. Population in the  $3D_{5/2}(m_j = +1/2)$  state is optically pumped to the qubit ground state  $|1\rangle$  using the  $4S_{1/2}(m_j = +1/2) \leftrightarrow 3D_{5/2}(m_j = -3/2)$  transition. Sideband cooling is performed on the  $4S_{1/2}(m_j = -1/2) \leftrightarrow 3D_{5/2}(m_j = -5/2)$  transition.

### 2.2.2. Free two-level ion

An ion interacting with a narrow-band coherent laser field is in most situations well approximated by a two-level system. The atomic Hamiltonian is then

$$H_A = \frac{\hbar\omega_0}{2} (|e\rangle\langle e| - |g\rangle\langle g|) = \frac{\hbar\omega_0}{2}\sigma_z, \quad (2.13)$$

where  $\omega_0$  is the energy difference between the electronic ground state  $|g\rangle$  and the excited state  $|e\rangle$ . For the last equality, a mapping to the Pauli matrices

$$\sigma_x = |g\rangle\langle e| + |e\rangle\langle g| \quad (2.14a)$$

$$\sigma_y = i(|g\rangle\langle e| - |e\rangle\langle g|) \quad (2.14b)$$

$$\sigma_z = |e\rangle\langle e| - |g\rangle\langle g| \quad (2.14c)$$

was used. The laser electric field interacting with the atom is treated as a plain wave propagating along  $x$ ,

$$\mathcal{E}(\mathbf{x}, t) = \hat{\epsilon} \mathcal{E}_0 \left[ e^{i(kx - \omega_1 t + \phi_1)} + \text{c.c.} \right], \quad (2.15)$$

where  $\hat{\epsilon}$  and  $\mathcal{E}_0$  are the unit polarization vector and field amplitude,  $k$  is the wave number, and  $\omega_1$ ,  $\phi_1$  are the laser frequency and phase, respectively. The interaction between the laser field and the atom can be written in a general form that holds both for dipole and quadrupole transitions,

$$H_{\text{LA}} = \frac{\hbar\Omega}{2} (\sigma_+ + \sigma_-) \left[ e^{i(kx - \omega_1 t + \phi_1)} + \text{c.c.} \right], \quad (2.16)$$

## 2. Ion storage and quantum state manipulation

with  $\sigma_+ = 1/2(\sigma_x + i\sigma_y) = |e\rangle\langle g|$  and  $\sigma_- = 1/2(\sigma_x - i\sigma_y) = |g\rangle\langle e|$  being the coupling operators between the ground and the excited state in the spin-1/2 algebra. The Rabi frequency  $\Omega$  defines the strength of the laser coupling and is proportional to the transition matrix element  $\langle g|H_{\text{LA}}|e\rangle$  and to the amplitude  $\mathcal{E}_0$  of the laser electric field. The analysis of the dynamics induced by the laser field can be simplified by a transformation to the interaction picture, treating  $H_{\text{LA}}$  as a perturbation of the bare atomic system described by  $H_{\text{A}}$ . The Hamiltonian  $H_{\text{LA}}$  in the interaction picture is given by the unitary transformation

$$\begin{aligned} H_{\text{int}} &= e^{iH_{\text{A}}t/\hbar} H_{\text{LA}} e^{-iH_{\text{A}}t/\hbar} \\ &= \frac{\hbar\Omega}{2} e^{i\omega_0 t\sigma_z/2} (\sigma_+ + \sigma_-) e^{-i\omega_0 t\sigma_z/2} \left[ e^{i(\phi'_1 - \omega_1 t)} + \text{c.c.} \right] \\ &= \frac{\hbar\Omega}{2} \left( e^{i\omega_0 t} \sigma_+ + e^{-i\omega_0 t} \sigma_- \right) \left[ e^{i(\phi'_1 - \omega_1 t)} + e^{-i(\phi'_1 - \omega_1 t)} \right] \\ &\approx \frac{\hbar\Omega}{2} \left[ e^{-i(\delta t - \phi'_1)} \sigma_+ + e^{i(\delta t - \phi'_1)} \sigma_- \right], \end{aligned} \tag{2.17}$$

with  $\delta = \omega_1 - \omega_0$  being the detuning of the laser from resonance and  $\phi'_1 = \phi_1 + kx$ . In the last step, terms oscillating at  $\omega_1 + \omega_0 \gg \delta$  have been neglected in a rotating wave approximation. For a resonant laser,  $\delta = 0$ , Eq. (2.17) further simplifies to

$$H_{\text{int}}^{(\delta=0)} = \frac{\hbar\Omega}{2} \left( e^{i\phi'_1} \sigma_+ + e^{-i\phi'_1} \sigma_- \right). \tag{2.18}$$

The unitary evolution under a resonant light field leads to a coherent population exchange between the states  $|g\rangle$  and  $|e\rangle$ . Starting in the ground state at time  $t = 0$ , the probability for finding the ion in the excited state is then given by

$$P_e(t) = \sin^2(\Omega t/2). \tag{2.19}$$

A measurement of this oscillatory behavior, called Rabi oscillations, is shown in Fig. 2.4 for an excitation on the  $4S_{1/2} \leftrightarrow 3D_{5/2}$  qubit transition in  $^{40}\text{Ca}^+$ . More generally, control of the laser phase factor  $\phi'_1$  and the excitation time  $t$  allows one to realize arbitrary rotations of a qubit state as is further described in section 2.3.2.

Up to now, the limited lifetime of the excited state,  $\tau$ , was neglected. This is admissible for the  $4S_{1/2} \leftrightarrow 3D_{5/2}$  transition in  $^{40}\text{Ca}^+$ , where the spontaneous decay rate satisfies  $\gamma \ll \Omega$ . However, for the  $4S_{1/2} \leftrightarrow 4P_{1/2}$  Doppler cooling transition with its short lifetime of  $\tau \approx 7$  ns, spontaneous decay of the excited state needs to be taken into account. The evolution of the atomic two-level-system, including spontaneous decay of the excited state, can be described with the optical Bloch equations, see e.g. Ref. [81]. For a continuous laser excitation, and neglecting the ion motion, the steady

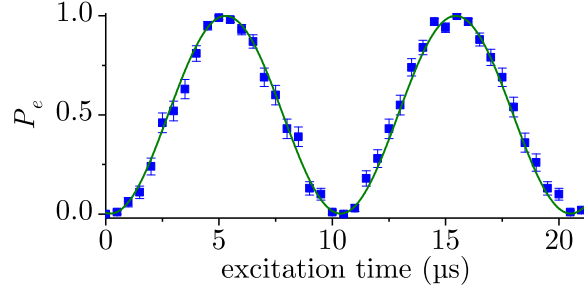


**Figure 2.4.** Experimental data showing Rabi oscillations on the  $4S_{1/2} \leftrightarrow 3D_{5/2}$  qubit transition of a single trapped  $^{40}\text{Ca}^+$  ion. Each data point is an average of 100 experiments and the error bars are given by quantum projection noise [80]. The solid line is a sinusoidal fit. The axial mode of the ion was sideband-cooled to suppress dephasing.

state probability of the ion to be in the excited state is given by

$$P_e^\infty = \frac{s/2}{1 + s + (2\delta/\gamma)^2}, \quad (2.20)$$

where  $s = 2|\Omega|^2/\gamma^2$  is the saturation parameter.

### 2.2.3. Harmonically confined ion

Within the pseudopotential approximation, a trapped ion is confined in a harmonic potential in all spatial directions, cf. Eq. (2.12). The following derivation of the laser-ion interaction is restricted to one spatial direction; the generalization to three dimensions is straightforward. The ion motion is described by a quantum harmonic oscillator

$$H_M = \hbar\omega_{\text{sec}} \left( \frac{1}{2} + n \right), \quad (2.21)$$

where  $\omega_{\text{sec}}$  is the secular frequency and  $n = \hat{a}^\dagger \hat{a}$  is the motional occupation number with  $\hat{a}^\dagger, \hat{a}$  being the raising and lowering operators of the harmonic oscillator. Including the motion into the unperturbed Hamiltonian,  $H_0 = H_A + H_M$ , the laser perturbation Hamiltonian  $H_{\text{LA}}$  in Eq. (2.16) can again be transformed to the interaction picture. For this, it is useful to rewrite the position operators in  $H_{\text{LA}}$  in terms of the creation and annihilation operators,  $x = \eta(\hat{a} + \hat{a}^\dagger)$ . The Lamb-Dicke parameter

$$\eta = k\Delta x \cos \alpha \quad (2.22)$$

thereby relates the extent of the ion wave packet in the motional ground state,  $\Delta x = \sqrt{\hbar/(2M\omega_{\text{sec}})}$ , to the laser wavelength  $\lambda = 2\pi/k$ , and  $\alpha$  is the angle between the secular motion and the laser propagation direction. For the 729 nm quadrupole transition in

## 2. Ion storage and quantum state manipulation

$^{40}\text{Ca}^+$ , and assuming a typical secular frequency of  $\omega_{\text{sec}} = 2\pi \times 1 \text{ MHz}$  with  $\alpha = 45^\circ$ , the Lamb-Dicke factor  $\eta \approx 0.07$  is a small number. The interaction Hamiltonian is then given by

$$\begin{aligned} H_{\text{int}} &= e^{iH_0t/\hbar} H_{\text{LA}} e^{-iH_0t/\hbar} \\ &\approx \frac{\hbar\Omega}{2} e^{i\omega_{\text{sec}}t n} \left[ e^{-i(\delta t - \phi_1)} \sigma_+ e^{i\eta(\hat{a} + \hat{a}^\dagger)} + e^{i(\delta t - \phi_1)} \sigma_- e^{-i\eta(\hat{a} + \hat{a}^\dagger)} \right] e^{-i\omega_{\text{sec}}t n} \quad (2.23) \\ &= \frac{\hbar\Omega}{2} \sigma_+ \exp \left[ i\eta \left( \hat{a} e^{-i\omega_{\text{sec}}t} + \hat{a}^\dagger e^{i\omega_{\text{sec}}t} \right) \right] e^{-i(\delta t - \phi_1)} + \text{h.c.}, \end{aligned}$$

where in the second line the rotating wave approximation was made. In the Lamb-Dicke regime, defined by  $\eta^2(2\bar{n} + 1) \ll 1$  with  $\bar{n}$  being the mean motional occupation number, the interaction Hamiltonian can be Taylor-expanded, which yields to lowest order<sup>2</sup>

$$H_{\text{int}} \approx \frac{\hbar\Omega}{2} \sigma_+ \left[ 1 + i\eta \left( \hat{a} e^{-i\omega_{\text{sec}}t} + \hat{a}^\dagger e^{i\omega_{\text{sec}}t} \right) \right] e^{-i(\delta t - \phi_1)} + \text{h.c.} \quad (2.24)$$

From Eq. (2.24), three terms can be identified. The first term leads to a resonant excitation at a detuning  $\delta = 0$ , the so-called carrier resonance. This carrier term,

$$H_{\text{car}} = \frac{\hbar\Omega}{2} \left( \sigma_+ e^{i\phi_1} + \sigma_- e^{-i\phi_1} \right), \quad (2.25)$$

gives rise to transitions of the type  $|n\rangle |g\rangle \leftrightarrow |n\rangle |e\rangle$  at a rate  $\Omega$  and is identical to the resonant excitation in Eq. (2.18), where the ion motion was neglected. The second term in Eq. (2.24), called first red sideband, is resonant for a detuning of  $\delta = -\omega_{\text{sec}}$  and has the form

$$H_{\text{rsb}} = \frac{\hbar\eta\Omega}{2} \left( \hat{a} \sigma_+ e^{i\phi_1} + \hat{a}^\dagger \sigma_- e^{-i\phi_1} \right), \quad (2.26)$$

where the global phase factor  $i$  was neglected. Excitation on the red sideband drives transitions of the kind  $|n\rangle |g\rangle \leftrightarrow |n-1\rangle |e\rangle$  at a rate

$$\Omega_{n,n-1} = \eta\Omega\sqrt{n} \quad (2.27)$$

and leads to entanglement between the electronic and motional degrees of freedom. The last term in Eq. (2.24) describes transitions on the blue sideband and is resonant for a detuning of  $\delta = \omega_{\text{sec}}$ , with

$$H_{\text{bsb}} = \frac{\hbar\eta\Omega}{2} \left( \hat{a}^\dagger \sigma_+ e^{i\phi_1} + \hat{a} \sigma_- e^{-i\phi_1} \right). \quad (2.28)$$

<sup>2</sup> a more rigorous treatment of the ion motion leads to a slightly smaller Rabi frequency  $\Omega/(1 + q_x/2)$ , where  $q_x$  is the stability  $q$ -factor [69].

Excitation on the blue sideband drives transitions of the kind  $|n\rangle |g\rangle \leftrightarrow |n+1\rangle |e\rangle$  at a rate

$$\Omega_{n,n+1} = \eta\Omega\sqrt{n+1}. \quad (2.29)$$

On a transition with sufficiently small linewidth  $\gamma \ll \omega_{\text{sec}}$  and assuming sufficiently low Rabi frequencies  $\Omega \ll \omega_{\text{sec}}$ , one can spectrally resolve the motional sidebands, as shown in Fig. 2.5 for the  $4S_{1/2} \leftrightarrow 3D_{5/2}$  qubit transition in  $^{40}\text{Ca}^+$ .

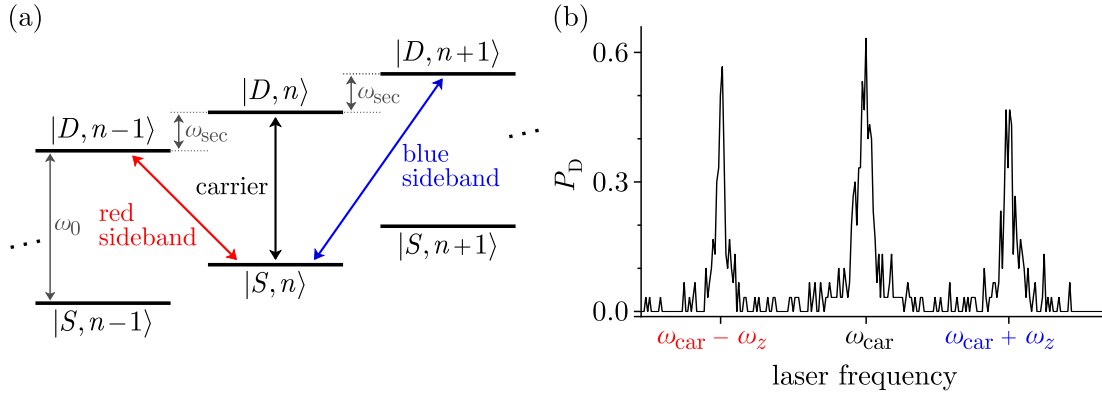


**Figure 2.5.** Resolved sideband spectroscopy on the  $4S_{1/2} \leftrightarrow 3D_{5/2}$  qubit transition. (a) Term scheme of the combined electronic and motional states. The frequency difference between carrier and sidebands equals the secular frequency  $\omega_{\text{sec}}$ . (b) Experimental spectroscopy data showing the mean excitation  $P_D$  to the  $3D_{5/2}$  state as function of the laser frequency. The three peaks correspond to the carrier and axial sidebands at an axial frequency of  $\omega_z \approx 2\pi \times 0.4$  MHz.

## 2.3. Quantum optics toolbox

The laser-ion interaction described in the previous section can be used to manipulate both the electronic and motional degrees of freedom of a trapped ion with high precision. Laser cooling techniques allow one to damp the ion motion into the motional ground state. Coherent manipulations of the quantum state of a single ion or multiple ions confined in the same trapping potential are facilitated by the interaction with a laser field. Such state manipulations are the basis for quantum gate operations in a trapped-ion quantum processor. Moreover, external electric fields can be sensed with high precision by employing the interaction between a laser field and a trapped ion. This section provides an overview of these techniques.

## 2. Ion storage and quantum state manipulation

### 2.3.1. Laser cooling

High-fidelity quantum gate operations require cooling of the ions' motional modes close to the ground state [82–84]. This is typically achieved in a two-step process. First, Doppler cooling is used to reduce the average motional quantum number to around  $\bar{n} \sim 10$ . This is well within the Lamb-Dicke regime, with  $\eta^2(2\bar{n} + 1) \approx 0.1$ , assuming a Lamb-Dicke parameter of  $\eta = 0.07$ . Subsequently, a second cooling step, for instance sideband cooling, damps the ion motion very close to the motional ground state. In the following, the respective cooling techniques are explained.

#### Doppler cooling

In a simple picture, Doppler cooling of a trapped ion can be approximately described with the formalism used for free particles [69]. The key assumptions are that micromotion is sufficiently suppressed and that the secular frequencies  $\omega_{\text{sec}}$  are well below the decay rate  $\gamma$  of the excited state. The latter condition corresponds to assuming that photon scattering happens on a timescale much faster than the oscillation period of the secular motion, which is typically satisfied when driving the  $4S_{1/2} \leftrightarrow 4P_{1/2}$  Doppler-cooling transition in  $^{40}\text{Ca}^+$ . For this transition, the excited state  $P_{1/2}$  relaxes with a small probability to the metastable  $D_{3/2}$  state, cf. Fig. 2.3. A repump laser at 866 nm is therefore used to restore the population to the  $P_{1/2}$  state, thus establishing a closed cooling cycle.

The average force on an ion at rest due to excitation and spontaneous emission cycles on the cooling transition is given by [81]

$$\mathbf{F}_{\text{sc}} = \hbar\mathbf{k} \gamma P_e^\infty, \quad (2.30)$$

which equals the momentum transfer  $\hbar\mathbf{k}$  upon absorption of a photon from the laser field times the photon scatter rate  $\gamma P_e^\infty$ , with the excited state probability  $P_e^\infty$  given by Eq. (2.20). For an ion moving at a velocity  $\mathbf{v} \neq 0$ , the Doppler effect leads to a shift of the laser frequency, which can be described by an effective detuning  $\delta_{\text{eff}} = \delta - \mathbf{k}\mathbf{v}$ . The average force then becomes velocity-dependent, [81, 85]

$$\mathbf{F}_{\text{Doppler}} = \hbar\mathbf{k} \gamma \frac{s/2}{1 + s + (2[\delta - \mathbf{k}\mathbf{v}]/\gamma)^2}. \quad (2.31)$$

For a red-detuned laser beam,  $\delta < 0$ , the mean force is therefore larger when the ion moves towards the laser beam than when it moves away from it. As a consequence, an ion confined in a trap is on average decelerated and its mean kinetic energy approaches the cooling limit given by the Doppler temperature  $k_{\text{B}}T_{\text{Doppler}} \approx 7\hbar\gamma/20$  for  $s \ll 1$  and

$\delta = -\gamma/2$ , where  $k_B$  is the Boltzmann constant [69]. The Doppler limit can be equated with the mean kinetic energy of the secular motion,  $E_n = \hbar\omega_{\text{sec}}(\bar{n} + 1/2)$ . Assuming a secular frequency of  $\omega_{\text{sec}} = 2\pi \times 1$  MHz and using the natural linewidth  $\gamma = 2\pi \times 20$  MHz of the  $4S_{1/2} \leftrightarrow 4P_{1/2}$  Doppler-cooling transition yields a mean phonon number  $\bar{n} = 6.5$  for optimal Doppler cooling conditions.

### Sideband cooling

Cooling beyond the Doppler limit can be achieved by sideband cooling [86]. This requires a transition where the motional sidebands can be resolved, such as the  $4S_{1/2} \leftrightarrow 3D_{5/2}$  transition in  $^{40}\text{Ca}^+$ . In addition, the ion motion needs to be in the Lamb-Dicke regime, which is typically the case after Doppler-cooling. The sideband cooling process can be understood in a simple picture, illustrated in Fig. 2.6. The 729 nm

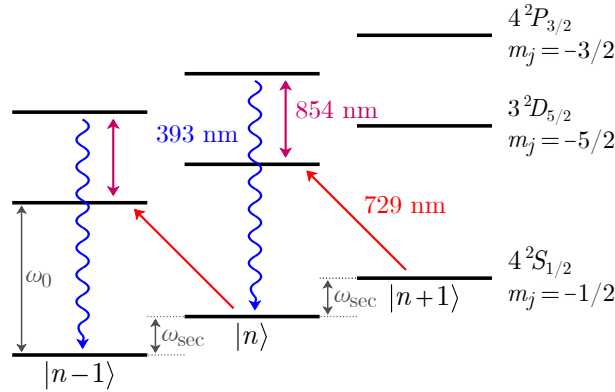


**Figure 2.6.** Illustration of the sideband cooling process. Excitation on the red sideband of the  $4S_{1/2} \leftrightarrow 3D_{5/2}$  sideband cooling transition reduces the motional quantum number  $n$  by one. The  $3D_{5/2}$  state is coupled to the short-lived  $4P_{3/2}$  state, from where the population rapidly decays back to the  $4S_{1/2}$  state, thereby dissipating the motional energy  $\hbar\omega_{\text{sec}}$  to the environment.

cooling laser is detuned by  $\delta = -\omega_{\text{sec}}$  to address the first red sideband of the sideband cooling transition  $S_{1/2}(m_j = -1/2) \leftrightarrow D_{5/2}(m_j = -5/2)$ . Upon excitation to the  $D_{5/2}$  state, the motional quantum number is reduced from  $n$  to  $n - 1$ . The lifetime of the  $D_{5/2}$  state is quenched by the application of an additional 854 nm laser, resonant with the  $D_{5/2}(m_j = -5/2) \leftrightarrow P_{3/2}(m_j = -3/2)$  transition. Within the Lamb-Dicke regime, the excited  $P_{3/2}$  state relaxes predominantly on the carrier transition back to the  $S_{1/2}(m_j = -1/2)$  state. With a small probability, the  $P_{3/2}$  state decays to the  $D_{3/2}$  state, cf. Fig. 2.3. Population lost in this channel is restored by an additional application of the 866 nm laser during sideband cooling. Once the ion has reached the motional ground state,  $|n = 0\rangle$ , the excitation probability to the  $D_{5/2}$  state is zero, cf. Eq. (2.27). The motional ground state is therefore a dark state, into which the motional

## 2. Ion storage and quantum state manipulation

state population is eventually pumped with a probability close to unity.

### 2.3.2. Qubit manipulation

In current trapped-ion quantum processors, a universal set of quantum gates is available, typically comprised of single qubit operations in conjunction with multi-qubit entangling gates [20]. For the implementation of quantum algorithms, as well as for the quantum optics experiments described in this thesis, the same three-step sequence is applied: preparation of the quantum state, state manipulation, and state readout. A brief description of these steps is given in this section. More detailed information can be found in Refs. [20, 69].

#### State preparation

The ground state population of a Doppler-cooled ion is typically distributed evenly over the two Zeeman sublevels  $S_{1/2}(m_j = -1/2)$  and  $S_{1/2}(m_j = 1/2)$ . The first step of the state preparation is to optically pump the entire population to the same Zeeman sublevel, for instance to the  $m_j = -1/2$  state. This is done by addressing the optical pumping transition,  $S_{1/2}(m_j = 1/2) \leftrightarrow D_{5/2}(m_j = -3/2)$ , cf. Fig. 2.3 (b). A simultaneous application of the 854 nm laser couples the metastable  $D_{5/2}$  state to the  $P_{3/2}$  state, from which the population predominantly relaxes to the  $m_j = -1/2$  ground state. Population captured in the  $D_{3/2}$  state is restored by an additional application of the 866 nm laser. For most experiments, the preparation of the electronic state is followed by ground state cooling of the motional state, as described in the previous section.

#### State manipulation

The qubit state is manipulated in a sequence of laser pulse operations. For the trap characterization described in chapter 7, these operations are single laser pulses of variable length and frequency, as further described in the next section. More generally, in the context of quantum computing, quantum algorithms are implemented by subsequent application of elementary gate operations. Arbitrary rotations of a single qubit state, encoded on the  $S_{1/2} \leftrightarrow D_{5/2}$  transition, can be realized by excitation with a resonant laser pulse. The unitary evolution under such an interaction is described by the propagator [16]

$$\begin{aligned}\hat{U} &= \exp\left(-iH_{\text{int}}^{(\Delta=0)}t/\hbar\right) \\ &= I \cos(\theta/2) - i(\sigma_x \cos \phi'_1 - \sigma_y \sin \phi'_1) \sin(\theta/2),\end{aligned}\tag{2.32}$$

where  $H_{\text{int}}^{(\Delta=0)}$  is the resonant interaction Hamiltonian given by Eq. (2.18) and  $I$  is the identity operator. The propagator applied to the qubit state  $|1\rangle$  gives the superposition state  $\hat{U}|1\rangle = \cos(\theta/2)|1\rangle - ie^{i\phi'_1}\sin(\theta/2)|0\rangle$ , where the rotation angle  $\theta = \Omega t$  is controlled by the length  $t$  of the laser pulse and the angle  $\phi'_1$  is set by the laser phase.

Entanglement of the electronic states of different ions can be created by utilizing their collective motion in the confining potential. A widely used approach employs a bichromatic laser pulse which couples the states  $|11, n\rangle \leftrightarrow |00, n\rangle$  of two ions via the intermediate states  $|10, n \pm 1\rangle$  and  $|01, n \pm 1\rangle$  [83]. After a certain time, the laser interaction maps the state  $|11\rangle$  to a maximally entangled state  $(|11\rangle + |00\rangle)/\sqrt{2}$ . The gate can be easily extended to generate entangled states of larger qubit numbers,  $(|111\dots\rangle + |000\dots\rangle)/\sqrt{2}$ , by simultaneously illuminating multiple ions.

### State readout

A projective measurement of the qubit state is performed by exciting the strong  $S_{1/2} \leftrightarrow P_{1/2}$  transition with the Doppler-cooling laser. A qubit superposition state  $\alpha|1\rangle + \beta|0\rangle$  is then projected on either the state  $|1\rangle$  or  $|0\rangle$  with probabilities  $\alpha^2$  and  $\beta^2$ , respectively. If projected to the state  $|1\rangle \equiv S_{1/2}$ , the ion will scatter fluorescence photons at 397 nm, which can be detected electronically using a photomultiplier tube or a CCD camera. The presence or absence of fluorescence is then associated with the two states  $|1\rangle$  or  $|0\rangle$ , respectively. The probabilities  $\alpha^2$  and  $\beta^2$  are reconstructed by repeatedly measuring identically prepared states.

### 2.3.3. Trap characterization

An important characteristic of an ion trap is the magnitude and direction of uncontrolled electric fields, which lead to unwanted forces on the ions. How a trapped ion is affected by such fields, depends on their time-dependence. Static fields, also called stray electric fields, lead to a shift of the ion position away from the RF null, which causes micromotion with an amplitude in excess to the intrinsic amount described by Eq. (2.9). A large amount of micromotion leads to a degradation of the Rabi flop time on the qubit carrier transition, limits the ability to Doppler cool the ion into the Lamb-Dicke regime and can also reduce the uncooled ion lifetime in the trap [72]. Static stray fields may emanate for example from small dust particles on the trap electrodes which get ionized by the lasers, and they can be canceled by applying corresponding DC control fields. This requires, however, a measurement of the amount of micromotion in the first place. A very precise method to determine the micromotion amplitude uses resolved sideband spectroscopy and is explained below.

Time-varying electric fields, typically called electric field noise, can excite the ion's

## 2. Ion storage and quantum state manipulation

secular motion, if the noise has a spectral component that is resonant with one of the secular frequencies. Such an excitation is referred to as motional heating and has detrimental effects on the quantum gate fidelities [87]. Different sources of electric field noise causing motional heating are discussed in chapter 3.3. A way to quantify the amount of heating using sideband spectroscopy is described in the second part of this section.

### Measuring the micromotion amplitude

The micromotion oscillation in a Paul trap leads to an effective modulation of the laser electric field  $\mathcal{E}$  exciting the ion [72]

$$\begin{aligned}\mathcal{E}(\mathbf{x}, t) &= \mathcal{E}_0 e^{ik(x+x_{\text{MM}}) - i\omega_1 t} \\ &= \mathcal{E}_0 e^{i(kx - \omega_1 t)} \sum_{m=-\infty}^{\infty} J_m(\beta) e^{im\Omega_{\text{RF}} t},\end{aligned}\tag{2.33}$$

where  $\mathcal{E}_0$  is the amplitude of the laser electric field without modulation. The term  $x_{\text{MM}}(t) = A_{\text{MM}} \cos \alpha \sin(\Omega_{\text{RF}} t)$  describes the micromotion with amplitude  $A_{\text{MM}}$  and at an angle  $\alpha$  relative to the laser beam, with  $\Omega_{\text{RF}}$  being the RF drive frequency. In the second line of Eq. (2.33), a Bessel function expansion was made, where  $J_m$  is the Bessel function of the first kind. The modulation index  $\beta$  is given by [72]<sup>3</sup>

$$\beta = kA_{\text{MM}} \cos \alpha.\tag{2.34}$$

In the resolved sideband regime, the laser modulation described by Eq. (2.33) manifests as sidebands in the spectrum of a resonant transition with a frequency spacing of the sidebands of  $\Omega_{\text{RF}}$ . The resonant peak at  $m = 0$  is referred to as the carrier and has an excitation strength proportional to  $J_0(\beta)$ . The higher order sidebands with  $m \neq 0$  have relative strengths proportional to  $J_m(\beta)$ . The modulation index  $\beta$ , and therefore the micromotion amplitude along the laser direction, can thus be determined by measuring the Rabi frequencies on different micromotion sidebands. With regard to Eq. (2.33) and employing the proportionality between Rabi frequency and laser electric field,  $\Omega \propto \mathcal{E}$  [69], it holds that

$$\frac{\Omega_c}{\Omega_{m1}} = \frac{J_0(\beta)}{J_1(\beta)},\tag{2.35}$$

<sup>3</sup> the formula corresponds to Eq. (21) in Ref. [72], corrected for the additional factor  $1/\Omega_{\text{RF}}$  which seems to be a mistake.

where  $\Omega_c$  and  $\Omega_{m1}$  are the Rabi frequencies on the carrier and first micromotion sideband, respectively. Assuming that  $\beta \lesssim 2.4$ , the modulation index  $\beta$  is uniquely defined by the ratio of Rabi frequencies in Eq. (2.35). For arbitrarily large  $\beta$ , the Rabi frequency on an additional micromotional sideband has to be measured, to uniquely determine  $\beta$ . In practice, the micromotion amplitude is often minimized by simply minimizing the Rabi rate  $\Omega_{m1}$  on the first sideband.

### Sideband thermometry

The excitation of a secular mode by electric field noise can be quantified in terms of the motional heating rate  $\Gamma_h$ , which is defined as the change of the mean motional quantum number  $\bar{n}$  with time,

$$\Gamma_h = \dot{\bar{n}}. \quad (2.36)$$

For small motional quantum numbers  $\bar{n} \lesssim 1$ , a robust and simple method to determine  $\bar{n}$  is the so-called sideband ratio method. An ion in the electronic ground state  $S_{1/2}$  is excited to the  $D_{5/2}$  state with a resonant laser pulse of duration  $t$  on the red or blue sideband. The probabilities  $P_D^{(\text{rsb})}$  and  $P_D^{(\text{bsb})}$  for a successful excitation on the respective sidebands are then given by [69]

$$P_D^{(\text{rsb})}(t) = \sum_{n=1}^{\infty} P_n \sin^2 \left( \frac{\Omega_{n,n-1}t}{2} \right), \quad (2.37a)$$

$$P_D^{(\text{bsb})}(t) = \sum_{n=0}^{\infty} P_n \sin^2 \left( \frac{\Omega_{n,n+1}t}{2} \right), \quad (2.37b)$$

with the Rabi rates defined in Eqs. (2.27) and (2.29).  $P_n$  is the occupation probability of the motional state  $n$  for which a thermal distribution is typically assumed [69],

$$P_n = \frac{\bar{n}^n}{(\bar{n} + 1)^{n+1}}. \quad (2.38)$$

The ratio  $R = P_D^{(\text{rsb})}/P_D^{(\text{bsb})}$  is then only a function of  $\bar{n}$  [69],

$$\begin{aligned} P_D^{(\text{rsb})}(t) &= \sum_{k=1}^{\infty} \left( \frac{\bar{n}}{\bar{n} + 1} \right)^k \frac{1}{(\bar{n} + 1)} \sin^2 \left( \frac{\Omega_{k,k-1}t}{2} \right) \\ &= \frac{\bar{n}}{\bar{n} + 1} \sum_{k=0}^{\infty} \left( \frac{\bar{n}}{\bar{n} + 1} \right)^k \frac{1}{(\bar{n} + 1)} \sin^2 \left( \frac{\Omega_{k+1,k}t}{2} \right) \\ &= \frac{\bar{n}}{\bar{n} + 1} P_D^{(\text{bsb})}(t). \end{aligned} \quad (2.39)$$

## 2. Ion storage and quantum state manipulation

By measuring the mean excitation on the red and blue sideband of identically prepared motional states, one can then determine the mean motional quantum number as

$$\bar{n} = \frac{R}{1 - R}. \quad (2.40)$$

From the form of Eq. (2.39) it is evident, that the ratio method is most sensitive for motional state numbers  $\bar{n} \lesssim 1$ . For  $\bar{n} \gg 1$ , the ratio  $R$  gets close to one which results in an increasing error in the measured  $\bar{n}$ . An alternative method, suited to determine larger  $\bar{n}$ , is to measure Rabi oscillations on the carrier transition, which shows a dependence on the motional state to second order in  $\eta$  [88],

$$P_D^{(\text{car})}(t) = \frac{1}{2} \left[ 1 - \sum_n P_n \cos((1 - \eta^2 n)\Omega t) \right]. \quad (2.41)$$

The mean motional quantum number  $\bar{n}$  is then found by fitting Eq. (2.41) to Rabi flop data, using  $\bar{n}$  as a free parameter.

### 3. Surface trap arrays

Microfabrication technologies allow one to structure complex electrode patterns required for the realization of advanced surface traps [89–93]. This approach has been used to realize two-dimensional ion lattices with lattice constants  $s_t$  between 40  $\mu\text{m}$  and 500  $\mu\text{m}$  [52–55, 94]. A central aspect for the usage of ion lattices for quantum information processing is the question of how to realize coherent quantum processes across different lattice sites. Coupling of three ions in a triangular array with  $s_t = 40 \mu\text{m}$  has recently been demonstrated using Coulomb-mediated well-to-well interactions [95]. For high-fidelity entangling operations, however, the coupling rate needs to exceed the motional heating rate, which has not been realized up to date. The high heating rates in surface traps stem from the fact that trapping potentials with suitable inter-ion distances  $s_t$  are difficult to realize far from the surface, where lower heating rates can be expected [87]. The requirement of having a small lattice constant  $s_t$  could be relaxed when using different coupling schemes, for instance Rydberg excitation [35] or ultrafast, high-power laser pulses [59]. These approaches are, however, technically challenging, come with their own sets of difficulties and are not further considered in this thesis.

This chapter provides an overview of key concepts relevant for the implementation of an ion-lattice quantum processor based on surface trap arrays. The focus is thereby on two-dimensional point trap arrays and linear trap arrays, where ion-shuttling operations are employed to realize interactions between ions in adjacent lattice sites – an approach that will be further developed in the later chapters. First, general considerations for the design and operation of microfabricated surface trap arrays are given. Subsequently, a Coulomb-mediated coupling mechanism for next-neighbor lattice interactions is explained. This mechanism has been used in the past to observe motional coupling of ions across a DC double-well potential [56–58]. Furthermore, it is described how ion-shuttling can be used to locally enhance the coupling strength between specific trapping sites, as proposed in Ref. [54, 96], and an entangling gate sequence is outlined. The chapter closes with a section on motional heating, including a brief discussion of known sources, their scaling behavior and mitigation methods.

### 3.1. General considerations

The realization and operation of two-dimensional surface trap arrays requires a specific electrode structure in the first place. For the operation of an array, additional aspects such as laser access, loading of ions in different trapping sites, and the implementation of quantum logic operations need to be considered as well. These points are briefly discussed in the following subsections.

#### 3.1.1. Electrode arrangement

Two-dimensional arrays of individual ion traps can be composed of surface point traps or linear traps, as illustrated in Fig. 3.1 for a square lattice of ions. For the case of a point trap array, shown in (a), a single RF electrode is periodically interspersed with GND electrodes allowing confinement of ions in all three spatial directions above their respective GND electrodes. The point-like nature of the RF nulls in this configuration restricts the trapping site occupancy to single ions, since the Coulomb repulsion pushes multiple ions off the RF null where they experience excess micromotion. A point trap array has the advantage that arbitrary ion lattices can be realized by choosing the appropriate pattern for the GND electrodes. In a linear trap array, Fig. 3.1 (b), collinear

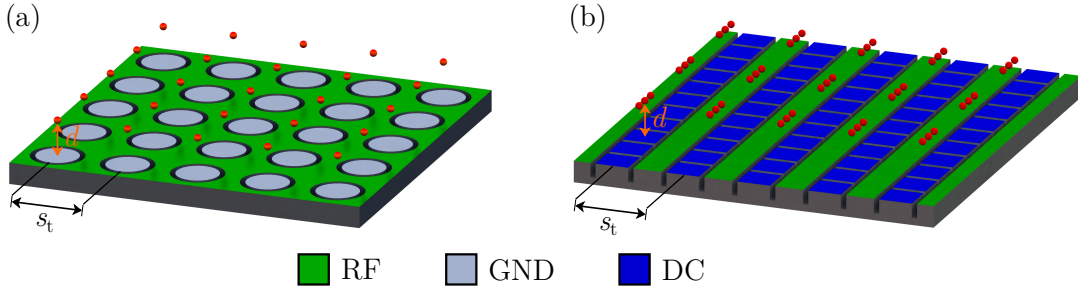


**Figure 3.1.** Surface trap realizations of ion lattices. The individual trapping sites are at a distance  $d$  from the trap surface, with mutual distances given by the lattice constant  $s_t$ . (a) Array of point traps suitable to store a single ion (red spheres) per trapping site. (b) Array of linear traps where multiple ions can be stored in each site.

RF rails are alternated with segmented DC rails, creating parallel linear traps. A square lattice of trapping sites can be created by setting periodic voltages for axial confinement on the DC segments, thus creating a multiwell structure along the trap axes. Triangular lattices can be accomplished by shifting every second line of trapping sites by half a lattice period along the axes of the linear traps. The linear nature of the RF nulls allows storing multiple ions per trapping site without subjecting them to excess micromotion.

A geometric constraint for the design of surface trap arrays arises from the exponential decrease of trapping potentials with increasing ion-surface separation  $d$ , on length scales

given by the electrode dimensions [67]. In other words, a potential landscape created by voltages on a set of electrodes cannot be efficiently maintained at distances  $d$  much larger than the size of the electrodes, since the spatial variation of the potential averages out. In a trap array, this implies that the ion-surface separation  $d$  needs to be smaller than the lattice constant  $s_t$ , which is defined by the periodic structure of the trap electrodes, i. e.,

$$d \lesssim s_t. \quad (3.1)$$

This general design rule, which is typically fulfilled in surface trap arrays [52–55], has severe implications for the miniaturization of such arrays since a smaller lattice constant  $s_t$  can only be achieved by a similar reduction of the ion-surface separation  $d$ . One is therefore confronted with conflicting design goals: On the one hand, reducing the lattice constant  $s_t$  is crucial for the exchange of quantum information between adjacent trapping sites. On the other hand, the motional heating rate typically increases strongly with decreasing ion-surface separation leading to a degradation of quantum gate fidelities [87]. These points are discussed further in sections 3.2 and 3.3.

Fine control over the potential landscape, as required for a realistic operation of surface trap arrays, requires a lot more electrodes than depicted in the simplified illustration, Fig. 3.1. In particular, control electrodes for compensation of stray electric fields (micromotion compensation), for fine control of secular frequencies and mode orientations and for ion shuttling might be desirable. While sub-micron electrodes are feasible using microfabrication technologies [89], two spatial requirements typically limit the number of control electrodes that can be fitted in a trap array: First, control electrodes need to create suitable electric fields at the ion positions which requires a certain electrode size and placement, see e. g. Ref. [68]. Second, electrodes and their connection lines need to have a low electric resistance which typically restricts shrinking them down too much. Examples of a realistic point trap array and linear trap array are presented in chapters 5 and 8, respectively. The issue of connection line resistance is further discussed in chapter 7, where the suitability of a high-temperature superconductor as ultra-low resistivity trap material is investigated.

### 3.1.2. Laser access

As for any ion trap, laser access has to be considered during the design of a trap array. The ion-surface separation  $d$  typically sets the dimension of the waist of laser beams propagating along the chip surface, because stray light from the surface has to be avoided. Furthermore, one has to consider the expansion of the typically used Gaussian laser beams, which can lead to clipping of the laser beam at the chip edge. For arrays of

### 3. Surface trap arrays

moderate size, the trap chip can be structured to avoid clipping, for instance by etching or laser dicing. Beams parallel to the chip surface are not suitable if the array dimension significantly exceeds the beams' Rayleigh lengths. In such cases, beams propagating perpendicular to the chip surface and passing through dedicated slots might be used. Through-chip slots can also help to avoid charging of the trap chip induced by laser light [97–99] and have been realized in surface ion traps, see e.g. Ref. [91]. However, slots significantly add to the complexity of the trap fabrication. In more advanced designs, integrated optics such as waveguides [100] or diffractive mirrors [101, 102] could be used as well.

#### 3.1.3. Array operation

The large amount and the spatial proximity of trapping sites in trap arrays require specific experimental techniques for their operation. Besides qubit coupling across the trapping sites, discussed in the next section, these include techniques for lattice loading, addressed qubit operations and state readout. Site specific loading of ions can be achieved by using a two-step ionization process with two orthogonal photoionization lasers crossing at the location of a trapping site. This approach, when combined with a pre-cooled source of atoms, allows for fast and reliable loading without diminishing the lifetime and coherence of ions in adjacent sites [53]. Single qubit gates with very little crosstalk to adjacent ions have been demonstrated using waveguides with Bragg couplers integrated into the trap chip [100]. Another approach for single qubit gates would be the usage of global microwave radiation fields in combination with magnetic field gradients [103] or the usage of a qubit Raman transition [22], employing the crossed Raman beam geometry to address a specific ion. Qubit readout requires a detection method, which spatially resolves the individual ions, such as a CCD camera. Alternatively, the fluorescence of each trapping site could be imaged onto an individual channel of a multi-channel photo-multiplier tube detector [104]. Global qubit operations and tasks such as laser cooling and optical pumping, can be performed simultaneously on all trapping sites using global laser beams. A setup for the production of highly-elliptical beams for Doppler-cooling illuminating multiple trapping sites at once is described in chapter 4.2.2.

Excellent vacuum conditions are another crucial aspect for the operation of surface trap arrays. The large number of stored ions and the relatively shallow trapping potentials in surface traps make it desirable to reduce both the number and kinetic energy of background gas particles, thus mitigating the impact of collisions. Both can be achieved by operating the trap array in a cryogenic environment at temperatures of a few K, where extremely low pressures have been demonstrated [105].

## 3.2. Tunable well-to-well interactions

One of the key ingredients for a quantum processor based on surface trap arrays is the creation of entanglement between ions. For ions confined within the same trapping site, state-of-the-art protocols employing the shared ion motion can be used for this task [16, 20]. For entangling operations between ions in different sites, motional coupling can still be mediated by the Coulomb interaction [58]. However, the coupling strength  $\Omega_c \propto 1/s_t^3$  in this approach depends crucially on the inter-ion distance  $s_t$ . The basic interaction mechanism is described below, following the derivation in Refs. [56–58]. Subsequently, a way to enhance the coupling rate by local shuttling operations and an outline for a simple entangling sequence are presented.

### 3.2.1. Interaction mechanism

Ions confined in individual trapping sites of a lattice interact with their neighbors due to the Coulomb interaction, which couples their secular motion as illustrated in Fig. 3.2. The dominant coupling term is a dipole-dipole interaction [56]. This can be intuitively

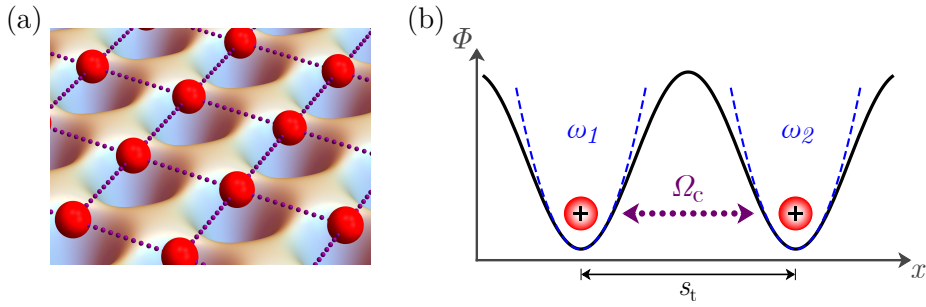


**Figure 3.2.** Motional coupling between ions in individual trapping sites. (a) Illustration of a lattice potential generated by a trap array. Ions (red spheres) are confined at small mutual distances such that motional coupling mediated by the Coulomb interaction (purple dots) becomes relevant. (b) Cross section through two adjacent trapping sites. The motion of the two ions is strongly coupled when the secular frequencies are resonant,  $\omega_1 = \omega_2$ . The coupling strength  $\Omega_c$  crucially depends on the inter-ion distance  $s_t$ .

understood when considering the ions in their respective wells as oscillating charges  $Q$ , separated by a distance  $s_t$  much larger than their oscillation amplitudes  $\Delta\mathbf{r}$ . The interaction potential of two dipoles associated with a specific secular mode is then [106]

$$U_{\text{dd}} = \frac{1}{4\pi\epsilon_0} \frac{\mathbf{d}_1\mathbf{d}_2 - 3(\mathbf{d}_1\hat{\mathbf{s}}_t)(\mathbf{d}_2\hat{\mathbf{s}}_t)}{s_t^3}, \quad (3.2)$$

where  $\mathbf{d}_{1,2} = Q\Delta\mathbf{r}_{1,2}$  are the electric dipole moments of the two ions,  $\hat{\mathbf{s}}_t$  is the unit vector of their relative position and  $\epsilon_0$  is the electric constant. While in principle arbi-

### 3. Surface trap arrays

trary secular modes can be coupled by the dipole-dipole interaction  $U_{\text{dd}}$ , the following discussion is restricted to modes with aligned dipole moments,  $\mathbf{d}_1 \parallel \mathbf{d}_2$ , which are either parallel or orthogonal to  $\hat{\mathbf{s}}_t$ . Writing the secular motion in terms of creation and annihilation operators  $a^\dagger, a$  of the confining harmonic oscillators,  $\Delta\mathbf{r} = \sqrt{\hbar/(2m\omega)}(a + a^\dagger)$ , and neglecting fast oscillating terms (rotating wave approximation), the dipole-dipole potential is, up to a sign, given by [57]

$$U_{\text{dd}} \approx \frac{\hbar\Omega_c}{2}(a_1a_2^\dagger + a_1^\dagger a_2), \quad (3.3)$$

with a motional coupling rate

$$\Omega_c = \frac{\varsigma Q^2}{2\pi\epsilon_0 M} \frac{1}{\sqrt{\omega_1\omega_2} s_t^3}, \text{ and } \varsigma = \begin{cases} 1 & \text{for } \mathbf{d}_{1,2} \parallel \hat{\mathbf{s}}_t \\ 1/2 & \text{for } \mathbf{d}_{1,2} \perp \hat{\mathbf{s}}_t \end{cases}. \quad (3.4)$$

Here  $M$  is the ions' mass and  $\omega_1, \omega_2$  are their uncoupled motional frequencies. The Eigenfrequencies of the motional modes in the coupled basis are given by [58]<sup>1</sup>

$$\tilde{\omega}_1 = \bar{\omega} + \sqrt{\delta_{\text{well}}^2 + \Omega_c^2/4} \quad (3.5)$$

$$\tilde{\omega}_2 = \bar{\omega} - \sqrt{\delta_{\text{well}}^2 + \Omega_c^2/4}, \quad (3.6)$$

with the average well frequency  $\bar{\omega} = (\omega_1 + \omega_2)/2$  and the relative well detuning  $\delta_{\text{well}} = (\omega_2 - \omega_1)/2$ . For a large detuning  $\delta_{\text{well}} \gg \Omega_c$  the motion of the two ions can be considered independent. In the resonant case,  $\delta_{\text{well}} \approx 0$ , the ions' motion is strongly coupled and the motional frequencies show an avoided crossing with a splitting of  $\Omega_c$  [56, 57]. The coupling rate  $\Omega_c$  then defines the rate at which the two harmonic oscillators exchange their motional excitations. Assuming an initial motional state  $|n_1, n_2\rangle$ , the ions' motional quantum numbers  $n_1, n_2$  will swap under evolution of the dipole-dipole interaction after a time  $\tau_{\text{swap}} = \pi/\Omega_c$ . For arbitrary times, the ions' motion will be in an entangled state with all other motional states that satisfy energy conservation. In particular, the state  $|0, 1\rangle$  will evolve to a fully entangled state  $(|0, 1\rangle + |1, 0\rangle)/\sqrt{2}$  after a time  $\tau_{\text{swap}}/2$  [57].

#### 3.2.2. Ion shuttling for enhanced interaction strength

The motional coupling strength  $\Omega_c$  depends crucially on the inter-ion distance  $s_t$ , cf. Eq. (3.4). Assuming, for instance, a lattice of  $^{40}\text{Ca}^+$ -ions with mutual distance  $s_t = 500 \mu\text{m}$  identical to the array in Ref. [53], and further assuming a typical secular frequency of  $\omega = 2\pi \times 1 \text{ MHz}$  and  $\varsigma = 1$ , one calculates a motional coupling rate of

<sup>1</sup> the definition of  $\Omega_c$  in Ref. [57] and used here differs to that in Refs. [56, 58] by a factor two.

$\Omega_c \approx 2\pi \times 1.4$  Hz. This corresponds to a swap time of  $\tau_{\text{swap}} \approx 2.2$  s, about twice as long as the lifetime of the  $D_{5/2}$  qubit state and not suited for gate operations in a quantum processor. In contrast, the ion lattice presented by Mielenz et al. [55], designed as prototype of a 2D quantum simulator, has a lattice constant of  $s_t = 40$   $\mu\text{m}$ . The corresponding coupling rate for  $^{40}\text{Ca}^+$  ions would be  $\Omega_c \approx 2\pi \times 2.7$  kHz for otherwise identical parameters, and coherent motional exchange has indeed recently been demonstrated in this array by Hakelberg et al. [95]. However, for an array with such a small lattice constant, the small ion-surface separation  $d$  required by the trap array design rule, Eq. (3.1), is likely to cause a high motional heating rate (see section 3.3). In fact, the array used by Hakelberg et al. has an ion-surface separation  $d = s_t = 40$   $\mu\text{m}$  and the observed heating rate is on par with the motional coupling rate,  $\Gamma_h \approx \Omega_c$ , limiting the fidelity of the coupling process on a single motional quanta level [95].

The trap array design rule  $d \lesssim s_t$  may be relaxed using local shuttling operations, which reduce the distance between selected trapping sites for the time of a gate operation while leaving the rest of the array unaffected. This approach, originally proposed by Kumph et al. for point trap arrays [96], is illustrated in Fig. 3.3. In a point trap array,

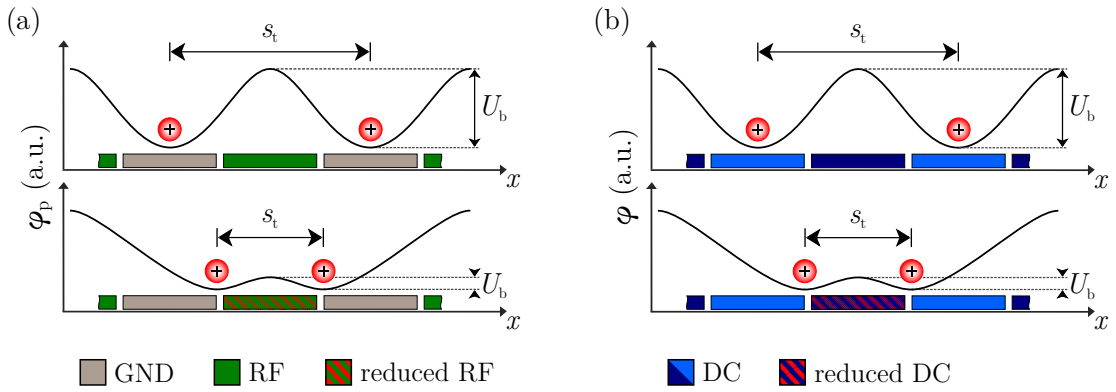


**Figure 3.3.** Illustration of local ion-shuttling operations in surface trap arrays. (a) In a point trap array and across the radial direction of a linear trap array, the confining multiwell potential is created by RF voltages. The inter-ion spacing  $s_t$  can be decreased by reducing the RF voltage in between two trapping sites. This comes along with a reduction of the pseudo potential barrier  $U_b$ . (b) Along the axial direction of a linear trap array, multiwells are created by DC voltages on the segmented DC rails. A decrease of the inter-ion spacing  $s_t$  is achieved by reducing the DC voltage on the electrode between two sites.

(a), ions in adjacent trapping sites are separated by a potential barrier  $U_b$  created by the confining RF potential. A local reduction of the RF voltage on the electrode in between the sites (green and red striped) lowers the size of  $U_b$  and reduces the inter-ion distance  $s_t$ . As a side effect, the curvature of the confining potential is also diminished, leading to a lower secular frequency  $\omega_x$ . This additionally enhances the coupling rate  $\Omega_c$  if that mode is used for the interaction. The shuttling process works identical for

### 3. Surface trap arrays

the radial direction in a linear trap array, with one modification: the RF voltage is attenuated on an RF rail which changes the RF null for both adjacent linear traps along the entire length of the lattice. Along the axial direction of a linear trap array, the DC multiwell spacing can be controlled by the applied DC voltages. A simplified scenario is depicted in Fig. 3.3 (b). A positive DC voltages on the electrode between two trapping sites (dark blue) and comparably more negative voltages on the electrodes below the sites (light blue) create a potential barrier  $U_b$ . Upon reduction of the positive DC voltage on the central electrode (blue and red striped), the inter-ion separation  $s_t$  is again reduced, in complete analogy to the RF case. In a more realistic scenario, the shuttling might require multiple DC control voltages to be changed simultaneously to keep the ions positioned in the RF null.

The local shuttling operations described above can be used to realize a configuration  $s_t < d$  for the limited time required for a gate operation. If this time is kept short, a loss of cold ions due to a decreased trap depth is unlikely. Nevertheless, well-defined trapping potentials need to be sustained during the entire shuttling sequence. For instance, the potential barrier  $U_b$  at a reduced distance  $s_t$  needs to remain large enough to prevent merging of the trapping sites by uncontrolled stray electric fields from the chip surface. A quantitative understanding of the impact of local shuttling operations on the overall trapping potential can be gained by trap simulations of the electrode geometry, as it is shown in chapters 5.4.3 and 8.2.1. Additional constraints on the minimal value of  $s_t$  might be imposed by the electric strength of the trap material, which restricts the amplitude of applicable voltages; when operating in the regime  $s_t < d$ , substantially higher voltages are typically necessary to achieve a given confinement. The amount of voltage tunability in the RF domain might be limited as well, as discussed in detail in chapter 6.

#### 3.2.3. Outline of an entangling scheme

The design of the trap arrays described in this thesis is such as to confine ions in individual sites of a periodic lattice potential at a mutual distance  $s_t \approx 100 \mu\text{m}$  to  $s_t \approx 300 \mu\text{m}$ . This distance is locally reduced to  $s_t \approx 50 \mu\text{m}$  for entangling gate operations between ions in adjacent trapping sites using RF and DC control voltages. The general scheme envisioned for these entangling operations is as follows:

1. Ions in adjacent trapping sites are moved close to each other using a local shuttling process which is adiabatic in comparison to the secular frequencies  $\omega \sim 2\pi \times 1.0 \text{ MHz}$  to avoid motional excitation.
2. The ions' secular motion of a particular mode is strongly coupled by bringing their motional frequencies to resonance, using DC control voltages.

3. The ions electronic states are entangled under irradiation with suitable laser fields [58, 83].
4. The secular frequencies are tuned away from resonance to decouple the ions' motion.
5. The ion-ion separation  $s_t$  is restored adiabatically to the original value.

The limiting timescale of the above entangling scheme is set by the motional coupling rate  $\Omega_c$ , unless the actual entangling operation (step 3) is replaced by a so-called “fast gate” [59, 107]. At a reduced ion separation  $s_t \approx 50 \mu\text{m}$  and assuming a motional frequency of  $\omega \sim 2\pi \times 1.0 \text{ MHz}$ , one finds that  $\Omega_c \approx 2\pi \times 1.4 \text{ kHz}$  for  $^{40}\text{Ca}^+$ -ions, cf. Eq. (3.4). The shuttling processes (steps 1 and 5) as well as the secular frequency tuning (steps 2 and 4) should be fast compared to  $\Omega_c$ , to keep the entire sequence short, and they should be slow compared to the secular frequencies  $\omega \sim 2\pi \times 1.0 \text{ MHz}$  to avoid motional excitation (adiabatic limit). Under such conditions, the minimal time required for the entire entangling sequence would be around  $T_{\text{gate}} \sim 2\pi/\Omega_c \approx 0.7 \text{ ms}$ , which is almost a factor  $10^5$  shorter than the best coherence times  $T_2^* = 50 \text{ s}$  achieved with  $^{43}\text{Ca}^+$ -ions [21]. The motional coupling rate  $\Omega_c$  could be further enhanced using several ions per trapping site [57].

### 3.3. Motional heating

Motional heating describes the random excitation of the secular motion of trapped ions by a fluctuating electric field and is an important source of decoherence in trapped-ion quantum computers [108, 109]. Motional heating drives the ions out of the Lamb-Dicke regime, thus limiting the number of quantum gates that can be consecutively applied. Furthermore, motional heating also affects the fidelity of a single entangling gate [83, 84]. While heating in macroscopic traps is often too small to be a limiting factor, it is a severe impediment for the development of large-scale quantum processors based on surface traps due to the strong scaling of the heating rate with the ion-surface separation  $d$  [110, 111]. The origin of the heating in surface traps is generally associated with processes on the chip surface, but the microscopic mechanisms behind it remain an open field of research [87].

In the following, important sources of motional heating as well as their scaling behavior are described. In particular, a connection between the distance scaling of surface noise and the scaling of the motional coupling rate  $\Omega_c$  described in the previous section is made. Finally, methods to mitigate motional heating are discussed.

### 3. Surface trap arrays

#### 3.3.1. Sources of electric field noise

The heating rate  $\Gamma_h$  is defined as the increase of the average motional quantum number  $\bar{n}$  with time, cf. Eq. (2.36). Motional heating is fundamentally caused by electric field noise coupling to the ion's charge and driving the secular motion. The relation between the heating rate  $\Gamma_h$  and the electric field noise spectral density  $S_E$  is given by [87]

$$\Gamma_h = \frac{Q^2}{4M\hbar\omega} S_E, \quad (3.7)$$

where  $\hbar$  is the reduced Planck constant,  $Q$  and  $M$  are the ion's charge and mass and  $\omega$  is its secular frequency. The origin of electric field noise is diverse, but noise sources relevant for surface ion traps typically fall into one of three categories: technical noise, Johnson-Nyquist noise, and surface noise [87], which are described below. Information on the dominant noise source can be gained by measuring the scaling of the heating rate  $\Gamma_h$  with frequency  $\omega$ , trap chip temperature  $T$  and ion-surface separation  $d$ .

Technical noise is typically associated with drive electronics such as RF or DC power supplies, but also includes pickup noise from the laboratory environment on the cabling entering the vacuum vessel. Technical noise does not have a specific scaling with frequency  $\omega$ , since it may be caused by diverse external sources. For the same reason, technical noise is also independent of the temperature  $T_{\text{trap}}$  of the trap chip, opening a way to distinguish it from on-chip noise sources like surface noise if the setup allows for variation of  $T_{\text{trap}}$ . Furthermore, technical noise penetrating through trap supply lines can be electrically filtered, which is a more practical method of noise distinction and allows one to make technical noise contributions (in principle) arbitrarily small. Johnson-Nyquist noise (JN) is caused by thermal fluctuations of charge carriers and is present in any resistor  $R$ . JN has a voltage noise spectral density [112, 113]

$$S_V^{(\text{JN})} = 4k_B T R, \quad (3.8)$$

where  $T$  is the temperature of the resistor and  $k_B$  is Boltzmann's constant. The flat frequency dependence of JN (white noise) may be altered by electrical filters placed between the resistor causing the noise and the trap electrode it is connected to. The temperature  $T$  in Eq. (3.8) is that of the resistor and might be independent of the trap chip temperature  $T_{\text{trap}}$ . In practice, a clear distinction between JN and technical noise is often difficult and requires precise knowledge of the transfer function of the electrical filters and an accurate estimate of the JN level of the resistors in the setup. Technical noise and JN lead to voltage noise  $S_V$  on the trap electrodes, which translates to electric

field noise  $S_E$  at the position of the ion, [87]

$$S_E = \frac{S_V}{\delta_c^2}, \quad (3.9)$$

with the characteristic distance  $\delta_c$  being a geometry-dependent quantity that defines the conversion between voltage noise on a given trap electrode and electric field noise at the ion position. A general relation between  $\delta_c$  and the ion-surface separation  $d$  is not given. The term “surface noise” comprises multiple sources of electric field noise originating from metallic and dielectric surfaces in the vicinity of trapped ions, foremost the trap chip itself. Such noise can be significant, as shown by in situ cleaning experiments where the heating rate was reduced by two orders of magnitude [114, 115]. However, the microscopic mechanisms behind the sources of surface noise are not well understood [87]. Prominent examples of models proposed to explain the experimental findings are fluctuating patch potentials, adatom dipole fluctuators and adatom diffusion [87]. These models typically predict a strong dependence of the noise on the ion-surface separation  $d$ , mostly  $S_E \propto d^{-4}$ , which was recently observed experimentally [110, 111]. The typically predicted frequency dependence scales as  $S_E \propto 1/\omega$  and the noise is generally considered to be thermally activated, i. e., it increases with rising trap chip temperature  $T_{\text{trap}}$  [87].

It is illustrative to compare the predicted distance scaling of surface noise with the scaling of the motional coupling rate  $\Omega_c$ . This can be done by assuming that the lattice constant  $s_t$  in a trap array is similar to the ion-surface separation  $d$ , i. e.,  $s_t \sim d$ , as suggested by the trap array design rule, Eq. (3.1). In this case one finds that  $\Omega_c \propto d^{-3}$ , cf Eq. (3.4). Clearly, for the design of trap arrays in which high-fidelity entangling gates are to be realized, one would like to choose the ion-surface separation  $d$  in such a way that the condition  $\Omega_c \gg \Gamma_{\text{dec}}$  is best fulfilled, where  $\Gamma_{\text{dec}}$  is the dominant decoherence rate. Such an optimization is currently out of reach, due to the lack of knowledge of what actually causes surface noise and of how to build an ion trap with a specific heating rate. However, one can argue that the optimal ion position is likely to be not extremely close to the surface, given the fact that the motional heating rate – one of the sources of decoherence – scales as  $\Gamma_h \propto d^{-4}$  for many kinds of surface noise. In fact, the only two-dimensional ion lattice where motional coupling has been observed has an ion-surface separation of  $d = 40 \mu\text{m}$  and is limited by motional heating with  $\Gamma_h \approx \Omega_c$  [95]. This is the main motivation for choosing a larger ion-surface separation,  $d = 80 \mu\text{m}$  and  $d = 120 \mu\text{m}$ , for the linear trap array described in chapter 8.

### 3. Surface trap arrays

#### 3.3.2. Noise mitigation

Several approaches are known to decrease the electric field noise experienced by a trapped ion. For technical noise, the obvious strategy is to use low-noise supply electronics in the first place and to electronically filter all connection lines that enter the vacuum vessel, in particular those connected to trap electrodes. JN can be reduced by using low-resistance materials for trap electrodes and connection lines. Care needs to be taken in the design of electronic filters, which may contain resistive components that produce JN. For surface noise, there is no recipe regarding trap materials and surface properties that ensures a low heating rate. However, two general trends have been observed. First, in situ cleaning of the trap surface can drastically reduce the heating rate [114–116]. Second, the noise level is typically reduced by about two orders of magnitude when operated at cryogenic temperatures ( $\sim 10$  K), in agreement with the general understanding that sources of surface noise are thermally activated [37]. The reduced motional heating, together with the extremely low achievable pressure, are the main arguments for the operation of surface trap arrays in a cryogenic environment.

## 4. Experimental setup

The experimental setup for the trapped-ion experiments described in this thesis is composed of three elements: a cryogenic vacuum vessel with integrated passive electronics, an optical setup and an experimental control system. The cryogenic vacuum system provides the ultra-high vacuum (UHV) environment required for ion storage and state manipulation at a typical operating temperature of  $T \approx 10$  K. The integrated electronics are used for enhancing the RF drive voltage and low-pass filtering the DC voltages. The optical setup produces the various laser beams at the required wavelengths and allows for beam steering and intensity as well as frequency tuning. The computer control system administers the hardware and manages the sequences of laser pulses sent to the ions for quantum state manipulation. In the following sections, an overview of the three elements of the experimental setup is given.

### 4.1. Cryogenic vacuum vessel

The cryogenic vacuum vessel with the integrated electronics is specifically designed for a quick replacement of ion traps, allowing for a fast assessment of different trap designs on timescales of a few days. A general overview is provided in the first section. The cryogenic electronics are described subsequently. Detailed information on the entire system can be found in the PhD thesis of Michael Niedermayr [117].

#### 4.1.1. General setup

The cryogenic vacuum system, schematically shown in Fig. 4.1, consists of an 8" spherical octagon attached to a vacuum casing. The evacuated area is between this outer casing and the coldhead mounted within. The coldhead contains the combined displacer and regenerator of a Gifford-McMahon closed-cycle cryostat which provides the cooling of the setup. Within the coldhead, the temperature is decreased in two stages with an intermediate temperature of about 50 K and a final base temperature of about 10 K. Two radiation shields made from 5 mm thick copper and thermally connected to the two cooling stages create a cryogenic environment for the trap chip and the cryogenic electronics within the spherical octagon. Electrical connectivity for trap operation is provided by 20 coaxial cables that are thermally anchored at each of the two cooling

#### 4. Experimental setup

stages and that connect to BNC feedthroughs at the outer housing of the vacuum vessel. Unshielded cables for the readout of temperature diodes and heating of the cold stages for faster warm-up are connected to a D-sub feedthrough (not shown). Optical access for laser manipulation is provided by windows in the heat shields on axis with the octagon's viewports. Viewports and windows have a broadband anti-reflection coating. The ions are imaged through an additional window at the bottom flange of the setup. Fig. 4.1 (b) shows a cross section through the octagon with the beam paths of the lasers.

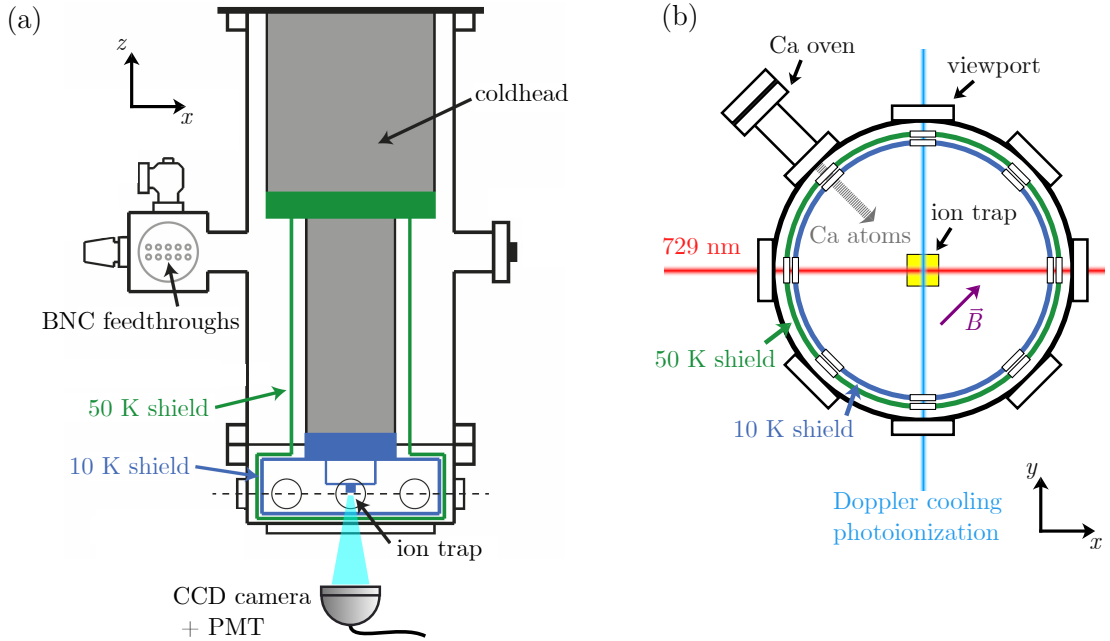


**Figure 4.1.** Cryogenic vacuum system. (a) Cross section through the vacuum vessel. The ion trap is thermally anchored to the coldhead and enclosed by the 10 K and the 50 K heat shields. Electrical signals enter the vessel via feedthroughs. Ions are imaged through viewports at the bottom of the setup. (b) Cross section through the bottom part of the vacuum vessel. Ions are loaded from a calcium oven. Optical access for Doppler cooling, photoionization and the qubit laser at 729 nm is possible from two perpendicular directions, at 45° to the quantization axis set by the magnetic field  $\vec{B}$ . Figure adapted from Ref. [117].

The lasers for Doppler cooling (397 nm and 866 nm) and photoionization (422 nm and 377 nm), as well as the 854 nm repumper, are sent along the same path for initial ion trapping. A more tightly focused 397 nm Doppler cooling beam is sent in the opposite direction along the same path for an independent and more precise alignment of the Doppler cooling beams. The tighter focus reduces stray light from the chip surface. A second, perpendicular beam path is used for the qubit laser at 729 nm. The ions' quantization axis, defined by the magnetic field  $\vec{B}$  from coils outside the vacuum chamber, is at 45° relative to both beam paths. Ions are loaded by photoionization of a flux of neutral calcium atoms. These atoms are generated in an oven at the room-temperature

side of the vacuum setup and ballistically move through apertures in the heat shields.

#### 4.1.2. Cryogenic electronics

The trap chip is mounted on a copper carrier that is directly attached to the second cooling stage of the coldhead. Printed circuit boards (PCBs) with cryogenic electronics for RF enhancement and DC low-pass filtering are connected to the same carrier, as shown in Fig. 4.2. The proximity of the RF electronics to the trap keeps the capacitance of the wiring low, which is crucial for realizing the required RF enhancement [118, 119]. Filtering of the DC signals close to the trap minimizes the possibility of unfiltered pickup noise and reduces Johnson-Nyquist noise of the cabling resistance [87]. The temperature of the trap carrier is measured with a diode sensor.

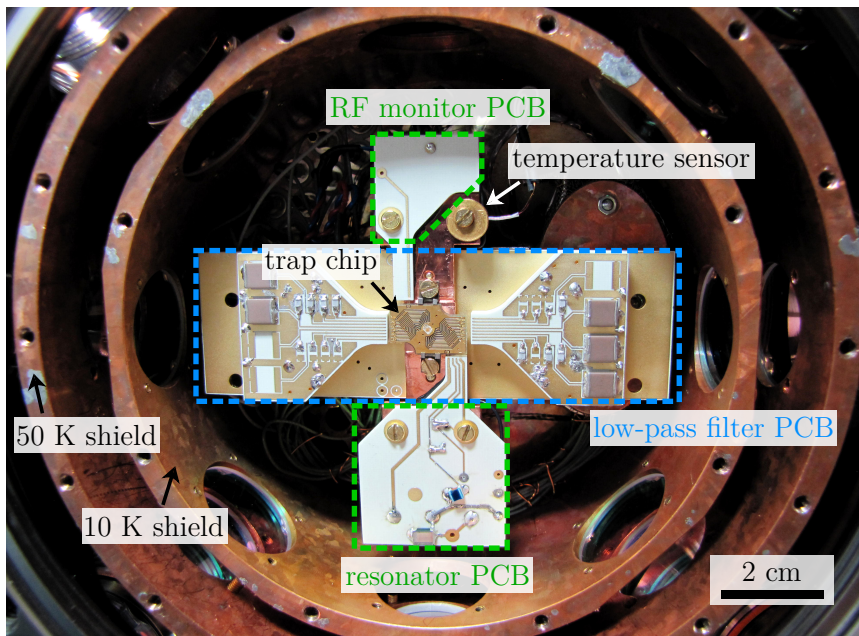


**Figure 4.2.** Mounted trap chip with cryogenic electronics PCBs. The trap chip is attached to a copper holder at the center of the octagon, in direct thermal contact with the 10 K-stage of the coldhead. The shapes of the surrounding supply PCBs facilitate optical access from two directions. A diode sensor measures the temperature close to the trap chip.

The 20 coaxial cables routed within the cryostat are all identical and can be used for either DC or RF signals. The electrical contact between the coaxial cables and the electronics PCBs is established by spring connectors (pogo pins), allowing for a fast exchange of the entire trap carrier. In the default setup, shown in Fig. 4.2, two coaxial cables are used to supply and monitor the RF drive voltage. The remaining cables carry DC signals. The PCBs with the RF drive electronics and the RF monitor components are on two opposite sides of the trap chip. 16 low-pass filtered DC channels are located

#### 4. Experimental setup

on the other two sides. Wire bonds are used to connect the trap chip to the RF and DC supply lines. Schematic circuits of the RF and DC supply electronics are shown in Fig. 4.3. While the low-pass filters used in the different experiments are all identical, the resonator components vary, and more specific information on the resonators is given in the respective later chapters. The general circuit for RF enhancement, shown in (a),

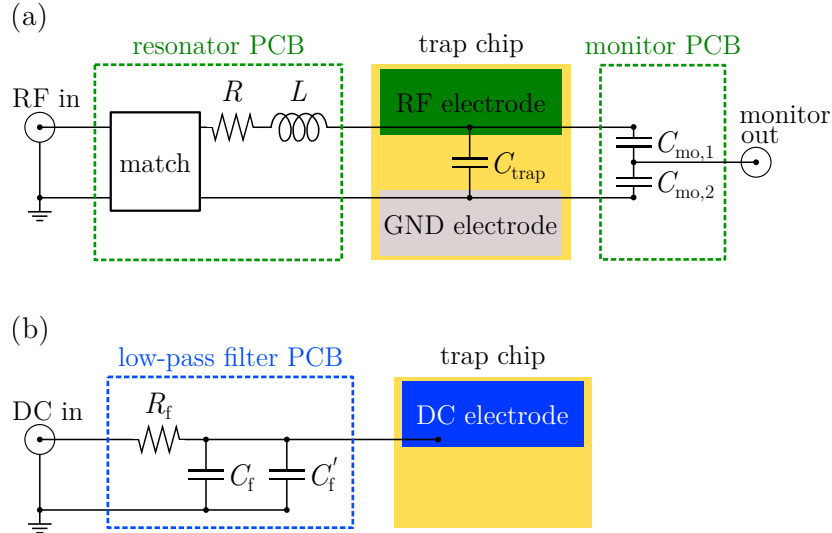


**Figure 4.3.** Schematics of the cryogenic electronics. (a) The RF supply voltage is enhanced by an RF resonator connected to the trap’s RF electrode. A capacitive divider allows to monitor the voltage at the trap. (b) First order RC filters are used to low-pass filter the DC voltages supplying the trap’s DC electrodes.

employs an inductance  $L$  with high quality factor, connected to the trap’s RF electrodes. The inductance forms a tank resonator with the attached capacitances of the trap,  $C_{\text{trap}}$ , and of the RF monitor to GND. The monitor is a capacitive divider with  $C_{\text{mo},1} \ll C_{\text{mo},2}$ , such that the coaxial cable connected to the monitor output affects the resonator only negligibly. A matching circuit is used to match the resonator’s impedance to the  $50\ \Omega$  coaxial supply line. The resonator enhances the RF source voltage with a voltage gain of [118]

$$G_V = \sqrt{\frac{Q\Omega_{\text{RF}}L}{R_s}}, \quad (4.1)$$

where  $Q = \Omega_{\text{RF}}L/R$  is the resonator’s quality factor at the on-resonant RF drive frequency  $\Omega_{\text{RF}}$ ,  $R_s = 50\ \Omega$  is the source impedance and perfect impedance matching is assumed. The resistance  $R$  sums up all resistances of the circuit. Fig. 4.3 (b) shows the first order RC filters used to low-pass filter the DC channels, which supply the trap’s DC

electrodes. Each filter consists of a resistor  $R_f = 100 \Omega$ <sup>1</sup> and two capacitors  $C_f = 330 \text{ nF}$ <sup>2</sup> and  $C'_f = 470 \text{ pF}$ <sup>3</sup> placed in parallel, yielding a cutoff frequency of  $f_c = 4.8 \text{ kHz}$  and a nominal noise reduction of about 50 dB at  $f = 1 \text{ MHz}$ . While the smaller capacitance  $C'_f$  does not influence the noise-reduction up to the MHz range, it ensures that the low-pass filter behavior extends across the self-resonant frequency of the larger capacitance  $C_f$ , which is around 8 MHz according to the specifications. Apart from the cryogenic filters, no additional filter stages were used.

## 4.2. Optical setup

The optical setup consists of 6 individual laser systems, with additional optics for beam overlap and focusing, and optics for ion imaging and state readout. A general overview of the entire optical setup is given in the following subsections. More detailed information on the laser systems for photoionization can be found in the master's thesis of Regina Lechner [120]. The lasers for Doppler cooling and repumping are described in the PhD thesis of Muir Kumph [121], the qubit laser at 729 nm in the master's thesis of Roman Stricker [122]. The final beam shaping and overlapping optics are described in the PhD thesis of Michael Niedermayr [117]. In the end of this section, optics for the production of a laser sheet are described, that were specifically built in the course of this thesis for Doppler cooling in 2D trap arrays.

### 4.2.1. General setup

The 6 lasers used for the ion trapping experiments can be divided in three groups: photoionization, Doppler cooling and qubit manipulation. In the following, the laser systems are briefly described.

#### Photoionization

For photoionization (PI),  $^{40}\text{Ca}$  atoms are first resonantly excited on the  $4^1\text{S}_0 \rightarrow 4^1\text{P}_1$  transition at 422 nm and then ionized using a second laser at 377 nm. The 422 nm light is produced by frequency doubling an 844 nm diode laser using a non-linear crystal and a cavity, which is stabilized to the laser with the Hänsch-Couillaud locking scheme [123]. The 377 nm light is generated by a free-running diode laser.

---

<sup>1</sup> Vishay, Y1625100R000Q9R

<sup>2</sup> Kemet, C2220C334J1GACTU

<sup>3</sup> Kemet, C0805C471J1GACTU

## 4. Experimental setup

### Doppler cooling and detection

For Doppler cooling and qubit state detection, the  $4^2S_{1/2} \rightarrow 4^2P_{1/2}$  transition of  $^{40}\text{Ca}^+$  at 397 nm is used (see Fig. 2.3). Since this is not a closed-cycle cooling transition, a second laser at 866 nm is needed to repump population on the  $3^2D_{3/2} \rightarrow 4^2P_{1/2}$  transition. The 397 nm light is generated by a frequency-doubled diode laser at 794 nm, which is stabilized to an external cavity using the Pound-Drever-Hall (PDH) locking scheme [124]. The laser frequency is adjusted by tuning the length of the cavity using a piezo-element. The diode laser that generates the repump light at 866 nm is stabilized to a similar cavity using the PDH method as well.

### Qubit manipulation

Light at 729 nm is used to drive the quadrupole qubit transition  $4^2S_{1/2} \rightarrow 3^2D_{5/2}$  of  $^{40}\text{Ca}^+$ . An additional laser at 854 nm drives the  $3^2D_{5/2} \rightarrow 4^2P_{1/2}$  transition to pump out the population from the metastable  $3^2D_{5/2}$  state, allowing for efficient sideband cooling and for a “reset” of the qubit state. The 854 nm light is generated by a diode laser that is stabilized to a cavity using the PDH technique. The light at 729 nm is generated in a different laboratory, using a titanium-sapphire laser which is pumped by a diode-pumped solid state laser. This laser is stabilized to an external high-finesse cavity and has a spectral linewidth of a few Hz. A fraction of the light is sent through a 200 m long polarization-maintaining (PM) single-mode (SM) fiber connection to the laboratory, where the experiments described in this thesis were performed. After transmission through the fiber the laser linewidth is increased to around 1 kHz due to fiber noise [125]. This light is amplified by a tapered amplifier.

### Beam overlap and focusing

The light generated by the 6 laser systems is routed through SM PM fibers to the optical table with the vacuum chamber. There, light for Doppler cooling and qubit manipulation is sent through acousto-optical modulators (AOMs) for adjustment of frequency and beam power, which allows one to electronically control laser pulses (see section 4.3). At this stage, the two near-infrared lasers at 854 nm and 866 nm are overlapped. The beams are routed further through a second set of PM SM fibers to the final optics stage. There, the two laser beams for PI and the Doppler cooling beam at 397 nm are overlapped with the two beams in the near-infrared. The overlapped beams are then focused using a single, common lens, which is mounted on an  $xyz$ -translation stage to adjust the focal position with respect to the ion trap. The 397 nm Doppler cooling beam can alternatively be sent in opposite direction to the ion, allowing to optimize the focus and position of this beam independently of the other lasers. The

qubit manipulation laser at 729 nm is focused onto the ion by its own lens, mounted on an  $xyz$ -translation stage, and sent to the trap at  $90^\circ$  to the other beams (see Fig. 4.1).

### Fluorescence detection

For ion detection, fluorescence light on the 397 nm Doppler cooling transition is collected by an objective, collimated and split in a 50/50 beam splitter. The beam splitter outputs are spectrally filtered and sent to a CCD camera and a photo-multiplier tube (PMT), respectively. The beam path to the PMT additionally passes through an aperture used as spatial block for stray light. The camera image is also used for initial beam alignment using topological features of the trap chip surface as reference and for a rough micromotion compensation. The latter works by slightly reducing the RF confinement and compensating the resulting shift in ion position, that occurs due to stray electric fields. The PMT signal is used for qubit state readout, see chapter 2.3.2.

#### 4.2.2. Laser sheet for Doppler cooling

The final focusing optics described above create spherical Gaussian beams with focal beam waists of about  $w_0 \approx (20 - 100) \mu\text{m}$ . Such beams are not suited for simultaneous addressing of multiple ions in a trap array with trapping site distances on the order of  $100 \mu\text{m}$ . Therefore, a setup for the creation of a light sheet for Doppler cooling was built to enable simultaneous trapping in several sites. The aspect ratio of the sheet dimensions can be varied between 1/10 and 1/100 with a focused waist of the 397 nm beam of  $10 \mu\text{m}$  in the direction perpendicular to the trap surface. A schematic of the setup is shown in Fig. 4.4 (a). Two 30 mm cage systems<sup>4</sup> are used to independently generate highly elliptical collimated beams at 397 nm and 866 nm wavelengths. These beams are then overlapped, expanded in a telescope and focused on the trap. Each cage system contains a fiber collimator and five lenses, which realize two independent telescopes along the  $x$ - and  $y$ -direction, respectively. The telescope that expands the beam in  $y$ -direction consists of the first two cylindrical lenses, both aligned for focusing along  $y$ , and the spherical third lens. The expansion along the  $x$ -direction is set by this spherical third lens and the last two lenses, which are cylindrical and aligned to collimate the beam along the  $x$ -axis. The usage of two-cylindrical lenses for each spatial direction allows one to create a collimated beam with variable ellipticity. The output of the two cage systems is overlapped using an edge filter<sup>5</sup> and the overlapped beams are expanded in another telescope, consisting of two spherical lenses and contained in a 60 mm cage

---

<sup>4</sup> Thorlabs

<sup>5</sup> Semrock, BLP01-594R-25

#### 4. Experimental setup

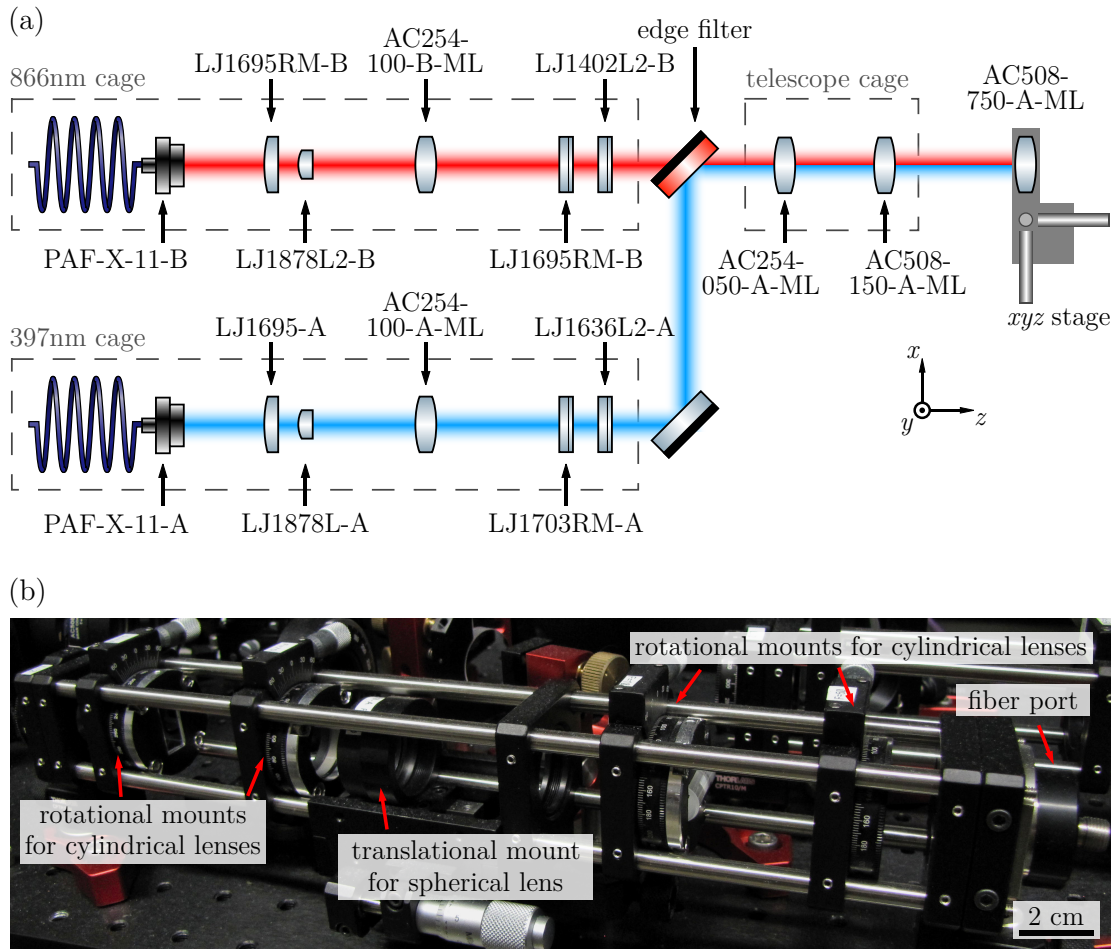


**Figure 4.4.** Optical setup for the realization of a laser sheet for Doppler cooling. (a) A combination of cylindrical lenses and a spherical lens in two independent cage systems is used to create highly elliptical, collimated beams of 397 nm and 866 nm light. The two elliptical beams are overlapped, further expanded and focused using spherical optics. The components' labels are Thorlabs part numbers. (b) Photograph of the cage system for the 397 nm light. The cylindrical lenses are attached to precision rotational mounts, the central spherical lens is held on a translational mount for fine adjustment of the focal position.

system<sup>6</sup>. Finally, the beams are focused onto the ions using a single spherical lens mounted on an  $xyz$ -translation stage. The final focusing optics are optimized for the 397 nm beam used for imaging. Fig. 4.4 (b) shows a photograph of the cage system used to create the elliptical 397 nm beam. The cylindrical lenses are attached to precision rotational mounts<sup>7</sup> to correct for astigmatism. The focusing can be fine-tuned using the  $z$ -translation stage<sup>8</sup> on which the spherical lens is mounted.

The shapes of the focused 397 nm and 866 nm beams were measured with a beam profiler<sup>9</sup>. Along the tightly focused direction (perpendicular to the trap surface), the minimal beam waists are  $w_{0,y} \approx 10 \mu\text{m}$  for the 397 nm beam and  $w_{0,y} \approx 25 \mu\text{m}$  for the 866 nm beam. In the direction parallel to the chip surface, the waist can be adjusted from  $w_{0,x} \approx 150 \mu\text{m}$  to  $w_{0,x} \approx 1000 \mu\text{m}$  for both wavelengths while maintaining the tight focus in  $y$ -direction. The laser sheet setup was used for ion-trapping in the linear-trap array, described in chapter 8, and to trap ions in a linear surface trap with ion-electrode separation of  $d \approx 60 \mu\text{m}$ , as described in the PhD thesis of Kirill Lakhmanskiy [126].

### 4.3. Experiment control

The experimental setup is electronically controlled by LabView-based computer programs. Two programs are used to read out the temperature controller<sup>10</sup> of the cryostat and to control a DC power supply<sup>11</sup> that supplies the voltages to the trap's DC electrodes. The main part of the experiment's automation is bundled in a third program, which controls the RF source of the trap drive<sup>12</sup>, interfaces with three peripheral component interconnect (PCI) cards<sup>13</sup> and communicates with a pulse sequencer box [127]. The PCI cards provide analog voltage outputs and input counters. The outputs are used to control the drivers of the AOMs for the 397 nm, 866 nm and 854 nm beams, allowing one to set their frequency and power [121]. One of the PCI cards' input counters is used to count the ion-fluorescence photons arriving at the PMT. The pulse sequencer box produces pulses of RF signals and digital outputs (TTL). The TTL pulses are sent to the AOM drivers to switch the 397 nm, 866 nm and 854 nm beams on and off. The RF pulses are used to drive the AOM for the 729 nm beam, which allows the generation of complex pulse sequences of 729 nm light with adjustable duration, frequency, phase and amplitude of the individual pulses. Typical examples of experimental sequences are

---

<sup>6</sup> Thorlabs

<sup>7</sup> Thorlabs, CRM1P/M

<sup>8</sup> Thorlabs, CT1 and SM1Z (for the 866 nm cage)

<sup>9</sup> Spiricon, SP620U

<sup>10</sup> Cryocon, Model 24 temperature controller

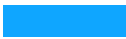
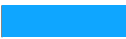
<sup>11</sup> iseg, EHS F 205x-F

<sup>12</sup> Marconi Instruments, 2024 signal generator, 9 kHz - 2.4 GHz

<sup>13</sup> National Instruments, 2x PCI-6733, 1x PCI-6711

#### 4. Experimental setup

shown in Figs. 4.5 and 4.6, for the case of driving a Rabi oscillation on a micromotion sideband and performing a heating rate measurement as used in experiments described in chapter 7.

| step     | Doppler cooling                                                                   | optical pumping                                                                   | pulse               | detection                                                                          | repumping                                                                           |
|----------|-----------------------------------------------------------------------------------|-----------------------------------------------------------------------------------|---------------------|------------------------------------------------------------------------------------|-------------------------------------------------------------------------------------|
| duration | 3 ms                                                                              | 2 ms                                                                              | varied              | 5 ms                                                                               | 220 $\mu$ s                                                                         |
| 397 nm   |  |                                                                                   |                     |  |  |
| 866 nm   |  |  |                     |  |  |
| 854 nm   |                                                                                   |  |                     |                                                                                    |  |
| 729 nm   |                                                                                   | $\nu_{\text{OP}}$                                                                 | $\nu_{\text{mmsb}}$ |                                                                                    |                                                                                     |

**Figure 4.5.** Experimental sequence for a measurement of the mean excitation on the micromotion sideband. The entire sequence is typically repeated 50 to 100 times to collect statistics. The frequency of the 729 nm beam is adjusted to drive the transition for optical pumping ( $\nu_{\text{OP}}$ ) or the micromotion sideband of the qubit transition ( $\nu_{\text{mmsb}}$ ). The pulse length is varied to observe a Rabi oscillation.

| step     | Doppler cooling                                                                     | optical pumping                                                                     | sideband cooling                                                                    | waiting | sideband pulse                      | detection                                                                             | repumping                                                                             |
|----------|-------------------------------------------------------------------------------------|-------------------------------------------------------------------------------------|-------------------------------------------------------------------------------------|---------|-------------------------------------|---------------------------------------------------------------------------------------|---------------------------------------------------------------------------------------|
| duration | 3 ms                                                                                | 2 ms                                                                                | 12.6 ms                                                                             | varied  | 78 $\mu$ s                          | 5 ms                                                                                  | 1 ms                                                                                  |
| 397 nm   |  |                                                                                     |                                                                                     |         |                                     |  |  |
| 866 nm   |  |  |  |         |                                     |  |  |
| 854 nm   |                                                                                     |  |  |         |                                     |                                                                                       |  |
| 729 nm   |                                                                                     | $\nu_{\text{OP}}$                                                                   | $(\nu_{\text{SBC}}, \nu_{\text{OP}}) \times 6$                                      |         | $\nu_{\text{rsb}}/\nu_{\text{bsb}}$ |                                                                                       |                                                                                       |

**Figure 4.6.** Experimental sequence for a measurement of the mean excitation on the red or blue sideband transition for a given waiting time, as required for a heating rate measurement. The entire sequence is repeated typically 50 to 100 times to collect statistics. During the sideband cooling step the frequency of the 729 nm beam is alternately adjusted to drive the transitions for sideband cooling ( $\nu_{\text{SBC}}$ ) and optical pumping ( $\nu_{\text{OP}}$ ). The sideband pulse is applied to either the red sideband ( $\nu_{\text{rsb}}$ ) or the blue sideband ( $\nu_{\text{bsb}}$ ).

## 5. 2 D point trap array “Ziegelstadl”

The “Ziegelstadl” trap is the first two-dimensional ion trap array built in Innsbruck using microfabrication technologies. The design is a miniaturized version of an earlier, larger array fabricated with PCB technology [54] and was designed by Muir Kumph [121]. The elementary building blocks of the Ziegelstadl array are surface point traps which are repeated in a quasi-periodic fashion on a microchip, thus realizing a two-dimensional lattice of ions in individual trapping sites. Entanglement between ions in adjacent sites is mediated by the Coulomb interaction following the approach described in chapter 3.2. In contrast to static ion trap arrays [52, 53, 55], the design relies on ion-shuttling in two spatial directions to couple ions in adjacent trapping sites. This requires varying the RF voltage on segmented RF electrodes. The trap was fabricated in collaboration with the group of Johannes Edlinger at the research center for microtechnology of the University of Applied Sciences in Dornbirn, Austria (FHV)<sup>1</sup>.

The chapter starts with an overview of the trap design, the fabrication process and the different trap wafers produced. It follows a detailed description of the electrical tests that were performed to assess the quality of the individual wafers and to provide feedback for the fabrication. Subsequently, the unsuccessful ion loading attempts are described, followed by a failure analysis and suggested improvements.

### 5.1. Trap design and fabrication

This section provides an overview of the electrode layout and trap functionality. The fabrication steps are briefly summarized as well, a more detailed description can be found in the PhD thesis of M. Kumph [121].

#### 5.1.1. Electrode layout

The trap consists of 18 individual electrodes arranged in a quasi-periodic fashion on the chip surface as shown in Fig. 5.1. A large, quadratic area of RF electrodes (green and red) is interspersed with 16 elliptical DC electrodes (gray and blue) that form a  $4 \times 4$  square lattice. Above each DC electrodes, at a distance  $d \approx 46 \mu\text{m}$  from the chip

---

<sup>1</sup> Forschungszentrum Mikrotechnik, FH Vorarlberg, Dornbirn, Austria.

## 5. 2D point trap array “Ziegelstadl”

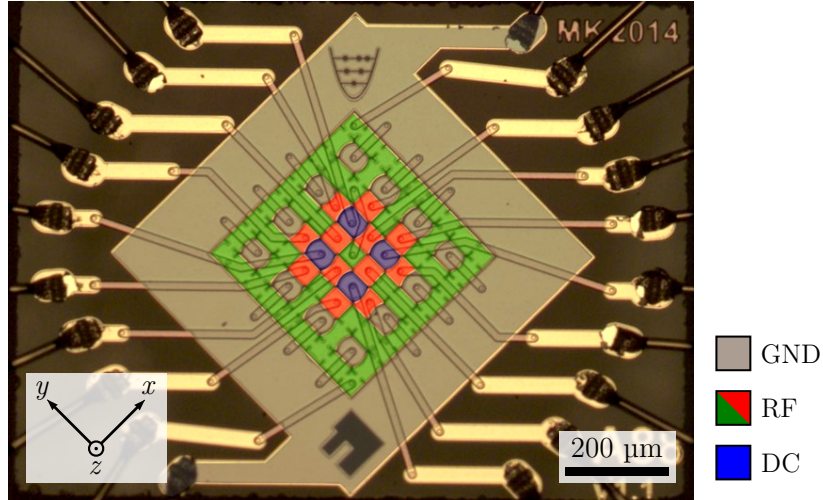


**Figure 5.1.** False color image showing the electrode layout of the Ziegelstadl trap. The RF electrodes (green and red) are interspersed with elliptical DC electrodes (gray and blue) creating 16 individual point traps, arranged in a  $4 \times 4$  array. Traces on a lower metal layer connect the inner electrodes to the bonding pads. These traces produce elevated topological features on the chip surface, visible as “stripes”. The inner 12 RF electrodes (red) are individually connected, as are the inner four DC electrodes (blue).

surface, an RF null is created. The trapping sites have a lattice constant of  $s_t = 100 \mu\text{m}$  given by the spacing of the DC electrodes. Due to the point-like character of the sites, only RF voltages are required for confinement in all three spatial directions. The outer 12 DC electrodes are connected on-chip to the GND electrode (gray) that surrounds the main RF electrode (green). The central 4 DC electrodes (blue) are individually connected to allow for additional DC control voltages. The inner 12 RF segments (red) are individually connected as well. This enables a dynamic control of the distance between the inner trapping sites as explained in the next section. The electrodes are connected to bonding pads at the chip edge through traces on a lower metal layer, except for the GND electrode which is directly connected. The two metal layers are separated by a dielectric layer with vias to allow for a connection of the electrodes to the traces. The entire chip has a size of only about  $1.4 \times 1.1 \text{ mm}^2$ . The bonding pads are located at the two short sides of the chip, restricting laser access to the direction perpendicular to the long sides. The elliptical shape of the DC electrodes sets the orientation of the two in-plane motional modes along the  $x, y$  directions (cf. Fig. 5.1), ensuring overlap of both modes with a single laser beam, for instance for Doppler cooling.

### 5.1.2. RF-controlled shuttling operations

The distance between ions in adjacent trapping sites,  $s_t = 100 \mu\text{m}$ , is too large to efficiently couple the ions’ motion and entangle them: the coupling rate at this distance

is  $\Omega_c \approx 2\pi \times 60$  Hz for a secular frequency of  $\omega_x \approx 2\pi \times 3$  MHz, given by Eq. (3.4) with  $\varsigma = 1$ . The individually connected RF segments allow for local, RF-controlled shuttling operations, as introduced in chapter 3.2.2 and illustrated in Fig. 5.2. In the standard

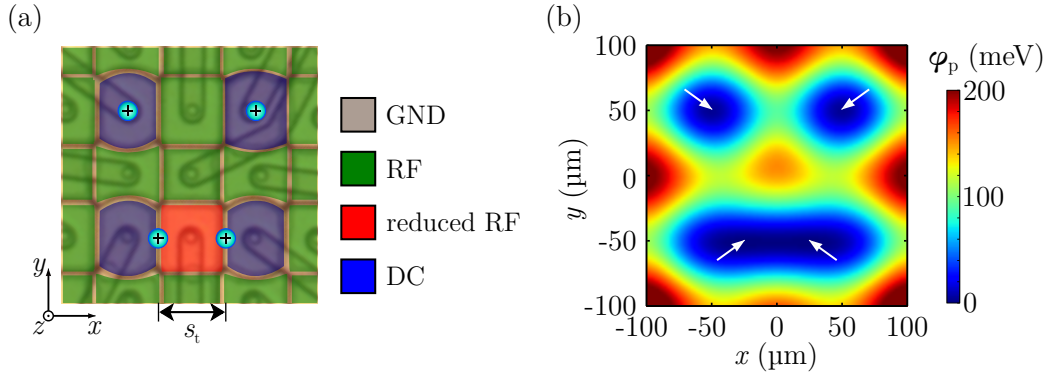


**Figure 5.2.** RF-controlled shuttling operations. (a) The distance between adjacent ions (blue spheres) can be locally reduced by decreasing the RF voltage  $U_{\text{RF}}$  on one of the individually connected RF electrodes in the chip center (red). (b) Simulation of the confining pseudo potential  $\varphi_p$  for a local reduction of the RF voltage  $U_{\text{RF}} = 27$  V<sub>RMS</sub> by 75 % at a drive frequency of  $\Omega_{\text{RF}} = 2\pi \times 46.5$  MHz. The white arrows mark the positions of the trapping sites.

configuration, all RF segments are at the full RF voltage  $U_{\text{RF}}$ . A local reduction of the RF voltage on one of the RF segments, marked red in Fig. 5.2 (a), leads to a reduction of the distance  $s_t$  between the two neighboring ions while leaving all other trapping sites almost unaffected. The simulated confining pseudo potential is shown in (b). Upon local reduction of the RF voltage  $U_{\text{RF}}$  by 75 %, the distance  $s_t$  is reduced by a factor of two to 50  $\mu\text{m}$  and at the same time the secular frequency at the positions of the ions is reduced to  $\omega_x = 2\pi \times 0.6$  MHz, leading to a significant enhancement of the motional coupling rate from  $\Omega_c \approx 2\pi \times 60$  Hz to  $\Omega_c \approx 2\pi \times 2.3$  kHz.

The locally controlled RF shuttling operations can be parallelized. Defining columns of the ion lattice along  $x$  and rows along  $y$ , every second pair of ions in each of the columns can be shuttled simultaneously along the  $x$ -direction. Shuttling operations along  $y$  can be parallelized in a similar way. The total amount of RF drives required to operate a scalable array is thus 5, taking into account the main-RF electrode that always remains at the full RF voltage.

### 5.1.3. Fabrication

The trap fabrication at FHV employed a multilayer process with two metal layers separated by one dielectric layer. All layers were applied by sputter processes, their structuring was done using photolithography with wet etching or reactive ion etching (RIE) [89]. A schematic cross section of the multilayer structure is shown in Fig. 5.3. On

## 5. 2D point trap array “Ziegelstadl”

top of a 550  $\mu\text{m}$  thick Pyrex substrate, a first metal layer (M1) with nominal thickness of  $t_{\text{M1}} = 1 \mu\text{m}$  was applied and structured, followed by an  $\text{SiO}_2$  dielectric layer with nominal thickness of  $t_{\text{diel}} = 1 \mu\text{m}$ . Holes in the dielectric were opened at the later positions of the vias. The second metal layer (M2) was applied with a nominal thickness of  $t_{\text{M2}} = 1 \mu\text{m}$ . Prior to structuring this layer, a final gold layer with a nominal thickness of  $t_{\text{Au}} = 500 \text{ nm}$  was evaporated, using about 5 nm titanium as adhesion promoter. The gold evaporation was done in the cleanroom in Innsbruck, the wafers were sent back to FHV for the final lift-off and dicing. During the testing of the chips, it became apparent that the thickness of the dielectric layer is likely to be reduced at the edges of traces on the M1 layer (marked with green arrows in Fig. 5.3). For the metalization of layers M1 and M2, different materials were used, as listed in Tab. 5.1. Mostly, the electrodes were made from copper or aluminium. Additional layers of titanium with a thickness of a few tens of nm were used as adhesion promoters to the adjacent substrate and dielectric

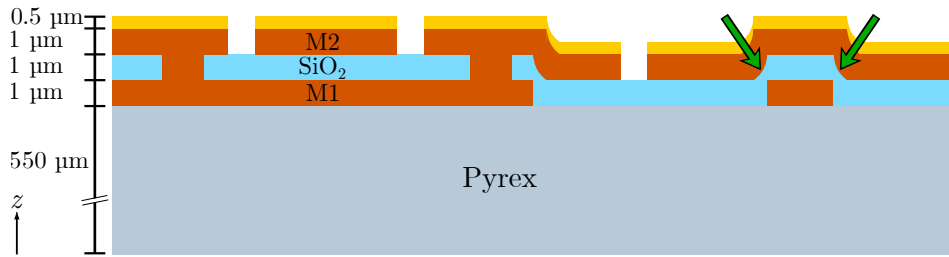


**Figure 5.3.** Schematic cross section of the Ziegelstadl chip showing the multilayer structure. The green arrows mark positions where the nominal thickness of the dielectric  $\text{SiO}_2$  layer is reduced due to the topology induced by a trace on the M1 layer.

**Table 5.1.** Specifications of the wafer fabrication runs. Each metalization layer is sandwiched between two thin Ti adhesion layers (not listed). The ‘+ Au’ notation indicates a final gold top layer. In fabrication runs 3 to 6, an uncontrolled drift in the dielectric’s deposition parameters occurred, leading to a change in stoichiometry to  $\text{SiO}_x$ ,  $x < 2$ .

| fab. run                            | # wafers | metalization |         | structuring    | dielectric     | version |
|-------------------------------------|----------|--------------|---------|----------------|----------------|---------|
|                                     |          | M1           | M2      |                |                |         |
| 1                                   | 2        | Cu           | Cu      | wet etch       | $\text{SiO}_2$ | 1.0     |
| 2                                   | 2        | Cu           | Cu      | wet etch       | $\text{SiO}_2$ | 1.0     |
| modified mask design                |          |              |         |                |                |         |
| 3                                   | 2        | Ti           | Ti + Au | RIE            | $\text{SiO}_x$ | 1.1     |
| 4                                   | 1        | Cu           | Cu + Au | RIE / wet etch | $\text{SiO}_x$ | 1.1     |
| 5                                   | 2        | Cu           | Cu + Au | wet etch       | $\text{SiO}_x$ | 1.1     |
|                                     | 3        | Cu           | Cu + Au | wet etch       | $\text{SiO}_x$ | 1.1     |
| 6                                   | 3        | Al           | Al + Au | wet etch       | $\text{SiO}_x$ | 1.1     |
| dielectric stoichiometry adjustment |          |              |         |                |                |         |
| 7                                   | 4        | Al           | Al + Au | wet etch       | $\text{SiO}_2$ | 1.1     |

layer. A similarly thin titanium finish on the M2 layer prevented the buildup of a thick oxide layer prior to the final gold evaporation. In the first two fabrication runs, an earlier design of the photolithography mask was used and no gold was evaporated. For traps from these wafers, reliable wire bond connections to the supply PCBs could not be established, mainly due to too small bonding pads. These problems are described in the master's theses of Kirsten Langer [128] and Martin Meraner [129]. Fig. 5.4 shows a comparison between the earlier version of the trap design (1.0) and the recent version (1.1), where the bonding pads were enlarged. A detailed description of the differences between the two versions can be found in Ref. [129]. In fabrication run 3, the M1 and

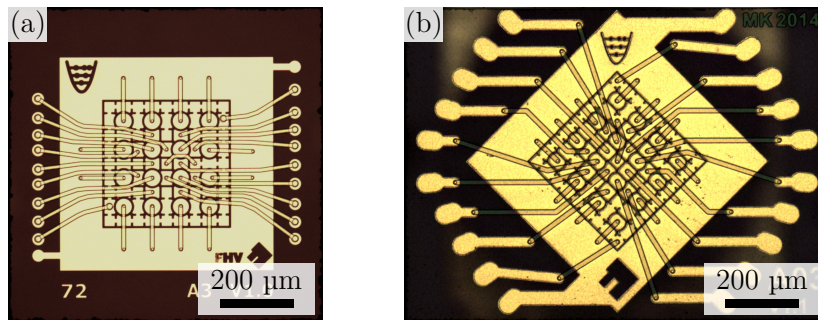


**Figure 5.4.** Microscope images of the trap array versions 1.0 (a) and 1.1 (b). The main differences in the new design are the larger bonding pads, the elliptical shape of the DC electrodes and the rotation of the array by 45°.

M2 layers were purely made out of titanium, the patterning was done with RIE. These traps turned out to be unusable; all electrodes were shorted to the GND electrode, as described in more detail in the next section. The possible origin of these shorts are the high voltage differences between the M1 and M2 layer building up during the plasma etch. This hypothesis was corroborated by an identical behavior of chips from fabrication run 4, where the thin Ti finish on the M2 layer was structured with RIE. To resolve this problem, subsequent wafers were metalized with Cu or Al, which can be structured with a wet etch. For the fabrication runs 3 to 6, the process parameters for the oxygen flow rate during the deposition of the dielectric layer drifted away. This caused a deficiency in the oxygen content of the deposited layer, with a change in stoichiometry to  $\text{SiO}_x$  with  $x < 2$  [130]. The degradation in stoichiometry is evident from the brownish color of test stripes, shown in Fig. 5.5, that were coated along with the trap wafers. For the fabrication run 7, the process parameters were readjusted to ensure an  $\text{SiO}_2$  stoichiometry with optimal insulating properties in terms of conductivity [131] and dielectric loss [132].

## 5. 2D point trap array “Ziegelstadl”

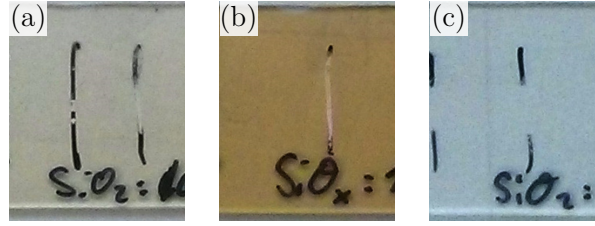


**Figure 5.5.** Degradation of the dielectric  $\text{SiO}_2$  layer due to drifts in the coating parameters. The photographs show test stripes coated along with the trap wafers and held before the same white background. The stripes exhibit slight (a) and strong (b) change in stoichiometry to  $\text{SiO}_x$ , as indicated by the color. The brownish coloring in (b) suggests an oxygen content  $x < 1.6$  [133]. For the stripe in (c), the deposition parameters were readjusted.

## 5.2. Electrical characterization

In a first characterization, the fabricated traps were subjected to a DC breakdown test. This allowed for a fast assessment of the basic electrical performance to give feedback for the trap production at FHV. The setup for these tests is shown in Fig. 5.6. A probe station setup in the cleanroom, shown in (a), was used to test various trap chips across a wafer. Individual trap chips were also wire bonded and inserted into a small vacuum chamber for tests at pressures around  $1 \times 10^{-6}$  mbar. The electrical setup for the DC tests is shown in (b). A voltage difference  $U_{\text{DC}}$  from a DC power supply<sup>2</sup> is applied at the bonding pads of two trap electrodes. Mainly, the main-RF electrode and the GND electrode were connected (green and gray in Fig. 5.1). In the ideal case, the electrodes behave as a capacitor with capacitance  $C_{\text{el}}$  and infinite equivalent parallel resistance (EPR), i. e., the leakage current  $I_1$  through the trap chip is zero. The leakage

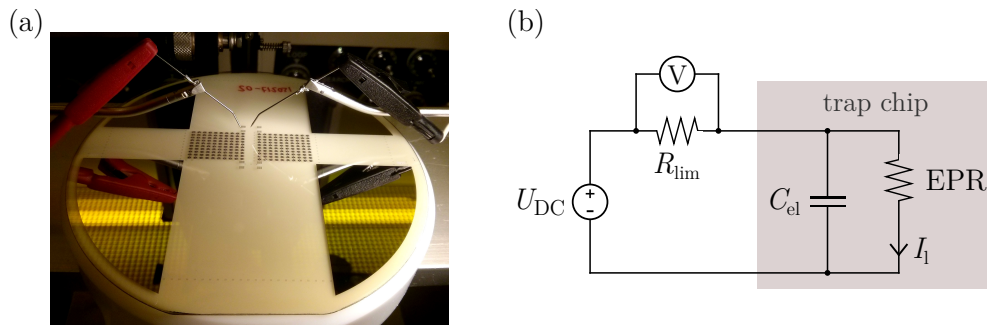


**Figure 5.6.** Setup for DC breakdown tests. (a) Probe station setup with a trap wafer. Specific electrodes are tested by connecting their bonding pads to the probe needles. (b) Schematic test circuit. A DC voltage  $U_{\text{DC}}$  is applied between two trap electrodes with mutual capacitance  $C_{\text{el}}$  and equivalent parallel resistance EPR. The leakage current  $I_1$  is determined by the voltage drop on the series resistor  $R_{\text{lim}}$ .

<sup>2</sup> TTi, PLH250-P, 250 V, 0.375 A

current was measured by the voltage drop on a resistor  $R_{\text{lim}}$  connected in series with the trap chip. Typically, high resistance values  $R_{\text{lim}} = 200 \text{ k}\Omega$  or  $R_{\text{lim}} = 120 \text{ k}\Omega$  were used to limit the current in case of dielectric breakdown of the chip and to increase the sensitivity of the measurement, which is about  $1 \text{ nA}$ , given by the resolution of the voltage meter<sup>3</sup>.

### Test results

For traps with pure Ti metalization (fabrication run 3) the electrical tests revealed an electrical connection of all inner trap electrodes to the outer GND electrode. Typical resistances of these connections were a few to a few tens of  $\Omega$  making the traps unusable. Attempts to remove these shorts by application of electrical currents in vacuum resulted in structural damage of the chip, as shown in Fig. 5.7 (a), and eventually destruction of the chip at higher currents, (b). For these attempts, the voltage was applied between the main-RF electrode and the outer GND ring. The clearly visible damage reveals the location of the electrical shorts at the trace of the main-RF electrode on the M1 layer.

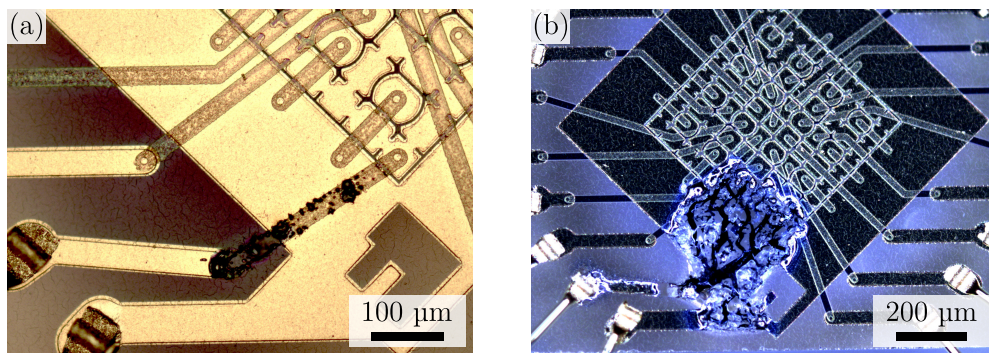


**Figure 5.7.** Microscope images of the traps with pure Ti metalization (fabrication run 3) after trying to remove the shorts between the main-RF and GND electrodes. (a) Localized damage at the M1 trace of the main-RF electrode after application of low currents of a few tens of mA. (b) Dark-field image showing the destruction of the chip after application of a current of  $I_1 \approx 120 \text{ mA}$ , voltage-limited at  $U_{\text{DC}} = 24 \text{ V}$ .

Traps with Cu and Al metalization (fabrication runs 4 to 7) were tested in a voltage range  $U_{\text{DC}} = (0 - 200) \text{ V}$ . Breakdown in these traps was detected by a sudden, significant increase in leakage current  $I_1$  and was exclusively caused by a failure of the dielectric layer. This is evident from two facts: First, the measured breakdown voltages  $U_{\text{break}}$  widely vary between different samples and wafers, although the gap widths  $w_{\text{gap}} = 4 \text{ }\mu\text{m}$  between the electrodes are identical for all samples. Additional tests of single chips in vacuum showed values for the breakdown voltage similar to those measured under atmospheric pressure. For these reasons, arcing or surface flash-over are unlikely

<sup>3</sup> Agilent, U1241A multimeter

## 5. 2D point trap array “Ziegelstadl”

to be the cause of the breakdown. Second, structural damage of the trap chips after breakdown, visible under the microscope, always included the dielectric layer and was generally found far away from electrode gaps. Typical electric test data for the traps with Cu and Al metalization are shown in Fig. 5.8. A clear difference in performance was observed between trap versions 1.0 and 1.1. Version 1.0 data, shown in (a), were highly reproducible with low leakage currents  $I_1 \lesssim 0.01 \mu\text{A}$  and breakdown voltages  $U_{\text{break}} \approx (80 - 120) \text{V}$ . The version 1.1 data, shown in (b), had in general significantly higher leakage currents and exhibited a variety of different behaviors. Strongly fluctuating leakage currents were observed, typically connected to lower breakdown voltages  $U_{\text{break}} \lesssim 130 \text{V}$ , e.g. chips A09 and A88. Strong variations in the value of  $I_1$  were found even for different electrodes on the same chip, as shown by the A09 data. On the other hand, some chips showed breakdown voltages  $U_{\text{break}} > 200 \text{V}$ , for instance chip A00. Even after the readjustment of the  $\text{SiO}_2$  layer stoichiometry for fabrication run 7, different traps showed vastly varying behavior. An example of this are chips A88 and A89, which were placed directly next to each other on the same wafer during fabrication run 7. For traps from this latest fabrication, only about 20% were considered “good” samples showing low leakage currents  $I_1 \lesssim 1 \mu\text{A}$  and breakdown voltages  $U_{\text{break}} > 200 \text{V}$ , such as chip A00.

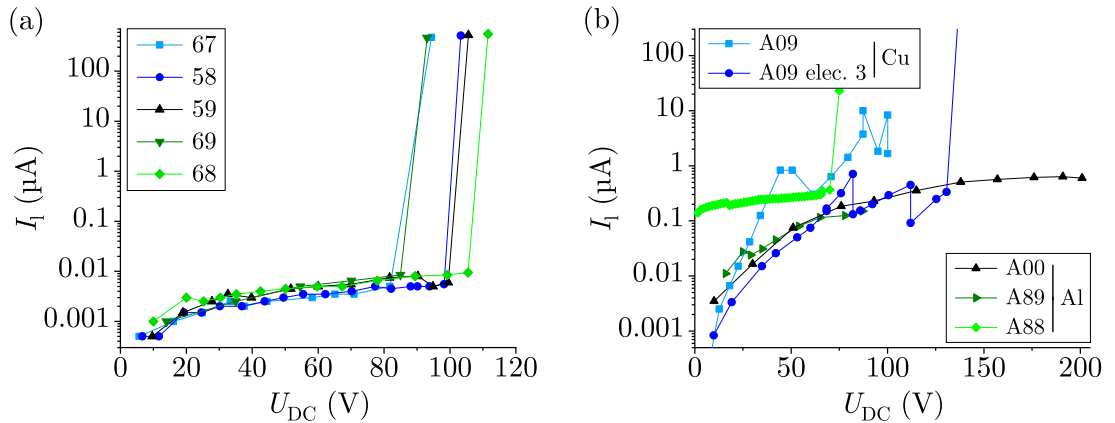


**Figure 5.8.** Typical test data showing the leakage current  $I_1$  between the main-RF and GND electrodes as function of the applied DC voltage  $U_{\text{DC}}$  for version 1.0 traps (a) and version 1.1 traps (b). For chip A09, an additional data set was taken for the leakage current between one of the central DC electrodes (“elec. 3”) and GND. The data for the Al metalization, chips A00, A89 and A88 are from fabrication run 7. The sensitivity of the measurement is about 1 nA.

An additional phenomenon exhibited by the trap chips, including the “good” samples, are aging effects of the dielectric, as shown in Fig. 5.9. For most traps, a significant reduction of the leakage current was observed upon applying high DC voltages. An example of this is given in (a) for three Al traps with  $\text{SiO}_2$  stoichiometry. Typical

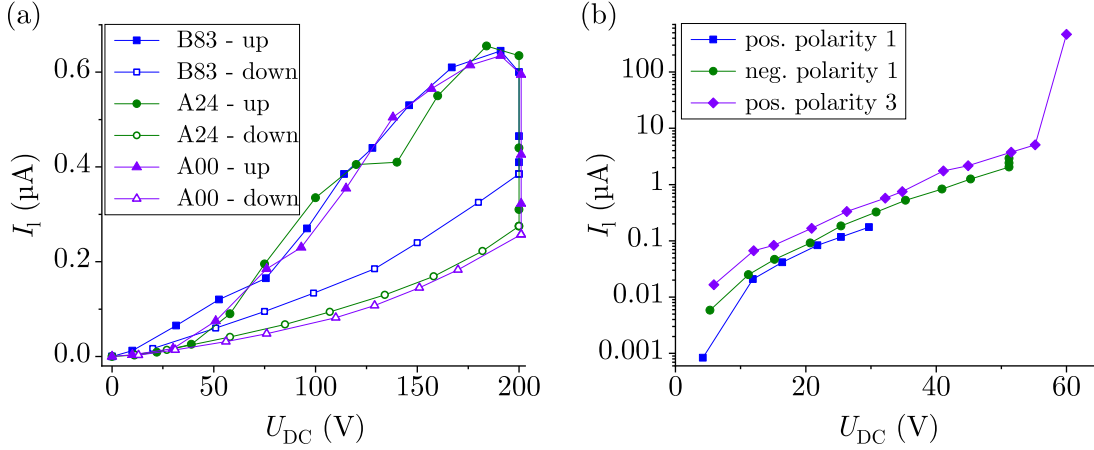


**Figure 5.9.** Aging effects of the dielectric layer. (a) Decrease of the leakage current upon application of high DC voltages observed in Al traps from fabrication run 7. Data sets labeled ‘up’ correspond to the initial ramp up of the voltage to  $U_{\text{DC}} = 200$  V. The sets labeled ‘down’ correspond to the voltage ramp down after a waiting time of a few tens of minutes. (b) Degradation of the dielectric until breakdown observed in a Cu trap from fabrication run 5. The voltage was ramped up with alternating polarity. Data for the second cycle (not shown here) were ranging between the sets for the first and third cycle.

relaxation times for  $I_1$  were around 30 min. Once the leakage current had settled, it remained on a low level, indicating a permanent improvement of the dielectric insulation. Similar relaxation effects were also observed in Cu traps. In some cases, on the other hand, samples exhibited increasing leakage currents until breakdown. This effect could be reproduced by repeatedly inverting the polarity of the applied DC voltage, as shown in Fig. 5.9 (b) for a Cu trap. Several Al traps from fabrication run 7 ( $\text{SiO}_2$  dielectric stoichiometry), tested previously up to  $U_{\text{DC}} = 200$  V without breakdown, showed the same failure upon polarity swap of the maximally applied voltage.

Breakdown and aging could be correlated with micro-discharge events, that could be observed with a microscope during the DC tests. These discharge events often but not always led to structural damage of the trap chip. At first, the damage was not destructive and the trap still sustained the applied DC voltage. The likelihood of trap failure increased, however, as the number of micro-discharge events grew with rising DC voltage. Fig. 5.10 shows microscope images of trap samples after observation of micro-discharge events. The structural damage occurred exclusively at the edges of traces on the M1 layer, to which the voltage difference  $U_{\text{DC}}$  relative to the above metal layer was applied.

## 5. 2D point trap array “Ziegelstadl”

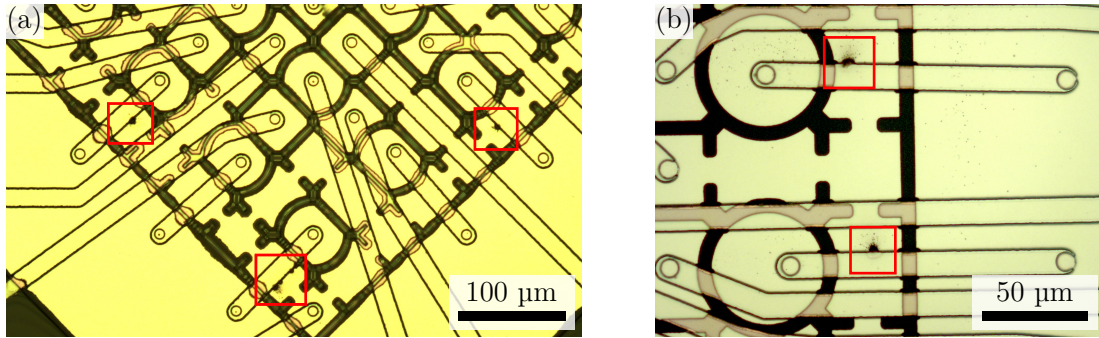


**Figure 5.10.** Microscope images of structural damage due to micro discharge events found in Al and Cu traps. (a) Version 1.1 trap from fabrication run 7. (b) Version 1.0 trap. In both cases the voltage was applied between the main-RF and GND electrodes.

### 5.3. Ion-loading attempts

Two trap chips of fabrication run 7 were prepared for ion loading. Prior to mounting, both chips were subjected to a DC voltage test up to  $U_{DC} = 30$  V, showing stable leakage currents with a magnitude of  $I_1 = 0.15$   $\mu$ A and  $I_1 = 0.10$   $\mu$ A, respectively, similar to the “good” samples shown in Fig. 5.9 (a). Larger DC voltages were not applied during preselection to avoid a possible damage of the samples. The trap chips were glued to a specifically designed interposer PCB using a low vapor pressure epoxy<sup>4</sup> at a curing temperature of 120 °C for about 20 min. The traps’ surfaces were cleaned by carefully brushing off larger particles with a 25  $\mu$ m-diameter gold wire and by blowing the chips with nitrogen. Other than that, no cleaning steps were applied. Subsequently, the traps were wire bonded to the interposer PCB using the same 25  $\mu$ m diameter gold wire. Fig. 5.11 shows images of a mounted trap chip. The interposer PCB, shown in (b), serves to interface the trap chip with the RF and low-pass filter PCBs on the trap mount. Traces on the interposer top side are bonded on one end to the trap chip. On the other end they can either be bonded to a low-pass filter line connected to the DC supply or they can be bonded to a small pad on the interposer, which is connected to the RF supply through traces on the bottom side of the interposer (shown as green overlay). For the loading attempts reported here, all RF segments were connected to the RF resonator. A capacitive divider, used to monitor the RF voltage on the trap chip, is connected through the main-RF electrode on the trap chip, which has two bonding pads on opposite ends of the chip. The form of the interposer with the concave roundings allows for laser access along the direction free of wire bonds. The interposer is clamped to the copper mount with the supply PCBs as shown in Fig. 5.11 (a). For electrical insulation of the RF traces on the interposer bottom side, a 1  $\times$  1 cm Pyrex

<sup>4</sup> Agilent, Torr Seal

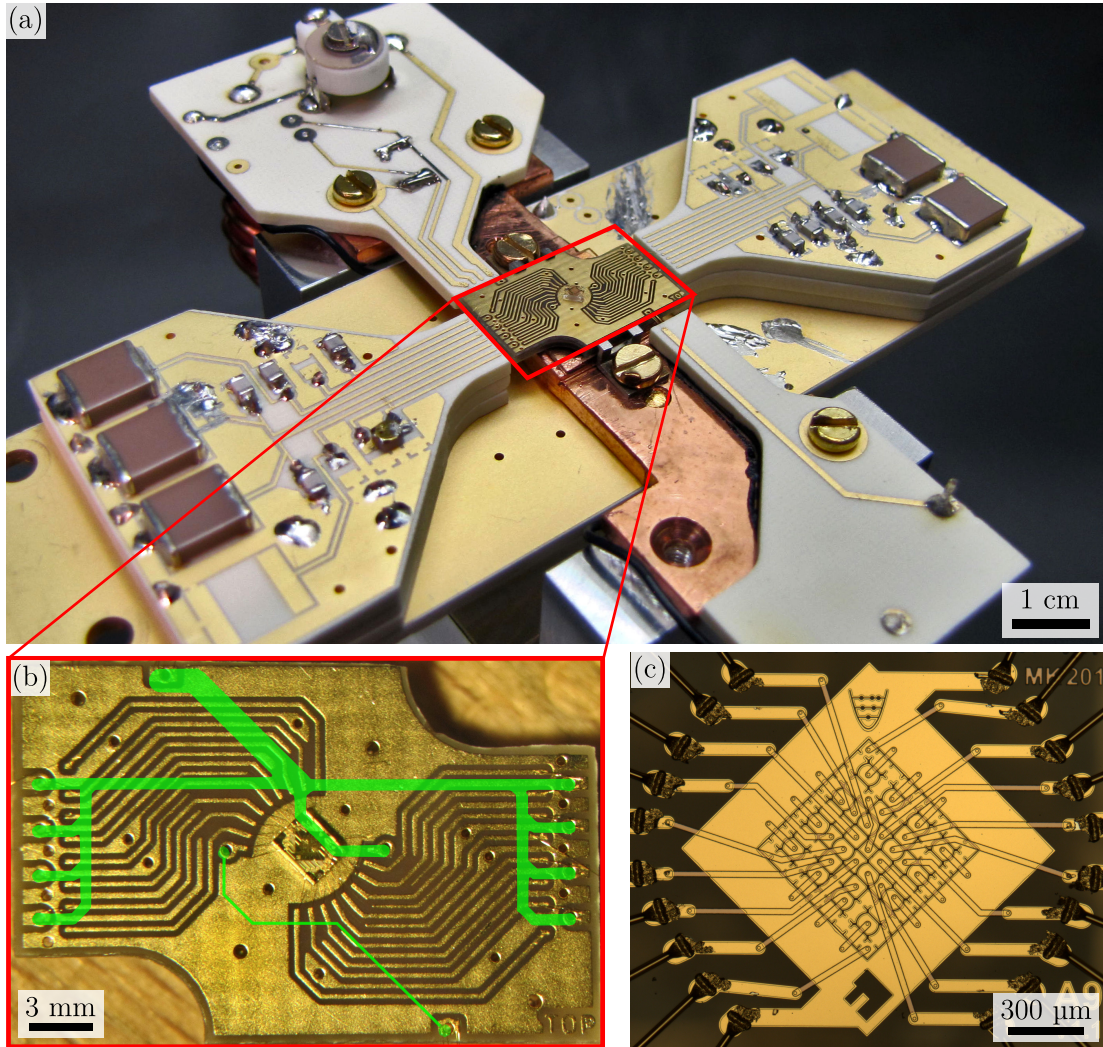


**Figure 5.11.** Setup for the loading attempts in cryogenic environment. (a) Trap holder with RF and low-pass filter PCBs and the interposer PCB. (b) Magnified view of the interposer PCB with the trap chip at the center. Overlaid in green are the RF supply lines at the back of the interposer. (c) Microscope image of the first chip used during the loading attempts.

## 5. 2D point trap array “Ziegelstadl”

plate with 550  $\mu\text{m}$  thickness is placed between the interposer and the Cu mount, the thermal contact is increased with thermal grease<sup>5</sup>.

An RF resonator was built to drive the trap chips. A schematic of the circuit is shown in Fig. 5.12. The resonator coil is of toroidal shape and consists of 25 windings with a 1 mm diameter copper wire around a phenolic core<sup>6</sup> giving rise to an inductance of  $L = 620 \text{ nH}$ . The joint capacitance of the trap and the interposer PCB,  $C_{\text{trap}} \approx 20.5 \text{ pF}$ , is calculated from the resonance frequency at 42 MHz of the unmatched resonator. For impedance matching, a trimmer with  $C_{\text{im},1} = (12 - 100) \text{ pF}$ <sup>7</sup>, and a fixed-value capacitor with  $C_{\text{im},2} = 147 \text{ pF}$ <sup>8</sup> are used. The additional inductance  $L_{\text{im}} = 1 \mu\text{H}$ <sup>9</sup> prevents a DC voltage build-up at the RF electrodes. A capacitive divider with  $C_{\text{mo},1} = 1 \text{ pF}$ <sup>10</sup> and  $C_{\text{mo},2} = 47 \text{ pF}$ <sup>11</sup> is used to monitor the RF voltage on the trap. At the operating temperature of  $T \approx 10 \text{ K}$  the resonance was measured at 49.2 MHz and a resonator quality factor  $Q \approx 250$  was inferred from the width of the resonance [118].

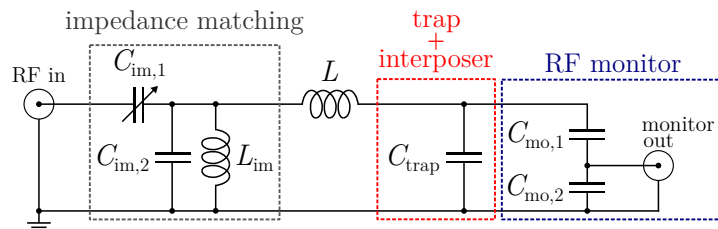


**Figure 5.12.** Resonator circuit for the loading attempts in the Ziegelstadl traps. The components are described in the main text.

After cool-down, an RF voltage of  $U_{\text{RF}} \approx 33 \text{ V}$  ( $23 \text{ V}_{\text{RMS}}$ ) at a drive frequency of  $\Omega_{\text{RF}} = 2\pi \times 49.2 \text{ MHz}$  was applied to the first trap chip and a trapping attempt was made. Such a voltage leads to simulated secular frequencies of the three motional modes between (2.3 - 5.4) MHz with the largest stability factor  $q_z \approx 0.31$  and a trap depth of 36 meV<sup>12</sup>. After a few hours of operation without trapping success, the resonance in the RF monitor signal was lost, indicating destruction of the trap chip. The second trap chip was inserted and first powered at a lower RF voltage of  $U_{\text{RF}} \approx 23 \text{ V}$  ( $16 \text{ V}_{\text{RMS}}$ ) at  $\Omega_{\text{RF}} = 2\pi \times 49.2 \text{ MHz}$ , corresponding to a trap depth of 18 meV. At this voltage the trap could be operated for several days. The laser frequencies and beam positions relative to the trap were scanned and different oven currents were used to vary the

<sup>5</sup> Apiezon, N Grease

<sup>6</sup> Micrometals, T80-0

<sup>7</sup> Johanson Manufacturing, 9328

<sup>8</sup> Cornell Dubilier, MC08FA101J-F (100 pF) and MC12FA470J-F (47 pF) in parallel

<sup>9</sup> Murata, LQW2UAS1R0J00L

<sup>10</sup> Cornell Dubilier, MC08CD010D-F

<sup>11</sup> Cornell Dubilier, MC12FD470J-F

<sup>12</sup> Trap simulations are done with the “electrode package” for python by R. Jördens (<https://github.com/nist-ionstorage/electrode>); see also [134, 135].

number and energy distribution of the emitted calcium atoms. The presence of neutral atoms was verified by the observation of atomic fluorescence at a wavelength of 422 nm. Furthermore, the DC voltages on the 4 inner DC segments were varied by  $\pm 2$  V in order to compensate horizontal stray fields. For the vertical direction up to  $\pm 10$  V were applied. However, trapping remained unsuccessful. Upon raising the RF drive voltage to  $U_{\text{RF}} \approx 30$  V, the trap was destroyed as indicated by the loss of the electric resonance in the RF monitor signal. Both chips were inspected under the microscope and several small craters between RF electrodes and the GND electrode were found. All detected failures were located on the edges of traces on the M1 layer and were similar in appearance to the failures observed in the DC breakdown tests, shown in Fig. 5.10.

## 5.4. Failure analysis and suggested improvements

The most apparent problem found in the electrical characterization of the Ziegelstadl chips is the trap destruction at RF voltages above  $U_{\text{RF}} \sim 25$  V, making trapping impossible. The origin of the failures could be traced back to the dielectric layer, explanations for their cause remain speculative. Other possible improvements concern the surface topology and via-placement and, more generally, the trap design itself. These points are discussed in the following.

### 5.4.1. Dielectric layer

The structural damage of the trap chips was exclusively found at the edges of traces on the M1 layer, where the dielectric layer is expected to have a reduced thickness, see Fig. 5.3. Indeed, assuming a reduction of the nominal thickness of the  $\text{SiO}_2$  layer,  $t_{\text{diel}} = 1$   $\mu\text{m}$ , by a factor 5 at the trace locations and further assuming a typical breakdown field strength of  $5.6$   $\text{MV cm}^{-1}$  [136], one finds an expected voltage strength of about 100 V. The strong variation in breakdown voltages for traps from the same wafer and across the wafers could then be explained by a non-uniform reduction of the dielectric layer thickness. The difference in behavior between chip versions 1.0 and 1.1 is somewhat surprising. It might be connected to the different mask design for photolithography or by an unnoticed change in fabrication process parameters. The measured fluctuations of the leakage current seen for version 1.1 traps and the aging effects indicate an opening and closing of conductive micro channels between the M1 and M2 layers associated with the observed micro discharge events. The presence of such micro channels could be connected to micro pores in the dielectric layer in conjunction with the ability of Al and Cu to grow “whiskers” [137, 138]. The reason for the apparently smaller RF breakdown voltages compared to DC breakdown remains unclear. The observed increase

## 5. 2D point trap array “Ziegelstadl”

in leakage current until trap destruction upon polarity change of the applied DC voltage during the breakdown tests indicate a more disruptive impact of AC signals. A likely solution of the above stated problems would be an increase of the nominal thickness of the dielectric layer. Unfortunately, this was not possible at the facilities at FHV due to limitations in the sputter process used to apply the SiO<sub>2</sub> layer. Alternatively, the metal layers could be reduced in thickness to mitigate the nominal thickness reduction at the trace edges. This would be the less desirable solution since it increases the trace resistances with possibly negative impact on heating rates and grounding of the electrodes (these effects are explained in more detail in chapter 7.2).

### 5.4.2. Surface topology

Another concern is the surface smoothness (topology), which caused light scattering during the trapping attempts, despite the fact that the focused  $2\sigma$ -width of the 397 nm beam used for Doppler cooling and imaging,  $w_{397} \approx 10 \mu\text{m}$ , is considerably smaller than the ion surface separation  $d \approx 46 \mu\text{m}$ . In particular the intermetallic vias, placed at the center of the trapping sites, caused point-like stray light similar to an uncrystallized trapped ion. While the amount of scattered light was not large enough to have prevented the observation of ions, a stray light reduction is certainly desirable. In a first step, the vias could be moved towards the electrode edges, outside the trapping region. Ultimately, planarization steps in the fabrication could be used to eliminate the surface topology.

### 5.4.3. Pseudo potential barrier

The third suggested improvement concerns the trap’s electrode layout. Simulations of the RF shuttling process revealed a severe weakness in terms of well separation due to the specific electrode geometry of point trap arrays. Fig. 5.13 (a) shows the geometry of the central region in the Ziegelstadl array. Attenuation of the RF voltage on the adjustable electrode (bright green) by 75 % reduces the inter-ion distance  $s_t$  by a factor of two to  $50 \mu\text{m}$ . The voltage reduction leads to additional electric field lines along the  $x$ -direction between the main RF electrode and the adjustable electrode, as illustrated by the purple arrows. In consequence, an additional electric quadrupole forms right in between the two trapping sites, giving rise to an additional pseudo potential minimum at  $(x, y) = (0, 0) \mu\text{m}$ . Fig. 5.13 (b) shows the simulated pseudo potential  $\varphi_p(y)$  that separates the two trapping sites, i. e., for each position  $y$  the vertical position  $z$  is adjusted to follow the potential minimum. The potential  $\varphi_p(y)$  has the shape of a triple-well due to the additional minimum at the origin. This leads to an extremely

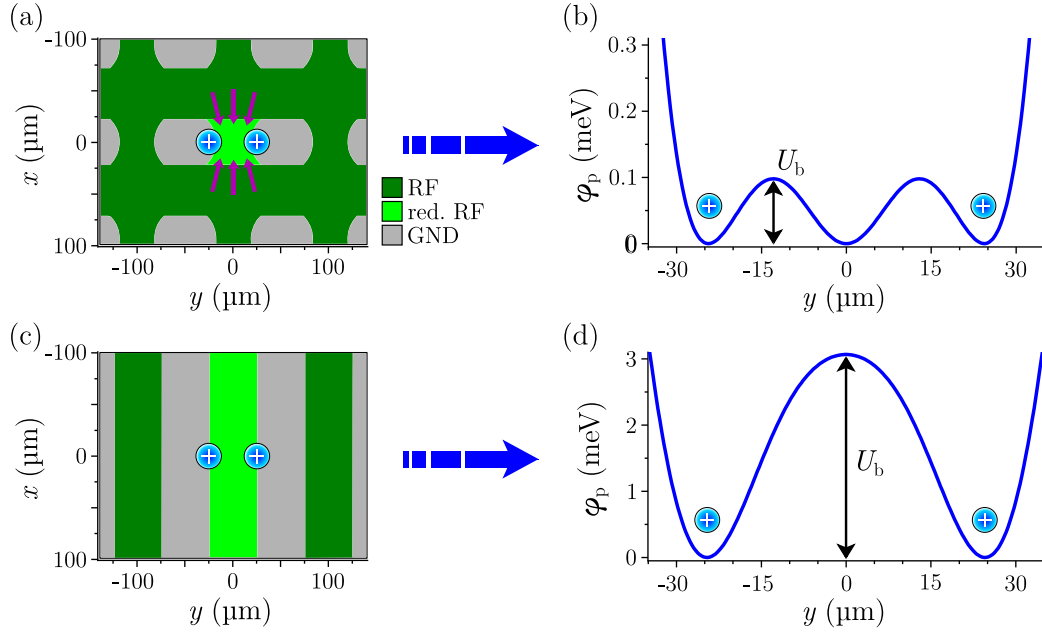


**Figure 5.13.** Potential barrier  $U_b$  during RF shuttling processes for a point trap array (a) and a linear trap array (c). Trap simulations of the corresponding pseudo potential  $\varphi_p(y)$  between the two trapping sites are shown in (b) and (d), respectively. The purple arrows in (a) illustrate additional electric field lines present during a voltage reduction on the segmented RF electrode (bright green).

small potential barrier  $U_b \approx 0.1$  meV for realistic trapping parameters<sup>13</sup>. Such a small barrier makes the RF-shuttling operations vulnerable towards stray electric fields. For stray field strengths  $E_{y,z} \sim (10 - 30)$  V m<sup>-1</sup> at the trapping position, the triple well is morphed into a single well. Such stray fields are not unlikely in surface traps with comparable or even larger ion-surface separation [99, 139]. The barrier  $U_b$  can be increased by superimposing the RF pseudo potential with a DC double-well potential. For suitable DC voltages on the order of 1 V on the addressable RF and DC electrodes the barrier reaches  $U_b = 3$  meV. At the same time, however, the trap depth is reduced from 39 meV to 29 meV.

A different approach to enhance the barrier is to entirely eliminate the unwanted pseudo potential minimum at the origin by choice of a suitable electrode geometry. Replacing the point trap array by parallel linear traps, illustrated in Fig. 5.13 (c), introduces a continuous translational symmetry of the trap geometry along the  $x$ -direction<sup>14</sup>. Consequently, electric field lines cannot have an  $x$ -component and no additional minimum is created. Similar to the point trap array, the inter-ion distance  $s_t$  is reduced

<sup>13</sup> Parameters for zero RF attenuation:  $U_{\text{RF}} = 40$  V at  $\Omega_{\text{RF}} = 2\pi \times 47.6$  MHz,  $\omega_x, \omega_y, \omega_z = 2\pi \times (2.8, 3.9, 6.7)$  MHz,  $q_z = 0.4$ .

<sup>14</sup> The convention to align the axis of a linear trap with the  $z$ -direction is ignored here to keep the notation consistent with the point trap array.

## 5. 2D point trap array “Ziegelstadl”

by attenuating the RF voltage on the adjustable RF rail (bright green). For a voltage attenuation of 46 %,  $s_t$  is reduced by a factor of two to  $50\ \mu\text{m}$ . The pseudo potential  $\varphi_p(y)$  separating the two trapping sites, shown in Fig. 5.13 (d), has the shape of a double well with a well barrier  $U_b \approx 3.1\ \text{meV}$ <sup>15</sup>, a factor 30 larger compared to the point trap array. The barrier can be increased even further by keeping the stability parameter  $q_r$  constant during the RF shuttling process. This requires an increase of the RF voltage on the outer RF electrodes, which is not possible in the point trap array since it would affect the stability of the outer trapping sites. An additional advantage of the linear trap array is the significantly smaller RF attenuation needed to bring adjacent ions close. This reduces the technical requirements on the tunable RF source as explained in chapter 6.

The above considerations show that a linear trap array is better suited to create well-defined trapping sites at distances relevant for entangling operations. A new generation of trap arrays based on parallel linear traps is presented in chapter 8.

---

<sup>15</sup> Parameters for zero RF attenuation:  $U_{\text{RF}} = 40\ \text{V}$  at  $\Omega_{\text{RF}} = 2\pi \times 30.5\ \text{MHz}$ ,  $\omega_r = 2\pi \times 4.3\ \text{MHz}$ ,  $q_r = 0.4$ .

## 6. Tunable RF fields in cryogenic traps

Adjusting the RF voltage level on different trap electrodes enables exact positioning and shifting of the RF null in trapped-ion setups. As such, this technique has been used to overlap the ion position with a neutral atom cloud [140] or with light fields [141], and to shuttle ions over hundreds of  $\mu\text{m}$  [54, 110, 142]. Individual control of RF fields is also a fundamental requirement for the well-to-well entangling operations in the 2D trap arrays described in chapters 5 and 8. For the general scheme of such an entangling operation, outlined in chapter 3.2.3, tunable RF fields are employed to decrease the distance  $s_t$  between adjacent trapping sites, thus enhancing the motional coupling rate  $\Omega_c$ . The adjacent potential wells are then tuned on-resonant using DC control fields, the ions are entangled, and the wells are tuned out of resonance again. Subsequently, the distance  $s_t$  is increased to its initial value by tuning again the RF fields.

Tunable RF voltages in ion traps have been realized by means of helical resonators with multiple tap points [141], capacitive networks [110, 140, 142–144] and multiple RF resonators [54, 96, 145]. In the latter two approaches, the RF voltages are typically set using mechanically adjustable capacitors. Voltage-controlled capacitors (varactor diodes) are used in the design of Kumph et al. [54, 96]. Electronic tunability allows for a dynamic change of the trapping potential and is imperative to implement RF shuttling processes in ion trap arrays. Varactor diodes, like most electronic components, are typically not specified for applications well below room-temperature. In fact, many semiconductor components fail to work in cryogenic environment due to a freeze-out of charge carriers [146]. However, ion trap arrays benefit strongly from the operation in cryogenic environment due to the excellent vacuum and reduced motional heating, see chapter 3.3. In cryogenic ion-trapping experiments, the RF resonators driving the traps must be located in the cold stage due to the low electrical conductivity of the wiring going to the room-temperature parts of the experiment [119]. Therefore, varactor diodes used for the implementation of switchable RF fields need to be tested for compatibility with the cryogenic temperatures  $T \sim 10\text{ K}$  present in such setups.

The first part of this chapter examines the electronic requirements on varactor diodes for the implementation of tunable RF fields using capacitive networks and phase-stabilized resonator circuits. The particular focus is on the tuning range, voltage

## 6. Tunable RF fields in cryogenic traps

strength and impact of the varactor's intrinsic RF losses. In the second part several commercially available varactor diodes are characterized in terms of tunability and quality factor at different temperatures down to  $T = 8$  K. These measurements are performed in a resonator prototype, which is designed to be part of a circuit for the implementation of tunable RF fields using two phase-stabilized resonators.

### 6.1. Requirements on tunable RF circuits

Voltage-controlled capacitors (varactors) are semiconductor diodes whose capacitance strongly depends on the applied voltage when operated in reverse-bias mode. Varactor diodes can thus be used to realize a tunable load capacitance in RF circuits as shown in Fig. 6.1. The varactor diode's intrinsic junction capacitance  $C_{\text{jun}}$  is tuned by adjusting

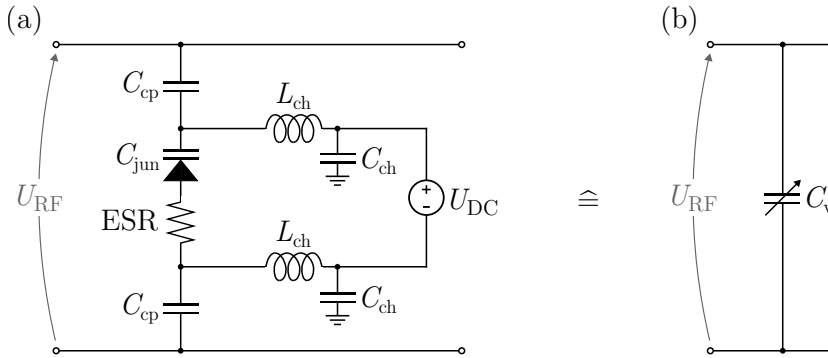


**Figure 6.1.** Realization of an electrically tunable load capacitance in an RF circuit. (a) The capacitance of the varactor diode  $C_{\text{jun}}$  is set by the DC bias voltage  $U_{\text{DC}}$ . The RF choke components  $L_{\text{ch}}$ ,  $C_{\text{ch}}$  and coupling capacitors  $C_{\text{cp}}$  decouple the DC supply from the RF circuit. (b) The equivalent circuit with the electrically tunable capacitor  $C_v$ .

the reverse bias voltage  $U_{\text{DC}}$ . The equivalent series resistance (ESR) takes into account possible RF losses intrinsic to the varactor. The reactive choke components  $L_{\text{ch}}$  and  $C_{\text{ch}}$  form a low-pass filter that suppresses the RF signal on the DC supply line. A possible influence of the DC line on the RF circuit, for instance from additional resistive components or line termination, is suppressed as well, which is particularly important if the varactor is used to tune an RF resonator with high quality factor  $Q$ . The capacitors  $C_{\text{cp}}$  couple the RF signal to the varactor and block DC voltages such that the voltage  $U_{\text{RF}}$  in the RF circuit is independent of the bias voltage  $U_{\text{DC}}$ . In the limit  $C_{\text{cp}} \gg C_{\text{jun}}$  and neglecting the DC supply, which is realistic for suitable choke components, one can identify  $C_v \approx C_{\text{jun}}$ . In this limit the equivalent circuit in (b) has the full tuning range of the varactor diode.

For a varactor diode to be used in an ion trap RF resonator, three requirements have to be met: a large tuning range, a large reverse breakdown voltage and small RF

losses. Generally, the tuning range sets the achievable ratio between RF voltages on different trap electrodes and thereby defines by how much the RF null can be shifted. The varactor's breakdown voltage should be much larger than the applied RF voltage. Furthermore, the modulation of the varactor capacitance by the applied RF drive should be negligible in order to avoid an amplitude modulation of the RF voltage driving the trap. Such a modulation would translate to a modulation of the pseudo potential and could possibly parametrically excite the radial ion modes. RF losses may reduce the RF resonator's voltage gain and can furthermore induce phase shifts between the RF voltage on different trap electrodes. A large phase shift leads to excess micromotion that cannot be compensated and might even make the trap unstable.

These requirements are quantified for the specific RF circuits presented in the following sections. A more accurate treatment of the impact of phase differences on ion trajectories considering specific trap geometries can be done using Monte Carlo simulations [145]. This approach is also suited to study the effect of jitter in the ratio of RF voltages on different trap electrodes, which is not considered here.

### 6.1.1. Capacitive networks

Capacitive networks have been used in the past to realize different levels of RF voltage on trap electrodes, using mechanically tunable capacitors [110, 140, 142–144]. Fig. 6.2 shows three examples of such networks. Circuits (a) and (c) have been used in trapped-ion experiments, circuit (b) is a synthesis of the two. Each network is driven by an RF source  $U_s$  amplified by an RLC resonator, where the capacitive part is formed by the network components. For simplicity, only two trap RF electrodes,  $C_{el,1}$  and  $C_{el,2}$ , are considered. The schemes are easily extendable to a larger number of RF electrodes. Furthermore, the discussion is limited to reducing the voltage  $U_2$  on electrode  $C_{el,2}$  relative to the voltage  $U_1$  on electrode  $C_{el,1}$ , i. e. only values  $\zeta \leq 1$  are considered, where the voltage ratio

$$\zeta = U_2/U_1 \tag{6.1}$$

has been introduced. Values  $\zeta > 1$  correspond to swapping the roles of electrodes  $C_{el,1}$  and  $C_{el,2}$  and are hence implicitly included in the analysis. The most simple network, shown in Fig. 6.2(a) and used in the work of Kim et al. [142, 144], consists of a parallel circuit of the first trap electrode  $C_{el,1}$  and the series capacitance of the second electrode  $C_{el,2}$  with a tunable capacitor  $C_v$ . In this configuration, the full RF voltage within in the resonator is applied at the first electrode,  $U_1 = U_{RF}$ , while the voltage on the

## 6. Tunable RF fields in cryogenic traps

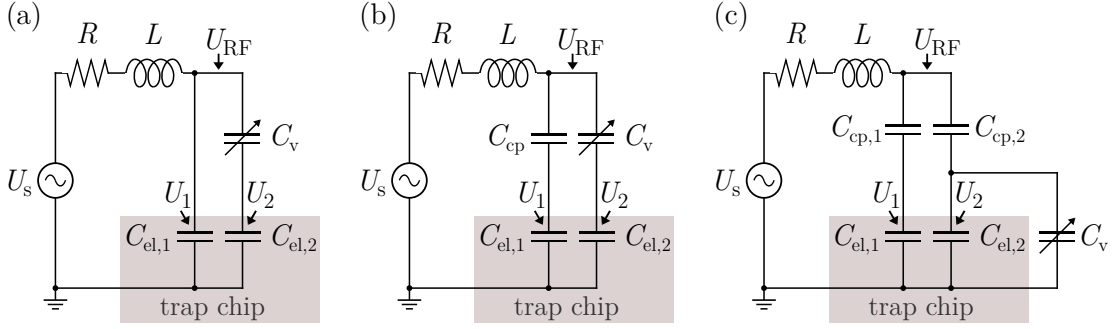


**Figure 6.2.** Capacitive networks for driving two trap electrodes  $C_{\text{el},1}$ ,  $C_{\text{el},2}$  at different RF voltage. The capacitances within the gray shaded area are intrinsic to the trap chip. Matching networks to adjust the resonator impedance to the source impedance are omitted.

second electrode is reduced by the capacitive divider ratio

$$\frac{U_2}{U_{\text{RF}}} = \frac{Z_{C_{\text{el},2}}}{Z_{C_{\text{el},2}} + Z_{C_v}} = \frac{C_v}{C_{\text{el},2} + C_v}, \quad (6.2)$$

where  $Z_C = -i/(\Omega_{\text{RF}}C)$  is the impedance of a capacitor. Fig. 6.3 (a) shows the corresponding voltage tunability for typical trap electrode capacitances  $C_{\text{el},1} = C_{\text{el},2} = 10$  pF. For a varying tuning capacitance  $C_v \in [1.1, 90]$  pF, RF voltage ratios  $\zeta$  between 0.1 and 0.9 can be achieved. From the form of Eq. (6.2) it is clear that the value  $U_2 = U_{\text{RF}}$  ( $\zeta = 1$ ) can only be reached asymptotically in the limit  $C_v \rightarrow \infty$ . The opposite limit,  $U_2 = 0$  ( $\zeta = 0$ ), is realized for  $C_v = 0$ . However, values  $C_v \lesssim 1$  pF are in practice hard to realize due to parasitic capacitances present in every setup. As  $C_v$  is tuned, the total capacitance of the network,

$$C_{\text{tot}} = C_{\text{el},1} + \frac{C_{\text{el},2}C_v}{C_{\text{el},2} + C_v}, \quad (6.3)$$

varies as well, which causes a shift of the circuit's resonance frequency. To prevent this, one could add an additional electrically tunable capacitor in parallel (not considered here), to keep  $C_{\text{tot}}$  constant. A voltage ratio  $\zeta = 1$  can be reached by considering the more symmetric network in Fig. 6.2 (b), where both trap electrodes are part of a capacitive divider. While the voltage  $U_1$  on the first electrode is fixed by the value of the coupling capacitor  $C_{\text{cp}}$ ,  $U_2$  is again adjustable by tuning  $C_v$ , Eq. (6.2). The voltage tunability for this network is shown in Fig. 6.3 (b) for the case  $C_{\text{cp}} = 30$  pF. The ratio  $\zeta = 1$  is realized for a tuning capacitor value of  $C_v = C_{\text{cp}}$ , while  $\zeta = 0$  is again reached in the limit  $C_v = 0$ . The required tuning range for  $C_v$  is therefore set by the value of the coupling capacitor  $C_{\text{cp}}$ . The choice for  $C_{\text{cp}}$  is a compromise between minimizing the required tuning range and maximizing the RF voltage at the trap electrodes. This can

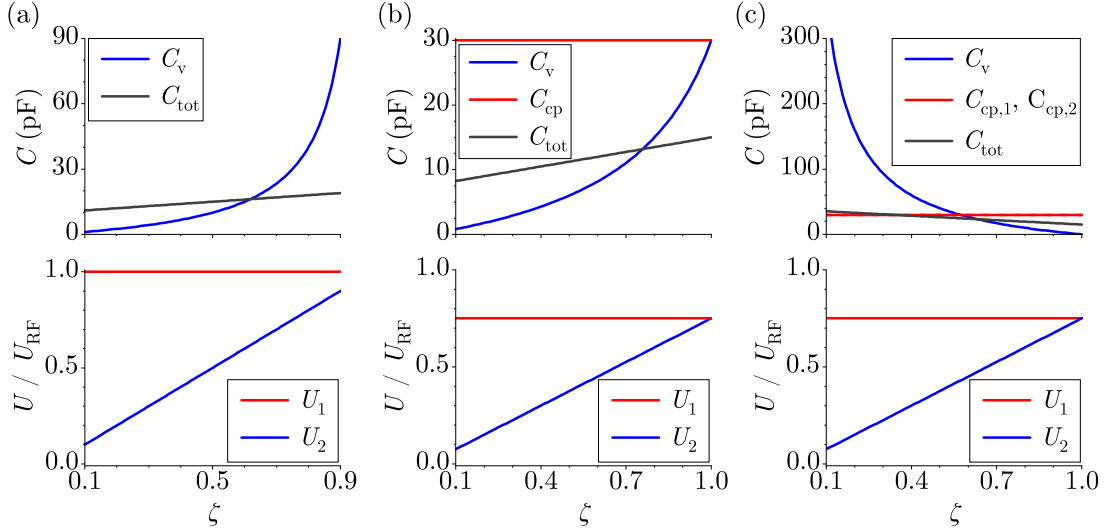


**Figure 6.3.** Required capacitance range of  $C_v$  (top) and resulting trap voltages  $U_1, U_2$  (bottom) for the three capacitive networks (a), (b), (c) in Fig. 6.2. The curves assume typical trap electrode capacitances  $C_{\text{el},1} = C_{\text{el},2} = 10$  pF.

be seen in the bottom plot of Fig. 6.3 (b). The RF voltage  $U_1$  on trap electrode  $C_{\text{el},1}$  is only 75% of the full voltage  $U_{\text{RF}}$  provided by the resonator. For further decreasing  $C_{\text{cp}}$ , an even smaller fraction of the available RF voltage is actually applied to the trap electrodes. The third network, shown in Fig. 6.2 (c), was used by Herskind et al. [143]. As for the previous network, both trap electrodes are part of a voltage divider, making a voltage ratio  $\zeta = 1$  accessible. The difference is that the tunable capacitance  $C_v$  is connected in parallel to the second trap electrode  $C_{\text{el},2}$ , which turns out to be unfavorable. The voltage tunability for this network is shown in Fig. 6.3 (c) with  $C_{\text{cp},1} = C_{\text{cp},2} = 30$  pF. The limit  $\zeta = 0$  is reached for  $C_v \rightarrow \infty$  leading to a significant enhancement of the required tuning range compared to the network (b).

Of the three circuits considered, the network in Fig. 6.2 (b) seems most promising for an implementation with varactor diodes, since it offers the largest accessible range for the voltage ratio  $\zeta$  within a finite varactor tuning range. However, even for this network, several tens of pF tuning range are required in order to achieve a significant change in the voltage ratio  $\zeta$ . At the same time, the varactor needs to withstand very high voltages. The RF voltage applied to the varactor is on the order of the RF trap drive voltage  $U_{\text{RF}}$ , which has to be significantly smaller than the varactor's breakdown voltage if the varactor is to be tuned at all. Assuming a value  $U_{\text{RF}} \sim 100$  V, typical for surface traps, leads to a required breakdown voltage  $U_{\text{br}}$  above a few hundred V. In addition, the varactor diode should have low RF losses, quantified by its ESR. A non-zero ESR leads to an effective Ohmic resistance  $\Delta R$  in addition to the resonator's

## 6. Tunable RF fields in cryogenic traps

resistance  $R$ . For the network in Fig. 6.2 (b), one finds in the limit of small ESR

$$\Delta R = \text{Re}\{Z_{\text{tot}}\} \approx \frac{C_{\text{el},2}^2(C_{\text{el},1} + C_{\text{cp}})^2 C_{\text{v}}^2}{(C_{\text{el},1}C_{\text{el},2}C_{\text{cp}} + C_{\text{el},2}C_{\text{cp}}C_{\text{v}} + C_{\text{el},1}(C_{\text{el},2} + C_{\text{cp}})C_{\text{v}})^2} \text{ESR}, \quad (6.4)$$

where  $Z_{\text{tot}}$  is the total impedance of the capacitive network. The capacitive prefactor in Eq. (6.4) is rising monotonously with increasing  $C_{\text{v}}$  and eventually saturates. For the example capacitances in Fig. 6.3 (b) and assuming  $C_{\text{v}} = 30$  pF, the prefactor equates to  $\Delta R \approx \text{ESR}/4$ . For the other two networks, similar expressions, linear in ESR, can be derived<sup>1</sup>. The additional resistance  $\Delta R$  needs to be compared to the resonator's resistance  $R$ . For a typical RF resonator with quality factor  $Q = 100$ , inductance  $L = 2$   $\mu\text{H}$  and resonance frequency  $\Omega_{\text{RF}} \approx 2\pi \times 30$  MHz, one finds  $R = \Omega_{\text{RF}}L/Q \approx 3.8$   $\Omega$ . A varactor with an ESR on the order of 1  $\Omega$  would therefore already notably affect the voltage gain of the RF resonator. Apart from limiting the voltage gain, the ESR can also induce a phase difference  $\Delta\phi$  between the RF voltages  $U_1, U_2$  on the trap electrodes. Substituting  $Z_{C_{\text{v}}} = -i/(\Omega_{\text{RF}}C_{\text{v}}) + \text{ESR}$  in Eq. (6.2), one finds for the networks in Fig. 6.2 (a) and (b)

$$\tan(\Delta\phi) = \frac{\text{Im}\{U_2/U_{\text{RF}}\}}{\text{Re}\{U_2/U_{\text{RF}}\}} = -\frac{C_{\text{el},2}C_{\text{v}}}{C_{\text{el},2} + C_{\text{v}}} \Omega_{\text{RF}} \text{ESR}, \quad (6.5)$$

assuming all other capacitors are ideal such that  $U_1$  is in phase with  $U_{\text{RF}}$ . For the example capacitances in Fig. 6.3 (b) and assuming  $C_{\text{v}} = 30$  pF, this equates to a phase error  $\Delta\phi \approx -0.07^\circ \Omega^{-1} \text{ESR}$  in the limit of small angles. The phase error for the network in Fig. 6.3 (c) has the same magnitude<sup>2</sup>. For an ESR in the range of 1  $\Omega$ , phase differences are therefore negligible.

In summary, capacitive networks are in principle suited to implement electrically tunable RF fields in ion traps. However, the requirements on the varactor diodes, in particular the combination of high tuning range and large breakdown voltage, are difficult to meet for commercially available components. Tab. 6.1 lists typical parameters of selected semiconductor diodes with tunable capacitance. The components from Infineon and Macom, specified as varactor diodes, have junction capacitances  $C_{\text{jun}}$  in the required range of a few to a few tens of pF, with low ESR values in the range of a few  $\Omega$ . However, the breakdown voltages are low, on the order of a few tens of V. The models from IXYS and Rohm have about one order of magnitude larger breakdown voltages and junction capacitances. However, these components are specified as Schottky rectifiers and their ESR is not listed. Therefore, the usability of these components

<sup>1</sup> for the networks in Fig. 6.3 (a) and (c) the prefactors are 0.18 and 0.27, respectively, using the same capacitance values  $C_{\text{el},1} = C_{\text{el},2} = 10$  pF,  $C_{\text{v}} = C_{\text{cp},1} = C_{\text{cp},2} = 30$  pF.

<sup>2</sup>  $\Delta\phi \approx 0.12^\circ \Omega^{-1} \text{ESR}$ , using  $C_{\text{el},1} = C_{\text{el},2} = 10$  pF,  $C_{\text{v}} = C_{\text{cp},1} = C_{\text{cp},2} = 30$  pF.

**Table 6.1.** Room-temperature specifications of semiconductor diodes with tunable junction capacitance  $C_{\text{jun}}$ . For the diodes from IXYS and Rohm, the ESR is not available in the data sheets.

| model            | material | $U_{\text{br}}$ (V) | $C_{\text{jun}}$ (pF) | ESR ( $\Omega$ ) |
|------------------|----------|---------------------|-----------------------|------------------|
| Infineon BB640   | Si       | 30                  | $\approx (3 - 69)$    | 1.2              |
| Macom MA46H204   | GaAs     | 22                  | $\approx (2 - 20)$    | 10               |
| IXYS DGS 20-018A | GaAs     | 180                 | $\approx (25 - 300)$  | N/A              |
| Rohm SCS220AE2   | SiC      | 650                 | $\approx (37 - 500)$  | N/A              |

has to be tested. Even then, the breakdown voltages of the Schottky diodes is with a few hundred V barely enough for application in an ion trap drive. The effective RF voltage applied to a diode can be reduced by making the diode part of a capacitive divider. The resulting decrease in tuning range could then be compensated by using several components in parallel. This approach is, however, limited by the small spatial volume typically available in cryogenic setups. The operation in a cryostat adds an additional constraint on the component selection. Since the operability of semiconductor components is typically not specified at temperatures below  $T \approx -55^\circ\text{C}$ , component tests for cryogenic compatibility are imperative (cf. section 6.2).

### 6.1.2. Multiple resonators

An alternative implementation of tunable RF voltages employs multiple RF resonators and was used in the works of Kim [145] and Kumph [54, 96]. With this approach, the ratio of RF voltages on different trap electrodes can be extended to negative values,  $\zeta < 0$ . The basic circuit depicted in Fig. 6.4 shows two trap electrodes connected to separate RF oscillators and powered by independent drives. The parasitic capacitance  $C_c$

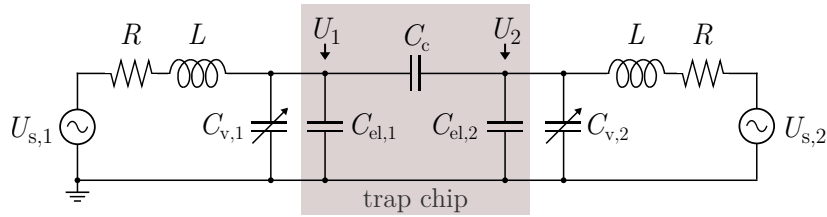


**Figure 6.4.** Circuit with two RF resonators driving two different trap electrodes  $C_{\text{el},1}, C_{\text{el},2}$ . The capacitances within the gray shaded area are intrinsic to the trap chip. Networks for impedance matching are omitted.

between the trap electrodes leads to a coupling of the two resonators. As consequence, the amplitude and phase of each of the trap voltages  $U_1, U_2$  depend on both RF drives. In particular, for drives with different amplitudes,  $U_{s,1} \neq U_{s,2}$ , the trap voltages will in general have a non-zero phase difference, even if the drives are in phase. Such a phase

## 6. Tunable RF fields in cryogenic traps

lag on the trap electrodes results in excess micromotion and eventually instability of the ion trap. In the following, the drives are assumed to be in phase. Additional tuning capacitors  $C_{v,1}, C_{v,2}$ , realized with varactor diodes, can then be used to phase-stabilize the trap voltages and maintain a zero phase lag, as has previously been demonstrated in a trapped-ion experiment [54]. The underlying mechanism for this stabilization is described in the following. The possibility of using an alternate scheme without tuning capacitors, solely relying on phase control of the two drives is discussed in section 6.3.

### Basic theory of coupled electric resonators

Differential equations for the trap voltages  $U_1(t), U_2(t)$  can be derived following the procedure in Ref. [147], using Kirchhoff's laws

$$\left( L \frac{d^2}{dt^2} + R \frac{d}{dt} \right) [(C_1 + C_c) U_1(t) - C_c U_2(t)] + U_1(t) = \hat{U}_{s,1} \sin(\Omega_{\text{RF}} t), \quad (6.6a)$$

$$\left( L \frac{d^2}{dt^2} + R \frac{d}{dt} \right) [(C_2 + C_c) U_2(t) - C_c U_1(t)] + U_2(t) = \hat{U}_{s,2} \sin(\Omega_{\text{RF}} t), \quad (6.6b)$$

where  $C_1 = C_{\text{el},1} + C_{v,1}$  and  $C_2 = C_{\text{el},2} + C_{v,2}$  are the total load capacitances of the two resonators. The system of equations (6.6) can be decoupled using a basis transformation. Evaluating the superposition (6.6a) +  $m$ (6.6b) and comparing coefficients one finds after some algebra the two eigenmode components

$$U_e(t) = U_1(t) + m_e U_2(t), \quad (6.7a)$$

$$U_o(t) = U_1(t) + m_o U_2(t), \quad (6.7b)$$

with

$$m_e = \frac{C_1 - C_2 + \sqrt{(C_1 - C_2)^2 + (2C_c)^2}}{2C_c}, \quad (6.8a)$$

$$m_o = \frac{C_1 - C_2 - \sqrt{(C_1 - C_2)^2 + (2C_c)^2}}{2C_c}. \quad (6.8b)$$

For the symmetric case of two identical oscillators,  $C_1 = C_2$ , Eqs. (6.8) reduce to the standard result [147]  $m_{e,o} = \pm 1$ . One can thus identify  $U_e$  with the even mode, where  $U_1, U_2$  oscillate in phase, and  $U_o$  with the odd mode, where the trap voltages have a relative phase shift of  $\pi$ . In the uncoupled basis, the differential equations (6.6) can be cast in the form of a simple harmonic oscillator

$$\left( \frac{d^2}{dt^2} + \gamma \frac{d}{dt} + \omega_{e,o}^2 \right) U_{e,o}(t) = f_{e,o} \sin(\Omega_{\text{RF}} t), \quad (6.9)$$

with a damping factor  $\gamma = R/L$  and resonance frequencies

$$\omega_e^2 = \frac{C_1 + C_2 + 2C_c + \sqrt{(C_1 - C_2)^2 + (2C_c)^2}}{2L[C_1C_2 + C_c(C_1 + C_2)]}, \quad (6.10a)$$

$$\omega_o^2 = \frac{C_1 + C_2 + 2C_c - \sqrt{(C_1 - C_2)^2 + (2C_c)^2}}{2L[C_1C_2 + C_c(C_1 + C_2)]}. \quad (6.10b)$$

For  $C_1 = C_2$  this reduces to  $\omega_e^2 = (LC_1)^{-1}$  and  $\omega_o^2 = [L(C_1 + 2C_c)]^{-1}$  with a mode splitting  $\Delta\omega = \omega_e - \omega_o \approx \omega_e C_c / C_1$  in the limit  $C_c \ll C_1$ . The drive amplitudes are given by

$$f_e = \omega_e^2 (\widehat{U}_{s,1} + m_e \widehat{U}_{s,2}), \quad (6.11a)$$

$$f_o = \omega_o^2 (\widehat{U}_{s,1} + m_o \widehat{U}_{s,2}). \quad (6.11b)$$

The steady state solution of the uncoupled differential equation (6.9), the textbook problem of a driven harmonic oscillator, can be written in the well-known form

$$U_{e,o}(t) = A_{e,o} \sin(\Omega_{\text{RF}} t + \varphi_{e,o}), \quad \text{where} \quad (6.12a)$$

$$A_{e,o}(t) = \frac{f_{e,o}}{\sqrt{(\omega_{e,o}^2 - \Omega_{\text{RF}}^2)^2 + \gamma^2 \Omega_{\text{RF}}^2}}, \quad (6.12b)$$

$$\varphi_{e,o}(t) = \arctan\left(\frac{\omega_{e,o}^2 - \Omega_{\text{RF}}^2}{\gamma \Omega_{\text{RF}}}\right) - \frac{\pi}{2}. \quad (6.12c)$$

From the eigenmodes, the trap voltages can be reconstructed using the inverse of the transformation given by Eq. (6.7),

$$U_1(t) = \frac{m_e U_o(t) - m_o U_e(t)}{m_e - m_o}, \quad (6.13a)$$

$$U_2(t) = \frac{U_e(t) - U_o(t)}{m_e - m_o}. \quad (6.13b)$$

### Active mode suppression

The forced oscillations of the trap voltages  $U_1$  and  $U_2$  have a sinusoidal form,  $U_{1,2} = A_{1,2} \sin(\Omega_{\text{RF}} t + \varphi_{1,2})$ , where the amplitudes  $A_{1,2}$  and phases  $\varphi_{1,2}$  are given by Eqs. (6.13) and (6.8). In the general case, the trap voltages are not in phase,  $\Delta\varphi = \varphi_2 - \varphi_1 \neq 0$ . This stems from the fact that the drive frequency  $\Omega_{\text{RF}}$  cannot simultaneously be resonant with both eigenmodes due to the splitting of the eigenfrequencies. For a specific choice of capacitances, however, it is possible to suppress the excitation of one of the eigenmodes, in which case both trap voltages will become proportional to the remain-

## 6. Tunable RF fields in cryogenic traps

ing eigenmode and will thus oscillate in phase (or  $180^\circ$  out of phase). The principle is illustrated in Fig. 6.5. Initially, symmetric resonators are considered with  $C_1 = C_2$

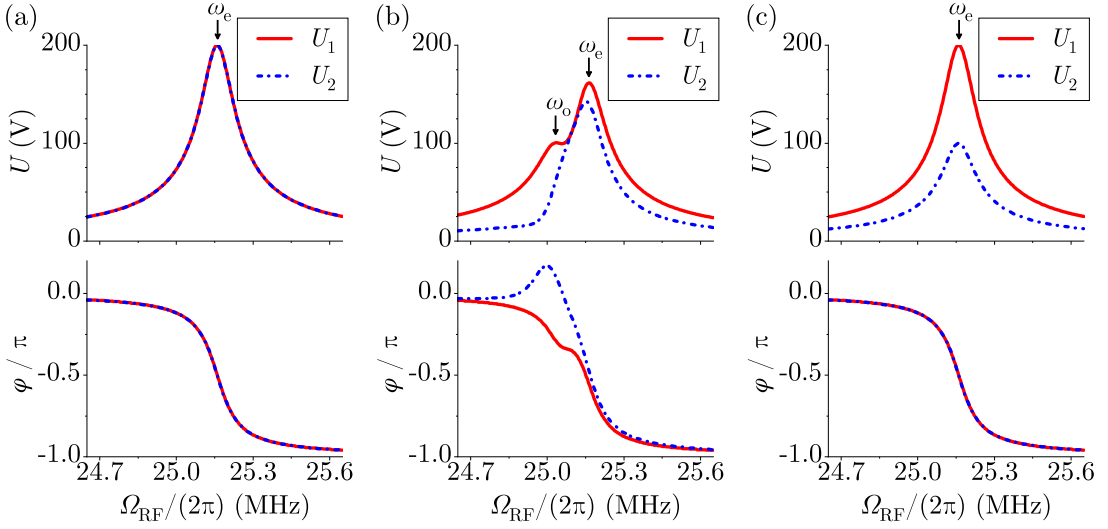


**Figure 6.5.** Bode diagrams of the trap voltages  $U_1, U_2$  in the circuit of two capacitively coupled resonators with  $C_{1,2} = 20$  pF,  $C_c = 0.1$  pF,  $L = 2$   $\mu$ H and  $R = 1.58$   $\Omega$ , corresponding to a quality factor  $Q = 200$ . Both RF drives are assumed to be in phase. (a) For equal driving,  $\hat{U}_{s,1} = \hat{U}_{s,2} = 1$  V, only the even mode is populated. (b) For asymmetric driving,  $\hat{U}_{s,1} = 1$  V and  $\hat{U}_{s,2} = 0.5$  V, the odd mode becomes visible. (c) The odd mode excitation can be suppressed by adjusting the resonators' capacitances  $C_1, C_2$ , for identical drive conditions as in (b).

such that  $m_e = +1, m_o = -1$ . From Eqs. (6.12b) and (6.11) one can see that the odd mode is completely suppressed for equally strong driving,  $\hat{U}_{s,1} = \hat{U}_{s,2} = 1$  V. The resulting trap voltages  $U_1, U_2$  have the same amplitude ( $\zeta = 1$ ) and are in phase as shown in (a). Upon reducing the second drive amplitude to  $\hat{U}_{s,2} = 0.5$  V, (b), the odd mode becomes excited, leading to a phase difference between the trap voltages. At the even mode frequency  $\omega_e$ , where the amplitudes are maximal, the phase lag is about  $\Delta\varphi \approx 15^\circ$ . The phase difference at  $\omega_e$  depends on the ratio between eigenmode splitting  $\Delta\omega = \omega_e - \omega_o \approx \omega_e C_c / C_1$  and resonance width  $\delta\omega \sim \omega_e / Q \approx R / L$ .  $\Delta\varphi$  is maximal for  $\Delta\omega \sim \delta\omega$ , which turns out to be the typical scenario: For better resolved eigenmodes,  $\Delta\omega \gg \delta\omega$ , the trap voltage ratio  $\zeta$  cannot be varied significantly. The limit  $\Delta\omega \ll \delta\omega$  is hard to realize experimentally since the coupling capacitance  $C_c$  is given by the trap geometry and the resonator  $Q$  needs to be sufficiently large to achieve the required trap voltages. For a ratio  $\Delta\omega / \delta\omega$  decreased by a factor 100 compared to the scenario in Fig. 6.5 (b), the phase shift would still be  $\Delta\varphi \approx 1^\circ$ . The phase shift can be completely canceled, however, by suppressing the odd mode. This is shown in subplot (c). For a capacitance change  $\delta C_1 = -0.05$  pF,  $\delta C_2 = 0.1$  pF the odd mode vanishes and the trap

voltages correspond to the drive voltage ratio  $\widehat{U}_{s,2}/\widehat{U}_{s,1} = 1/2$  at full voltage gain.

From Eqs. (6.11) one can derive an analytical formula for the change in capacitance required to suppress the unwanted eigenmode. For a trap voltage ratio  $\zeta > 0$  one would naturally suppress the odd mode, i. e.,  $f_o \stackrel{!}{=} 0$ , leading to a constraint for  $C_2$ . It is easy to verify that the trap voltage ratio  $\zeta$  is then given by the ratio of drive strengths,  $\zeta = U_2/U_1 = \widehat{U}_{s,2}/\widehat{U}_{s,1}$ . In addition, one can keep the even mode frequency  $\omega_e$  constant by constraining also  $C_1$  through Eq. (6.10a). As a result one finds

$$C_1 = C_i + C_c (\zeta - 1) , \quad (6.14a)$$

$$C_2 = C_i + C_c \left( \frac{1}{\zeta} - 1 \right) , \quad (6.14b)$$

where  $C_i$  is an offset satisfying  $C_1 = C_2$  for  $\zeta = 1$ . The formulas derived for the case  $\zeta < 0$  are identical to Eqs. (6.14). Fig. 6.6 (a) shows the variation in  $C_1, C_2$  for an initial capacitance  $C_i = 20$  pF and coupling capacitance  $C_c = 0.1$  pF. In either of the half

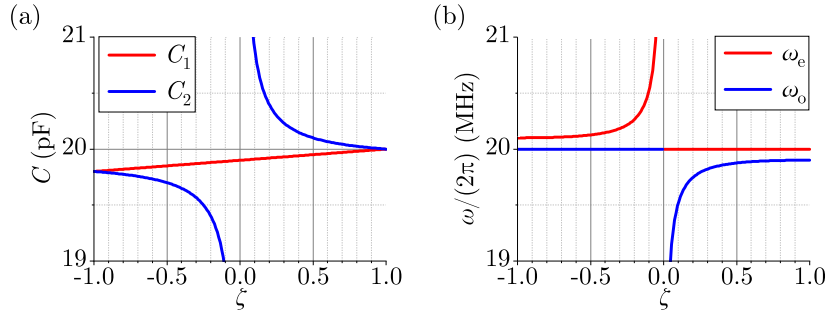


**Figure 6.6.** Required capacitance change (a) and resulting eigenfrequency variation (b) for a suppression of the odd mode ( $\zeta > 0$ ) or even mode ( $\zeta < 0$ ) with simultaneous stabilization of the target mode frequency. The resonator’s coupling capacitance is  $C_c = 0.1$  pF, the initial load capacitances are  $C_i = 20$  pF.

spaces  $\zeta \gtrless 0$ , a large variation in the trap voltage ratio can be achieved with only a small capacitance tuning range. For instance, for  $\zeta \in [0.1, 1]$  about 1 pF tuning range for  $C_2$  is required, for  $C_1$  it is only a fraction of that. The tuning range is proportional to  $C_c$ , such that a small coupling capacitance is beneficial for this approach. Tuning over the entire range  $\zeta \in [-1, 1]$  is not possible due to the singularity in  $C_2$  at  $\zeta = 0$ . The mode suppression comes along with a frequency shift of the suppressed mode, as shown in subplot (b). For  $\zeta > 0$ , the even mode is stabilized to a constant value, while the odd mode gets shifted further out for  $\zeta \rightarrow 0$ . For  $\zeta < 0$ , the roles of the two modes are reversed.

In summary, multiple RF resonators allow one to realize large variations in the trap voltage ratio  $\zeta$  using tunable capacitors for phase stabilization. The required varactor

## 6. Tunable RF fields in cryogenic traps

tuning range is about 1 pF for a realistic resonator coupling capacitance  $C_c = 0.1$  pF. This tuning range is significantly smaller than the range necessary in capacitive networks. In the scheme presented, the entire RF voltage is applied to the tunable capacitor, such that the required breakdown voltages are in the kV range, as is the case for the capacitive networks. It is, however, possible to trade off the requirements on breakdown voltage for tuning range by making the varactor diode part of a capacitive voltage divider. The corresponding circuit is described in the next section.

### 6.2. Operation of a tunable resonator at cryogenic temperatures

This section describes a resonator prototype developed to implement tunable RF fields with two resonators in a cryogenic environment. The resonator builds on the work of Kumph [54, 96] and uses varactor diodes as a capacitive tuning element. Semiconductor components, such as varactor diodes, are typically not specified for operation at cryogenic temperatures. One of the major limitations for the applicability at low temperatures is charge carrier freeze out [146]. While this phenomenon affects in particular intrinsic silicon and germanium components, other materials, for instance  $n$ -type GaAs, have been reported to be operable down to  $T = 4.2$  K [146]. The performance of several commercially available varactor diodes as tuning elements of the resonator prototype is assessed at three temperatures,  $T \approx 300$  K,  $T \approx 77$  K and  $T \approx 10$  K. The diodes are characterized in terms of capacitance tunability and quality factor  $Q$ .

The final version of the prototype is described in detail in the following. The varactor test results at  $T \approx 300$  K and  $T \approx 77$  K were obtained in an earlier version of the circuit. This does not affect the conclusions drawn from the measurements.

#### 6.2.1. Resonator setup

The schematic circuit of the resonator prototype is shown in Fig. 6.7. The actual electric resonator consists of a home-built coil with inductance  $L \approx 900$  nH described further below and the attached load capacitances. The main load  $C_{\text{trap}} = 20$  pF<sup>3</sup> simulates the RF electrode of an ion trap. An additional capacitive divider consisting of the capacitances  $C_{\text{mo},1} = 5$  pF<sup>4</sup> and  $C_{\text{mo},2} = 100$  pF<sup>5</sup> allows one to monitor the voltage inside the resonator. The resistance  $R_{\text{mo}} = 1$  k $\Omega$ <sup>6</sup> limits the backaction of a low-impedance terminated monitor line on the resonator. The total load capacitance is tuned by the

<sup>3</sup> Cornell Dubilier, MC12CD100D-F, 10.0(5) pF, 500 V (two components in parallel).

<sup>4</sup> Cornell Dubilier, MC12CD050D-F, 5.0(5) pF, 500 V.

<sup>5</sup> Cornell Dubilier, MC18FD101J-F, 100(5) pF, 500 V.

<sup>6</sup> Yageo Europe, RC0805, 1 k $\Omega$ .

## 6.2. Operation of a tunable resonator at cryogenic temperatures

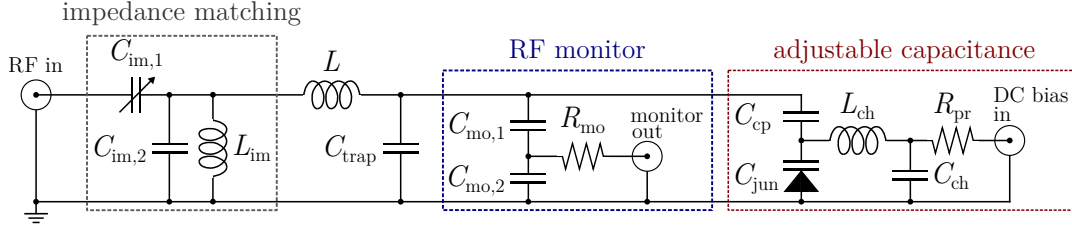


**Figure 6.7.** Schematic circuit of the electrically tunable resonator prototype.

capacitive divider network consisting of the fixed value capacitor  $C_{cp} = 10 \text{ pF}$ <sup>7</sup> and the tunable varactor capacitance  $C_{jun}$ . The divider reduces the amount of RF voltage that is applied to the varactor such as to lower the requirements on the varactor's breakdown voltage. The varactor capacitance  $C_{jun}$  is tuned by the applied DC bias. The RF voltage within the DC bias line is suppressed by the first order choke with  $L_{ch} = 1 \text{ }\mu\text{H}$ <sup>8</sup> and  $C_{ch} = 4 \text{ nF}$ <sup>9</sup>. The resistance  $R_{pr} = 510 \text{ k}\Omega$ <sup>10</sup> limits the DC current in case of a breakdown of the varactor diode. The resonator is impedance-matched to the  $50 \text{ }\Omega$  coax input line by the two matching capacitors  $C_{im,1} = (8 - 50) \text{ pF}$ <sup>11</sup> and  $C_{im,2} = 320 \text{ pF}$ <sup>12</sup>. The values for the matching capacitors is determined by circuit simulation<sup>13</sup> using the previously determined  $Q$  value of the unmatched resonator. Adjusting the value of the trimmer  $C_{im,1}$ , the circuit can be matched for either of the three temperatures  $T \approx 300 \text{ K}$ ,  $T \approx 77 \text{ K}$  and  $T \approx 10 \text{ K}$ , with a residual power reflection of below 10% on resonance. The inductance  $L_{im} = 1 \text{ }\mu\text{H}$ <sup>14</sup> ensures that the DC level at the trap electrodes is grounded and has negligible influence on the matching network. The tests at  $T \approx 300 \text{ K}$  and  $T \approx 77 \text{ K}$  were performed in an earlier version of the prototype with  $C_{cp} = 5 \text{ pF}$ <sup>15</sup> and  $C_{ch} = 2 \text{ nF}$ <sup>16</sup>. These values were doubled in the final version to increase the resonator tuning range and choke suppression, respectively. For the test of the varactor bandwidth described at the end of this section,  $R_{pr}$  was reduced to  $R_{pr} \approx 1 \text{ }\Omega$ <sup>17</sup> to eliminate low-pass filter effects.

Fig. 6.8 (a) shows a photograph of the resonator prototype integrated to the cryogenic setup described in chapter 4.1. The entire circuit, including the RF monitor and tuning

<sup>7</sup> Cornell Dubilier, MC12CD100D-F, 10.0(5) pF, 500 V.

<sup>8</sup> Murata, LQW2UAS1R0J00L, 1.00(5)  $\mu\text{H}$ , 370 mA, 1.75  $\Omega$ .

<sup>9</sup> Cornell Dubilier, MC22FA202J-F, 2.0(1) nF, 100 V (two components in parallel).

<sup>10</sup> RALEC, RTT05, 510(5) k $\Omega$ , 125 mW.

<sup>11</sup> Johanson Manufacturing, 9710-5, (8-50)pF trimmer, 250 V.

<sup>12</sup> Cornell Dubilier, MC18FD221J-F, 220(11) pF, 500 V and MC18FD101J-F, 100(5) pF, 500 V (in parallel).

<sup>13</sup> for circuit simulation the software LTspice by Analog Devices was used.

<sup>14</sup> Murata, LQW2UAS1R0J00L, 1.00(5)  $\mu\text{H}$ , 370 mA, 1.75  $\Omega$ .

<sup>15</sup> Cornell Dubilier, MC12CD050D-F, 5.0(5) pF, 500 V.

<sup>16</sup> Cornell Dubilier, MC22FA202J-F, 2.0(1) nF, 100 V.

<sup>17</sup> Yageo Europe, RC0805, 1  $\Omega$ .

## 6. Tunable RF fields in cryogenic traps

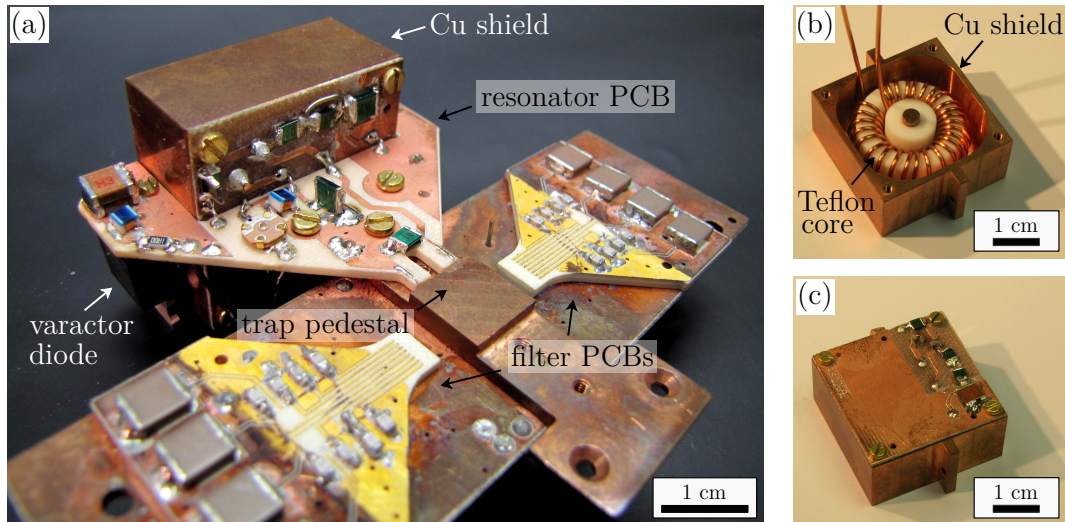


**Figure 6.8.** Photographs of the electrically tunable resonator prototype. (a) The resonator PCBs, including the varactor diode and RF monitor components, are integrated to the cryogenic trap holder with attached DC filter stage. The arrangement allows for the integration of a second, identical resonator at the bottom right. (b) The resonator coil has a PTFE (Teflon) core and is enclosed by a copper shield covered by a PCB, (c).

network, is placed on a compact arrangement of two PCBs and a copper enclosure, which shields the resonator coil. The structure has a size of about  $5 \times 4 \times 3.5 \text{ cm}^3$  and is located on one side of the central ion trap pedestal, leaving room for a second, identical resonator circuit on the opposite side. The spatial separation of the two resonators minimizes coupling effects that add to the unavoidable capacitive coupling via the trap electrodes. The inductive coupling is further reduced by the copper shield, which encloses the resonator coil from 5 sides as shown in Fig. 6.8 (b). The 6th side is closed by one of the PCBs, (c). The toroidal resonator coil consists of 28 turns of a 1 mm diameter copper wire around a PTFE (Teflon) core<sup>18</sup>. PTFE spacers hold the coil rigidly within the enclosure. Apart from shielding the RF magnetic fields, the copper enclosure also eliminates the influence of additional capacitances between the coil and the inner heat shield of the cryostat. This ensures that the resonator remains impedance-matched upon insertion into the cryostat.

### Frequency tuning

Several commercially available varactor diodes, listed in Tab. 6.2, were tested as capacitive tuning elements. All components are Schottky diodes and use silicon-carbide (SiC) or gallium-arsenide (GaAs) technology. Silicon diodes were not considered, due to their likely incompatibility with the ultimate target temperatures  $T \approx 10 \text{ K}$ . The compo-

<sup>18</sup> core dimensions: 24 mm outer diameter, 14 mm inner diameter, 8 mm width.

## 6.2. Operation of a tunable resonator at cryogenic temperatures

**Table 6.2.** Room-temperature specifications of the varactor diodes used as capacitive tuning elements. The limits for  $C_{\text{jun}}$  are data sheet values for a bias voltage of  $U_{\text{DC}} = 250$  V and  $U_{\text{DC}} \gtrsim 0$  V, respectively. The tuning range  $\Delta C_{\text{tot}}$  is calculated by inserting these limits into Eq. (6.15) with  $C_{\text{cp}} = 5$  pF. For the IXYS diode, the  $\Delta C_{\text{tot}}$  value in parentheses corresponds to  $C_{\text{cp}} = 10$  pF.

| label   | model               | material | $U_{\text{br}}$ (V) | $C_{\text{jun}}$ (pF)  | $\Delta C_{\text{tot}}$ (pF) |
|---------|---------------------|----------|---------------------|------------------------|------------------------------|
| Cree    | Cree C3D20065D      | SiC      | 650                 | $\approx (40 - 380)$   | 0.49                         |
| Infin 1 | Infineon IDV02S60C  | SiC      | 600                 | $\approx (10 - 60)$    | 1.28                         |
| Infin 2 | Infineon IDW12G65C5 | SiC      | 650                 | $\approx (50 - 430)$   | 0.40                         |
| Infin 3 | Infineon IDW30G65C5 | SiC      | 650                 | $\approx (110 - 1050)$ | 0.19                         |
| Rohm    | Rohm SCS220AE2      | SiC      | 650                 | $\approx (37 - 500)$   | 0.55                         |
| STM 1   | STM STPSC20H065C    | SiC      | 650                 | $\approx (48 - 480)$   | 0.42                         |
| STM 2   | STM STPSC40065C-Y   | SiC      | 650                 | $\approx (100 - 1250)$ | 0.22                         |
| IXYS    | IXYS DGS 20-018A    | GaAs     | 180                 | $\approx (25 - 300)$   | 0.75 (2.54)                  |

nents were selected based on their large reverse breakdown voltage  $U_{\text{br}} > 100$  V, large junction capacitance  $C_{\text{jun}}$  on the order of tens of pF and large tuning range of about a factor 10. These specifications make such varactors ideal candidates for tuning of RF resonators. However, the varactor's RF losses and their low-temperature behavior are not specified and need to be assessed.

The junction capacitance  $C_{\text{jun}}$  of the varactor diodes is adjusted with the DC bias voltage from a DC power supply<sup>19</sup> and sets the adjustable capacitance contribution to the resonator load

$$C_{\text{adj}} = \frac{C_{\text{cp}}C_{\text{jun}}}{C_{\text{cp}} + C_{\text{jun}}}, \quad (6.15)$$

where  $C_{\text{cp}}$  is the capacitor with which the varactor forms a divider. The expected tuning range  $\Delta C_{\text{tot}}$  for each varactor follows by inserting the limits in junction capacitance  $C_{\text{jun}}$  into Eq. (6.15). These limits are determined by the specified capacitance values at a bias voltage  $U_{\text{DC}} \gtrsim 0$  V and  $U_{\text{DC}} = \min(U_{\text{br}}, 250 \text{ V})$ , respectively. The maximal bias voltage  $U_{\text{DC}} = 250$  V, given by the range of the power supply, is sufficient since the junction capacitances of the tested varactor diodes change very little for voltages  $U_{\text{DC}} > 200$  V. The limits of  $C_{\text{jun}}$  and expected tuning range  $\Delta C_{\text{tot}}$  are listed in Tab. 6.2. The calculation assumes a value  $C_{\text{cp}} = 5$  pF as used in the tests at  $T \approx 300$  K and  $T \approx 77$  K. For the IXYS diode,  $\Delta C_{\text{tot}}$  is also given for  $C_{\text{cp}} = 10$  pF used in the test at  $T \approx 10$  K.

<sup>19</sup> TTI, PLH250-P, 250 V, 0.375 A.

### Quality factor

All fixed value capacitors in the resonator circuit, including the capacitance  $C_{\text{trap}}$  simulating an ion trap, are mica components with a high quality factor  $Q > 1000$ , specified at 10 MHz. Similarly, the trimmer  $C_{\text{im},1}$  in the matching network was selected for high- $Q$  operation, with its specified value of  $Q > 250$  at 100 MHz. Therefore, the quality factor of the resonator will in the best case be limited by the resistance of the wiring, in particular the coil  $L$ . A second source of dissipation might be introduced by the adjustable capacitance network, since a varactor with low quality factor could reduce the resonator's  $Q$ . Furthermore, the DC bias line can potentially reduce the quality factor, even though the RF-voltage on the DC line is strongly reduced by the choke components. The level of RF currents within the varactor and the bias line changes as the varactor diode's capacitance  $C_{\text{jun}}$  is varied. For decreasing  $C_{\text{jun}}$ , the RF current is decreased within the varactor and increased in the bias line. To separate out the impact of varactor diode and bias line on the resonator  $Q$ , additional tests were done, where the varactor diode was replaced by fixed-valued mica capacitors with low RF loss.

### 6.2.2. Experimental results

To assess the performance of the resonator prototype, the circuit is connected to an impedance analyzer<sup>20</sup>. The power reflection coefficient  $r^2 = |S_{11}^2|$  and power gain  $G_V^2 = |S_{21}|^2$  are measured as a function of RF drive frequency  $\Omega_{\text{RF}}$  for different values of the DC bias voltage. From a Lorentzian fit to the gain  $G_V^2$ , or equivalently the reflection  $r^2$ , the resonance frequency  $\omega_0$  and  $Q$ -factor are determined with  $Q = 2\omega_0/\delta\omega$ , where  $\delta\omega$  is the full width at half maximum of the resonance peak [118]. Fig. 6.9 shows typical data of the measured gain. From the measured resonance frequency  $\omega_0$  and the coil inductance  $L$  the total load capacitance of the resonator is calculated as  $C_{\text{tot}} = 1/(\omega_0^2 L)$ . The resulting data for the various varactor diodes and temperatures  $T$  is shown in Fig. 6.10.

#### Tests at room temperature

The 8 varactor diode models listed in Tab. 6.2 were tested at room temperature,  $T \approx 300$  K. The top plot in Fig. 6.10 (a) shows the total resonator capacitance  $C_{\text{tot}}$  as function of the DC bias voltage  $U_{\text{DC}}$ . The measured tuning range is in good agreement with the estimates in Tab. 6.2. It is interesting to note that  $C_{\text{tot}}$  changes approximately linearly with  $U_{\text{DC}}$ . The reason for this is the interplay of the inverse proportionality of the capacitive divider, Eq. (6.15), and the tuning profile of the varactor diodes.

<sup>20</sup> AEA technology, Via Bravo II Dual Port Vector Impedance Analyzer, 100 kHz - 200 MHz. And Rohde & Schwarz, ZNB 8 Vector network analyzer, 9 kHz - 8.5 GHz.

## 6.2. Operation of a tunable resonator at cryogenic temperatures

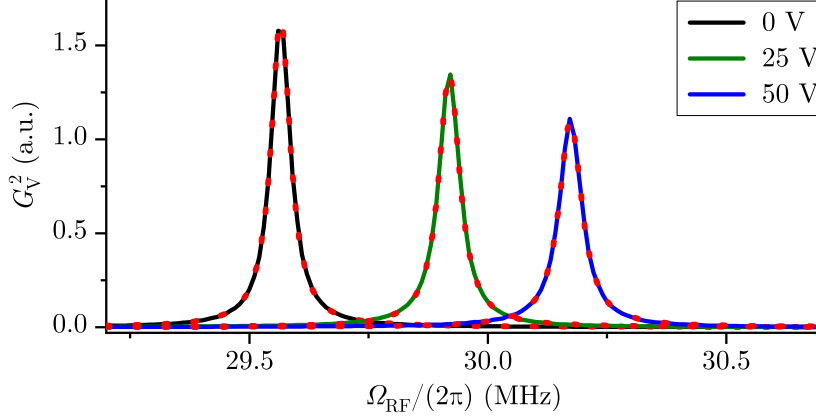


**Figure 6.9.** Typical data showing the power gain  $G_V^2$  of the resonant circuit as function of the drive frequency  $\Omega_{\text{RF}}$  for different DC bias voltages applied to the varactor diode. The dotted red lines are Lorentzian fits.

The plot at the bottom of Fig. 6.10 (a) shows the quality factor  $Q$  of the resonator as function of  $U_{\text{DC}}$ . The flat dependence observed for all diodes except Infin1 indicates that the adjustable capacitance network affects the resonator  $Q$  only negligibly. In particular, the  $Q$  of the varactor diodes does not limit the resonator  $Q$  as shown by the reference data point (golden diamond). For this reference point, the varactor diode was replaced by a low-loss capacitor<sup>21</sup> with  $C_{\text{ref}} = 100$  pF, for which a comparable resonator  $Q$  is measured. A notable exception from the general behavior is found for the diode Infin1 (dark red circles), where a drastic drop in  $Q$  is measured such that the diode was excluded from further tests.

### Tests at liquid nitrogen temperature

From the 8 models tested at room temperature, 4 models were selected for a test in a liquid Nitrogen bath at  $T \approx 77$  K. These were the models that showed a large tuning range  $\Delta C_{\text{tot}} > 0.4$  pF at room temperature while maintaining a high  $Q$ . The results for  $T \approx 77$  K are shown in Fig. 6.10 (b). For the models Cree, Rohm and STM1, the tuning range is comparable to that at room temperature. Likewise, the quality factor  $Q$  maintains its flat dependence on  $U_{\text{DC}}$ . In general, the resonator  $Q$  is about a factor 4 higher than at room temperature. A striking difference can be observed for the model IXYS (violet diamonds), where the breakdown voltage is reduced to  $U_{\text{br}} \approx 100$  V. For bias voltages  $U_{\text{DC}} > 100$  V, there is a strongly increasing leakage current through the diode. Nevertheless, the diode has a significant tuning range  $\Delta C_{\text{tot}} \approx 0.7$  pF for  $U_{\text{DC}} < 100$  V. Within this range, the drop in  $Q$  can be attributed to the impact of the

<sup>21</sup> Cornell Dubilier, MC12FA101J-TF, 100(5) pF, 100 V

## 6. Tunable RF fields in cryogenic traps

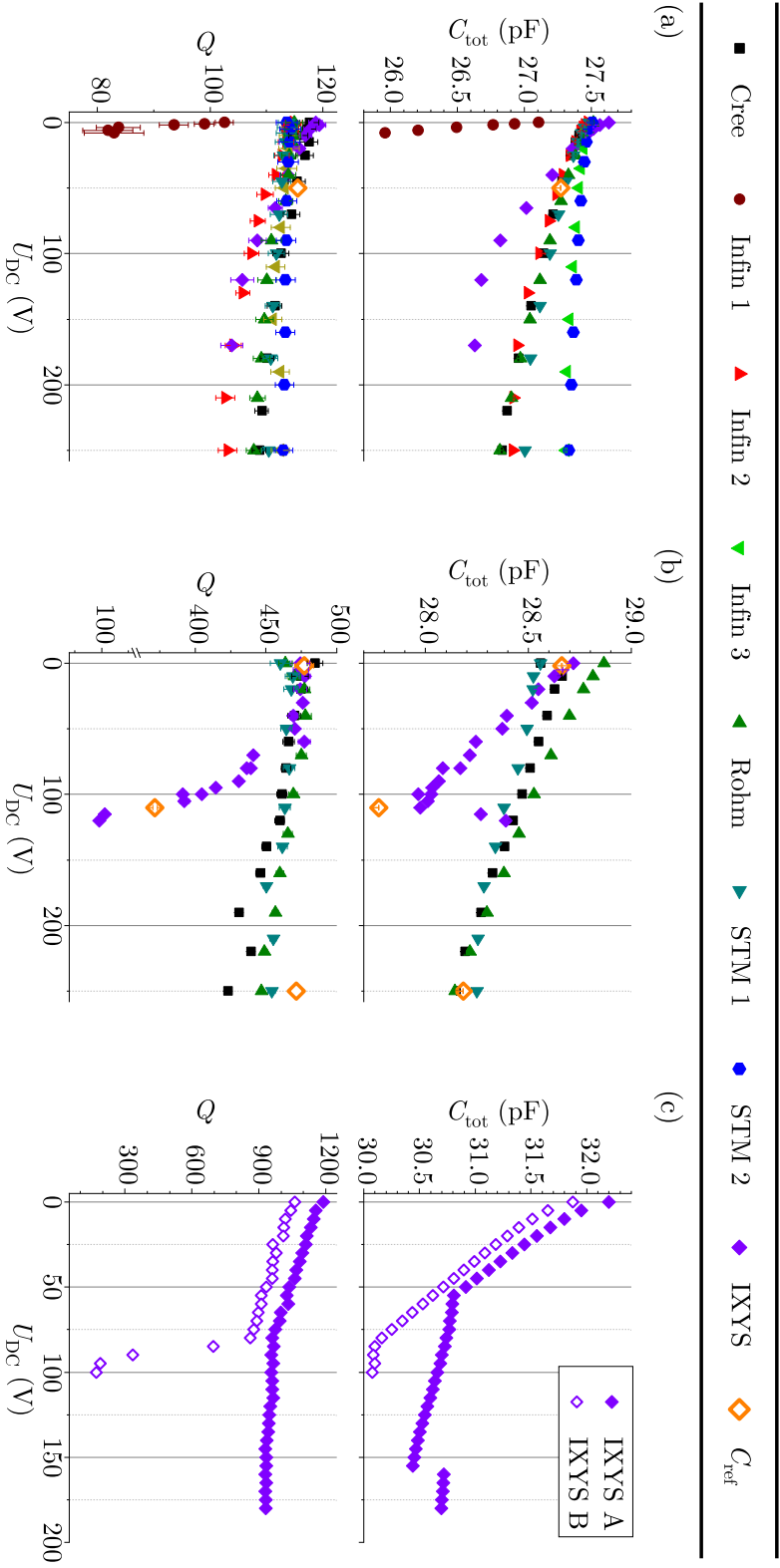


**Figure 6.10.** Characterization of the resonator tunability and quality factor using different varactor diode models at three temperatures: (a) room-temperature, (b)  $T = 77$  K and (c)  $T = 8$  K. The plots on the top show the change in resonator capacitance  $C_{\text{tot}}$  as function of the applied DC bias voltage  $U_{\text{DC}}$ . The bottom plots show the corresponding resonator quality factor  $Q$ . The labels in the legend correspond to Tab. 6.2. Golden diamonds mark reference points where fixed value mica capacitors replace the varactor diode. The horizontal positions of the reference points is chosen to match the  $C_{\text{tot}}$  values of the varactor data. The two curves in (c) correspond to different, nominally identical diode specimen.

DC bias line as the measurements with low-loss reference capacitors<sup>22 23 24</sup> show.

### Tests at liquid helium temperature

The 4 models from the liquid Nitrogen test and the model Infin3 were tested in the cryogenic setup described in chapter 4.1 at a base temperature of  $T \approx 8$  K. At this temperature, only the GaAs diode from IXYS remained tunable, while for the SiC models the tunability “froze out” at temperatures  $T \lesssim 60$  K. Fig. 6.10 (c) shows the results for two, nominally identical IXYS diodes at  $T \approx 8$  K. For  $U_{\text{DC}} \lesssim 50$  V both specimen show basically identical results with a tuning range  $\Delta C_{\text{tot}} \approx 1$  pF and  $Q \approx 1000$ . The increase in tuning range compared to the  $T \approx 77$  K test stems from the larger value of the divider capacitor  $C_{\text{cp}}$  in the final version of the resonator prototype. The behavior of the two specimen differs for  $U_{\text{DC}} \gtrsim 50$  V. For specimen A, the capacitance  $C_{\text{tot}}$  changes with a reduced slope up to  $U_{\text{DC}} \approx 150$  V, where a sudden jump in  $C_{\text{tot}}$  occurs. The quality factor remains above  $Q > 900$ . For specimen B, breakdown is observed for  $U_{\text{DC}} \gtrsim 75$  V. Despite the reduced breakdown voltage compared to room temperature, the IXYS diodes show in general a sufficient tuning range  $\Delta C_{\text{tot}} > 1$  pF at the target temperature  $T \approx 10$  K while maintaining a high resonator  $Q$ .

The varactor bandwidth was tested for specimen B by adding an AC signal to the DC bias voltage  $U_{\text{DC}}$ , while resonantly driving the resonator at an RF drive frequency of  $\Omega_{\text{RF}} \approx 2\pi \times 30$  MHz. The additional AC signal leads to a modulation of the RF amplitude within the resonator induced by the shift in resonance frequency. The contrast of this modulation remained constant up to a bias modulation frequency of 10 kHz, at which point ring-down effects of the resonator [148] distorted the waveform. The occurrence of ring-down effects above this 10 kHz threshold is compatible with the resonator’s quality factor  $Q \approx 1000$  and resonance frequency of  $\Omega_{\text{RF}} \approx 2\pi \times 30$  MHz.

## 6.3. Discussion and outlook

The goal of this chapter was to implement an electric circuit for the realization of tunable RF fields in cryogenic ion traps. To this end, a resonator prototype with electrically tunable capacitance was assembled and tested. The usage of varactor diodes as electronic tuning elements requires components with high reverse breakdown voltage, large junction capacitance and tuning range, and high quality factor. The performance of several varactor diodes using SiC and GaAs technology was assessed at cryogenic

<sup>22</sup>  $C_{\text{ref}} = 37$  pF: Cornell Dubilier, MC08CA100D-F, 10.0(5) pF, 100 V and MC08EA270J-F, 27.0(14) pF, 100 V in parallel.

<sup>23</sup>  $C_{\text{ref}} = 47$  pF: Cornell Dubilier, MC12FD470J-F, 47.0(24) pF, 500 V.

<sup>24</sup>  $C_{\text{ref}} = 220$  pF: Cornell Dubilier, MC12FA221J-F, 220(11) pF, 100 V.

## 6. Tunable RF fields in cryogenic traps

temperatures. Four diode models met the requirements for tunability and quality factor down to liquid Nitrogen temperatures. At the target temperature of  $T \approx 10$  K, only the GaAs diodes from IXYS remained tunable. While these components are not being produced anymore, remaining stock items can still be found on the market. In general, many GaAs diodes seem to have been superseded by the newer SiC technology. For the tested SiC models, tunability “froze out” at temperatures  $T \lesssim 60$  K. Further component tests are therefore important. For instance, Vishay currently produces a GaAs diode with large tuning range<sup>25</sup>. While the specified reverse breakdown voltage  $U_{\text{br}} = 40$  V for this diode is more than four times smaller compared to the tested diode from IXYS, the much smaller packaging size could allow for the integration of multiple diodes in series to reduce the RF voltage applied to each individual diode. Another alternative to using the IXYS diodes would be local heating of the SiC diodes on a thermally isolated part of the PCB. In that way, the varactors could be operated at  $T \gtrsim 60$  K while the rest of the resonator and the ion trap would remain close to the base temperature  $T \approx 10$  K. Such an approach was used for the high-temperature superconducting traps, cf. chapter 7.1.2.

The design of the tunable resonator prototype allows for a straightforward extension to a two-resonator drive by adding a second, identical resonator to the setup. This would enable the RF shuttling processes envisioned in the linear trap array described in chapter 8. The measured capacitance tuning range of about 1 pF makes RF voltage ratios  $\zeta \in [0.1, 1]$  accessible. In the simulations of the linear trap array, significantly smaller ratios of  $\zeta \in [0.7, 1]$  are used to realize a 25  $\mu\text{m}$  shift of the RF null. Phase-stabilization of the two-resonator drive could be realized by a feedforward control of the DC bias voltages applied to the varactors. Alternatively, the RF monitor signal can be used as input for feedback electronics [54, 96]. The bandwidth tests of the varactor diode suggest that RF shuttling processes can be done with a rate of at least 10 kHz, which is an order of magnitude faster than the envisioned ion-coupling rate of  $\Omega_c \approx 2\pi \times 1$  kHz, cf. chapter 8. The entangling rate for the scheme outlined in chapter 3.2.3 would therefore not be limited by the RF shuttling process. Ring-down effects of the electric resonator, which were the limiting factor in the bandwidth tests, might pose a fundamental limit to RF tuning rates in schemes, where resonators are used for voltage enhancement. The critical rate at which these effects become relevant scales with the inverse of the resonator  $Q$ , leading to a trade-off between maximal RF tuning rate and voltage gain. This problem could be mitigated using resonators with a moderate  $Q$  that are sourced by pre-amplified signals, as was recently implemented [149]. The realization of this approach in cryogenic setup remains, however, a challenge.

---

<sup>25</sup> Vishay, VSKY10401406.

Finally, it should be noted that tunable RF fields realized with multiple resonators do not necessarily need a tunable capacitance for phase control. Considering again the system of two capacitively coupled resonators, depicted in Fig. 6.4, one can do away with the adjustable capacitances  $C_{v,1}, C_{v,2}$ . Controlling instead both the amplitudes and phases of the RF resonators' drive fields  $U_{s,1}, U_{s,2}$ , one could achieve arbitrary RF voltage ratios  $\zeta$  on the trap voltages  $U_1, U_2$  with zero phase lag as well. This is shown by the circuit simulation data<sup>26</sup> in Fig. 6.11. The settings for the sources  $U_{s,1}$  and

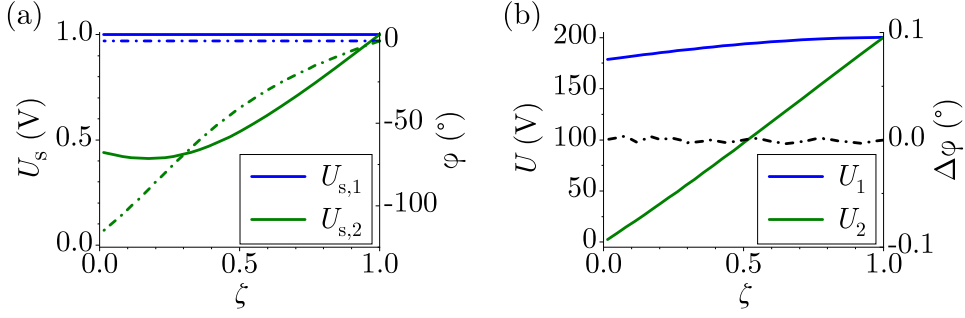


**Figure 6.11.** Realization of tunable RF fields by amplitude and phase control of the RF drive fields in a system of two capacitively coupled RF resonators, cf. Fig. 6.4. (a) Amplitudes (solid lines) and phases (dashed lines) of the two drive fields as function of the RF voltage ratio  $\zeta$ . (b) Corresponding amplitudes (solid lines) and phase difference (dashed line) of the RF voltages on the trap electrodes. The resonators' parameters are identical to that in Fig. 6.5, with  $C_{1,2} = 20$  pF,  $C_c = 0.1$  pF,  $L = 2$   $\mu$ H and  $R = 1.58$   $\Omega$ .

$U_{s,2}$  are shown in (a). While  $U_{s,1}$  is kept unchanged, the amplitude and phase of  $U_{s,2}$  are adjusted to set arbitrary ratios  $\zeta \in [0, 1]$ <sup>27</sup>. The corresponding trap voltages  $U_1$  and  $U_2$  are shown in (b). While  $U_2$  shows an approximately linear dependence on  $\zeta$ ,  $U_1$  stays almost constant at the full resonator gain. The phase lag  $\Delta\phi$  between the trap voltages is practically zero. The data suggest that a feed-forward to the source voltages, controlling both amplitude and phase, is sufficient to stabilize the phase of the RF voltages on the trap electrodes. Alternatively, it might be possible to generate an error signal from the RF phase on the trap electrodes using an RF monitor to feedback on the drive signals. According to the data in Fig. 6.11 (a), such a feedback scheme should be straightforward to implement in the range from  $\zeta = 1$  down to the minimum in the amplitude of  $U_{s,2}$  at around  $\zeta \approx 0.2$ <sup>28</sup>, since in this range the source amplitudes and phases are bijective functions of  $\zeta$ . Another point is the robustness of the phase

<sup>26</sup> For circuit simulation the software LTspice by Analog Devices was used.

<sup>27</sup> It might be possible to extend the range to  $\zeta \in [-1, 1]$  by adjusting the RF drive frequency  $\Omega_{\text{RF}}$  at  $\zeta = 0$  from the even mode frequency  $\omega_e$  to the odd mode frequency  $\omega_o$ .

<sup>28</sup> The position of this minimum depends on the resonator parameters, in particular the coupling capacitance  $C_c$ . The minimum arises since at small  $\zeta$  values, a larger source amplitude at strongly shifted phase is required to cancel the parasitic RF fields coupled through  $C_c$ . For smaller  $C_c$ , the minimum shifts towards  $\zeta = 0$ .

## 6. Tunable RF fields in cryogenic traps

stabilization scheme towards fluctuations in the source signals. Using again circuit simulations and taking an intermediate value  $\zeta = 0.5$ , a phase lag of  $\Delta\phi = 1^\circ$  on the trap electrodes is reached for a source amplitude deviation of 2% or a source phase deviation of  $2^\circ$  from the optimal values. For comparison, the stabilization scheme with varactor diodes as tuning element shows an identical requirement on phase stability of the drives and a slightly larger robustness to amplitude deviations of about 4%, considering again a phase lag of  $\Delta\phi = 1^\circ$  and  $\zeta = 0.5$ . This suggests that controlling the drive phases might be a viable alternative to using varactor diodes for phase stabilization, and with a greatly reduced technical overhead.

## 7. Superconducting surface traps

Superconductors are intriguing materials due to their vanishing electrical resistance and the expulsion of external magnetic fields (Meissner-Ochsenfeld effect) below a critical temperature  $T_c$ . These properties make them interesting as novel trap materials, in particular due to the possibility of reduced electric field noise. While no such advantage was observed in Nb and NbN surface traps [150, 151], the question remains open for high-temperature superconductors. As such, surface traps made from  $\text{YBa}_2\text{Cu}_3\text{O}_7$  (YBCO) were studied in the course of this thesis in a joint project with Kirill Lakhmanskiy and Dominic Schärfl. These studies constitute the first tests of high-temperature superconducting surface ion traps reported to date. YBCO is a ceramic superconductor with a critical temperature that can be as high as  $T_c \approx 93\text{ K}$ , depending on the exact stoichiometry [152, 153]. The high  $T_c$  value enables trapped-ion experiments within a large temperature range below  $T_c$ . The trap chip design, developed by D. Schärfl, proved to be a versatile tool for novel trapped-ion experiments. Specific on-chip YBCO structures allowed for an integrated and temperature-tunable source of white noise to be implemented. This source was used to benchmark the sensitivity of a single ion to electric field noise and allowed for a measurement of the superconducting transition in YBCO with an ion as a probe. Both experiments are described in the PhD thesis of K. Lakhmanskiy [126] and in a joint article [154], along with a study of electric field noise from a gold surface with a previously unobserved spectrum deviating from a power law.

The focus within this thesis is on the applicability of YBCO to future ion trap designs, complementing the above-mentioned experiments. Heating rate studies with new trap materials, such as YBCO, are needed to help explain the surface noise affecting trapped-ion experiments [87]. Furthermore, in the quest for scaling up trapped-ion quantum computers, microfabricated traps are becoming ever more complex [54, 55, 90, 155]. The growing numbers of electrodes require long lead wires whose resistance will eventually become a significant source of motional heating and will also limit the capability to ground the electrodes in the RF domain. The availability of ultra-low resistance wires, as provided by a high-temperature superconductor, avoids these problems at moderate cryogenic temperatures available in setups cooled with liquid Nitrogen.

The chapter starts out with an overview of the YBCO trap design and experimental

## 7. Superconducting surface traps

setup. Subsequently, the effect of long superconducting lead wires on motional heating and RF grounding of DC electrodes is discussed, followed by a presentation of the corresponding experimental data on RF grounding and motional heating. In an additional experiment, the electric field noise in a chip with exposed YBCO surface is studied. The chapter closes with a discussion of these results.

### 7.1. Trap design

A detailed description of the trap development, simulation, fabrication and operation can be found in the master's thesis of D. Schärfl [156]. The most important aspects are summarized in this section. Parameters and procedures deviating from those described in Ref. [156] are compiled in appendix A.

#### 7.1.1. Electrode layout and fabrication

The trap's electrode layout, shown in Fig. 7.1 (a), is based on a previously used linear surface trap design [157, 158]. Two asymmetric RF rails (green) lead to radial confinement in the  $xy$ -plane at an ion-surface separation  $d \approx 225 \mu\text{m}$ . DC electrodes (blue) allow for axial confinement along the  $z$ -direction. The trap electrodes are made from YBCO with an additional gold top layer. The gold layer ensures operability of the trap above the critical temperature  $T_c$ , where YBCO is a poor conductor. An important element are the two DC electrodes C1 and C2 (light blue), placed symmetrically around the trap center. Using wire bonds, the electrodes C1 and C2 can be connected to meander resistors  $R_m$  on the sides of the trap (violet). These resistors, shown in Fig. 7.1 (d), are made from YBCO only, i. e. without gold top layer. The poor conductivity of YBCO for  $T > T_c$  allows for resistances  $R_m$  in the  $\text{k}\Omega$  range within a small spatial region. There are three meanders with different lengths and resistances in each of the four trap quadrants. The meander resistors at the lower chip edge, when connected to electrodes C1 and C2, realize large resistance electrode leads that can be employed as on-chip noise sources, as described in more detail in section 7.2. Identical meander lines at the top of the chip are used to monitor the YBCO film resistance through a 4-wire measurement.

Two chips, A and B, from different wafers are used in the experiments. The main difference is that, in chip B, the gold top layer is etched away in an area of  $740 \times 580 \mu\text{m}^2$  at the trap center in order to expose the YBCO surface to a trapped ion. Figs. 7.1 (b) and (c) show microscope images of the central trapping region in chips A and B, respectively. Furthermore, chips A and B differ in the type and thickness of the YBCO film. The film thickness is increased for chip B in order to reduce the meander resistance  $R_m$ . The chip properties are summarized in Tab. 7.1.

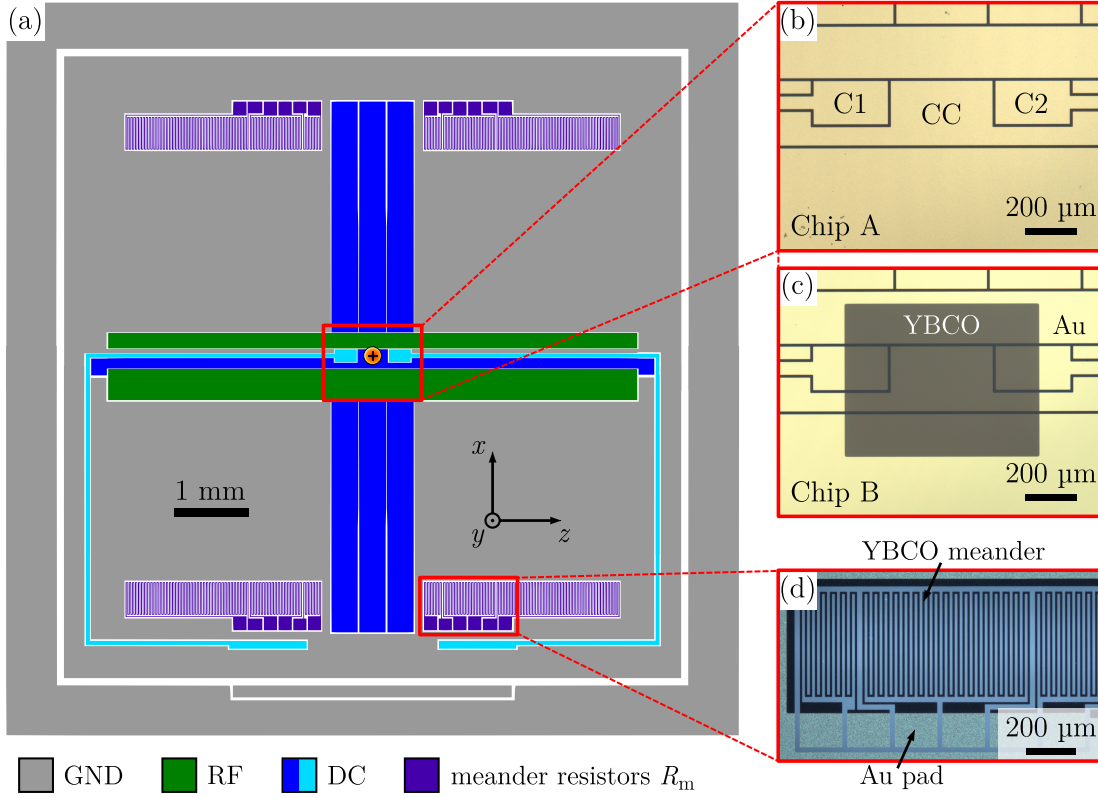


**Figure 7.1.** Electrode layout of the YBCO traps. (a) RF and DC electrodes made from YBCO with an additional gold top layer allow for confinement of an ion (orange circle) at the trap center. Dedicated DC electrodes (C1 and C2, light blue) can be connected to on-chip meander resistors  $R_m$  (violet) made from YBCO only. (b) Microscope image of the central trapping region for chip A with DC electrodes C1, C2 and CC. (c) The same region for chip B, where the gold top layer has been etched away to expose the YBCO (visible as gray rectangle). (d) Dark-field image of the YBCO meander resistors  $R_m$  (black) with gold bonding pads.

**Table 7.1.** Properties of the two trap chips A and B used in the experiments.

| Chip | substrate | YBCO film |           |         | Au layer thickness | exposed surface at trap center |
|------|-----------|-----------|-----------|---------|--------------------|--------------------------------|
|      |           | type      | thickness | $T_c$   |                    |                                |
| A    | sapphire  | s         | 50 nm     | 85(1) K | 200 nm             | Au                             |
| B    |           | m         | 300 nm    | 89(1) K |                    | YBCO                           |

## 7. Superconducting surface traps

The trap wafers are coated by ceraco ceramic coating GmbH<sup>1</sup>. The YBCO film is grown epitaxially on a CeO<sub>2</sub>-buffered 500  $\mu\text{m}$  thick sapphire wafer. Fig. 7.2 shows SEM images of the YBCO films of chips A and B. For trap chip A, a so-called s-type film with a thickness of 50 nm is applied. For trap chip B, an m-type film is used, which allows for an increased film thickness of 300 nm. While the s-type film has a smooth matrix with small CuO<sub>x</sub>-segregations, the m-type film has a more porous surface with fewer segregations. These are typical appearances according to ceraco. The high critical current densities of  $j_c(77\text{ K}) = 3.3\text{ MA/cm}^2$  (s-type) and  $j_c(77\text{ K}) = 3.4\text{ MA/cm}^2$  (m-type), measured at ceraco, indicate the good crystallinity of the films. Directly after the YBCO film growth, the additional 200 nm gold layer is deposited in the same evaporation chamber. Patterning and dicing of the wafers is done by STAR Cryoelectronics<sup>2</sup>. At the position of the YBCO meander electrodes the gold layer is removed by a wet etch process. The same process is used to expose the YBCO surface at the trap center of chip B. Afterwards the electrodes are patterned by argon ion milling. Before dicing, the chips are coated with a photoresist in order to protect the surface. This resist is removed with acetone in a cleaning step before chip installation.

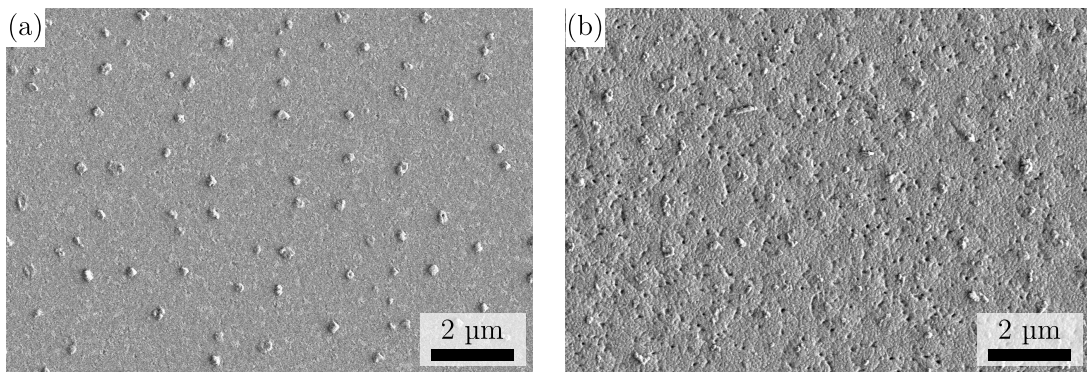


**Figure 7.2.** SEM images of the YBCO films produced at ceraco coating GmbH. (a) s-type film of Chip A. (b) m-type film of chip B.

### 7.1.2. Trap setup and operation

Prior to mounting, the trap chips are cleaned with acetone and then methanol for 4 min each in an ultrasonic bath. The chips are dried under nitrogen flow and are afterwards glued to a copper carrier using a varnish<sup>3</sup> as adhesive. Two thin stripes of polyether ether ketone (PEEK) with a thickness of 125  $\mu\text{m}$  are used as spacers between the copper stage and the trap chips. The spacers create a thicker layer of varnish,

<sup>1</sup> ceraco ceramic coating GmbH, Rote-Kreuz-Str. 8, 85737 Ismaning, Germany

<sup>2</sup> STAR Cryoelectronics, 25-A Bisbee Court, Santa Fe, NM 87508-1338, USA

<sup>3</sup> Lake Shore Cryotronics, VGE-7031

which reduces the stress on the adhesive due to the differential thermal expansion of the trap substrate and the copper carrier during temperature cycles of the cryogenic vacuum vessel. The varnish is cured at 100 °C for about 1 h. After the cure, the trap is thermally anchored to the copper carrier using about 130 wire bonds with a 25  $\mu\text{m}$  diameter gold wire, placed on the four chip edges. Afterwards, the trap electrodes are wire-bonded to the supply PCBs. Fig. 7.3 shows photographs of the mounted trap.

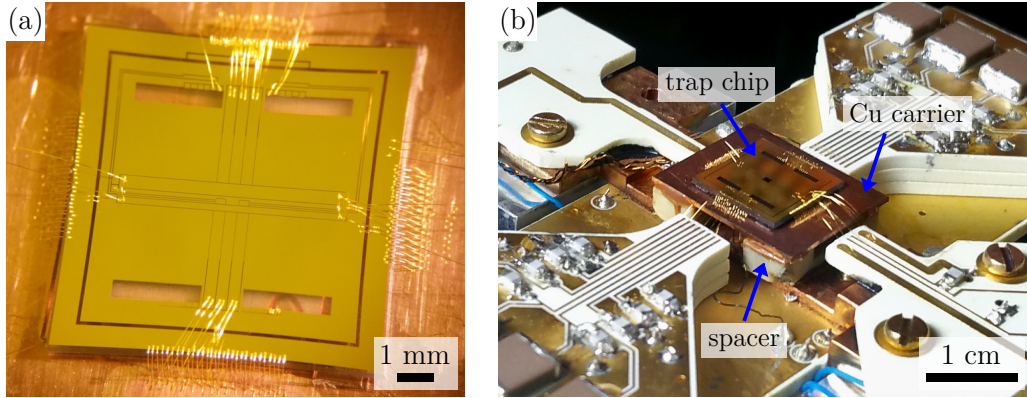


**Figure 7.3.** Mounted trap chip. (a) The trap chip is glued to a copper carrier that can be heated from below. The four rectangular chip regions that are not covered in gold contain the YBCO meander resistors. The YBCO film is transparent due to its small thickness. Wire bonds connect the trap electrodes with the RF and DC supplies. Additional wire bonds at the 4 chip edges thermally anchor the trap chip to the copper carrier. (b) PEEK spacers thermally decouple the heatable copper carrier with the trap chip from the surrounding electronics PCBs.

Each of the DC electrodes is bonded to an individual DC low-pass filter line. The C1 and C2 electrodes are either directly bonded to their filter lines or they are connected through a YBCO meander resistor, by first bonding each electrode to its meander and then the meander to the filter line. The RF electrode is connected on one side of the trap chip to the resonator PCB. On the other side it is connected to a capacitive divider, used for monitoring the RF voltage on the trap during operation, cf. chapter 4.1.2. One additional YBCO meander is connected to a 4-wire resistance measurement circuit, the remaining meander resistors are shorted to the trap’s main ground electrode.

The copper carrier to which the trap is attached can be resistively heated from below and is thermally decoupled from the surrounding PCBs by PEEK spacers as shown in Fig. 7.3 (b). The thermal decoupling reduces the heat load on the cryostat and helps to maintain the cryogenically pumped vacuum. The decoupling is characterized using two Si diode temperature sensors attached on the backside of the carrier and near the capacitive divider board, respectively. Raising the temperature of the trap chip from the cryogenic base temperature  $T \approx 10\text{ K}$  to  $T \approx 200\text{ K}$  changes the temperatures of the electronics PCBs by only a few kelvin as characterized in appendix A.1. As the

## 7. Superconducting surface traps

copper carrier is heated, thermal gradients on the order of a few kelvin build up between the trap chip and the copper carrier. These gradients can be calibrated out using the four-wire resistance measurement as described in appendix A.1. After calibration, the trap chip temperature can be determined with an accuracy of about 1 K.

### Trap operation

The trap is operated at RF voltages  $U_{\text{RF}} \approx (180 - 240)$  V at  $\Omega_{\text{RF}} = 2\pi \times 17.58$  MHz, corresponding to a stability factor  $q \approx (0.40 - 0.53)$ <sup>4</sup>. The radial frequencies vary within  $\omega_{r,1}, \omega_{r,2} \approx 2\pi \times (1.6 - 3.3)$  MHz, depending on the applied RF voltage and DC confinement. The axial frequencies are set within  $\omega_z \approx 2\pi \times (0.4 - 1.8)$  MHz by scaling the applied DC voltages. For all experiments, described in section 7.3, a linear trap configuration is maintained, i. e.,  $\omega_z < \omega_{r,1}, \omega_{r,2}$ . The DC voltage sets for axial confinement and micromotion compensation are given in appendix A.2. The central DC electrodes C1 and C2 are either directly connected to the DC filter stage, or connected through meander resistors. Meanders with a length of 5.18 mm are used both as superconducting electrode leads for electrodes C1 and C2 as well as for the 4-wire measurement of the YBCO resistance.

## 7.2. Superconducting electrode leads

The on-chip YBCO meander structures attached to electrodes C1 and C2 are used to assess the performance of long superconducting electrode leads on a trapped ion. The meanders have a length of 5.18 mm, a width of 10  $\mu\text{m}$  and a thickness of 50 nm (for chip A). For temperatures  $T < T_c \approx 85$  K, the YBCO leads are in the superconducting regime with zero DC resistance. For comparison, an electrode lead with identical geometry but made from copper has a resistance of about 22  $\Omega$  at  $T = 80$  K, assuming a typical resistivity of  $\rho_{\text{Cu}} = 0.22 \times 10^{-8}$   $\Omega\text{m}$  [159]. Superconducting leads (and trap electrodes) might, therefore, become important in future trap designs where the lead lengths and resistances will grow with increasing trap complexity. Large lead resistances can disrupt the trap performance in two ways: by increasing the motional heating rate  $\Gamma_h$  and by limiting the grounding capability of DC electrodes in the RF domain, as will be explained and quantified in this section.

Fig. 7.4(a) shows a schematic illustration of the trap, with two identical meander resistors  $R_m$  connected to the DC electrodes C1 and C2 (blue). The RF electrodes are

---

<sup>4</sup> RF voltages and  $q$  factors are determined by comparing the measured secular frequencies with trap simulations. All trap simulations in this chapter, unless stated otherwise, are performed with the electrode package for python by R. Jördens (<https://github.com/nist-ionstorage/electrode>); see also [134, 135].

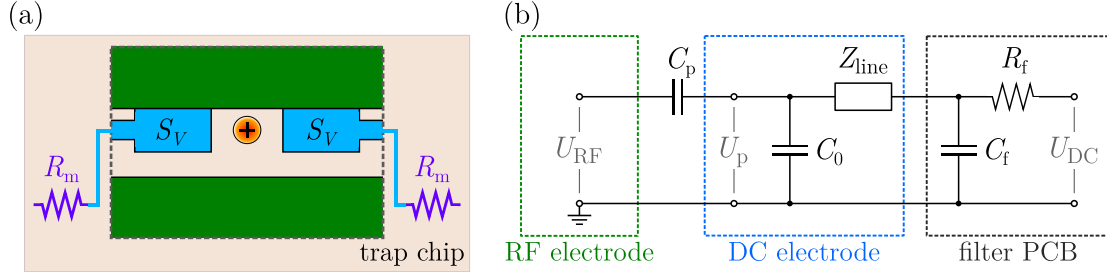


**Figure 7.4.** (a) Schematic illustration of the on-chip noise source. Meander resistors  $R_m$  (violet), connected to the trap electrodes C1, C2 (blue), produce uncorrelated voltage noise  $S_V$  on the electrodes, which adds up to electric field noise  $S_E$  at the position of the ion (orange circle). (b) Circuit model for the RF grounding of DC trap electrodes. The parasitic capacitance  $C_p$  leads to an RF pickup voltage  $U_p$  at the DC electrode. The magnitude and phase of  $U_p$  depend on the total impedance of the DC electrode to GND, in particular the connection line impedance  $Z_{\text{line}}$ .

colored green. The meanders produce uncorrelated Johnson noise (JN) which adds to the electric field noise at the trap center (marked with an orange circle). The noise contribution by each of the meanders is  $S_E = 4k_B T R_m / \delta_c^2$ , cf. Eqs. (3.8) and (3.9) in chapter 3.3, where  $T$  is the trap chip temperature and  $\delta_c$  is the geometry-dependent characteristic distance. For temperatures  $T > T_c$ , the large meander resistance  $R_m \sim 10 \text{ k}\Omega$  creates a significant contribution to the heating rate  $\Gamma_h$ , which can be employed as a source of white noise integrated to the trap chip. More relevant for this thesis is the case  $T < T_c$ . In this temperature regime, the meanders are in the superconducting state and should add negligibly to  $\Gamma_h$ , thus realizing long, ultra low-noise electrode leads. The performance of these leads is assessed by measuring the heating rate.

The second detrimental effect of large lead resistances is the presence of RF pickup voltages  $U_p$  on the DC electrodes due to improper grounding in the RF domain. Such pickup voltages then induce RF electric fields at the ion position, which in turn result in excess micromotion that cannot be compensated in either of the following cases: the net RF pickup field has a field component along the trap's axial direction, or, there is a phase lag between the net RF pickup field and the RF drive field of the trap [72]. The mechanism leading to the generation of pickup voltages on trap electrodes is illustrated in Fig. 7.4 (b). The RF drive voltage  $U_{\text{RF}}$  is applied to the trap's RF electrode (green box). The parasitic capacitance  $C_p$  between the trap electrodes couples the DC electrode (blue box) to the RF electrode leading to an RF pickup voltage  $U_p$  on the DC electrode. The magnitude and phase of  $U_p$  depends on how well the DC electrode is connected to GND. The parasitic capacitance  $C_0$  between the DC and the GND electrode on the trap chip does typically not provide sufficient grounding such that an additional grounding capacitance is needed, often provided by the DC filter capacitance  $C_f \gg C_0$ . The amplitude and phase of the RF pickup voltage  $U_p$  thus

## 7. Superconducting surface traps

crucially depends on the impedance  $Z_{\text{line}}$  of the connection line, which in general consists of a resistive and an inductive part,  $Z_{\text{line}} = R_{\text{line}} + i\Omega_{\text{RF}}L_{\text{line}}$ . For the setup shown in Fig. 7.4 (a), the meander resistances  $R_{\text{m}}$  lead to large connection line impedances  $Z_{\text{line}}$  for temperatures  $T > T_c$ , causing significant RF pickup voltage  $U_{\text{p}}$  on electrodes C1 and C2 with correspondingly strong pickup fields at the ion position. However, in the superconducting state,  $T < T_c$ , the pickup fields should be small, due to the vanishing resistance  $R_{\text{m}} \approx 0$ .

In the following, a quantitative estimate is derived for the RF pickup fields expected for  $T > T_c$  and  $T < T_c$ . The discussion is limited to the central electrodes C1, C2 and CC (cf. Fig. 7.1 (b)) and to the axial components  $E_z$  of their pickup fields. Axial contributions from other electrodes are negligible in magnitude. Radial pickup field components are in general either negligibly small or they are in-phase with the RF drive field (due to a predominantly inductive connection line impedance  $Z_{\text{line}}$ ) and can thus be compensated. The axial RF field generated by the RF electrodes is assumed to be negligible (linear trap). A detailed validation of these assumptions is given in appendix A.3. With respect to Fig. 7.4 (b), the ratio  $\epsilon_{\text{p}}$  of RF pickup voltage  $U_{\text{p}}$  to RF drive voltage  $U_{\text{RF}}$  is given by

$$\epsilon_{\text{p}} = \frac{U_{\text{p}}}{U_{\text{RF}}} = \frac{Z_{\parallel}}{Z_{\parallel} + Z_{C_{\text{p}}}}, \text{ with } Z_{\parallel} = \left( \frac{1}{Z_{C_{\text{f}}} + Z_{\text{line}}} + \frac{1}{Z_{C_0}} \right)^{-1} \quad (7.1)$$

and  $Z_C = 1/(i\Omega_{\text{RF}}C)$  being the impedance of a capacitor. The relative phase  $\phi_{\text{p}}$  between pickup voltage  $U_{\text{p}}$  and drive voltage  $U_{\text{RF}}$  is irrelevant here, since only the axial component of the corresponding pickup field is considered. The following discussion is, therefore, limited to the absolute value  $|\epsilon_{\text{p}}|$  without further mentioning. It is illustrative to look at the extreme cases of Eq. (7.1). For  $Z_{\text{line}} \gg Z_{C_0}$ , the filter capacitance will be effectively disconnected and the DC electrode will not be grounded,  $\epsilon_{\text{p}} \approx C_{\text{p}}/(C_{\text{p}} + C_0) \sim 1/2$  since the parasitic capacitances  $C_{\text{p}}$  and  $C_0$  are typically of the same order of magnitude. In the opposite case,  $Z_{\text{line}} \approx 0$ , the pickup ratio is  $\epsilon_{\text{p}} \approx C_{\text{c}}/C_{\text{f}} \ll 1$ , which can be made arbitrarily small by choosing a large filter capacitance  $C_{\text{f}}$ . The expected RF pickup ratios  $\epsilon_{\text{p}}$  for the trap electrodes C1, C2 and CC are listed in Tab. 7.2. While electrodes C1 and C2 are connected through meander resistors  $R_{\text{m}}$ , the CC electrode is directly connected to the DC filter stage. For  $T = 97 \text{ K} > T_c$ , the large meander resistance dominates the connection line impedance,  $Z_{\text{line}} \approx R_{\text{m}} = 14.9(2) \text{ k}\Omega$ , and leads to a significant pickup ratio  $\epsilon_{\text{p}}^{(\text{C1,C2})} = 5.4(16) \times 10^{-2}$  on electrodes C1 and C2. For typical RF drive voltages  $U_{\text{RF}} \sim 200 \text{ V}$  this ratio corresponds to a pickup voltage  $U_{\text{p}} \sim 10 \text{ V}$ . For  $T = 12 \text{ K} < T_c$ , the pickup ratio on C1 and C2 drops by about a factor 1000 to  $\epsilon_{\text{p}}^{(\text{C1,C2})} = 6.7(20) \times 10^{-5}$ , limited by the inductance  $L_{\text{line}} \approx 55 \text{ nH}$  of the

**Table 7.2.** Estimated RF pickup ratio  $\epsilon_p$  on the central DC electrodes C1, C2 and CC for two temperatures  $T = 12 \text{ K} < T_c$  and  $T = 97 \text{ K} > T_c$ . The estimates are calculated at an RF drive frequency  $\Omega_{\text{RF}} = 2\pi \times 17.58 \text{ MHz}$  using the electrical parameters in the lower part of the table, which are derived in appendix A.3.

| electrode         | C1, C2               | CC                       |                         |
|-------------------|----------------------|--------------------------|-------------------------|
| $\epsilon_p$      | $T = 12 \text{ K} :$ | $6.7(20) \times 10^{-5}$ | $4.6(5) \times 10^{-4}$ |
|                   | $T = 97 \text{ K} :$ | $5.4(16) \times 10^{-2}$ | $4.7(5) \times 10^{-4}$ |
| $C_p$             | 0.100(15) pF         | 0.883(48) pF             |                         |
| $C_0$             | 1.641(15) pF         | 0.780(65) pF             |                         |
| $L_{\text{line}}$ | 55 nH                | 43 nH                    |                         |
| $R_{\text{line}}$ | $T = 12 \text{ K} :$ | 95 m $\Omega$            | 48 m $\Omega$           |
|                   | $T = 97 \text{ K} :$ | 14.9(2) k $\Omega$       | 1044 m $\Omega$         |
| $C_f$             |                      | 330 nF                   |                         |
| $R_f$             |                      | 100 $\Omega$             |                         |

connection line. In comparison, the CC electrode has a roughly tenfold larger pickup ratio,  $\epsilon_p^{(\text{CC})} = 4.6(5) \times 10^{-4}$ , due to the larger parasitic capacitance  $C_p$ . The pickup ratio  $\epsilon_p^{(\text{CC})}$  changes only negligibly for  $T = 97 \text{ K} > T_c$ , since the line impedance of the CC electrode is limited by the inductive term.

The axial pickup fields  $E_z$  from the electrodes are proportional to the pickup voltages  $U_p$ . In analogy to Eq. (3.9) it holds

$$E_z(z) = \frac{U_p}{\delta_c(z)}, \quad (7.2)$$

where the characteristic distance  $\delta_c(z)$  is determined by trap simulation. Pickup fields  $E_z(z)$  from the different trap electrodes for  $U_p = 1 \text{ V}$  are shown in Fig. A.3 in appendix A.3, where it can be seen that the dominant fields are those from electrodes C1, C2 and CC. The pickup fields exert an additional oscillating force  $QE_z(z) \cos(\Omega_{\text{RF}}t + \phi_p)$  on the ion, leading to excess micromotion that cannot be compensated. Employing Newton's law and assuming that  $E_z(z)$  does not vary over the spatial extent  $2z_m$  of the micromotion oscillation, the micromotion amplitude is given by<sup>5</sup>

$$z_m = \frac{QE_z(z)}{M\Omega_{\text{RF}}^2}, \quad (7.3)$$

where  $Q$  is the ion's charge,  $M$  its mass and  $\Omega_{\text{RF}}$  the drive frequency. Inserting this

<sup>5</sup> Note: The ion's harmonic confinement is here neglected. For the solution of the full equation of motion, the factor  $\Omega_{\text{RF}}^2$  in eq. (7.3) has to be replaced by  $(\Omega_{\text{RF}}^2 - \omega_z^2)$ . The deviation is about 0.3% for the experimental parameters used in section 7.3.1,  $\Omega_{\text{RF}} = 2\pi \times 17.58 \text{ MHz}$  and  $\omega_z = 2\pi \times 1.0 \text{ MHz}$ .

## 7. Superconducting surface traps

amplitude into Eq. (2.34) in chapter 2.3.3 results in a micromotion modulation index of

$$\beta = kz_m \cos(\alpha) = \frac{kQ \cos(\alpha)}{M\Omega_{\text{RF}}^2} E_z(z), \quad (7.4)$$

with  $k$  being the wavenumber of the laser light and  $\alpha$  the angle between the laser beam and  $z_m$ . In the present setup all beams are propagating along the chip surface at an angle of about  $45^\circ$  relative to the trap axis  $z$ , i.e.  $\alpha \approx \pi/4$ . The estimate for the expected modulation index is given by combining the estimates for the RF pickup ratio  $\epsilon_p$  in Tab. 7.2 with Eqs. (7.2) and (7.4), employing the simulated pickup fields  $E_z$  from electrodes C1, C2 and CC. The resulting micromotion modulation index  $\beta$  per RF drive voltage  $U_{\text{RF}}$  is shown in Fig. 7.5. At the trap center,  $z = 0$ , no micromotion is expected,  $\beta = 0$ , due to the mirror symmetry of the trap. In fact, the geometry of the electrodes C1 and C2 is optimized such that all RF pickup field components from electrodes C1 and C2 cancel at the trap center  $\mathbf{r}_0$ ,  $\mathbf{E}(\mathbf{r}_0)^{(\text{C1})} + \mathbf{E}(\mathbf{r}_0)^{(\text{C2})} = 0$ , cf. Ref. [156]. For increasing distance  $z$  from the center, the pickup field  $E_z$  (and likewise  $\beta$ ) increases approximately linearly, both for electrode CC and for the combined fields from electrodes C1 and C2. At a temperature  $T = 97 \text{ K} > T_c$ , (a), the micromotion is dominated by the combined field  $E_z^{(\text{C1})} + E_z^{(\text{C2})}$ . For  $T = 12 \text{ K} < T_c$ , (b), the fields from C1 and C2 are drastically reduced and their contribution to  $\beta$  becomes negligible compared to that of electrode CC.

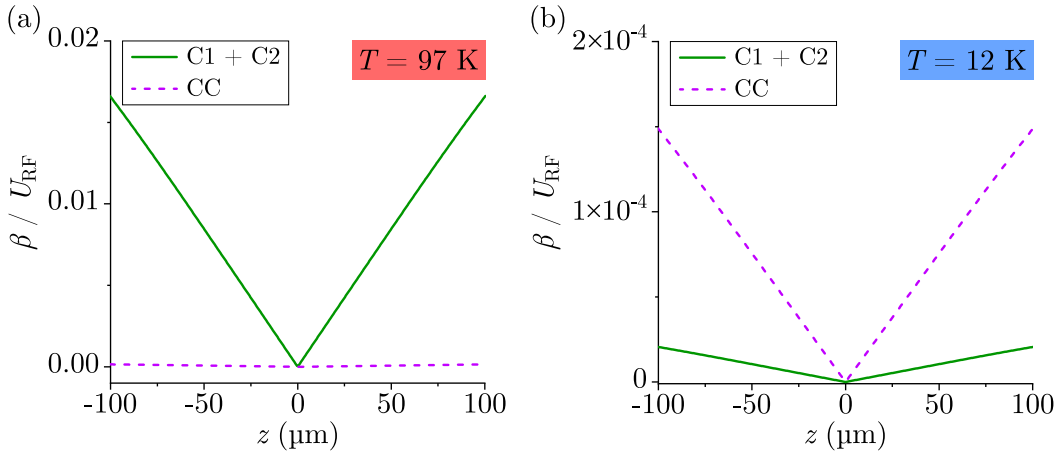


**Figure 7.5.** Simulated micromotion index  $\beta$  per applied volt of the RF drive voltage  $U_{\text{RF}}$  along the trap axis  $z$  for electrodes C1 + C2 and CC. The ‘+’ notation denotes the sum of axial pickup fields,  $E_z^{(\text{C1})} + E_z^{(\text{C2})}$ . (a) For  $T = 97 \text{ K} > T_c$  the combined pickup fields from electrodes C1 and C2 dominate. (b) For  $T = 12 \text{ K} < T_c$  the pickup field from CC dominates.

### 7.3. Experimental results

The performance of the superconducting meander leads connected to electrodes C1 and C2 is assessed in two studies. In the first study, the RF grounding capabilities of C1 and C2 are determined by measuring the micromotion modulation index  $\beta$  as function of the ion's axial position  $z$  at two different temperatures  $T > T_c$  and  $T < T_c$ . In the second study, the heating rate  $\Gamma_h$  is measured both below and above the superconducting transition. The data for  $T < T_c$  is compared to the heating rate without attached meander lead. In an additional experiment, the influence of an exposed YBCO surface on the heating rate  $\Gamma_h$  is studied. For this, heating rate data obtained in chip B, where the YBCO surface is exposed to the ion, are compared to  $\Gamma_h$  in chip A, where the trap center is entirely covered in gold. Furthermore, the spectral properties and temperature dependence of  $\Gamma_h$  in chip B are investigated.

#### 7.3.1. RF pickup study

In this first study, single ions are trapped at different positions  $z$  along the trap axis of chip A with an axial confinement of  $\omega_z = 2\pi \times 1.0$  MHz, using the voltage sets described in appendix A.2. The ion position is determined by a Gaussian fit of a CCD camera image. For each position, the micromotion is minimized by moving the ion in the radial plane. Subsequently, the amount of excess micromotion is determined by driving Rabi oscillations on the 729 nm carrier transition and the first order micromotion sideband. Fig. 7.6 shows an example of typical Rabi oscillations measured in the experiment. The Rabi frequencies of the carrier,  $\Omega_c$ , and first order micromotion

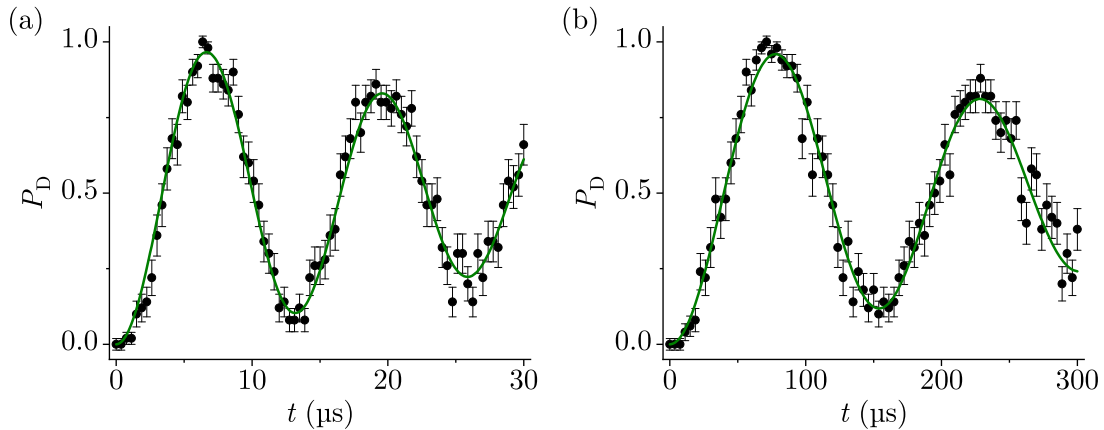


**Figure 7.6.** Typical Rabi oscillation data on the carrier (a) and first micromotion sideband (b). Error bars are given by quantum projection noise [80]. The solid lines are a damped Rabi fit with Eq. (2.41), yielding a mean motional quantum number of  $\bar{n} = 23(1)$  for the carrier and  $\bar{n} = 26(2)$  for the micromotion sideband.

## 7. Superconducting surface traps

sideband,  $\Omega_{m1}$ , are determined from a fit of the data with Eq. (2.41) in chapter 2.3.3, describing damped Rabi-oscillations. The modulation index  $\beta$  is then found by numerically solving Eq. (2.35) assuming that  $\beta \lesssim 2.4$ , which is the case for well-compensated micromotion. Fig. 7.7 shows the modulation index  $\beta$  as a function of axial position  $z$  measured for two temperatures  $T = (12, 97)$  K, below and above the critical temperature  $T_c = 85(1)$  K. The measured data show qualitative agreement with the simulated

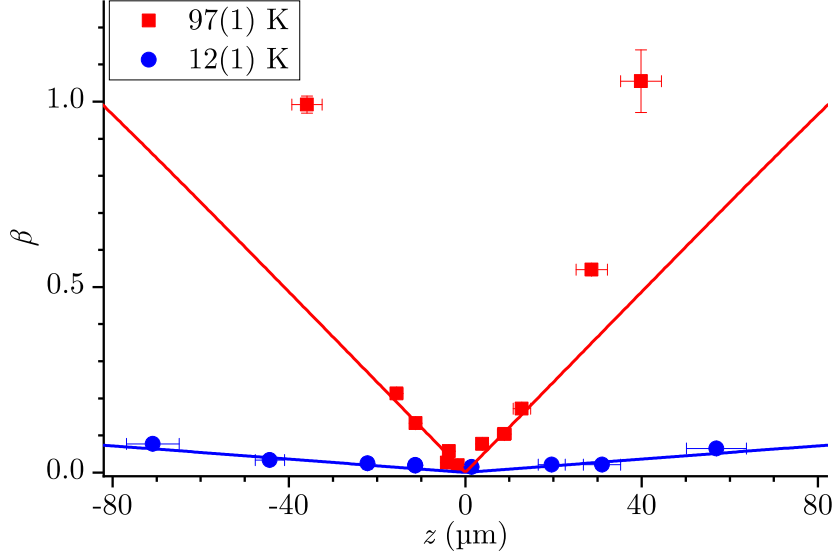


**Figure 7.7.** Micromotion modulation index  $\beta$  as function of the ion’s axial position  $z$  for temperatures  $T = 12(1)$  K  $< T_c$  and  $T = 97(1)$  K  $> T_c$ . The solid lines show a fit of the expected dependence to the data, yielding an RF pickup voltage  $U_p = 3.9(4)$  V on electrodes C1, C2 ( $T = 97$  K) and  $U_p = 0.28(4)$  V on electrode CC ( $T = 12$  K).

RF pickup fields on the central DC electrodes C1, C2, CC, cf. Fig. 7.5. The excess micromotion is in general much stronger for  $T = 97$  K  $> T_c$  than for  $T = 12$  K  $< T_c$ , with the exception of the trap center at  $z = 0$ . Here, the modulation index is minimal with  $\beta = 0.0190(8)$  at  $T = 97$  K, very close to the value at  $T = 12$  K,  $\beta = 0.0185(10)$ . This shows the cancellation of the axial pickup fields from electrodes C1 and C2 at the trap center due to the mirror symmetry of the trap. For  $z \neq 0$ , both data sets show an approximately linear increase with the distance from the trap center. The solid lines show a fit with the simulated  $\beta$  dependence (Fig. 7.5). For the data set at  $T = 97$  K, the fit gives an RF pickup voltage  $U_p = 3.9(4)$  V on electrodes C1 and C2. With the RF drive voltage  $U_{RF} = 238.0(14)$  V, inferred from comparing trap simulations to the measured trap frequencies, the fitted value of  $U_p$  corresponds to an RF pickup ratio  $\epsilon_p = |U_p/U_{RF}| = 1.6(2) \times 10^{-2}$ . The measured ratio is in reasonable agreement with the estimate  $\epsilon_p = 5.4(16) \times 10^{-2}$  in Tab. 7.2. For large distances from the trap center,  $|z| \gtrsim 20$   $\mu$ m, the measured modulation index  $\beta$  deviates from the prediction. The addi-

tional micromotion is most likely due to imperfect compensation settings and the data points were excluded from the fit. For the data set at  $T = 12$  K, the fit gives an RF pickup voltage  $U_p = 0.28(4)$  V on electrode CC. For this set, the RF drive voltage is  $U_{\text{RF}} = 218.5(21)$  V. The RF pickup ratio  $\epsilon_p = 1.3(2) \times 10^{-3}$  is about 10 times smaller than for the data set at  $T = 97$  K and is also in reasonable agreement with the estimate  $\epsilon_p = 4.6(5) \times 10^{-4}$  in Tab. 7.2. This indicates that RF grounding through the superconducting meander leads is comparable to the grounding of the CC electrode, which is directly attached to the filter line.

### 7.3.2. Heating rate measurements

The second study investigates the impact of the superconducting electrode leads on the axial heating rate  $\Gamma_h$ . Single ions are trapped at the trap center,  $z = 0$ , sideband-cooled to the motional ground state and  $\Gamma_h$  is determined with the sideband ratio method described in section 2.3.3. For each heating rate measurement, typically 5 delay times are used, each with around 1000 interleaved measurements on the blue and red sideband transitions. Typical data are shown in Fig. 7.8. Measurement uncertainties of  $\Gamma_h$  are derived from the uncertainties in the sideband mean excitations, which are in general consistent with quantum projection noise [80].

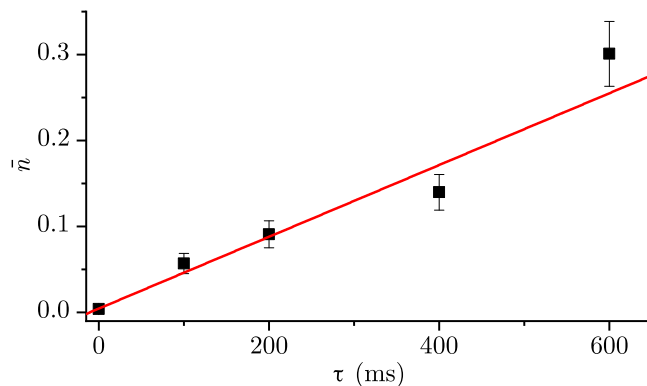


**Figure 7.8.** Typical heating rate data. The mean phonon number  $\bar{n}$  is determined for different waiting times  $\tau$ . The heating rate  $\Gamma_h$  is found by a linear fit to the data (solid line).

In a first experiment, the heating rate is measured in chip A, with the electrodes C1 and C2 connected through the 5.18 mm long meander leads. For these measurements, the axial frequency is constant at  $\omega_z = 2\pi \times 1.0$  MHz. Tab. 7.3 lists the results at three different temperatures  $T$ . For temperatures  $T < T_c = 85(1)$  K, the measured heating rate is low with values  $\Gamma_h = 0.23(2)$  phonons/s and  $\Gamma_h = 1.03(8)$  phonons/s at  $T = 12(1)$  K and  $T = 77(1)$  K, respectively. Upon raising the temperature above the superconducting transition,  $\Gamma_h$  increases by about a factor 1000 to  $\Gamma_h = 1026(67)$  phonons/s

## 7. Superconducting surface traps

**Table 7.3.** Measured heating rate  $\Gamma_h$  in chip A at different trap chip temperatures  $T = (12(1), 77(1))\text{K} < T_c$  and  $T = 97(1)\text{K} > T_c$  for an axial frequency  $\omega_z = 2\pi \times 1.0\text{MHz}$ . The heating rate estimates  $\Gamma_h^{\text{est.}}$  correspond to JN from the meander resistance  $R_m$  and are derived in appendix A.4.1.

| $T$ (K) | $\Gamma_h$ (phonons/s) | $R_m$ ( $\Omega$ )    | $\Gamma_h^{\text{est.}}$ (phonons/s) |
|---------|------------------------|-----------------------|--------------------------------------|
| 12(1)   | 0.23(2)                | $2.9 \times 10^{-9}$  | $1.8 \times 10^{-11}$                |
| 77(1)   | 1.03(8)                | $460 \times 10^{-9}$  | $2.3 \times 10^{-8}$                 |
| 97(1)   | 1026(67)               | $14.9(2) \times 10^3$ | 897(12)                              |

at  $T = 97(1)\text{K}$ . The measured value is in good agreement with the JN estimate  $\Gamma_h^{\text{est.}} = 897(12)\text{phonons/s}$  derived from the measured meander lead resistance  $R_m = 14.9(2)\text{k}\Omega$ , see appendix A.4.1. This proves that the heating rate above  $T_c$  is dominated by JN in the YBCO leads. When in the superconducting state, the meander leads have a negligibly small resistance of  $R_m \sim (1 - 1000)\text{n}\Omega$  in the MHz frequency range (see appendix A.4.1). Therefore, the heating rates measured for  $T < T_c$  cannot be caused by JN from superconducting leads. Nevertheless,  $\Gamma_h$  might still be limited by the superconducting leads, for instance due to electromagnetic pickup noise in the meander structures. This possibility is excluded by an additional measurement performed with chip B, where the frequency spectrum of the heating rate is measured in two configurations: i. with electrodes C1 and C2 connected through the YBCO meander leads and ii. directly connected to the filter lines. The results of these measurements are shown in Fig. 7.9. The frequency spectrum of the measured heating rate are well described by a power law

$$\Gamma_h(\omega_z) = c(\omega_z/\omega_0)^\alpha, \quad (7.5)$$

with  $\omega_0 = 2\pi \times 1\text{MHz}$ . Furthermore, the data shows nearly perfect agreement between configurations i. and ii. at temperatures  $T = 37\text{K}$  and  $T = 83\text{K}$  with power law exponents  $\alpha = 1.9(1) - 2.0(1)$ . For the data sets at  $T = 14\text{K}$ , configuration ii. has a power law exponent  $\alpha = 1.8(2)$  in agreement with the sets at higher temperatures, while the configuration i. shows a slightly smaller value  $\alpha = 1.4(1)$ . This deviation stems from the somewhat lower heating rates at small frequencies  $\omega_z \lesssim 2\pi \times 0.8\text{MHz}$  for configuration i. (with meander lead) and is likely to be caused by fluctuations, as suggested by the almost identical magnitudes  $c = 0.64(2)\text{phonons/s}$  and  $c = 0.68(7)\text{phonons/s}$  for sets i. and ii., respectively. In summary, the good agreement between configurations i. and ii. at three temperatures  $T < T_c$  proves that the noise limiting the heating rates in this temperature regime does not originate from the superconducting meander leads.

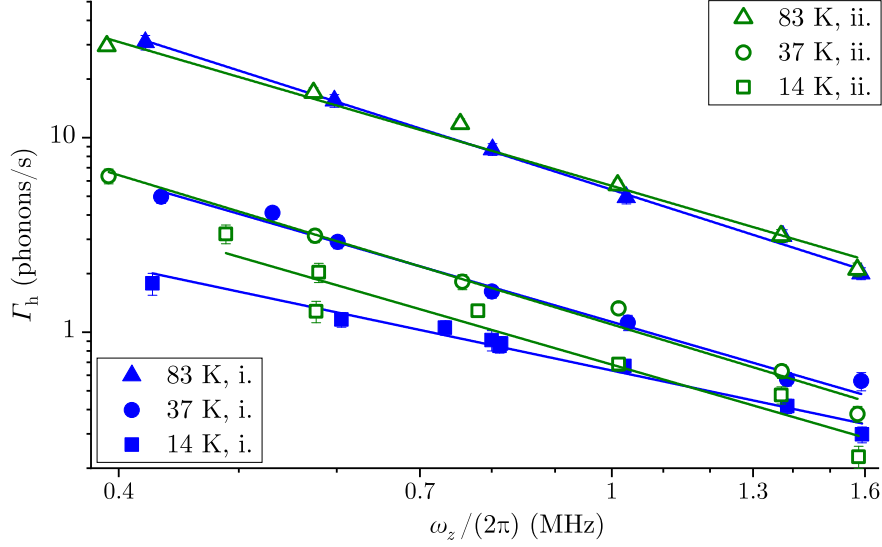


**Figure 7.9.** Comparison of heating rate spectra in chip B. Filled blue symbols show data taken in configuration i, where the electrodes C1 and C2 are connected through the YBCO meander leads. Open green symbols show the corresponding data taken in configuration ii, where all DC electrodes are directly connected to the filter lines. Solid lines are fits with a power law.

The remainder of this section investigates the heating rates in chip B, where the YBCO surface is exposed below the ion. Fig. 7.10 shows a comparison of the temperature dependence of  $\Gamma_h$  in chip B to that observed in chip A, where the surface below the ion is gold. The sets are for an axial frequency  $\omega_z = 2\pi \times 1.0$  MHz, and the temperature range is restricted to  $T < T_c$ . The data for  $T > T_c$  are not available in chip A, since for these measurements the electrodes C1 and C2 were connected to the meander leads, such that  $\Gamma_h$  was dominated by JN. In general, the heating rates in

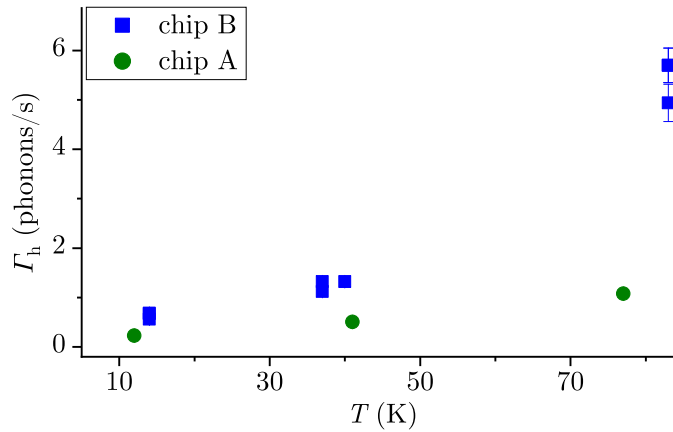


**Figure 7.10.** Comparison of the temperature scaling of the heating rate in trap chips A and B at  $\omega_z = 2\pi \times 1.0$  MHz.

## 7. Superconducting surface traps

both chips are of a comparable level. At the lowest temperature  $T \approx 10$  K, the heating rate in chip A is  $\Gamma_h = 0.23(2)$  phonons/s and about a factor 3 larger in chip B with  $\Gamma_h = 0.64(7)$  phonons/s. With rising temperature,  $\Gamma_h$  seems to increase slightly stronger in chip B, such that at temperatures  $T \approx 80$  K the heating rate in chip B is about a factor 5 larger than in chip A with  $\Gamma_h = 5.3(5)$  phonons/s and  $\Gamma_h = 1.1(1)$  phonons/s, respectively. However, additional data would be needed to corroborate a different scaling behavior.

In a final set of measurements in chip B, the accessible temperature range is extended to  $T > T_c$  using configuration ii. The otherwise limiting JN from the meander leads is eliminated in this configuration, since the electrodes C1 and C2 are directly connected to the filter lines. Fig. 7.11 (a) shows the heating rate  $\Gamma_h$  as function of trap chip temperature  $T$  for different secular frequencies  $\omega_z$ . All frequency sets show a similar

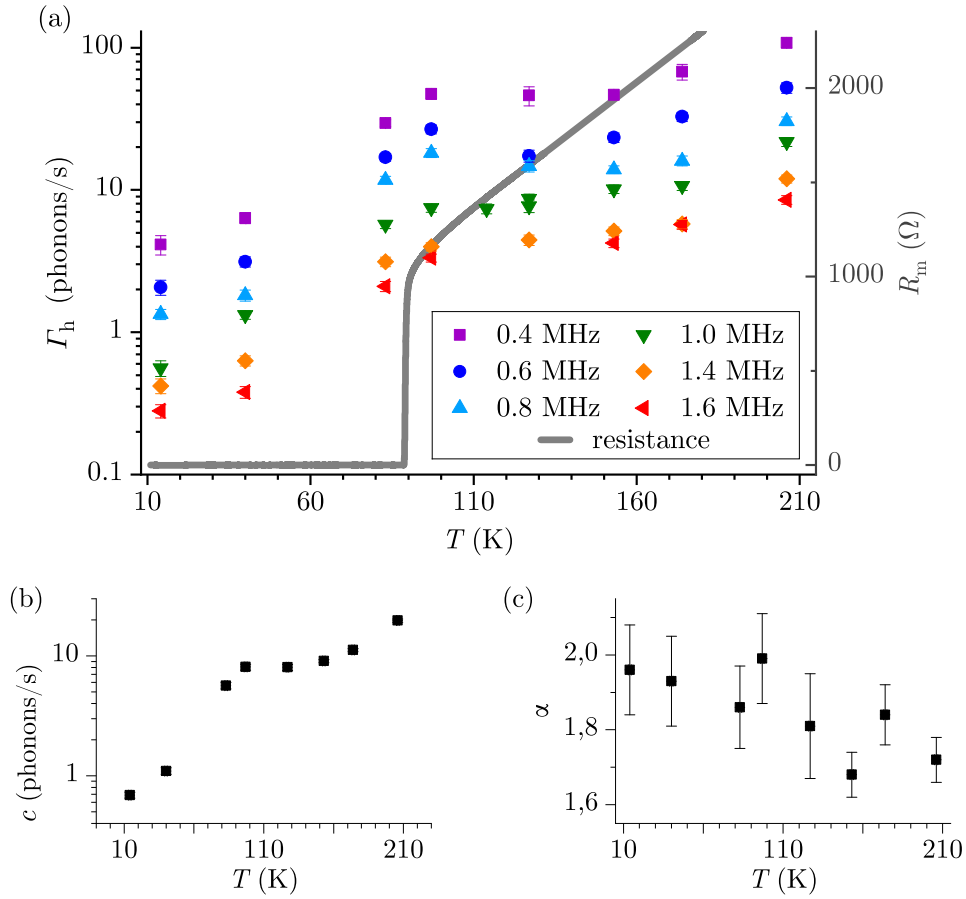


**Figure 7.11.** Temperature dependence of the heating rate  $\Gamma_h$  in trap chip B. (a) Data points show the heating rate  $\Gamma_h$  as function of trap temperature  $T$  for different secular frequencies  $\omega_z$ . Note the vertical log scale. The gray line (right scale) shows the YBCO meander resistance  $R_m$ . (b) and (c) show the temperature variation of the power law coefficient  $c$  and exponent  $\alpha$ , determined by a fit of Eq. (7.5) to the individual spectra in (a). The uncertainties in (b) are smaller than the data points.

temperature dependence: Below  $T \lesssim 90$  K the heating rate increases strongly with temperature. For  $T \gtrsim 90$  K the data show a pronounced plateau, where  $\Gamma_h$  is constant over a temperature range of about 50 K. The onset of this plateau region coincides with the critical temperature  $T_c = 89(1)$  K as evidenced by the 4-wire resistance measurement of an YBCO meander (gray data). For temperatures  $T \gtrsim 160$  K, the heating rate is rising further. The individual frequency sets are in good agreement with a power law spectrum. Figs. 7.11 (b) and (c) show the variation in power law coefficient  $c$  and exponent  $\alpha$  resulting from a fit with Eq. (7.5). While the magnitude  $c$  is rising rapidly for  $T < T_c$  and shows a plateau region for  $T > T_c$ , (b), no clear difference between the two temperature regimes is observable for the exponent  $\alpha$ , (c). Only a slight trend might be visible with the exponent changing continuously from  $\alpha \approx 2.0$  at  $T = 14(1)$  K to  $\alpha \approx 1.7$  at  $T = 210(1)$  K.

## 7.4. Discussion

The first experiments discussed in the previous section study RF grounding of electrodes connected through a long and thin YBCO meander lead. For temperatures above the superconducting transition, the large meander resistance inflicts a significant amount of excess micromotion. For  $T < T_c$ , the excess micromotion amplitude is strongly reduced. The data are in qualitative and reasonable quantitative agreement with estimates derived from the electrical model. The agreement between data and model for  $T < T_c$  suggests that grounding through the superconducting meander lead works similarly well as compared to a direct connection to the filter line that bypasses the meander lead. The limiting factor for the residual RF pickup voltages on the electrodes connected through the meander leads is the connection line inductance. One way to further suppress pickup voltages in future trap designs might be to engineer the electrode leads such that the line inductance is compensated by the line capacitance, i. e. make the self-resonant frequency of the connection line match the RF drive frequency.

The second study investigates the impact of the superconducting electrode leads on the motional heating rate  $\Gamma_h$ . For temperatures  $T < T_c$ , the meander leads do not limit the heating rate, which shows values around 1 phonon/s, comparable to other cryogenic surface traps [87]. For  $T > T_c$  the meander leads cause a significant amount of JN due to the poor conductivity of YBCO in the normal state. At  $T = 97(1)$  K the YBCO lead has a resistivity of  $\rho_{\text{YBCO}} \approx 1.4 \times 10^{-6} \Omega \text{ m}$ , calculated from the meander lead resistance  $R_m = 14.9(20)$  k $\Omega$  and its geometry (given in appendix A.4.1). For comparison, copper at  $T = 80$  K has a resistivity of  $\rho_{\text{Cu}} = 0.22 \times 10^{-8} \Omega \text{ m}$  [159], about a factor 670 smaller than  $\rho_{\text{YBCO}}$ . However, a copper lead with the same geometry as the YBCO meander would induce a Johnson noise limited heating rate of  $\Gamma_h^{(\text{JN})} \approx 1.1$  phonons/s, which

## 7. Superconducting surface traps

is on par with the value  $\Gamma_h = 1.03(8)$  phonons/s measured at  $T = 77$  K. This shows that superconducting lead wires can be beneficial already for lead lengths of a few mm. Future trap designs could for instance be realized with a multilayer structure, using a superconducting bottom layer to route supply leads to the trap electrodes on the top layer, which could be made from gold.

The final set of experiments investigates motional heating in chip B, where the YBCO surface at the trap center is exposed to the ion. This is the first time, motional heating has been measured above a high-temperature superconducting surface. Such measurements with new trap materials are important for the still incomplete understanding of surface noise. The heating rates in chip B have a similar magnitude  $\Gamma_h \sim 1$  phonon/s compared to those obtained for a gold surface in chip A, see Fig. 7.10. Such a heating rate corresponds to an electric field noise of  $S_E \sim 7 \times 10^{-15} \text{ V}^2 \text{ m}^{-2} \text{ Hz}^{-1}$  at  $\omega_z = 2\pi \times 1.0$  MHz, cf. Eq. (3.7), which constitutes the sensitivity of the experiment. Assuming for the moment that the measured heating rates originate from surface noise, a natural question would be whether the size of the exposed YBCO area of  $740 \times 580 \mu\text{m}^2$  is large enough to make statements about the relative noise strengths from a YBCO and a gold surface. Indeed, the noise contribution from the exposed YBCO area to the electric field noise at the ion position would be around 94% if the microscopic noise sources on the YBCO and gold surfaces had identical fluctuation strengths, as calculated in appendix A.4.4. Within the given sensitivity of  $S_E \sim 7 \times 10^{-15} \text{ V}^2 \text{ m}^{-2} \text{ Hz}^{-1}$ , it can thus be concluded that YBCO as trap material yields heating rates similar to those obtained in gold traps for operation at temperatures below  $T_c$ .

The detailed characterization of the heating rates in chip B, Fig. 7.11, reveals a power law spectrum with a power law exponent  $\alpha \approx 1.7 - 2.0$  and a peculiar temperature dependence: a strong noise increase with rising temperature for  $T \lesssim T_c = 89(1)$  K and a plateau region for  $T \gtrsim T_c$ . The measured data exclude several possible sources for the observed electric field noise. External noise sources like technical noise are independent of the trap chip temperature  $T$  and therefore cannot by themselves produce the measured temperature dependence. A possible correlation of external sources with  $T$  through a variation in the cryogenic DC filter attenuation is excluded as well: the filters' transfer function does not correlate with the temperature dependence of the heating rate, as shown in appendix A.4.3. JN from the trap electrodes, wiring and – to some extent – also the cryogenic DC filters does depend on the trap chip temperature  $T$ . However, these unfiltered sources have a flat spectrum<sup>6</sup>, leading to a  $1/f$  frequency dependence of the heating rate. A dominant contribution of these sources is therefore excluded by the power law exponent  $\alpha \approx 1.7 - 2.0$  of the measured heating rate. The

---

<sup>6</sup> The noise of the filters is negligible compared to the other sources, see appendix A.4.2.

expected total level of Johnson noise,  $S_{E,\text{tot}}^{(\text{JN})}$ , produced by electrodes, wiring and filters is calculated in appendix A.4.2. While  $S_{E,\text{tot}}^{(\text{JN})}$  is indeed negligible for temperatures  $T < T_c$ , it is smaller but of the same order of magnitude as the measured noise for  $T > T_c$ . At the highest temperature  $T = 206$  K, the estimated JN contribution to the measured noise is about 14%. The increase of the measured heating rate beyond the plateau region for  $T \gtrsim 160$  K and the slight tendency towards smaller power law exponents are therefore likely to be caused by an increasing JN contribution.

The coincidence between the critical temperature and the onset of the plateau region strongly suggests that processes within the YBCO film are involved in generating the measured heating rates. In fact, the kink at  $T_c$  in the measured temperature dependence is reminiscent of a second order phase transition. Such a behavior is observed for many physical quantities in high-temperature superconductors, foremost for the density of superconducting charge carriers [160], and similar temperature dependencies have been measured for AC loss [161], voltage noise caused by resistance fluctuations [162], for the magnetic susceptibility [163] and for the frequency variation of phonon modes [164]. The exclusion of technical noise and JN as dominant noise sources narrow down the origin of the measured heating rates to three possible explanations:

1. The dominant electric field noise originates directly from the bulk of the YBCO.
2. The dominant noise is caused by sources on the chip surface, which are excited by processes within the YBCO film, for instance by phonons.
3. The measured temperature dependence does not stem from the dominant noise source itself but from a temperature-dependent attenuation of the electric field noise by the YBCO film through screening currents. In this case the noise origin is unclear.

Further tests are necessary in order to identify the physical mechanism behind the measured temperature dependence of the heating rate. Concerning the noise screening hypothesis (3), one would expect a strong attenuation of noise sources located within the YBCO bulk or at the substrate-YBCO interface, similar to effects seen in cold-atoms experiments using superconducting chip traps [165, 166]. However, considering that the YBCO film imposes boundary conditions on the electric field noise [167], it might also influence the noise magnitude at the ion position of more distant noise sources. This hypothesis could be tested by injecting technical noise through one of the trap electrodes and measuring its dependence on the trap chip temperature. In-situ cleaning of the chip surface, e. g. by ion bombardment [114, 115], should allow one to differentiate between hypotheses 1 and 2, i. e. a dominant noise source on the chip surface or within the bulk. Another natural extension of the experiment would be to vary the thickness of

## 7. *Superconducting surface traps*

the YBCO film or its stoichiometry, in particular the oxygen content which controls the charge carrier density [153]. Such measurements might give interesting input for the understanding of the various phases in YBCO that are still not fully understood [168], should the noise origin prove to be within the YBCO bulk.

## 8. 2 D linear trap array “Bucket-brigade”

This chapter describes the development of a new generation of two-dimensional surface trap arrays, further advancing the core idea of the Ziegelstadl trap described in chapter 5. The goal is to arrange ions on a two-dimensional lattice of individual trapping sites to create a platform for quantum simulations. The building blocks of the new array are coplanar linear traps, as depicted in Fig. 3.1 (b) in chapter 3.1.1. A lattice of trapping sites in such an array is created by a combination of RF confinement (along the radial directions) and DC confinement (along the traps’ axial directions). Entanglement between ions in adjacent trapping wells can be mediated by the Coulomb interaction, provided that the well-to-well distance is sufficiently small. As for the Ziegelstadl array, local ion-shuttling operations are employed to enhance the Coulomb interaction between adjacent ions, facilitating the sequential creation of multi-qubit entangled states.

2D arrays of parallel linear traps offer several advantages over point trap arrays, such as the Ziegelstadl design: First, multiple ions can be trapped in a single trapping site without being subjected to excess micromotion. This allows one to store several qubits in every trapping site, in each of which the standard quantum logic toolbox for linear traps can be applied. In particular, entangling gates using the shared motion and sympathetic cooling techniques [169–171] can be used. Furthermore, storage of multiple ions per site enables stronger motional coupling across a potential barrier, since the coupling rate scales approximately with the number of ions in the crystal [57]. Second, ions can be shuttled along the linear trap axes, giving more flexibility to the qubit connectivity within the lattice. This point is further described in the next section. Third, the barrier separating two adjacent trapping sites during RF shuttling operations is significantly larger, as has been discussed in chapter 5.4.3. This makes the RF shuttling operations more robust against stray charges on the chip surface. Fourth, the technical overhead in terms of RF electronics is reduced. A linear trap array with parallelized RF shuttling operations (described in the next section) requires only two independent RF drives, as compared to five drives in a point trap array (cf. chapter 5.1.2).

The focus of the work described here is on the simplest instance of the envisioned linear trap array: two parallel linear traps with segmented DC electrodes. Such a design was fabricated by Infineon Austria<sup>1</sup> and is called “Bucket-brigade” (BB) trap due to the

<sup>1</sup> Infineon Technologies Austria AG, Villach, Austria

## 8. 2D linear trap array “Bucket-brigade”

operation principle employed for ion shuttling operations. The chapter starts out defining the design objectives, considering still the general case of a large linear trap array. It then moves on to the core part with simulations of the BB traps and the strategies developed to optimize the trap geometry and the shuttling processes. Afterwards, the fabrication of the BB traps is briefly outlined and electrical characteristics of the trap chips are presented. A more detailed description of the fabrication steps can be found in the master’s thesis of Gerald Stocker [172]. The chapter closes with an outlook on future experiments in the BB traps and proposals for extending the design to larger arrays with more than 100 trapping sites.

### 8.1. Objectives

Three main objectives were pursued for the design of the 2D linear trap array. First, trapping potentials with an optimized trap depth should be provided. This includes in particular maximizing the well-to-well barriers to enhance the robustness of the confining potential against stray electric fields. Second, entangling operations between ions in adjacent trapping sites should be enabled in two spatial directions. These first two objectives are both linked to the choice of a suitable ion-surface separation  $d$ . Third, to implement a shuttling process that changes the connectivity of the ions from that of a square lattice to that of a triangular lattice. The objectives are explained in more detail in this section.

#### 8.1.1. Next-neighbor interactions and ion-surface separation

In the envisioned trap array, the ions forming the quantum register will be distributed over different trapping sites. As a starting point for the trap simulations, a suitable distance  $s_t$  between adjacent trapping sites as well as the ion-surface separation  $d$  need to be chosen. Entangling operations between ions in adjacent sites require motional coupling with an interaction strength  $\Omega_c$  much larger than the motional heating rate  $\Gamma_h$ . Therefore, noting the scaling of the coupling rate  $\Omega_c \propto s_t^{-3}$ , a small trapping site distance  $s_t$  would be desirable, cf. Eq. (3.4). Choosing realistic values for the distance  $s_t \approx 50 \mu\text{m}$  and the secular frequency  $\omega_{\text{sec}} = 2\pi \times 1 \text{ MHz}$ , one calculates a coupling rate  $\Omega_c \approx 2\pi \times 1 \text{ kHz}$ . A reliable estimate of the motional heating rate  $\Gamma_h$  is unavailable due to its unknown origin. Literature values of heating rates at  $d \approx 50 \mu\text{m}$  and cryogenic temperatures range between  $\Gamma_h \sim (10 - 1000) \text{ phonons/s}$  [87]. The requirement  $\Omega_c \gg \Gamma_h$  therefore suggests a trap design with  $d \gg 50 \mu\text{m}$ , where a lower  $\Gamma_h$  can be expected due to the  $d^{-4}$  scaling of surface noises, cf. chapter 3.3. However, a significantly larger ion-surface separation is in conflict with the trap array design rule, Eq. (3.1), introduced

in chapter 3.1.1 which states that trapping potentials with  $d \gg s_t$  cannot be efficiently created. One can thus identify two rivaling design goals: on the one hand, optimizing for an efficient and deep trap and, on the other hand, operating at parameters  $s_t \ll d$  to fulfill the requirement  $\Omega_c \gg \Gamma_h$ .

To resolve this conflict, one of the aims of the new trap array is to explore an intermediate regime with a moderate ion-surface separation  $d \approx 100 \mu\text{m}$  and a variable distance  $s_t$  between trapping sites. In the default configuration, a site distance  $s_t \approx d$  ensures the efficient creation of trapping fields and large trap depths. During entangling operations, the distance is decreased to  $s_t \approx 50 \mu\text{m}$ . Essential for this approach is the usage of DC and RF shuttling techniques, as discussed in chapter 3.2.2. The moderate ion-surface separation  $d$  has the additional advantage of reducing the influence of stray electric fields from the trap surface, which should improve the stability of the trapping frequencies. Fig. 8.1 (a) illustrates the default trapping configuration. Collinear RF rails (green) realize parallel linear traps with trap axes along the  $z$ -direction. The segmented DC electrodes (blue) create a DC multiwell along the trap axes  $z$ . The combination of RF and DC fields thus defines a square lattice for trapped ions (blue spheres). Ion-Ion interactions between ions in adjacent trapping sites can be sequentially realized by decreasing the distance  $s_t$  between these ions. Following the general entangling scheme described in chapter 3.2.3, a specific secular mode of the ions is then brought into resonance, allowing for an entangling gate under simultaneous irradiation with laser light<sup>2</sup>. Subsequently, the inter-ion distance  $s_t$  is restored to the original value. Along the  $x$ -direction, the ion-shuttling operation is done by reducing the RF voltage on either odd or even RF rails, as shown in Fig. 8.1 (b) and (c), respectively. A whole line of ions can be pairwise entangled in two steps. Similarly, DC control voltages can be used to bring together adjacent ions along the  $y$ -direction, (d) and (e). In two steps, a whole column of ions can be pairwise entangled. A pairwise entanglement of all next-neighboring ions on the full lattice can therefore be realized in four steps. Furthermore, specific pairs of ions can be left unentangled by keeping their secular modes off-resonant and single qubit gates can be added between the entangling operations<sup>3</sup>. This gives flexibility for the creation of complex multi-qubit entangled states.

With such a sequential entangling scheme one could for instance create cluster states as resource for a measurement-based quantum processor [173]. Cluster states can be produced by the application of a controlled phase gate<sup>4</sup> on every pair of neighboring sites [174]. More generally, the motional coupling between ions in adjacent trapping

<sup>2</sup> A global laser field is necessary for parallelized entangling operations of different pairs of ions.

<sup>3</sup> Single qubit gates on specific ions require single-ion addressing, e.g. by using one of the methods described in chapter 3.1.3.

<sup>4</sup> e.g. realized by an entangling operation and single qubit rotations

8. 2D linear trap array “Bucket-brigade”

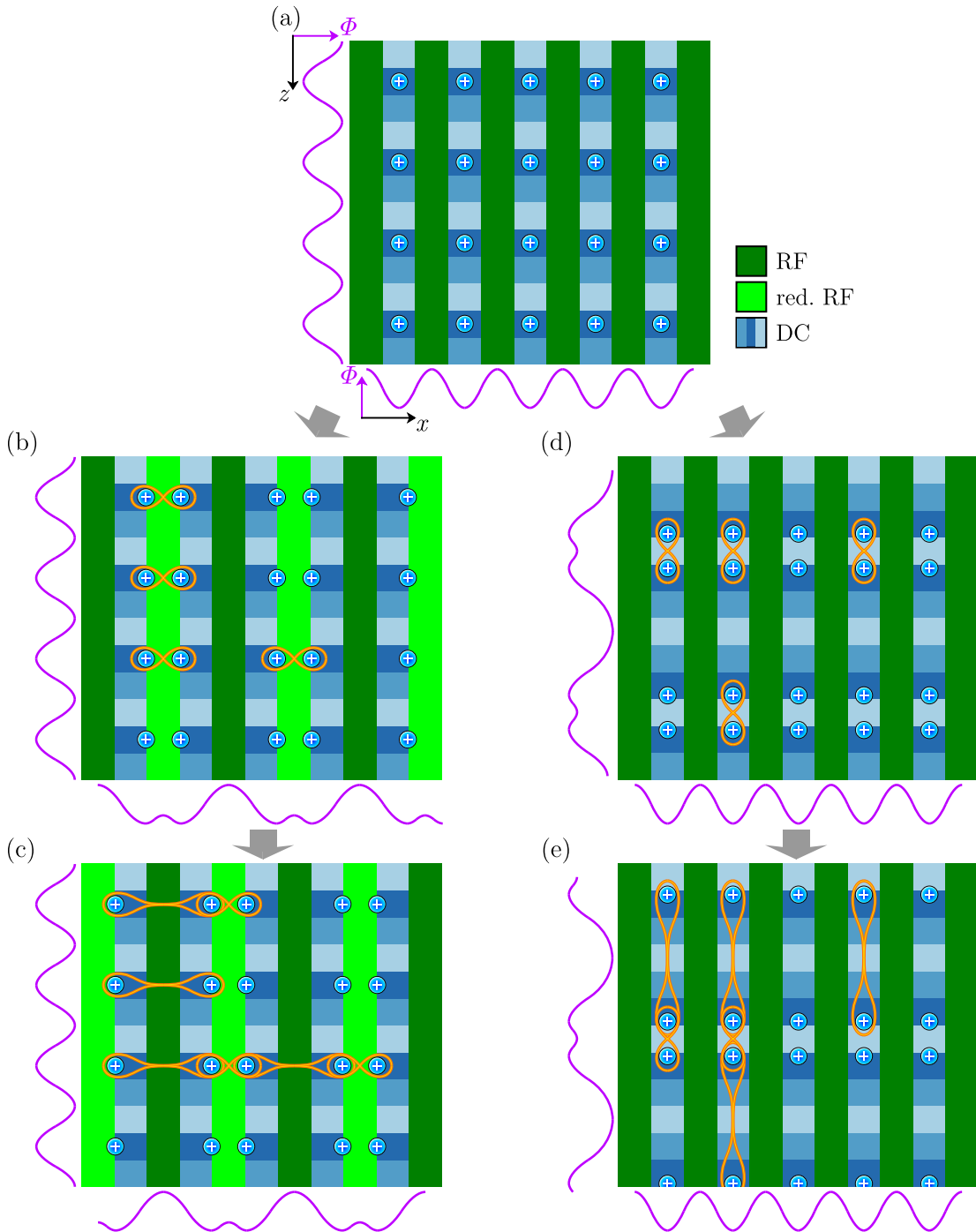


**Figure 8.1.** Schematic illustration of entangling operations between ions in adjacent trapping sites. In the default configuration (a) ions (blue spheres) are stored on a square lattice. Cross sections of the confining potential  $\Phi$  are depicted as violet lines. The distance between adjacent ions is reduced along the  $x$ -direction by adjusting the RF voltages (b), (c). Along the  $z$ -direction, the DC voltages are adjusted to bring adjacent ions close, (d), (e). The reduced ion-ion distance facilitates the creation of pairwise entanglement between adjacent ions (pictured in orange).

sites could be used for the simulation of spin models [58] in a sequential way. Another possibility might be to extend recent studies of entanglement propagation in a linear ion chain [175] to a two-dimensional ion lattice.

### 8.1.2. Lattice reconfiguration

The sequential entangling operations described in the previous section allow one to establish a square lattice of trapped ions with next-neighbor entanglement as illustrated in Fig. 8.2 (a). In addition, ions can be shuttled along the axes of the linear traps. This gives the flexibility to reconfigure the lattice type from square to triangular as shown in Figs. 8.2 (b), (c). After entangling adjacent ions along the  $x$  and  $z$  direction on the square lattice, every second line of ions is shuttled by one lattice period along the  $z$ -direction. A subsequent additional entangling operation along the  $x$ -direction establishes the connectivity of a triangular lattice. A fully connected triangular lattice can thus be created in 7 consecutive steps: four parallelized entangling operations (two along  $x$ , two along  $z$ ) to create the fully connected square lattice, one parallelized shuttling operation of every second line of ions and two parallelized entangling operations along  $x$ . The approach can be further extended by leaving out entangling operations between specific ion pairs or by shuttling more than one lattice period along  $z$ , thus engineering more complicated lattice connectivities. Shuttling within the ion lattice opens up other possibilities as well, such as tuning of the motional coupling strength  $\Omega_c$  or transport of quantum information, physically encoded in the ions, through the lattice.

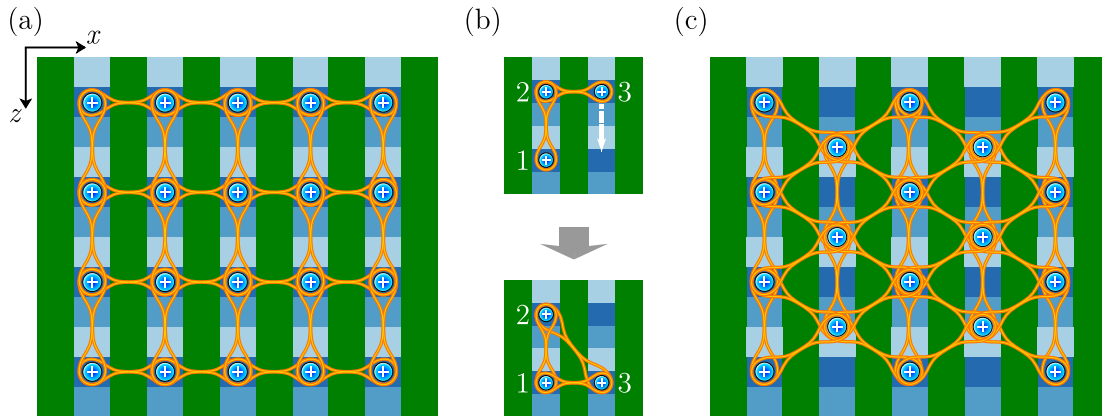


**Figure 8.2.** Schematic illustration of a lattice reconfiguration. (a) The default configuration is a square lattice with next-neighbor connectivity (pictured as orange lines), produced sequentially as illustrated in Fig. 8.1. (b) Shuttling of ion 3 along the trap axis  $z$  and subsequent entanglement with ion 1 creates a unit cell for a triangular lattice. This step can be parallelized to create a full triangular lattice with next-neighbor connectivity (c).

## 8. 2D linear trap array “Bucket-brigade”

Simultaneous shuttling of groups of ions requires in general sophisticated voltage sequences on the DC electrodes, using many degrees of freedom. When shuttling in a periodic DC multiwell potential, the number of DC control voltages can be significantly reduced by employing a periodic connectivity of the DC segments [90, 155]. The principle is illustrated in Fig. 8.3 (a). Setting every third DC segment to the same voltage (indicated by the color), creates a periodic DC potential along the  $z$ -direction. Potential minima can for instance be established above segments DC2 (as shown on the left) by application of a higher positive voltage on both adjacent segments DC1 and DC3, thus creating a multiwell of trapping sites with a well spacing of  $a_{\text{mw}}$ . Alternatively, the multiwell minima can be located above segments DC3 (middle) or DC1 (right), by exchanging the voltages on the segments. A voltage sequence connecting the different configurations is shown in (b). Starting with one of the well minima located at  $z_0 = 0$ , i. e. above segment DC2, the entire multiwell can be shifted towards more positive  $z$ -values by a voltage increase at DC1 and a simultaneous decrease at DC3. Upon reaching equal voltages on DC2 and DC3, lower than the voltage on DC1, the minimum will be located at  $z_0 = a_{\text{mw}}/6$ , right between electrodes DC2 and DC3. The multiwell can be further shifted towards  $z_0 = a_{\text{mw}}/3$ , by reverting the voltage sequence, however, with exchanged voltages on electrodes DC2 and DC3. Eventually, the multiwell will be located above the DC3 segments, having moved by one full segment. In this way, the multiwell can be continuously shifted across arbitrarily many lattice periods  $a_{\text{mw}}$  using only three control voltages. This type of shuttling has similarities with analogue shift register circuits (“bucket-brigade devices”) [176] and is therefore referred to as “bucket-brigade shuttling” (BB shuttling) within this thesis.

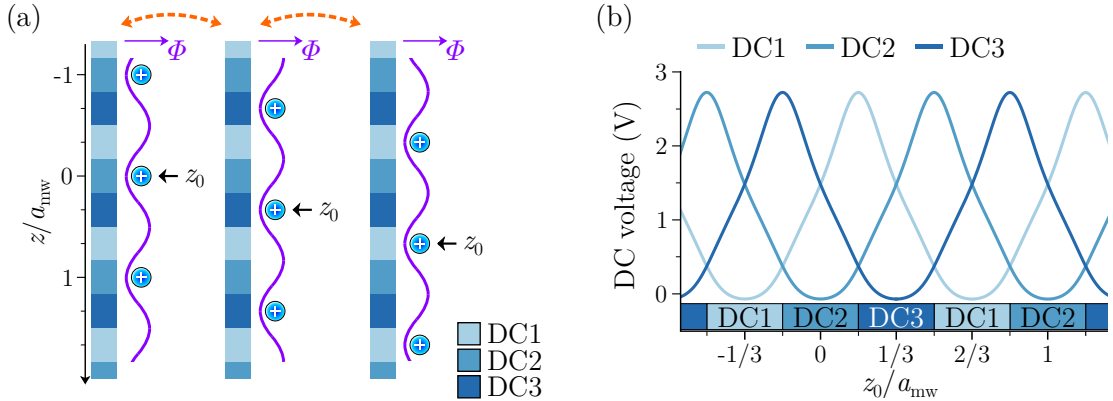


**Figure 8.3.** Concept of bucket-brigade shuttling. (a) The periodic assignment of voltages to the DC segments (indicated by the color) creates multiwell potentials with a lattice constant  $a_{\text{mw}}$ . The well minimum at  $z_0$  can be positioned above either of the three DC segments DC1, DC2 or DC3. (b) Voltage variation on the DC segments for a continuous shift of the minimum position  $z_0$  along the  $z$  axis. A shift of the entire multiwell requires only three independent DC channels, due to the spatial periodicity of the DC segments.

## 8.2. Trap design and simulation

This section is focused on the “Bucket-brigade” (BB) trap, which is the simplest instance of the envisioned 2D linear trap array. The BB trap consists of two parallel linear traps with segmented DC electrodes and implements the core operational principles outlined in the previous section: axial multiwell confinement; DC and RF shuttling of multiwells; motional coupling and entanglement between ions in adjacent trapping sites. The principle of BB shuttling, which is realized by a periodic connectivity of the DC segments, lends its name to the trap design.

The section is structured in the following way: First, the RF confinement in two collinear traps with mirror symmetry (twin traps) is analyzed. It is investigated how the geometry and relative RF voltage amplitudes change the position of the trapping sites and the pseudopotential barrier between them. The geometry is optimized in terms of trap depth and efficiency. In a second step, DC electrodes are introduced to create axial multiwell potentials. The BB shuttling principle is implemented to simulate independent translations of the two adjacent DC multiwells along the trap axes, using a total of only 8 voltage channels. A method is devised to characterize this BB shuttling process. The third step is the characterization of the shuttling processes that reduce the distance between the trapping sites. In radial direction, the distance reduction is done by adjusting the RF voltages. Along the axial direction, a special interaction zone with smaller DC segments is used.

All simulations were done with the “electrode package” for Python<sup>5</sup>, which employs a Biot-Savart-like law for electrostatics [67, 177] to calculate the electric fields produced by the trap electrodes. Necessary assumptions are an infinite ground plane surrounding the electrodes and no electrode gaps. For realistic trap geometries these assumptions have been found to lead to negligible imprecision in the calculated fields [135]. The advantage of this analytical approach over finite element or boundary element simulations is that the simulation is orders of magnitude faster, allowing one to investigate the electrode geometry over a wide range of parameters.

### 8.2.1. RF confinement in collinear twin traps

The RF confinement within the BB trap is created by three parallel RF rails separated by two DC rails as illustrated in Fig. 8.4. The two DC rails are set to ground (GND) for the simulations described in this section. The inner RF, outer RF and DC rails have widths  $w_i$ ,  $w_o$  and  $w_{DC}$ , respectively. This configuration produces two parallel linear traps, referred to as collinear twin traps in what follows. In a first step, the confining

<sup>5</sup> electrode package by R. Jördens (<https://github.com/nist-ionstorage/electrode>); see also [134, 135].

## 8. 2D linear trap array “Bucket-brigade”

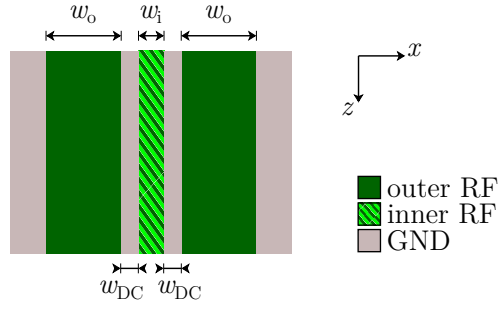


**Figure 8.4.** Electrode geometry for the study of RF confinement in collinear surface traps. Two outer RF rails (dark green) and one inner RF rail (hatched in green) create parallel linear traps with trap axes along the  $z$ -direction. The positions of the two RF nulls in the  $xy$ -plane are determined by the geometry and the ratio of RF voltages on the inner and outer RF rails. The lengths of the rails along the  $z$ -direction stretches longer than drawn.

RF pseudopotential is investigated. Upon varying the rail widths  $w_i$ ,  $w_o$ ,  $w_{DC}$ , three different regimes can be identified, that differ in the positions of the RF nulls and saddle points relative to each other. In general, the pseudopotential exhibits two RF nulls and two saddle points, while for specific geometries there is only a single RF null and saddle point, marking the transitions between the regimes. The three regimes are shown in Fig. 8.5 (a), where the pseudopotential  $\varphi_p$  is plotted in the radial plane ( $xy$ ). In regime I, the two RF minima (dark blue) and two saddle points (marked with a cross) are all aligned along the vertical direction,  $y$ . The first saddle point separates the two minima by a potential barrier  $U_b$ . The second saddle point is above the upper minimum and sets the global trap depth  $U_0$ . The trap efficiency and therefore the stability  $q$ -factor for the two minima can differ substantially for large vertical separations, due to the different distances  $d$  from the trap electrodes. A simultaneous operation of both minima in this regime is therefore difficult. In regime II, the two minima are aligned along the horizontal direction,  $x$ , and have equal trap efficiency. The first saddle point separates the minima and sets the double well barrier  $U_b$ . The second saddle point is above both minima, again defining  $U_0$ . Regime III is characterized by a complete separation of the two RF nulls. The two saddle points are situated above their respective minima and a double well barrier  $U_b$  can no longer be defined. The transition from one regime to the next is shown in Fig. 8.5 (b), where the inner rail width  $w_i$  is varied, while  $w_o = 200 \mu\text{m}$  and  $w_{DC} = 100 \mu\text{m}$  are kept constant. The top graph shows the positions  $\mathbf{r}_0$  of the two minima in the  $xy$  plane, the bottom graph shows the positions  $\mathbf{r}_b$  of the saddle points. The graphs reveal bifurcations at the transition points between the regimes. At the first bifurcation at  $w_i \approx 42 \mu\text{m}$ , the two minima merge and change their orientation from vertical (regime I) to horizontal (regime II). Right at the transition point, the quadratic term of the trapping potential vanishes, leading to a diverging RF voltage

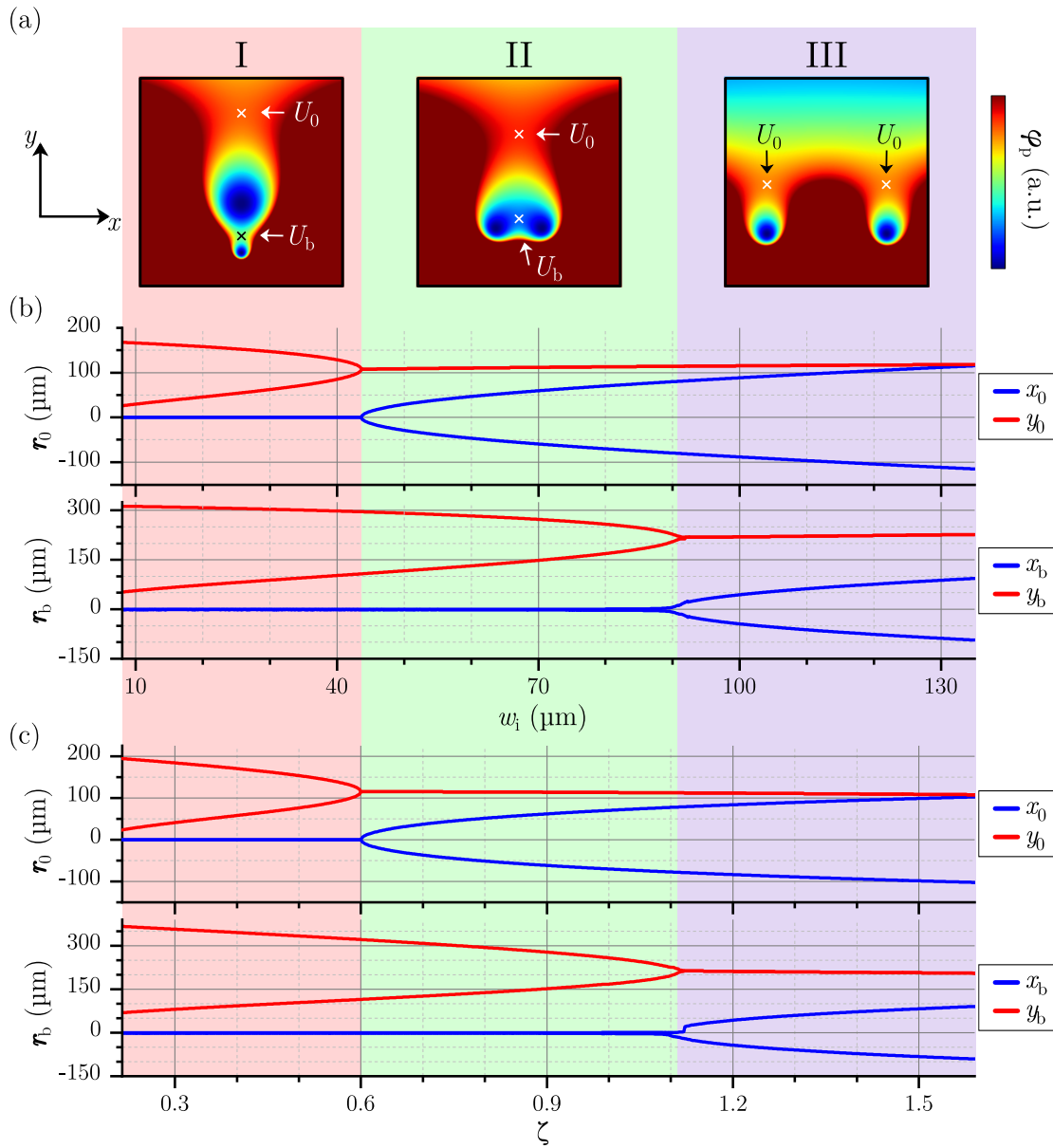


**Figure 8.5.** Qualitative equivalence between geometry change and RF shuttling in a twin-trap. (a) The positions of the two trapping sites (dark blue) and the two saddle points (marked with a cross) relative to each other allow to identify three regimes I, II, and III. Each regime can be realized by adjusting the electrode geometry or the RF voltage ratio  $\zeta$ . (b) Variation of the positions  $r_0$  of the potential minima and  $r_b$  of the saddle points as the inner RF rail width  $w_i$  is varied for fixed  $\zeta = 1$ . (c) A qualitatively equivalent variation in  $r_0$  and  $r_b$  can be seen for a fixed geometry when varying the RF voltage ratio  $\zeta$ .

## 8. 2D linear trap array “Bucket-brigade”

necessary to achieve a constant stability  $q$ -factor. The second bifurcation occurs at  $w_i \approx 90 \mu\text{m}$ , where the two saddle points change their orientation from vertical (regime II) to horizontal (regime III). It is interesting to note that the ion-surface separation  $d = y_0$  is practically constant in regimes II and III. The exact position of the bifurcation points separating the three regimes depends on the values of  $w_o$  and  $w_{\text{DC}}$ . A few general trends can be noted: The bifurcation points are shifted towards higher values of  $w_i$  for increasing  $w_o$ . This can be understood intuitively as broader outer RF rails push the minima closer together and favor the vertical orientation in regime I. The DC rail width  $w_{\text{DC}}$  mainly sets the ion-surface separation  $d$  in regimes II and III with larger values of  $d$  for increasing  $w_{\text{DC}}$ . For decreasing  $w_{\text{DC}}$  at fixed  $w_i$ , regime III with completely separated traps is favored.

Instead of using a geometrical control parameter, all three regimes I, II, III can also be realized by varying the RF voltage ratio

$$\zeta = \frac{U_{\text{RF}}^{(i)}}{U_{\text{RF}}^{(o)}}, \quad (8.1)$$

defined as the ratio of RF voltage  $U_{\text{RF}}^{(i)}$  on the inner RF rail to the voltage  $U_{\text{RF}}^{(o)}$  on the outer RF rail. Fig. 8.5 (c) shows an example of this. The top and bottom graphs again show the positions of the pseudopotential minima and saddle points, respectively. The control parameter  $\zeta$  is varied for a fixed geometry with  $w_i = 80 \mu\text{m}$ ,  $w_{\text{DC}} = 100 \mu\text{m}$  and  $w_o = 200 \mu\text{m}$ . The graphs are qualitatively equivalent to the ones in Fig. 8.5 (b). In particular, both bifurcations marking the transitions between the regimes, as well as the constant ion-surface separation  $d = y_0$  in regimes II and II, can be observed. The latter is important, since a significant reduction of the ion-surface separation  $d$  during RF shuttling operations would likely lead to a significant increase of the ion heating rate, eventually decreasing the fidelity of the well-to-well entangling operations. The similarity between the graphs in Fig. 8.5 (b) and (c) suggests that varying the RF voltages is in many aspects equivalent to changing the electrode geometry, when considering the effect on the trapping potential. This finding, which will be further corroborated below, is used to reduce the complexity of finding an optimal geometry for the BB traps.

Ions have previously been confined at fixed points in both regimes I and II within the same trap using different, static RF voltage ratios  $\zeta$ , as described by Tanaka et al. [178]. In that work, the smallest distance between parallel ion strings trapped in regime II was  $s_t \approx 60 \mu\text{m}$  at an ion-surface separation  $d \approx (240\text{-}270) \mu\text{m}$ , showing the feasibility to operate a trap under the condition  $s_t < d$ . In the BB traps, the goal is to *dynamically* reduce the distance  $s_t$  for the duration of an entangling operation, from an

initial value  $s_t \approx d$  into the inefficient regime  $s_t < d$ . Another difference to the design in Ref. [178] is the strong segmentation of DC electrodes in the BB trap design, which allows for the creation of DC multiwells and requires a more advanced fabrication.

The remainder of this section is devoted to finding the optimal twin trap geometry for the BB traps. The main optimization parameters are the trap efficiency (defined in Eq. (2.2) in chapter 2.1.1), the trap depth  $U_0$  and the height of the double-well barrier  $U_b$ , which separates the two linear traps. An optimal geometry would maximize these quantities within the targeted operation range of the trap, defined in the previous section: a variable distance between the linear traps in the range of  $s_t \approx (50-100) \mu\text{m}$  and a moderate ion-surface separation  $d \approx 100 \mu\text{m}$ . The complexity of the optimization problem can be significantly reduced by assuming the equivalence between varying the RF voltages and changing the electrode geometry, as suggested by Fig. 8.5. An optimization at one distance  $s_t$  with RF ratio  $\zeta = 1$  is then sufficient to optimizing the entire range of  $s_t$  for  $\zeta < 1$ . This will become evident at the end of this section. The equivalence between geometry variation and RF voltage tuning is further supported by the scaling of the double well barrier  $U_b$  with inter-trap distance  $s_t$ . Fig. 8.6 (a) shows the pseudopotential  $\varphi_p$  in the radial plane in regime II, with the two RF nulls at equal distance  $d$  from the trap surface and separated by  $s_t$ . The value of  $\varphi_p$  on the trajectory of minimal potential energy connecting the two trapping sites (illustrated by the dashed purple line) defines the double well potential  $Q\phi_{dw}(x)$ . The simulated

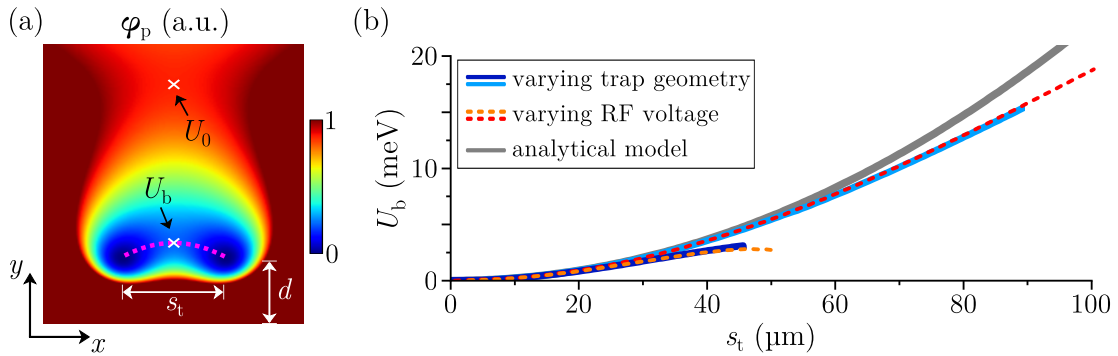


**Figure 8.6.** Universal scaling of the pseudopotential barrier  $U_b$ . (a) Confining pseudopotential  $\varphi_p$  in the  $xy$ -plane. The two RF nulls (dark blue), at a distance  $s_t$  from each other, are separated by a potential barrier  $U_b$ . The dashed purple line illustrates the path of minimal potential connecting the two sites. (b) Scaling of  $U_b$  with the inter-trap distance  $s_t$  for a constant radial frequency  $\omega_x$ . Solid lines show simulation results for two different geometries, where the rail width  $w_1$  is varied to change  $s_t$ , while keeping the RF voltages fixed ( $\zeta = 1$ ). Dashed lines show simulation results where the RF ratio  $\zeta$  is varied at fixed electrode geometry. The gray line is the barrier calculated from the double-well model, Eq. (8.3).

## 8. 2D linear trap array “Bucket-brigade”

double-well potentials are, to good approximation, of the form

$$\phi_{\text{dw}}(x) = ax^4 - bx^2. \quad (8.2)$$

This model potential is fully determined by a given inter-trap distance  $s_t = \sqrt{2b/a}$  and secular frequency  $\omega_x = \sqrt{4bQ/M}$ . The potential barrier between the two wells is then

$$U_b = \frac{Qb^2}{4a} = \frac{M\omega_x^2 s_t^2}{32}, \quad (8.3)$$

where  $M$ ,  $Q$  are the ion mass and charge. Fig. 8.6 (b) shows the potential barrier  $U_b$  as function of the distance  $s_t$ . Solid lines are simulation results for varying trap geometry without voltage attenuation,  $\zeta = 1$ . The varied parameter is the inner RF rail width  $w_i$  while the other widths are fixed at  $w_o = 50 \mu\text{m}$ ,  $w_{\text{DC}} = 40 \mu\text{m}$  (dark blue) and  $w_o = 200 \mu\text{m}$ ,  $w_{\text{DC}} = 100 \mu\text{m}$  (light blue). Dashed lines show simulation results for varying RF ratio  $\zeta$  at fixed trap geometry,  $w_i = 10 \mu\text{m}$ ,  $w_o = 50 \mu\text{m}$ ,  $w_{\text{DC}} = 40 \mu\text{m}$  (orange) and  $w_i = 80 \mu\text{m}$ ,  $w_o = 200 \mu\text{m}$ ,  $w_{\text{DC}} = 100 \mu\text{m}$  (red). All simulated data are closely approximated by the double-well potential model, Eq. (8.3), (gray line) for trap separations  $s_t$  much smaller than the ion surface separation  $d$  (roughly equal to the width  $w_{\text{DC}}$ ). The model overestimates the simulated barrier height at large separations  $s_t$  close to the transition to regime III, where  $U_b$  is no longer defined. The sudden end of the simulated  $U_b$  data at  $s_t \approx 50 \mu\text{m}$  and  $s_t \approx 90 \mu\text{m}$  marks this transition point.

The fact that the double-well barrier  $U_b$  is to good approximation determined by the trap’s radial frequency  $\omega_x$  and inter-trap distance  $s_t$ , Eq. (8.3), reduces the parameter space for the trap optimization to trap efficiency and potential depth  $U_0$ . The degrees of freedom that can be varied are the three rail widths  $w_i$ ,  $w_o$  and  $w_{\text{DC}}$ . The optimization procedure is based on a full parameter scan and can be divided in two steps. In step 1, the electrode geometry is constrained to minimize the error function  $[(s_t - s_{t,\text{target}}) + (d - d_{\text{target}})]$ , where  $s_{t,\text{target}}$  and  $d_{\text{target}}$  are target values for the inter-trap distance and the ion-surface separation. In the second step, the remaining free parameter is varied to determine the optimal geometry. An example of step 1 is shown in Fig. 8.7. First, the target distance  $s_t = 100 \mu\text{m}$  (chosen in the previous section) is defined at full central RF voltage,  $\zeta = 1$ . The two rail widths  $w_{\text{DC}}$  and  $w_o$  are then scanned while the third width  $w_i$  is adjusted to set  $s_t$  to the target value. This is shown in (a) and (b). The ion-surface separation  $d$  for each geometry is shown in (c). For each geometry, the RF voltage ratio  $\zeta$  is then adjusted to set  $s_t$  to the second target value  $s_t = 50 \mu\text{m}$  for the configuration with reduced central RF voltage. This is shown in (d) and (e). The ion-surface separation  $d$  at reduced central RF is shown in (f). The values of  $d$  are practically identical to the configuration at unity RF ratio  $\zeta$ , shown

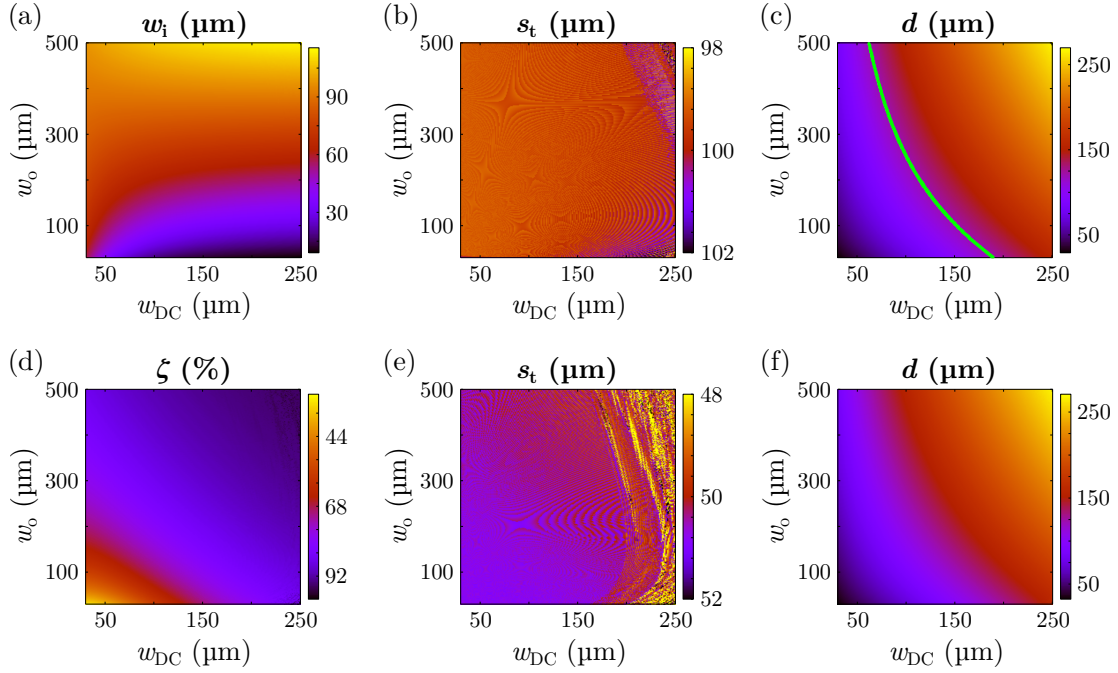


**Figure 8.7.** Optimization of the electrode geometry – Step 1. (a) The rail width  $w_i$  is adjusted for each set of widths  $w_{DC}, w_o$ , such that the trap distance is  $s_t = 100 \mu\text{m}$  within a tolerance of  $2 \mu\text{m}$  (b). The resulting ion-surface separation  $d$  is shown in (c). The green line highlights the  $d = 120 \mu\text{m}$  isoline. (d) Similarly, the RF ratio  $\zeta$  is adjusted for every geometry, such that  $s_t = 50 \mu\text{m}$  within a tolerance of  $2 \mu\text{m}$  (e). The resulting ion-surface separation  $d$  for reduced central RF voltage, shown in (f), is practically identical to (c), reflecting the earlier finding that  $d$  is approximately constant during RF shuttling. The fine grained structures visible in plots (b) and (e) are artifacts of the simulation related to the tolerances on the target values of  $s_t$ .

in (c). This is expected from the earlier finding, that the ion surface separation is constant during RF shuttling within regimes II and III, see Fig. 8.5 (c). Step 2 of the optimization procedure starts out by selecting all data from step 1 that lie on a specific ion-surface separation isoline  $d = \text{const}$ . The green line in Fig. 8.7 (c) illustrates this for the  $d = 120 \mu\text{m}$  isoline. The corresponding data are shown in Fig. 8.8. The values for the three rail widths along the isoline is given in (a). The secular frequency, (b), exhibits an optimum at  $w_o \approx 300 \mu\text{m}$ , which corresponds to optimal trap efficiency. The trap depth  $U_0$  shown in (c) peaks at slightly larger values  $w_o$ , but the dependence is quite weak such that the trap depth is almost optimal at  $w_o \approx 300 \mu\text{m}$ . The optimum for the double well barrier  $U_b$  (red line) also coincides with the secular frequency optimum, as expected from Eq. (8.3). Figs. 8.8 (d)-(f) show the corresponding quantities for the situation with reduced RF voltage. While the secular frequencies are in general lower than for  $\zeta = 1$ , the optimum is still at  $w_o \approx 300 \mu\text{m}$ . Also, the optimum for the trap depth  $U_0$  is not shifted significantly. This shows that the optimal geometry for an inter-

## 8. 2D linear trap array “Bucket-brigade”

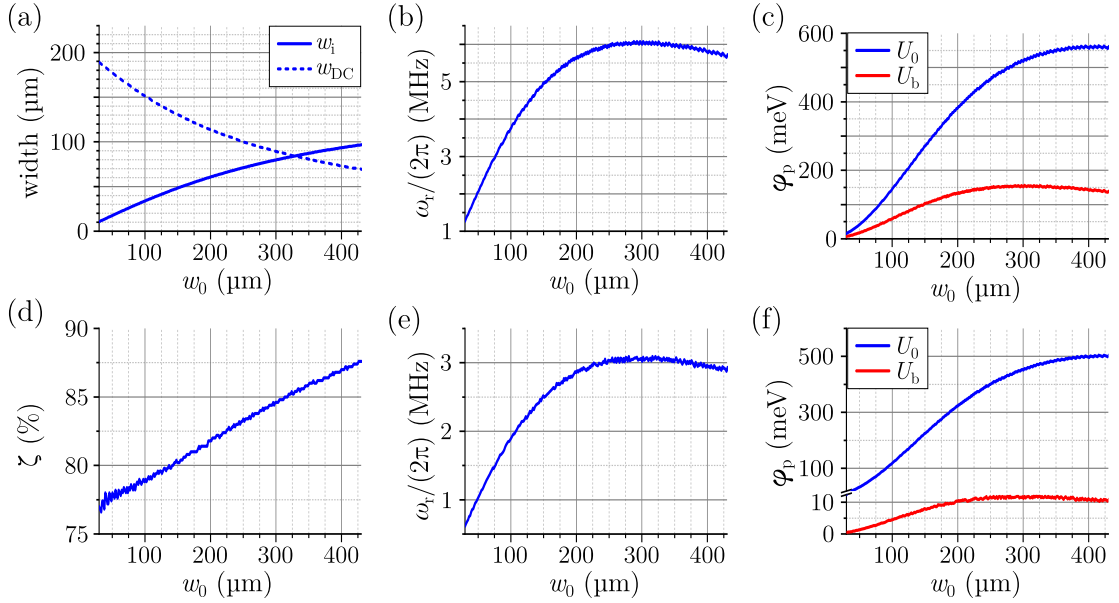


**Figure 8.8.** Optimization of the electrode geometry – Step 2. The data correspond to the  $d = 120 \mu\text{m}$  isoline highlighted in green in Fig. 8.7. The plots show trap parameters along the isoline for an RF voltage  $U_{\text{RF}} = 250 \text{ V}$  at a drive frequency of  $\Omega_{\text{RF}} = 2\pi \times 22 \text{ MHz}$ . (a) Electrode widths defining the trap geometry. (b) Radial frequencies  $\omega_r$  without RF attenuation on the central RF rail,  $\zeta = 1$ . (c) Trap depth  $U_0$  and double well barrier  $U_b$  for  $\zeta = 1$ . (d) Required RF voltage ratio  $\zeta$  to reduce the trap distance to  $s_t = 50 \mu\text{m}$ . The resulting radial frequencies  $\omega_r$ , trap depth  $U_0$  and well barrier  $U_b$  are shown in (e) and (f).

trap distance  $s_t = 100 \mu\text{m}$  at  $\zeta = 1$  is still nearly optimal for  $s_t = 50 \mu\text{m}$  at reduced RF, i. e., the entire RF shuttling process is optimized at once. Another interesting feature is that the RF ratio  $\zeta$  required to reduce the trap distance  $s_t$  to  $50 \mu\text{m}$  is closer to one with increasing width  $w_0$ . This can be intuitively understood by a stronger “pushing” effect on the trap minima by the RF fields from the outer RF rails.

The optimization procedure described above was applied to find an optimal geometry at two different ion-surface separations  $d = 80 \mu\text{m}$  and  $d = 120 \mu\text{m}$ , both with an inter-trap distance  $s_t = 100 \mu\text{m}$  at full RF ( $\zeta = 1$ ). For the  $d = 120 \mu\text{m}$  design, a geometry with  $w_{\text{DC}}$  slightly larger than the optimal parameter was chosen to make room for additional shield electrodes that reduce the RF pickup on the trap’s DC electrodes, further described in chapter 8.3. The final rail widths for the two fabricated designs are compiled together with all other geometrical trap parameters in Tab. 8.1 in the next section.

### 8.2.2. Axial multiwell confinement

This section describes the design of the DC electrodes necessary for axial confinement. The main idea is to segment each of the two DC rails into lines of island-like DC electrodes that are periodically connected directly on the trap chip. This allows one to create multiwell potentials along the two collinear trap axes with only a small number of DC channels, as introduced in section 8.1.2. A similar approach has been used to create a multiwell potential that periodically splits a long ion string [179]. In contrast to that work, the electrode periodicity in the BB traps is chosen such that translations of the multiwells along the trap axes are possible.

Fig. 8.9 gives an overview of the electrode geometry of the BB traps. The geometric parameters are compiled in Tab. 8.1. As seen in Fig. 8.9 (a), the BB traps have a central region, surrounded by four identical quadrants (NW, NE, SW, SE). For versatility, the multiwells in each quadrant can be controlled individually. The zoom-in, (b), shows the segmentation of the DC rails into individual island-like electrodes of length  $l_{DC}$ . Every third island electrode is connected to the same DC supply channel as illustrated by the different tones of blue. The resulting DC multiwell that creates axial confinement

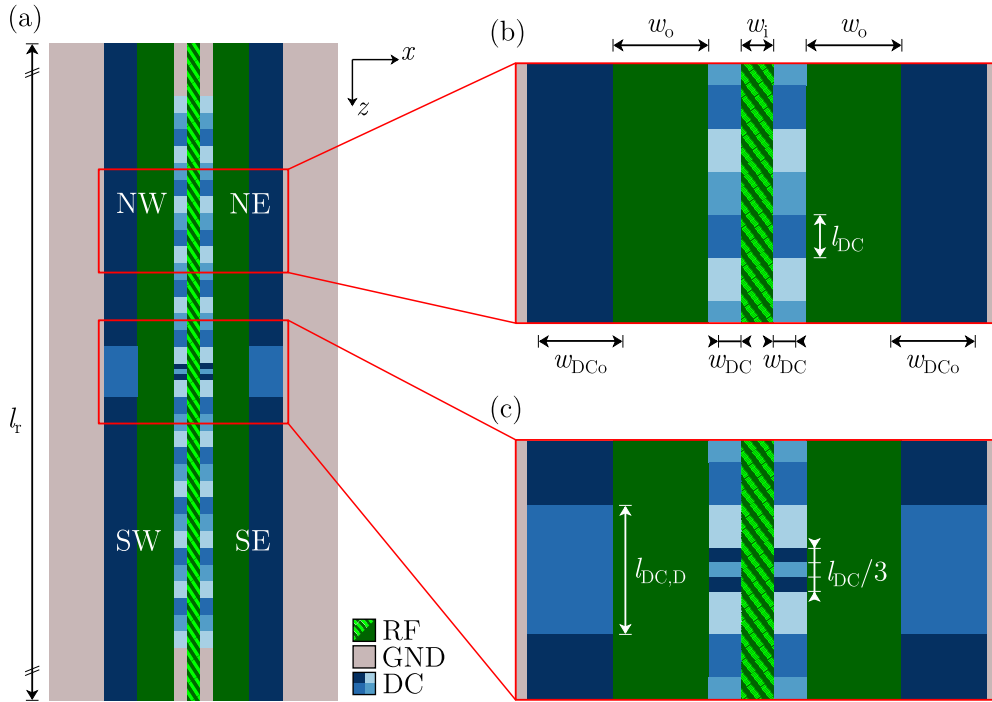


**Figure 8.9.** Electrode geometry of the BB traps. (a) Three collinear RF rails create radial confinement for two parallel linear traps. (b) Island-like DC electrodes of length  $l_{DC}$  are connected periodically as indicated by the different the tones of blue. The DC electrodes in the four trap quadrants (NW, NE, SW, SE) are connected independently. (c) In the axial interaction zone at the trap center the DC electrodes have a finer segmentation.

## 8. 2D linear trap array “Bucket-brigade”

**Table 8.1.** Geometric parameters of the BB trap designs with  $d = 80 \mu\text{m}$  and  $d = 120 \mu\text{m}$ . All values are in  $\mu\text{m}$ , apart from the number  $N_p$  of periodically repeating DC segments which is unitless.

| $d$        | $w_i$ | $w_o$ | $w_{\text{DC}}$ | $w_{\text{DC}o}$ | $l_r$ | $l_{\text{DC}}$ | $l_{\text{DC},\text{D}}$ | $N_p$ |
|------------|-------|-------|-----------------|------------------|-------|-----------------|--------------------------|-------|
| <b>80</b>  | 77    | 227   | 52              | 202              | 6000  | 102             | 306                      | 11    |
| <b>120</b> | 73    | 252   | 102             | 202              | 6000  | 102             | 306                      | 11    |

along the trap axis  $z$  thus has a lattice spacing of  $a_{\text{mw}} = 3l_{\text{DC}}$ . The additional outer DC electrodes with widths  $w_{\text{DC}o}$  (dark blue) are needed to overlap the two DC multiwells with their respective RF null. Two independent multiwells hence need a total of 8 DC channels for their operation. The length  $l_{\text{DC}} = 102 \mu\text{m}$  of the DC electrodes is a compromise: For smaller  $l_{\text{DC}}$ , the multiwell barrier  $U_{\text{mw}}$  that separates adjacent minima is decreased. For larger  $l_{\text{DC}}$ , the efficiency of the DC confinement goes down and the larger distance  $a_{\text{mw}}$  between trapping sites increases the required laser power of global beams illuminating the entire lattice. While the periodic connectivity of the DC islands drastically reduces the number of required DC channels, it also fixes the distance between adjacent trapping sites along the trap axes. For entangling operations along the  $z$ -direction, this distance needs to be reduced. This is possible in a dedicated axial interaction zone at the trap center, shown in Fig. 8.9 (c). Each of the two central DC islands is split into three segments of length  $l_{\text{DC}}/3$  and the outer DC rails have an independent segment of length  $l_{\text{DC},\text{D}}$ . The widths of the three central segments add up to  $l_{\text{DC}}$ . This allows one to extend the periodic DC pattern shown in (b) across the central region by setting the three central segments to the same voltage, which should facilitate seamless shuttling of the ions across the central region. The 35 individual DC segments along each DC rail can thus be grouped into  $N_p = 11$  periods of repeating DC voltages. This periodic configuration is employed for the remainder of this section.

The DC electrodes in the BB trap are designed to give independent control over the positions of the two multiwells in the left and right RF null. Furthermore, the axial frequencies  $\omega_z$  of the two multiwells can be adjusted independently. For the trapping sites *within* one multiwell (more specifically within one trap quadrant), independent micromotion compensation and adjustment of  $\omega_z$  is not possible due to the periodic connectivity of the DC segments. For the simulation of multiwell confinement and ion shuttling, an algorithm was developed that calculates voltage sets for axial confinement and micromotion compensation simultaneously at two arbitrary trapping positions  $\mathbf{r}_0^{(l)}$  and  $\mathbf{r}_0^{(r)}$  in the left and right RF null, respectively. This includes different axial trapping positions  $z_0^{(l)} \neq z_0^{(r)}$ . The voltage set for confinement at these two sites automatically creates additional sites with a spacing of  $a_{\text{mw}} = 3l_{\text{DC}}$  along the trap axes due to the

periodic connectivity of the DC segments. Necessary conditions for a trapping site at position  $\mathbf{r}_0$  are a vanishing axial electric field,  $E_z(\mathbf{r}_0) = 0$ , and a positive curvature,  $\partial_z^2\phi(\mathbf{r}_0) > 0$ . In addition,  $\mathbf{r}_0$  needs to be overlapped with the RF null, i. e.  $E_{x,y}(\mathbf{r}_0) = 0$ . The sets for micromotion compensation require control over the radial electric field components  $E_{x,y}(\mathbf{r}_0)$ . A shift of the trapping position along  $z$  can be realized by the axial field component  $E_z(\mathbf{r}_0)$ . This amounts to 8 field parameters (6 electric field components and 2 curvatures) for the two trapping sites at  $\mathbf{r}_0^{(l)}$  and  $\mathbf{r}_0^{(r)}$ . Let now  $\mathbf{b}$  be a vector of the desired 8 field parameters. Further, let  $\mathbf{x}$  be the unknown vector of voltages applied to the set of DC electrodes that produces  $\mathbf{b}$ . Then it holds  $\mathbf{b} = A\mathbf{x}$ , where the entries in the square matrix  $A$  are the contributions of the individual electrodes to the 8 field parameters. These entries are determined by simulating the electric potential when setting each of the DC electrodes in turn to 1 V, while grounding the rest of the trap. The unknown voltage set  $\mathbf{x}$  is then found by inversion of matrix  $A$ . This method only succeeds if  $A$  is of full rank, which requires at least 8 electrodes whose field and curvature contributions are linearly independent. Specifically, some of the DC electrodes need to be off the trap axis in order to create the necessary radial electric field components  $E_x, E_y$ . Fig. 8.10 shows the set of DC electrodes used for multiwell confinement in the BB traps. The set consists of three island electrodes below each RF null that repeat periodically along the  $z$ -axis plus two DC rails that are off-axis.

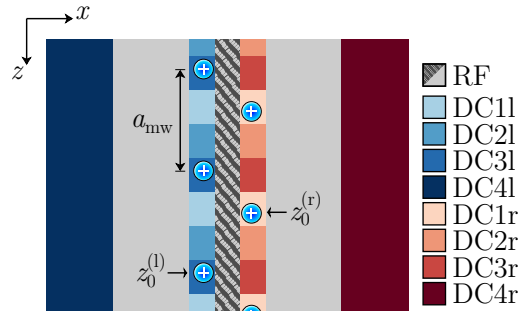


**Figure 8.10.** Set of DC electrodes for an independent translation of the left and right multiwell along the  $z$ -axis. Well locations in the left and right multiwells are given by the two well positions  $z_0^{(l)}$ ,  $z_0^{(r)}$ . The multiwell periodicity is  $a_{mw}$ .

For the default trap configuration, the same RF voltage is applied to the inner and outer RF rails,  $\zeta = 1$ . The DC multiwells in the left and right RF null are set to the same axial position,  $z_0^{(l)} = z_0^{(r)} = 0$ , and the voltage set for DC confinement is applied. The total confining potential  $\Phi$  in this “home” configuration is shown in Fig. 8.11, exemplarily for the trap design with ion-surface separation  $d = 120 \mu\text{m}$ . The potential for the  $d = 80 \mu\text{m}$  design is qualitatively identical. The trap parameters for both designs are listed in Tab. 8.2. The cross sections (a), (b), (c) in Fig. 8.11 show 18 individual

## 8. 2D linear trap array “Bucket-brigade”

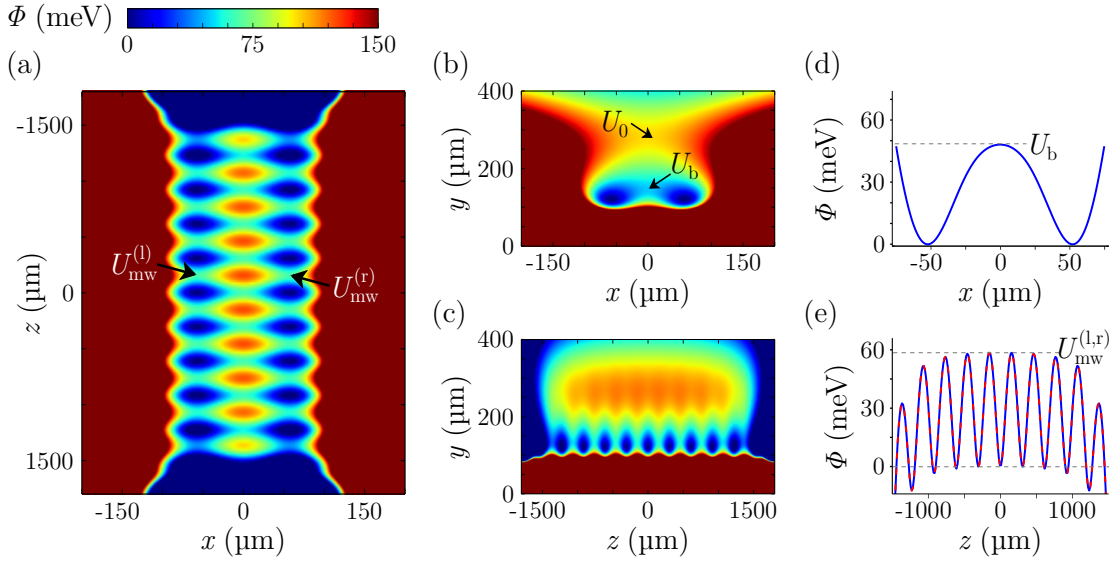


**Figure 8.11.** Trap confinement in the home configuration,  $z_0^{(l),(r)} = 0$ , with inter-trap distance  $s_t \approx 100 \mu\text{m}$  for the design with ion-surface separation  $d = 120 \mu\text{m}$ . Subplots (a), (b), (c) show cross sections of the total potential  $\Phi$  in the  $xz$ -,  $xy$ - and  $zy$ -plane, respectively, crossing the trapping site at  $r_0 = (-52.3, 121, 0) \mu\text{m}$ . The color scale is cut off at 150 meV. (d) Potential across the RF barrier between the two central trapping sites at  $x_0 = \pm 52.3 \mu\text{m}$ ,  $z_0 = 0$ . (e) Axial multiwell potential at  $x_0 = -52.3 \mu\text{m}$  (blue) and the identical potential at  $x_0 = 52.3 \mu\text{m}$  (dashed red). In all plots a DC offset field is subtracted from the data.

**Table 8.2.** Trap parameters in the home configuration,  $z_0^{(l),(r)} = 0$ , with  $s_t \approx 100 \mu\text{m}$  for the trapping site at  $x_0 = -s_t/2$ . The corresponding DC voltage sets for confinement and micromotion compensation are in Tab. B.1 in appendix B.1.

| $d$                                 | RF drive                    |        | secular freq.         |         | mode tilt     |       | trap depth            |         |
|-------------------------------------|-----------------------------|--------|-----------------------|---------|---------------|-------|-----------------------|---------|
| <b>120 <math>\mu\text{m}</math></b> | $U_{\text{RF}}$             | 142 V  | $\omega_z/(2\pi)$     | 1.0 MHz | $\vartheta_z$ | 0.00° | $U_0$                 | 102 meV |
|                                     | $\Omega_{\text{RF}}/(2\pi)$ | 23 MHz | $\omega_{r,1}/(2\pi)$ | 3.1 MHz |               |       | $U_b$                 | 48 meV  |
|                                     | $\zeta$                     | 1      |                       |         | $\vartheta_r$ | 41.2° | $U_{\text{mw}}^{(l)}$ | 59 meV  |
|                                     | $q$                         | 0.4    | $\omega_{r,2}/(2\pi)$ | 3.3 MHz |               |       | $U_{\text{mw}}^{(r)}$ | 59 meV  |
| <b>80 <math>\mu\text{m}</math></b>  | $U_{\text{RF}}$             | 118 V  | $\omega_z/(2\pi)$     | 1.0 MHz | $\vartheta_z$ | 0.00° | $U_0$                 | 134 meV |
|                                     | $\Omega_{\text{RF}}/(2\pi)$ | 36 MHz | $\omega_{r,1}/(2\pi)$ | 4.9 MHz |               |       | $U_b$                 | 99 meV  |
|                                     | $\zeta$                     | 1      |                       |         | $\vartheta_r$ | 15.7° | $U_{\text{mw}}^{(l)}$ | 53 meV  |
|                                     | $q$                         | 0.4    | $\omega_{r,2}/(2\pi)$ | 5.2 MHz |               |       | $U_{\text{mw}}^{(r)}$ | 53 meV  |

trapping sites, arranged in two columns along the two RF nulls. The potential  $\Phi$  is symmetric upon reflection at the  $xy$ - and  $zy$ -planes through the origin. An RF voltage of  $U_{\text{RF}} = 142 \text{ V}$  at  $\Omega_{\text{RF}} = 2\pi \times 23 \text{ MHz}$ <sup>6</sup> yields a stability  $q$ -factor of 0.4. The DC voltages for axial confinement (given in Tab. B.1 in appendix B.1.) are on the order of 1 V and give rise to an axial frequency  $\omega_z = 2\pi \times 1.0 \text{ MHz}$ . The DC confinement leads to a splitting of the radial frequencies,  $\omega_{r,1}, \omega_{r,2} = 2\pi \times (3.1, 3.3) \text{ MHz}$  and causes a tilt  $\vartheta_r = 41.2^\circ$  of the radial modes with respect to the vertical direction  $y$ , leading to almost equal laser cooling conditions for both radial modes, assuming laser beam propagation along the trap surface. The axial mode is aligned with the  $z$ -axis,  $\vartheta_z = 0$ . The 18 trapping sites are separated from each other by multiwell barriers  $U_{\text{mw}}^{(l)} = U_{\text{mw}}^{(r)}$  along the axial direction and the RF barrier  $U_b$  along the  $x$ -direction. These three potential barriers constitute local trap depths. The barrier  $U_0$  defines the global trap depth for ions in radial direction. All four barriers are well above the average kinetic energy  $E_{\text{th}} \approx 26 \text{ meV}$  of thermal gas molecules at room-temperature. Loading of ions and trap operation in a cryogenic environment or even at room temperature should therefore be possible.

The trapping sites' parameters are quite uniform across the multiwells. Existing deviations between the sites mainly result from the finite number of DC segments which causes DC fields calculated for the central sites to be non-ideal for sites at the trap edges. The secular frequencies at the outermost sites at  $z = \pm 1227 \mu\text{m}$  are shifted by around 10 kHz relative to the values at the central sites at  $z = 0$ . The radial mode tilt is slightly reduced at the outermost sites to  $\vartheta_r = 36.6^\circ$  while a small axial mode tilt  $\vartheta_z = 0.6^\circ$  is present. The trap depths  $U_0$  and  $U_{\text{mw}}$  are reduced by about 25 %, still well above thermal energies. The outermost trapping sites are also displaced from the RF null by about  $0.6 \mu\text{m}$ , giving rise to an acceptable level of excess micromotion: The RF electric field in the  $xz$ -plane of the laser beams has a magnitude of  $E_{\parallel} \approx 700 \text{ V m}^{-1}$ . The impact of this field on the trapping performance can be estimated by calculating the corresponding micromotion modulation index  $\beta$  at the 729 nm transition, see Eq. (7.4). For the resulting value of  $\beta \approx 0.7$ , trapping and even resolved sideband operations are still possible, see chapter 7.3.1. Part of the micromotion is actually caused by the axial RF field component  $E_z \approx 250 \text{ V m}^{-1}$ , which is non-zero at these outermost sites due to the finite lengths of the RF rails. For the trap design with  $d = 80 \mu\text{m}$ , the edge effects are comparable or even smaller. In particular the displacement of the outermost sites from the RF null is only about  $0.1 \mu\text{m}$  leading to a significantly smaller modulation

<sup>6</sup> The RF drive parameters are chosen in the following way. First, a maximally applicable RF voltage of  $U_{\text{RF}} = (300 - 400) \text{ V}$  is assumed (cf. section 8.3.2). In the configuration with reduced RF voltage on the inner RF rail, where the trap efficiency is decreased, the drive frequency  $\Omega_{\text{RF}}$  is then set to yield a stability factor of  $q = 0.4$  (cf. Tab. 8.3 in section 8.2.4). Keeping  $\Omega_{\text{RF}}$  constant, the RF voltage  $U_{\text{RF}}$  is then adjusted to achieve  $q = 0.4$  in the home configuration.

## 8. 2D linear trap array “Bucket-brigade”

index  $\beta \approx 0.1$ . If necessary, the edge effects could be reduced in future trap designs by an increased number of DC segments and an elongation of the RF rails.

Electric stray fields from the chip surface are also expected to shift ions off the RF null. It should be emphasized that stray fields with spatial variations along the extent of the multiwell cannot fully be compensated. The periodic connectivity of the DC island electrodes only allows for global compensation fields within each trap quadrant. A stray field of  $E_{\text{stray}} = 100 \text{ V m}^{-1}$  in radial direction would shift ions with radial frequencies  $\omega_r = 2\pi \times 4 \text{ MHz}$  by about  $0.4 \mu\text{m}$ . This is comparable to the shift of the outermost site due to edge effects discussed above. Typical values of stray fields in surface traps with similar ion-surface separation are ranging from a few tens to a few hundred  $\text{V m}^{-1}$  [99, 139]. Stray fields with spatial variation might consequently cause problems for the simultaneous operation of all trapping sites. In future designs, the number of compensation electrodes should therefore be increased.

In summary, both trap designs ( $d = 120 \mu\text{m}$  and  $d = 80 \mu\text{m}$ ) show similar results for the home configuration: All 18 trapping sites have standard secular frequencies of a few MHz, allow cooling of all motional modes and have trap depths typical for surface traps. Micromotion can in principle be compensated at all trapping sites, but only for one site per trap quadrant at a time, due to the periodic connectivity of the DC electrodes.

### 8.2.3. Lattice reconfiguration

The lattice reconfiguration processes introduced in section 8.1.2 require independent shuttling of the left and right multiwells relative to each other. In the BB trap design, these operations are realized using the principle of BB shuttling. The feasibility of the approach is demonstrated in this section by characterizing the trap performance at different multiwell positions across the entire parameter space  $z_0^{(l)}, z_0^{(r)} \in [-a_{\text{mw}}/2, +a_{\text{mw}}/2]$ , where  $z_0^{(l)}$  and  $z_0^{(r)}$  are the positions of the left and right multiwell, respectively, and  $a_{\text{mw}}$  is the multiwell lattice constant (cf. Fig. 8.10). Any trajectory through this parameter space corresponds to a specific shuttling process. The simulation of such a wide range of control parameters has the advantage that promising trajectories, for instance those with a minimal variation in axial frequency, can be quickly identified. However, the approach does not deliver a time-dependent voltage sequence that implements a specific temporal dependence  $z_0^{(l)}(t), z_0^{(r)}(t)$  of the well positions. Such voltage sequences can be engineered in various ways. Typically, the aim is to maintain low motional excitation during the shuttling (adiabatic transport) [180, 181] or to cancel excitations at the end of the sequence (diabatic transport) [40–43]. The full parameter scan presented here may serve as a starting point for such advanced algorithms.

By implementing the method of BB shuttling in the BB trap design, one can realize independent translations of the left and right multiwells with only 8 DC control voltages, applied to the 8 DC electrodes in Fig. 8.10. DC voltage sets for confinement at well positions  $z_0^{(l)}, z_0^{(r)} \in [-a_{\text{mw}}/2, +a_{\text{mw}}/2]$  are calculated by employing the algorithm for multiwell confinement, described in the previous section. For each set of positions, the axial frequencies are set to a constant nominal value  $\omega_z^{(l)} = \omega_z^{(r)} = 2\pi \times 1 \text{ MHz}$ . Fig. 8.12 shows the resulting DC voltages and trapping parameters of the central sites for the different multiwell positions for the  $d = 120 \mu\text{m}$  design. All site-specific quantities, for instance the actual axial frequency  $\omega_z$  shown in (a), are given for the central left trapping site only. The corresponding data for the right site are identical upon mirroring the plots at the bottom left to top right diagonal due to the trap's mirror symmetry. Similarly, the voltage plot for the DC11 electrode (i) contains all information for the other island electrodes. The data for adjacent electrodes are given by shifting the plot coordinates by  $l_{\text{DC}} = a_{\text{mw}}/3$  along both the abscissa and the ordinate (translational symmetry). For all positions  $z_0^{(l)}, z_0^{(r)}$ , the axial frequency (a) maintains the setpoint value  $\omega_z = 2\pi \times 1 \text{ MHz}$  within 10 kHz<sup>7</sup>. The strongest deviations are seen when both sites are located above edges between electrodes, i. e.,  $z_0^{(l,r)} \approx \pm a_{\text{mw}}/6, \pm a_{\text{mw}}/2$ , without mirror symmetry,  $z_0^{(l)} \neq z_0^{(r)}$ . In these regions, the applied DC voltage set for confinement starts to tilt the axial mode relative to the  $x$ -axis, as seen by maxima of the tilt angle  $\vartheta_z$  in (e). Upon raising the axial frequency setpoint by scaling the DC voltage set, this tilt is over-proportionally increased, which limits the maximally obtainable axial frequency to  $\omega_z \approx 2\pi \times 1.6 \text{ MHz}$ <sup>8</sup>. At positions with  $\vartheta_z = 0^\circ$ , this restriction does not apply. The radial modes (b), (c) show a variation of about 10 % across the full parameter space with a minimum mode splitting of  $\Delta\omega_r = \omega_{r,2} - \omega_{r,1} \approx 2\pi \times (150 - 200) \text{ kHz}$  on the diagonal  $z_0^{(l)} = z_0^{(r)}$  and up to  $\Delta\omega_r \approx 2\pi \times 600 \text{ kHz}$  otherwise. The variation of the radial mode tilt (d) relative to the surface normal follows this pattern with maximal tilts  $\vartheta_r \approx 40^\circ$  on the diagonal  $z_0^{(l)} = z_0^{(r)}$  and values down to  $\vartheta_r \approx 30^\circ$  otherwise. The RF barrier  $U_b$  and global trap depth  $U_0$  shown in (f) and (h) have similar variation patterns. The depths range within  $U_b \approx (48 - 60) \text{ meV}$ ,  $U_0 \approx (98 - 128) \text{ meV}$  with minimal values on the diagonal  $z_0^{(l)} = z_0^{(r)}$ . The multiwell barrier, (g), varies within  $U_{\text{mw}} \approx (50 - 78) \text{ meV}$ . The maxima of  $U_{\text{mw}}^{(l)}$  are reached at  $z_0^{(l)} \approx \pm a_{\text{mw}}/6, \pm a_{\text{mw}}/2$ , with little dependence on  $z_0^{(r)}$ , i. e.  $U_{\text{mw}}^{(l)}$  is maximal when the left multiwell sites are positioned above edges between electrodes. These electrodes then effectively form a single electrode with twice the length thus boosting the well depth. Finally, the DC voltages shown in (i), (j) are

<sup>7</sup> The deviations of  $\omega_z$  from the setpoint can be reduced iteratively by using the simulation result to rescale the voltage set for axial confinement. After one additional iteration, the deviations are well below 1 kHz.

<sup>8</sup> A larger maximal value of  $\omega_z$  can be achieved by raising the RF confinement.

## 8. 2D linear trap array “Bucket-brigade”

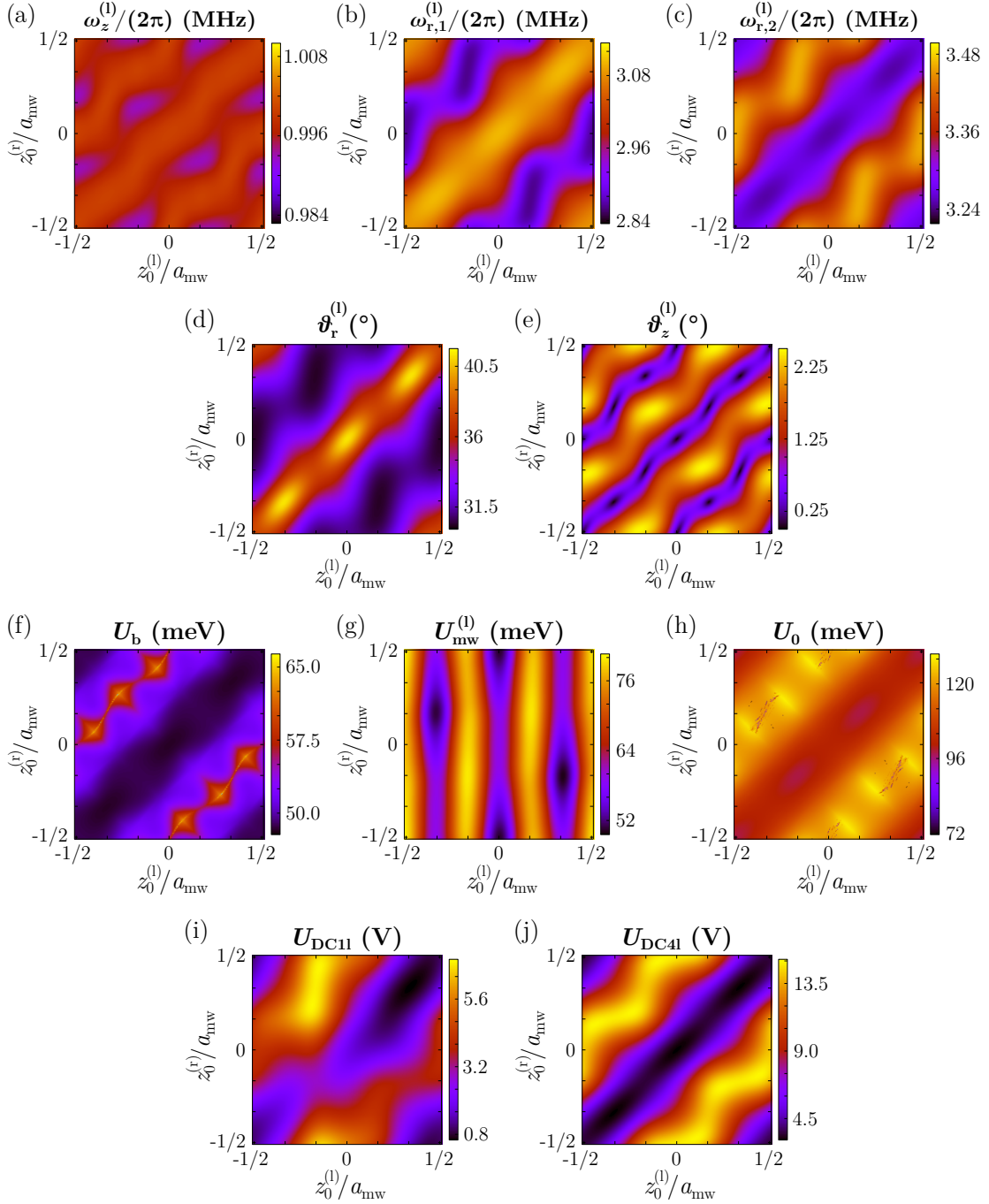


**Figure 8.12.** Bucket-brigade shuttling for the design with  $d = 120 \mu\text{m}$  ion-surface separation. The varied parameters are the positions  $z_0^{(l)}$ ,  $z_0^{(r)}$  of the left and right multiwell, respectively. Subplots (a)-(c) show the secular frequencies of the central left trapping site, (d) the tilt of the radial modes with respect to the vertical direction  $y$  and (e) the tilt of the axial mode with respect to the  $z$ -axis. Subplots (f)-(g) show the RF and multiwell potential barriers and the trap depth. The applied DC voltages are shown in (i) and (j). The RF drive parameters are the same as those in Tab. 8.2.

on the order of (1 - 10) V. Many patterns in the trap parameters discussed above can be traced back to patterns in the DC voltage variation. The most striking example is the maximum in radial mode splitting coinciding with positions of maximal DC voltage.

While the simulated trap parameters are in general rather homogeneous across the entire parameter space, there exist regions, where the parameter variations become maximal. Crossing these regions during a shuttling process might lead to undesired effects. For instance, variation of a given motional frequency during adiabatic shuttling can induce heating of the corresponding mode. Rapid changes in mode tilt can lead to mixing of mode populations. A large axial mode tilt makes this mode susceptible to electric field noise on the RF rails or to common mode fluctuations of all trap electrodes. Furthermore, the maximal rate of voltage change might be limited by the bandwidth of DC filters. The data in Fig. 8.12 allow one to optimize shuttling processes by choosing parameter space trajectories that avoid regions of maximal parameter variation. For example, during a lattice reordering operation one might want to shift the left multiwell by one lattice period  $a_{\text{mw}}$  relative to the right multiwell. The naive approach would be, to vary  $z_0^{(l)}$  by  $a_{\text{mw}}$  while keeping  $z_0^{(r)}$  at a fixed position, e. g.  $z_0^{(r)} = -a_{\text{mw}}/6$ . The corresponding parameter space trajectory is a horizontal line in the graphs in Fig. 8.12, which crosses twice the regions of maximal axial mode tilt, (e). These regions can be circumvented by slightly adjusting the right multiwell position  $z_0^{(r)}$ , leading to a more curved trajectory in parameter space.

Up to this point, only the parameters of the central trapping sites have been considered. Edge effects at the outer trapping sites are analyzed in the extreme configuration, where the two multiwells are shifted by  $a_{\text{mw}}/2$  relative to each other. In this configuration, shown in Fig. 8.13, confinement is maintained in 15 trapping sites. The trapping parameters across these sites are relatively homogeneous. Strong edge effects are only found at the outermost sites on the left (right) side at  $z_0 = 1238 \mu\text{m}$  ( $1077 \mu\text{m}$ ). These sites are shifted radially by  $2.5 \mu\text{m}$  ( $1.2 \mu\text{m}$ ), resulting in a strong micromotion modulation index  $\beta \approx 2.9$  (1.6). The secular frequencies are shifted by more than 200 kHz radially and more than 100 kHz axially, relative to the sites at the trap center. More problematic is, however, the very small trap depth  $U_0 \approx 10 \text{ meV}$ , which might lead to loss of ions at the outermost sites during a multiwell shuttling process. For the inner 13 sites with positions  $|z_0| < 900 \mu\text{m}$ , the edge effects are considerably reduced and comparable to those in the home configuration. The secular frequencies vary by only 2% across these sites, the radial mode tilt  $\vartheta_r$  changes by about  $3^\circ$  and the axial mode tilt  $\vartheta_z$  stays below  $0.7^\circ$ . While the well barriers get more shallow towards the edges of the trap, they always maintain reasonable values,  $U_b, U_{\text{mw}}^{(l)}, U_{\text{mw}}^{(r)} \gtrsim 40 \text{ meV}$  and  $U_0 > 60 \text{ meV}$ . Furthermore, these inner 13 sites have maximal radial shifts of  $0.7 \mu\text{m}$ , leading to modulation indices  $\beta < 1$ , which should still be sufficiently small for resolved

## 8. 2D linear trap array “Bucket-brigade”

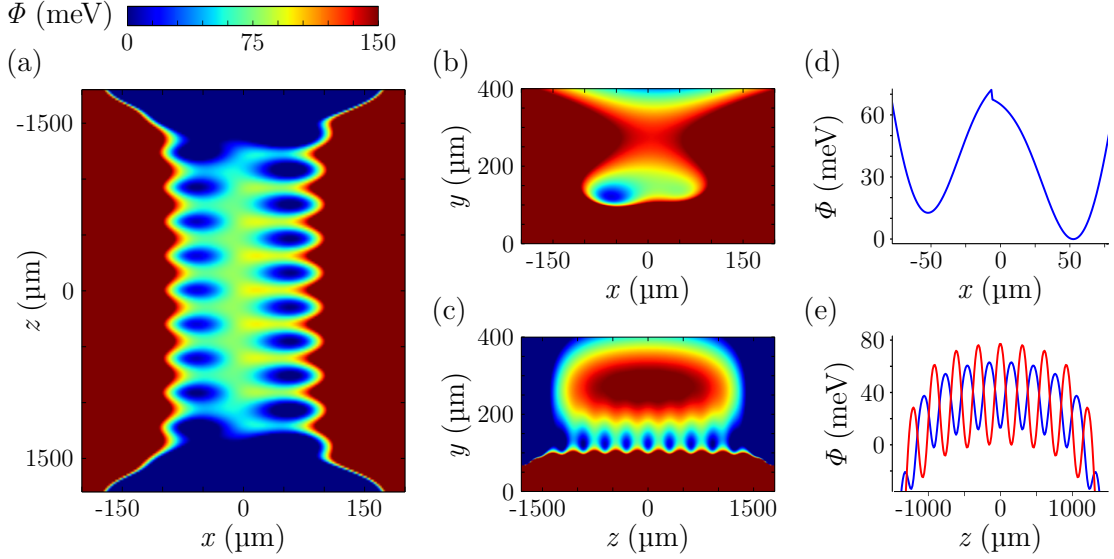


**Figure 8.13.** Trap confinement with the right multiwell shifted by  $a_{\text{mw}}/2$  relative to the home configuration for the  $d = 120 \mu\text{m}$  design. Subplots (a), (b), (c) show cross sections of the total potential  $\Phi$  in the  $xz$ -,  $xy$ - and  $zy$ -plane, respectively, crossing the trapping site at  $r_0 = (-52.3, 121, 0) \mu\text{m}$ . (d) Potential across the RF barrier between the two central trapping sites at  $x_0, z_0 = (-52.3, 0) \mu\text{m}$  and  $x_0, z_0 = (+52.3, -153) \mu\text{m}$ . (e) Axial multiwell potential at  $x_0 = -52.3 \mu\text{m}$  (blue) and  $x_0 = 52.3 \mu\text{m}$  (red). In all plots a DC offset field is subtracted from the data.

sideband operations. This might be useful for the implementation of single qubit transfer gates, where the state of an ions are coherently manipulated by shuttling through a stationary laser beam [44].

For the  $d = 80 \mu\text{m}$  design, the characterization of the BB shuttling process shows qualitatively identical results. Quantitatively, this design has a significantly increased homogeneity of the trapping site across the multiwells. Most strikingly is the possibility to maintain 19 trapping sites in the configuration where one multiwell is shifted by  $a_{\text{mw}}/2$ . All sites in this configuration, including the outermost sites, remain well confined with well barriers above 30 meV. Furthermore, the maximal radial shift of the sites is only  $0.7 \mu\text{m}$ , with a corresponding micromotion modulation index  $\beta \approx 0.5$ .

In summary, the BB shuttling process allows one to shift the left and right multiwells independently of each other across a full lattice period  $a_{\text{mw}}$ . The process characterization with the simulation of the entire range of multiwell positions can be used as starting point for further optimization of shuttling sequences, for instance to minimize motional heating of a mode that is used for gate operations. Variations in trapping parameters across the different trapping sites remain moderate during multiwell shuttling. Strong edge effects are only found at the outermost sites. The  $d = 80 \mu\text{m}$  design has smaller edge effects than the  $d = 120 \mu\text{m}$  design due to its smaller ion-surface separation. It

is worth mentioning that the concept of BB shuttling and the lattice reordering operations described here do not necessarily need island-like DC electrodes but can also be realized with meander-shaped electrodes that can be connected on the top metal layer. The characterization of the shuttling process with such a structure is shown in appendix B.2. Island-like electrodes were favored for the BB traps due to potentially easier controllable shuttling sequences and the availability of a multilayer fabrication process at Infineon that allows one to connect such electrodes.

#### 8.2.4. RF shuttling

Entanglement between ions in the left and right multiwells, i. e. across the RF barrier  $U_b$ , requires a reduced trap distance  $s_t$  along the  $x$ -direction. This is achieved by reducing the RF voltage ratio  $\zeta$ , Eq. (8.1). During such RF shuttling operations, the axial positions of the left and right multiwells are fixed at  $z_0^{(l)} = z_0^{(r)} \equiv z_0$ . The simulation of RF shuttling in the BB traps is shown in Fig. 8.14, exemplary for the  $d = 120 \mu\text{m}$  design. The multiwells' position  $z_0$  is varied over one period  $a_{\text{mw}}$  for different distances  $s_t \in [100 - 30] \mu\text{m}$  between the RF nulls. The foremost result is that the axial multiwell confinement can be preserved for all trap distances  $s_t$ . The axial frequency, (a), is maintained at the setpoint  $\omega_z = 2\pi \times 1.0 \text{ MHz}$  across the entire parameter space with maximal deviations of  $0.3 \text{ kHz}$ <sup>9</sup>. The strongest deviations coincide with positions of maximal axial mode tilt  $\vartheta_z \approx \pm 0.45^\circ$  shown in (e), as is the case in the BB shuttling process described in the previous section. Similarly, the multiwell barriers  $U_{\text{mw}}^{(l)} = U_{\text{mw}}^{(r)}$ , (h), are practically independent of the trap distance  $s_t$ , but show variations with  $z_0$  in the range  $U_{\text{mw}} \approx (60 - 80) \text{ meV}$ . The DC voltages, (j) and (k), required to create the multiwells, are on the order of a few volts. Slightly smaller voltages are required at smaller trap distances  $s_t$ . Regarding RF properties, the trap's stability factor  $q = 0.4$  is kept constant for all separations  $s_t$ , leading to practically constant radial frequencies, (b) and (c). The radial mode splitting has a slight dependence on  $z_0$ , with maximal variations of about  $20 \text{ kHz}$  and the radial mode tilt, (d), decreases from  $\vartheta_r \approx 40^\circ$  at  $s_t = 100 \mu\text{m}$  to  $\vartheta_r \approx 7^\circ$  at  $s_t = 30 \mu\text{m}$ . The RF barrier  $U_b$ , (g), goes down with decreasing  $s_t$ , as expected from Eq. (8.3). In contrast, the trap depth  $U_0$  shown in (i) is strongly increased up to  $U_0 \approx 1 \text{ eV}$  at  $s_t = 30 \mu\text{m}$ . This increase is explained by the decreasing efficiency to maintain two RF minima at small distances  $s_t$ : The RF voltage, (l), required for a stability factor  $q = 0.4$  increases up to  $U_{\text{RF}}^{(o)} = 500 \text{ V}$  at  $s_t = 30 \mu\text{m}$ . This large RF voltage boosts the trap depth  $U_0$  at the RF saddle position above the RF null. The red line in (l) shows the variation of the RF voltage ratio,  $\zeta \in [1, 0.78]$ ,

<sup>9</sup> The deviations of  $\omega_z$  from the setpoint can again be reduced iteratively by using the simulation result to rescale the voltage set for axial confinement.

## 8. 2D linear trap array “Bucket-brigade”

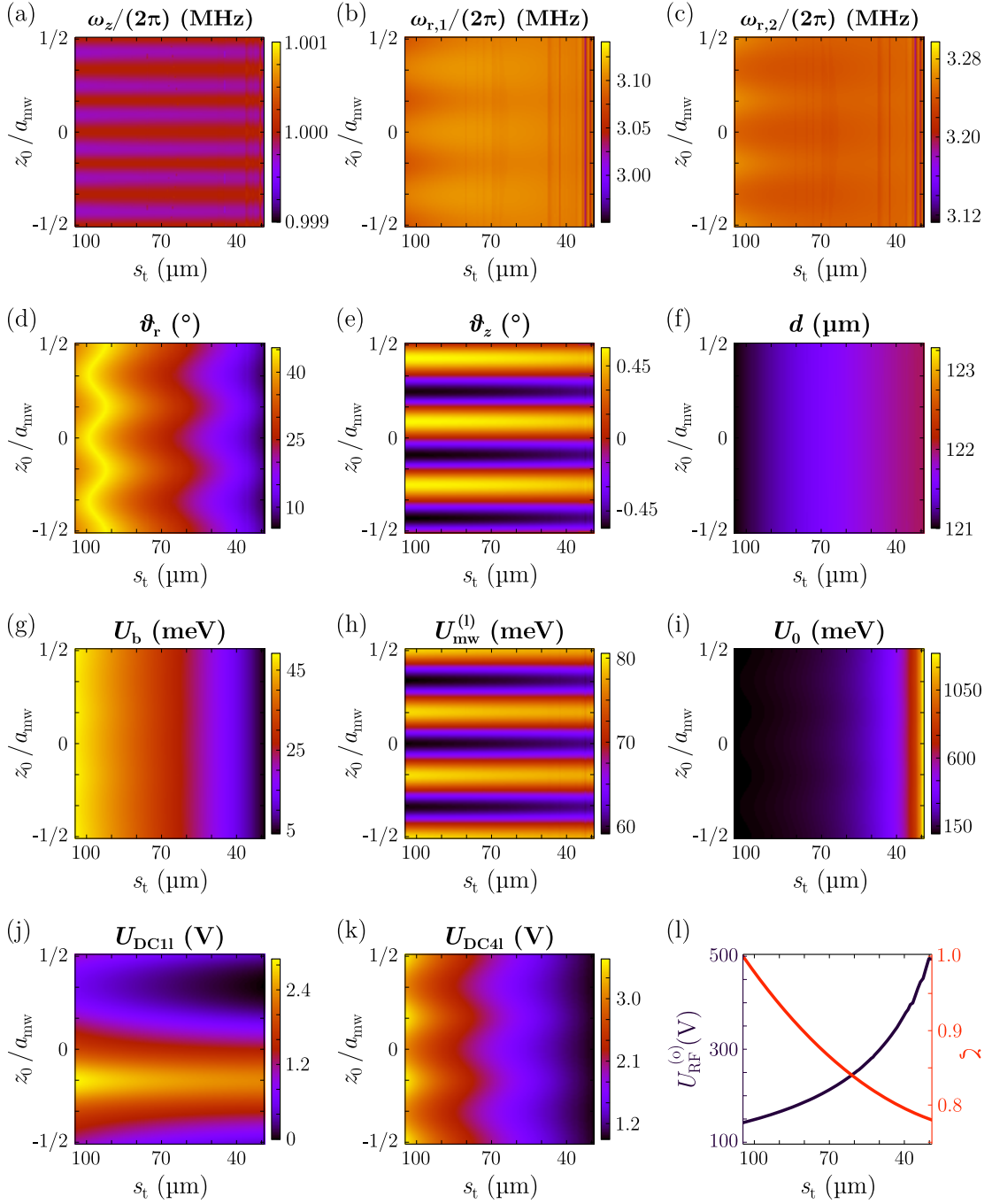


**Figure 8.14.** Simulation of the RF shuttling process used to reduce the distance  $s_t$  between the RF two nulls. The parameters varied are  $s_t$  and the position  $z_0$  of both multiwells. Subplots (a)-(c) show the secular frequencies of the central trapping sites, (d) the tilt of the radial modes with respect to the vertical direction  $y$  and (e) the tilt of the axial mode with respect to the  $z$ -axis. The variation in ion-surface separation  $d$  is shown in (f). Subplots (g)-(i) show the RF and multiwell potential barrier and the trap depth. The required DC voltages are shown in (j) and (k). (l) shows the RF voltage  $U_{\text{RF}}^{(o)}$  on the outer RF rail (black) and the RF ratio  $\zeta$  (red), which are independent of the axial multiwell position  $z_0$ .

corresponding to the different trap separations  $s_t$ . The characterization of RF shuttling in the  $d = 80 \mu\text{m}$  design shows qualitatively identical results. The largest difference is that the maximal radial mode tilt  $\vartheta_r \approx 45^\circ$  occurs at intermediate trap distances  $s_t \approx (60 - 70) \mu\text{m}$ .

The expected motional coupling across the RF barrier can be calculated at different inter-trap separations  $s_t$  using Eq. (3.4). The coupling is strongest for the axial mode, which has the smallest frequency of all secular modes. For the choice of  $s_t$ , one has to consider several, conflicting requirements. On the one hand, the coupling rate  $\Omega_c$  is increased with decreasing separation  $s_t$ . On the other hand, a decreasing  $s_t$  leads to a decreased pseudo potential barrier  $U_b$  and a growing value of the required RF voltage  $U_{\text{RF}}$ . A viable compromise is found for a separation  $s_t = 40 \mu\text{m}$ , at which the motional coupling rate  $\Omega_c = 2\pi \times 1.38 \text{ kHz}$  can be achieved for an axial frequency  $\omega_z = 2\pi \times 1 \text{ MHz}$ . The trap confinement in this “reduced RF” configuration, is shown in Fig. 8.15, exemplary for the  $d = 120 \mu\text{m}$  design. The potential for the  $d = 80 \mu\text{m}$  design is qualitatively identical. The trap parameters for both designs are listed in Tab. 8.3. The cross sections (a), (b), (c) in Fig. 8.15 show the 18 individual trapping sites with a trap separation  $s_t \approx 40 \mu\text{m}$ . The RF double well potential, (d), is well defined with a radial barrier of  $U_b = 8.5 \text{ meV}$ , in good agreement with the prediction of the double-well

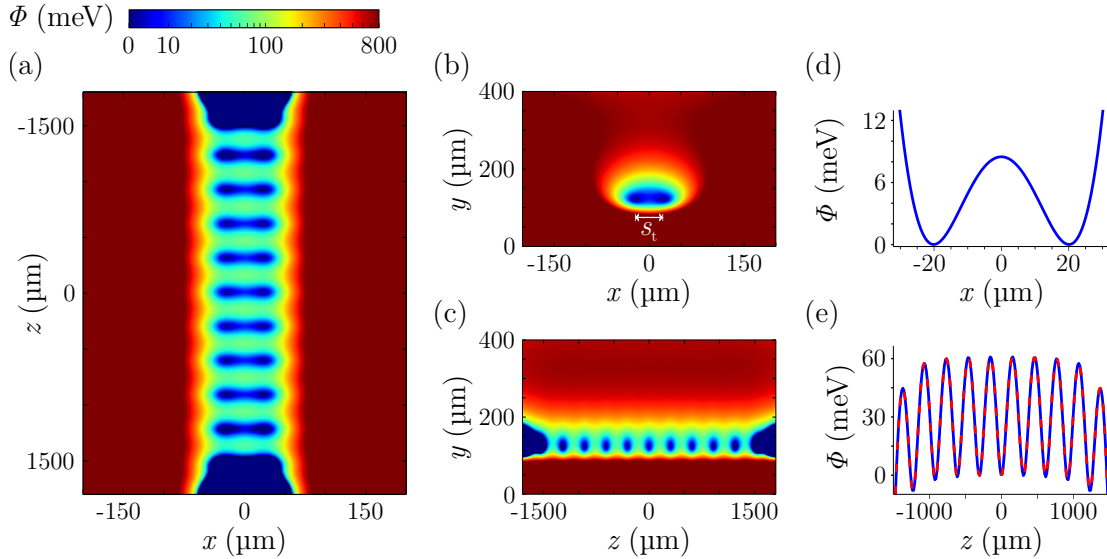


**Figure 8.15.** Trap confinement in the reduced RF configuration with  $s_t \approx 40 \mu\text{m}$  for the  $d = 120 \mu\text{m}$  design. Subplots (a), (b), (c) show cross sections of the total potential  $\Phi$  in the  $xz$ -,  $xy$ - and  $zy$ -plane, respectively, crossing the trapping site at  $r_0 = (-20.1, 121, 0) \mu\text{m}$ . The color scale is non-linear for better visibility of the minima. (d) Potential across the RF barrier between the two central trapping sites at  $x_0 = \pm 20.1 \mu\text{m}$ ,  $z_0 = 0$ . (e) Axial multiwell potential at  $x_0 = -20.1 \mu\text{m}$  (blue) and the identical potential at  $x_0 = 20.1 \mu\text{m}$  (dashed red). In all plots a DC offset field is subtracted from the data.

## 8. 2D linear trap array “Bucket-brigade”

**Table 8.3.** Trap parameters in the reduced RF configuration,  $s_t = 40 \mu\text{m}$ , at the position of the central left minimum at  $x_0 = -s_t/2, z_0 = 0$ . The corresponding DC voltage sets for confinement and micromotion compensation are in Tab. B.2 in appendix B.1.

| $d$                                 | RF drive                    |        | secular freq.         |         | mode tilt     |       | trap depth            |         |
|-------------------------------------|-----------------------------|--------|-----------------------|---------|---------------|-------|-----------------------|---------|
| <b>120 <math>\mu\text{m}</math></b> | $U_{\text{RF}}^{(o)}$       | 372 V  | $\omega_z/(2\pi)$     | 1.0 MHz | $\vartheta_z$ | 0.00° | $U_0$                 | 702 meV |
|                                     | $\Omega_{\text{RF}}/(2\pi)$ | 23 MHz | $\omega_{r,1}/(2\pi)$ | 3.1 MHz |               |       | $U_b$                 | 8.5 meV |
|                                     | $\zeta$                     | 0.796  |                       |         | $\vartheta_r$ | 10.2° | $U_{\text{mw}}^{(l)}$ | 61 meV  |
|                                     | $q$                         | 0.4    | $\omega_{r,2}/(2\pi)$ | 3.3 MHz |               |       | $U_{\text{mw}}^{(r)}$ | 61 meV  |
| <b>80 <math>\mu\text{m}</math></b>  | $U_{\text{RF}}^{(o)}$       | 316 V  | $\omega_z/(2\pi)$     | 1.0 MHz | $\vartheta_z$ | 0.00° | $U_0$                 | 531 meV |
|                                     | $\Omega_{\text{RF}}/(2\pi)$ | 36 MHz | $\omega_{r,1}/(2\pi)$ | 5.0 MHz |               |       | $U_b$                 | 20 meV  |
|                                     | $\zeta$                     | 0.708  |                       |         | $\vartheta_r$ | 13.3° | $U_{\text{mw}}^{(l)}$ | 57 meV  |
|                                     | $q$                         | 0.4    | $\omega_{r,2}/(2\pi)$ | 5.1 MHz |               |       | $U_{\text{mw}}^{(r)}$ | 57 meV  |

model, Eq. (8.3). Due to the decreased efficiency of the trap, the RF voltage required for a stability factor of  $q = 0.4$  is increased to  $U_{\text{RF}}^{(o)} = 372 \text{ V}$  on the outer RF rail. This significantly improves the trap depth to  $U_0 = 702 \text{ meV}$ . Secular frequencies are basically identical to the home configuration with  $\omega_{r,1}, \omega_{r,2} = 2\pi \times (3.1, 3.3) \text{ MHz}$  and  $\omega_z = 2\pi \times 1.0 \text{ MHz}$  at the trap center. The DC voltages remain on the order of 1 V, the multiwell barrier  $U_{\text{mw}}$  is practically unchanged and the axial mode remains aligned with the  $z$ -axis,  $\vartheta_z = 0$ . The radial mode tilt is reduced to  $\vartheta_r = 10.2^\circ$ .

The homogeneity of the 18 trapping sites is comparable to that in the home configuration. A notable difference is a slight increase in the inter-trap separation to  $s_t \approx 43 \mu\text{m}$  at the outermost sites, which is caused by the finite length of the RF rails. The larger separation leads to a decrease in coupling strength to  $\Omega_c \approx 2\pi \times 1.1 \text{ kHz}$  at the outermost trapping sites. In any case, parallelized entangling operations on all sites seem unrealistic, given the fact that stray charges morphing the trap curvatures cannot be compensated for all 18 trapping sites simultaneously. Both problems could be circumvented by entangling the sites sequentially. As for the home configuration, the edge effects are weaker in the  $d = 80 \mu\text{m}$  design.

In summary, lowering the RF voltage ratio  $\zeta$  in the BB trap leads to a reduction of the distance  $s_t$  between the two RF nulls, while maintaining the axial multiwell confinement for all 18 trapping sites. This allows one to couple the motion of two single ions confined in the left and right multiwells, respectively. A coupling rate  $\Omega_c \gtrsim 2\pi \times 1 \text{ kHz}$  can be achieved across the RF barrier at a distance  $s_t = 40 \mu\text{m}$  and axial frequency  $\omega_z = 2\pi \times 1 \text{ MHz}$ . The individual trapping sites at this distance remain well defined with double well barriers  $U_b \gtrsim 8 \text{ meV}$ . The distance reduction to  $s_t = 40 \mu\text{m}$  requires lowering the RF voltage on the central RF rail by about 20% in the  $d = 120 \mu\text{m}$  design and 30%

in the  $d = 80 \mu\text{m}$  design. Simultaneously, the RF voltage on the outer rails needs to be increased to  $U_{\text{RF}} \approx 370 \text{ V}$  and  $U_{\text{RF}} \approx 320 \text{ V}$ , respectively. The confining potential shows variations across the 18 trapping sites similar to the home configuration, small enough to confine ions in all sites simultaneously. The inhomogeneities between the trapping sites are even smaller in the  $d = 80 \mu\text{m}$  design. In both designs, micromotion compensation and adjustment of local secular frequencies are only possible for one trapping site per trap quadrant, due to the periodic connectivity of the DC island electrodes. This potentially limits the ability to couple the motion of several pairs of ions in parallel. Finally, it should be mentioned that lattice reordering using the BB shuttling process described in the previous section works in the reduced RF configuration as well. Edge effects are, however, much stronger than in the configuration with  $\zeta = 1$ , thus restricting the process to the central sites.

### 8.2.5. Axial interaction zone

Up to this point, the pattern of periodic DC voltages applied to the trap's DC island electrodes extended across the entire trap axis  $z$ , facilitating the calculation of voltage sets for multiwell confinement and the BB shuttling process. In this fully periodic configuration, the separation  $s_t^{(\text{ax})}$  between adjacent wells along  $z$  is given by the multiwell period  $a_{\text{mw}} = 306 \mu\text{m}$ . The motional coupling rate  $\Omega_c < 2\pi \times 5 \text{ Hz}$  at this distance, calculated for an axial frequency of  $\omega_z = 2\pi \times 1.0 \text{ MHz}$ , is by far too small for gate operations. The axial distance  $s_t^{(\text{ax})}$  can be reduced in the dedicated axial interaction zone at the trap center, where the DC island electrodes have a finer segmentation. Ions outside the interaction zone remain in a periodic DC multiwell potential maintained by the outer DC electrodes. Fig. 8.16 shows the set of DC electrodes used for axial confinement in the interaction zone. The set consists of 4 electrodes (red) in the central interaction zone and 4 electrodes (blue) at the trap edges. For the simulation of axial confinement, the voltages on the electrodes are assumed to have a mirror symmetry along both the central RF rail and along the  $x$ -axis through the center of the trap. In this way, the control of only two trapping sites, one at  $z_0^{(\text{c})}$  within the interaction zone and the other at  $z_0^{(\text{o})}$  in the outer region, is sufficient to create multiwells across the entire length of the trap. The position  $z_0^{(\text{c})}$  of the first site sets the reduced axial distance  $s_t^{(\text{ax})}$  between the central trapping sites. The position  $z_0^{(\text{o})}$  of the second site controls the location of all the outer trapping sites, which have a fixed spacing given by the lattice constant  $a_{\text{mw}}$ . The voltage sets for simultaneous confinement at the two positions  $z_0^{(\text{c})}$  and  $z_0^{(\text{o})}$  are calculated using the algorithm for multiwell confinement described in section 8.2.2. The voltage sets allow for independent tuning of the axial frequency and micromotion compensation at these two positions.

## 8. 2D linear trap array “Bucket-brigade”

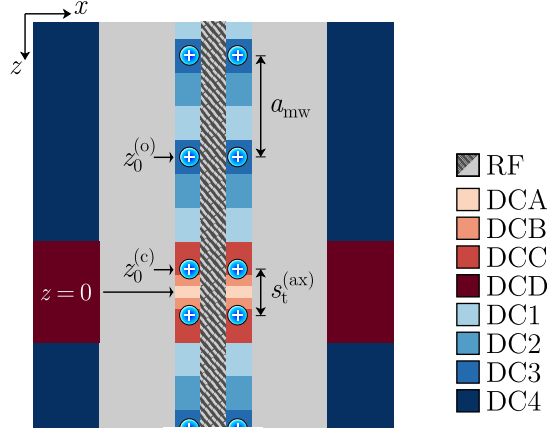


**Figure 8.16.** Set of DC electrodes used for confinement in the axial interaction zone. The applied voltages have a mirror symmetry both along the central RF rail and along the  $x$ -axis at  $z = 0$ . The position  $z_0^{(c)}$  defines the axial distance  $s_t^{(ax)}$  between the central trapping sites and can be set independently from the position  $z_0^{(o)}$  of the outer sites. The periodic connectivity of the outer DC electrodes (blue) creates DC multiwells with lattice spacing  $a_{mw}$ .

Fig. 8.17 shows the confining potential for a configuration, where the axial distance in the interaction zone is reduced to  $s_t^{(ax)} = 50 \mu\text{m}$ , exemplarily for the  $d = 120 \mu\text{m}$  design. The potential is qualitatively identical for the  $d = 80 \mu\text{m}$  design. The trap parameters for both designs are listed in Tab. 8.4. The cross sections (a), (b), (c) in Fig. 8.17 show 20 individual trapping sites arranged in two columns mirror-symmetrically along the two RF nulls. In (f), (g) and (h) a magnified view of the 4 central sites at  $\pm z_0^{(c)}$  with reduced axial separation  $s_t^{(ax)} = 2z_0^{(c)} \approx 50 \mu\text{m}$  is given. These central sites have radial frequencies  $\omega_{r,1}, \omega_{r,2} = 2\pi \times (3.1, 3.3)$  MHz identical to the home configuration. The axial mode has a frequency  $\omega_z = 2\pi \times 0.91$  MHz and is tilted by  $\vartheta_z = 8.0^\circ$  relative to the  $z$ -axis. The central sites are separated from each other by an axial double well barrier  $U_b^{(ax)} = 1.1$  meV. The axial barrier height is in good agreement with the 1.3 meV prediction from the double-well model, Eq. (8.3). The expected motional coupling between single ions in the central sites, calculated from Eq. (3.4), is  $\Omega_c = 2\pi \times 1.5$  kHz. The axial frequencies in the two central sites can be tuned individually. Micromotion compensation, however, is limited to shifting both sites simultaneously due to the low axial separation  $s_t^{(ax)} = 50 \mu\text{m}$ . On the other hand, given that  $s_t^{(ax)}$  is substantially smaller than the ion-surface distance  $d = 120 \mu\text{m}$ , stray fields might also not vary strongly between the two central sites. For the calculation of the voltage sets for frequency tuning and micromotion compensation, the assumption of an electrode mirror symmetry at the  $z = 0$  plane is dropped. Details are given in appendix B.1. As expected from the condition  $s_t^{(ax)} < d$ , the DC potential with  $s_t^{(ax)} = 50 \mu\text{m}$  is not created efficiently. This is evident from

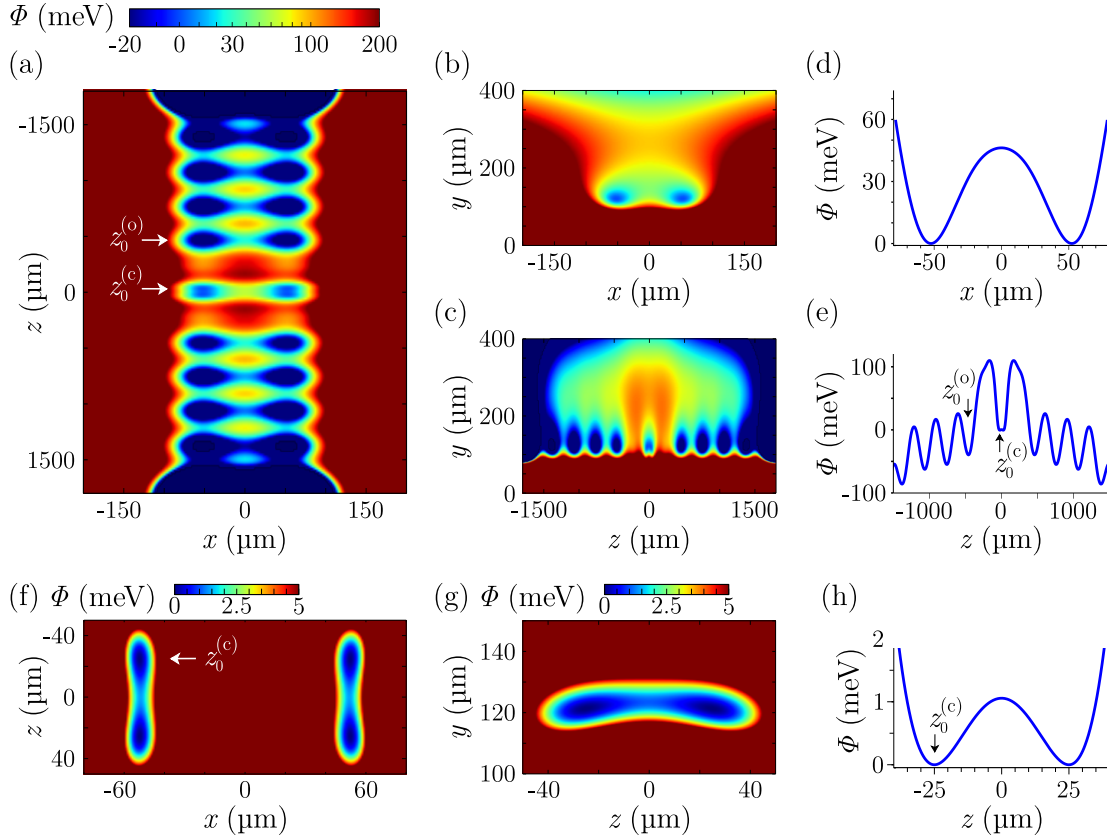


**Figure 8.17.** Trap confinement in the axial interaction configuration with reduced axial distance  $s_t^{(\text{ax})} = 50 \mu\text{m}$  at the trap center. Subplots (a), (b), (c) show cross sections of the total potential  $\Phi$  in the  $xz$ -,  $xy$ - and  $zy$ -plane, respectively, crossing the trapping site at  $r_0^{(c)} = (-52, 121, 25) \mu\text{m}$ . The color scale is non-linear for better visibility. (d) Potential across the RF barrier between the two central trapping sites at  $x_0^{(c)} = \pm 52 \mu\text{m}$ ,  $z_0^{(c)} = 25 \mu\text{m}$ . (e) Axial multiwell potential at  $x_0 = -52 \mu\text{m}$ . Subplots (f)-(h) show a zoom-in on the axial interaction zone. The color scale in (f) and (g) is adjusted for better visibility of the axial double well potential. In all plots a DC offset field is subtracted from the data.

the DC voltages, which are 10 times larger on the central electrodes than on the outer electrodes (cf. Tab. B.3 in appendix B.1). Furthermore, axial confinement cannot be increased to more than  $\omega_z = 2\pi \times 1.1 \text{ MHz}$ . At this axial frequency, the axial double well barrier is increased to  $U_b^{(\text{ax})} = 1.6 \text{ meV}$ , but also the axial mode tilt is quite strong,  $\vartheta_z = 19^\circ$ . Further scaling up the voltages for axial confinement adds to the tilt and reduces both  $\omega_z$  and  $U_b^{(\text{ax})}$  until eventually the double-well is morphed into a single well located at  $z = 0$ . The reason for this effect is that  $\vartheta_z$  is not constrained in the calculation of the voltage set for axial confinement, which also explains the deviation of the axial frequency  $\omega_z = 2\pi \times 0.91 \text{ MHz}$  in Tab. 8.4 from the setpoint value of 1.0 MHz. This issue could be fixed in future designs by adding more control electrodes. The outer 16 trapping sites, starting at  $\pm z_0^{(o)} \approx \pm 459 \mu\text{m}$  and further out, are produced

## 8. 2D linear trap array “Bucket-brigade”

**Table 8.4.** Trap parameters in the axial interaction configuration with reduced axial distance  $s_t^{(\text{ax})} = 50 \mu\text{m}$ , at the position of the central left minimum at  $x_0 \approx -50 \mu\text{m}$ ,  $z_0 = s_t^{(\text{ax})}/2$ . The corresponding DC voltage sets for confinement and micromotion compensation are in Tab. B.3 in appendix B.1.

| $d$                                 | RF drive                    |        | secular freq.         |          | mode tilt     |             | trap depth          |         |
|-------------------------------------|-----------------------------|--------|-----------------------|----------|---------------|-------------|---------------------|---------|
| <b>120 <math>\mu\text{m}</math></b> | $U_{\text{RF}}^{(o)}$       | 142 V  | $\omega_z/(2\pi)$     | 0.91 MHz | $\vartheta_z$ | $8.0^\circ$ | $U_0$               | 91 meV  |
|                                     | $\Omega_{\text{RF}}/(2\pi)$ | 23 MHz | $\omega_{r,1}/(2\pi)$ | 3.1 MHz  |               |             | $U_b$               | 46 meV  |
|                                     | $\zeta$                     | 1      |                       |          | $\vartheta_r$ | $33^\circ$  |                     |         |
|                                     | $q$                         | 0.4    | $\omega_{r,2}/(2\pi)$ | 3.3 MHz  |               |             | $U_b^{(\text{ax})}$ | 1.1 meV |
| <b>80 <math>\mu\text{m}</math></b>  | $U_{\text{RF}}^{(o)}$       | 118 V  | $\omega_z/(2\pi)$     | 0.99 MHz | $\vartheta_z$ | $2.2^\circ$ | $U_0$               | 153 meV |
|                                     | $\Omega_{\text{RF}}/(2\pi)$ | 36 MHz | $\omega_{r,1}/(2\pi)$ | 4.9 MHz  |               |             | $U_b$               | 100 meV |
|                                     | $\zeta$                     | 1      |                       |          | $\vartheta_r$ | $15^\circ$  |                     |         |
|                                     | $q$                         | 0.4    | $\omega_{r,2}/(2\pi)$ | 5.3 MHz  |               |             | $U_b^{(\text{ax})}$ | 1.4 meV |

by the periodic voltage pattern on the DC island electrodes, leading to multiwells with approximate well distance  $a_{\text{mw}}$ . For these outer sites, secular frequencies vary by less than 90 kHz, where the largest variation is found at the outermost sites at  $z_0 = \pm 1381 \mu\text{m}$ . The trap depths  $U_0$ ,  $U_b$ ,  $U_{\text{mw}}$  do not fall below 47 meV, except at the outermost sites, where  $U_0, U_b \approx 40 \text{ meV}$ ,  $U_{\text{mw}} = 24 \text{ meV}$ . Also, all sites have an acceptable micromotion modulation index  $\beta < 1$ , except the outermost ones, where  $\beta \approx 2$ .

The reduced axial distance  $s_t^{(\text{ax})} \approx 50 \mu\text{m}$  is established more efficiently in the 80  $\mu\text{m}$  design due to the closer proximity to the surface at identical length  $l_{\text{DC}}$  of the DC segments. A secular frequency  $\omega_z = 2\pi \times 0.99 \text{ MHz}$  can be realized at the central sites with one tenth of the voltage on the central DC electrodes compared to the 120  $\mu\text{m}$  design, and with a 4 times smaller axial mode tilt  $\vartheta_z = 2.2^\circ$ . The maximal possible axial frequency is twice as high,  $\omega_z = 2\pi \times 2.4 \text{ MHz}$  with  $\vartheta_z = 24^\circ$  and a barrier  $U_b^{(\text{ax})} = 6.5 \text{ meV}$ . The homogeneity of the outer 16 trapping sites is significantly better as well. The secular frequencies vary by less than 50 kHz with  $\vartheta_z < 0.15^\circ$ . The radial mode tilt  $\vartheta_r \approx 15^\circ$  does not change by more than  $0.5^\circ$ . The trapping sites are deeper with  $U_0, U_b, U_{\text{mw}} \gtrsim 100 \text{ meV}$ . Edge effects shifting the sites off the RF null are small, with micromotion modulation indices  $\beta \lesssim 0.1$  for all outer sites.

Finally, the configuration with reduced axial distance  $s_t^{(\text{ax})}$  needs to be seamlessly transformable to the home configuration in order to show the full functionality of the BB trap designs. This can be implemented with a two-stage shuttling process. In the first step, the initial separation  $s_t^{(\text{ax})} = 50 \mu\text{m}$  between the innermost sites is increased to  $a_{\text{mw}} = 306 \mu\text{m}$ , which corresponds to shifting the central sites from  $\pm z_0^{(c)} = \pm 25 \mu\text{m}$

to  $\pm a_{\text{mw}}/2$ . With the outer sites being at  $\pm z_0^{(o)} = \pm 3a_{\text{mw}}/2$ , a multiwell configuration with lattice spacing  $a_{\text{mw}}$  is realized. The second step then uses the BB shuttling process to shift the central multiwell site into the origin  $z = 0$ , thus matching the home configuration. This second step was demonstrated in section 8.2.3. A proof-of-principle realization of the first step is shown in Fig. 8.18 for the  $d = 120 \mu\text{m}$  design. A similar process can be found for the  $d = 80 \mu\text{m}$  design. The parameters for sequence step 0 on the very left of each plot in Fig. 8.18 match the axial interaction configuration of Fig. 8.17 with  $s_t^{(\text{ax})} = 50 \mu\text{m}$ . For the final sequence step 240 on the very right, multiwell confinement with a lattice constant  $a_{\text{mw}}$  across the entire length of the trap is established, matching the configuration used for BB shuttling. To realize the full shuttling process, voltage sequences for three different electrode sets are stitched together by linear interpolation of the voltage values at the stitching points. This procedure is explained in more detail in appendix B.3. Fig. 8.18(a) shows how the positions  $z_0^{(c)}$  and  $z_0^{(o)}$  of the central site and outer site, respectively, vary as the shuttling sequence evolves. While  $z_0^{(c)}$  moves quite uniformly from the initial position  $z_0^{(c)} = 25 \mu\text{m}$  (sequence step 0) to the final position  $z_0^{(c)} = 153 \mu\text{m} = a_{\text{mw}}/2$  (step 240), the outer site

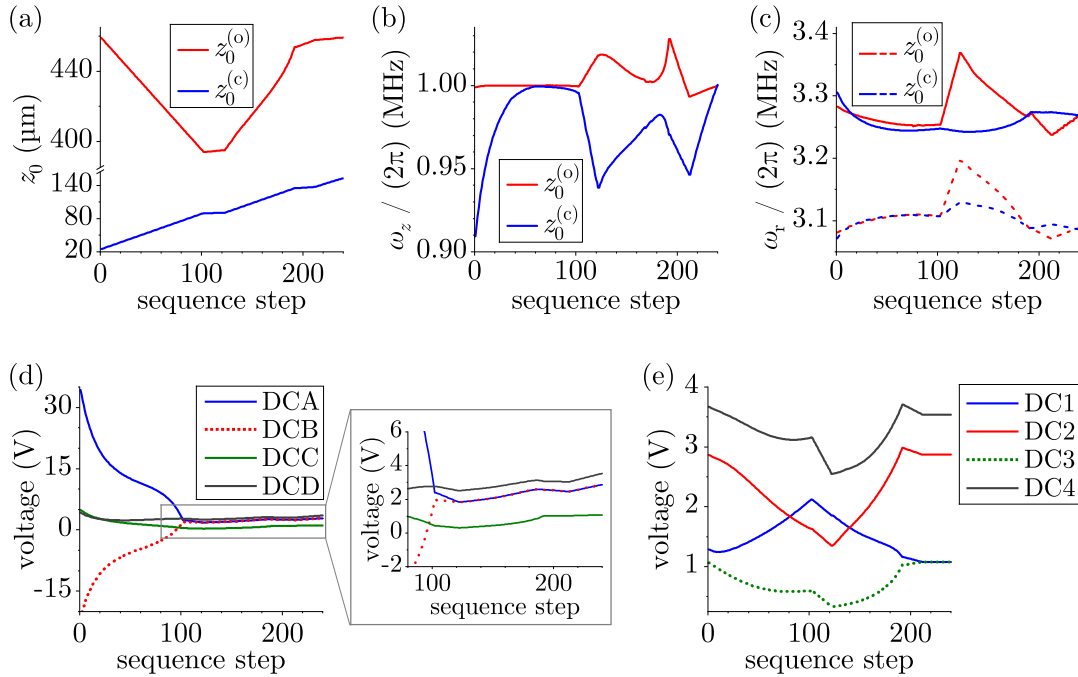


**Figure 8.18.** Shuttling sequence showing the transformation of the configuration with reduced axial distance,  $z_0^{(c)} = 25 \mu\text{m}$ , into the multiwell configuration  $z_0^{(c)} = a_{\text{mw}}/2$ ,  $z_0^{(o)} = 3a_{\text{mw}}/2$ . (a) Axial positions of the central site,  $z_0^{(c)}$ , and outer site,  $z_0^{(o)}$ . (b) Axial and (c) radial frequencies of the central and outer sites. (d), (e) DC voltages on the control electrodes.

## 8. 2D linear trap array “Bucket-brigade”

has identical start and end positions  $z_0^{(o)} = 459 \mu\text{m} = 3a_{\text{mw}}/2$  with an excursion to smaller values of  $z_0^{(o)} \approx 400 \mu\text{m}$  at intermediate sequence steps. This outer site shift is required for the convergence of the voltages on the central electrodes DCA and DCB to the same value which happens around sequence step 120, visible in (d). The otherwise smoothly varying electrode voltages, shown in (d) and (e), exhibit kinks at the two stitching points between the different electrode sets, at sequence steps 102, 123 and 192, 213. These kinks in the voltage variation lead to kinks in various trap parameters, e. g. in the secular frequencies, (b) and (c). To avoid motional excitation, the voltages would need to be ramped adiabatically over these points. Similarly, the kinks in  $z_0^{(c)}$  and  $z_0^{(o)}$  potentially limit the shuttling speed. A more optimal voltage sequence for the shuttling process may be found using for instance constrained optimization methods [182].

In summary, the dedicated axial interaction zone at the trap center allows one to reduce the axial distance  $s_t^{(\text{ax})}$  between the central trapping sites while maintaining the axial multiwell for the outer ions. This enables motional coupling of ions along the axial direction. At a distance  $s_t^{(\text{ax})} = 50 \mu\text{m}$ , the confinement in the central sites yields axial frequencies  $\omega_z \approx 2\pi \times 1 \text{ MHz}$  with an axial double-well barrier  $U_b^{(\text{ax})} \approx 1 \text{ meV}$ . The expected coupling rate for this configuration is  $\Omega_c \approx 2\pi \times 1 \text{ kHz}$ . Axial double-well barriers up to  $U_b^{(\text{ax})} = 6.5 \text{ meV}$  can be realized in the  $80 \mu\text{m}$  design at a larger frequency  $\omega_z = 2\pi \times 2.4 \text{ MHz}$ . In both designs, micromotion compensation is restricted to shifting both central sites simultaneously, which may be improved in future designs by adding additional control electrodes. Individual tuning of axial frequencies is possible. Finally, the configuration with reduced axial distance can be transformed into the home configuration by a shuttling process.

### 8.2.6. Comparison of the designs with $d = 120 \mu\text{m}$ and $d = 80 \mu\text{m}$

The discussion in the previous sections shows that the two trap designs with ion-surface separations  $d = 120 \mu\text{m}$  and  $d = 80 \mu\text{m}$ , respectively, are both suited to assess the main operational principles of the envisioned 2D linear trap array: axial multiwell confinement, DC and RF shuttling and motional coupling of ions in adjacent trapping sites in two spatial directions. Nevertheless, several differences between the two designs were revealed, pointing to specific advantages of the designs for different tasks:

- The  $120 \mu\text{m}$  design with its larger ion-surface separation  $d$  is likely to show a lower motional heating rate and the trapping potentials are more robust against stray electric fields. This might be a crucial advantage for motional coupling and entangling operations. Furthermore, a smaller reduction in the RF voltage on the central RF rail is required during RF shuttling operations. This is advantageous

for the technical realization of the reduced RF voltage, cf. chapter 6.1.

- The 80  $\mu\text{m}$  design requires a smaller RF voltage for its operation and has a larger trap depth in the home configuration. The latter point is important for experiments, where the entire lattice is used for ion storage. Furthermore, the trapping sites across the multiwells are more homogeneous, which is as well beneficial for experiments involving ions in the entire lattice, for instance experimental investigations of the BB shuttling process. Lastly, the closer proximity to the chip surface is a clear advantage for ion confinement in the axial interaction zone.

It should be pointed out, that the two designs presented here are a first iteration. More advanced designs could be conceived, allowing one to ease many of the limitations found. For instance, improvements could be made on the geometry of the DC electrodes, which were not optimized to the last in the current designs. A significant reduction of the edge effects should be possible by a proper design of the segments at the trap edges or simply by adding more segments. In general, a larger number of control electrodes would be desirable to allow for micromotion compensation and frequency tuning in more trapping sites simultaneously and for an improved control of the trapping potential in the axial interaction zone.

## 8.3. Fabrication

The BB traps were fabricated in the facilities of Infineon Austria<sup>10</sup> as part of the master's thesis of Gerald Stocker [172]. The main fabrication steps and concepts of the design realization are summarized at the beginning of this section. In the second part, the electrical properties of the chips are characterized. This includes measurements of resistances and capacitances, as well as DC breakdown tests. The results are used to determine estimates for Johnson noise from the trap electrodes and leads, the RF grounding of the DC electrodes, and the requirements on a two-resonator RF drive.

### 8.3.1. Multilayer structure

The fabrication of the BB traps employs a multilayer process established for Infineon products in the automotive sector. This ensures reliability and reproducibility of the traps' electrical properties. The traps are produced on 8 inch Silicon wafers<sup>11</sup>. In a first step, thermal oxide is grown to electrically isolate the substrate. In the next steps, three metal layers are deposited, separated by  $\text{SiO}_2$  oxide layers. The metal layers

<sup>10</sup> Infineon Technologies Austria AG, Villach, Austria.

<sup>11</sup> Boron-doped, Czochralski growth method, room-temperature resistivity  $\rho = 3 \times 10^{-2} \Omega \text{m}$ .

## 8. 2D linear trap array “Bucket-brigade”

mainly consist of Aluminium, with an admixture of 1 wt% Silicon and 0.5 wt% Copper (AlSiCu)<sup>12</sup>. On top of the AlSiCu, an additional thin layer of Titanium nitride (TiN) is applied<sup>13</sup>. The layers are structured using wet and plasma etch processes. Tab. 8.5 lists the different layers and their thicknesses. SEM images of a trap cross section are shown in Fig. 8.19. The top metal layer, M3, forms the trap electrodes. On the second metal layer, M2, leads are routed to connect island-like trap electrodes to the bonding pads at the trap edges. The first metal layer, M1, is mainly used as a ground layer to shield the Si substrate from laser light and to reduce RF leakage into the substrate [183]. Vias through the inter-metallic oxides connect the metal layers. The

**Table 8.5.** Multilayer structure of the fabricated BB traps. Thickness values are extracted from an SEM cross section of a trap chip. The numbers in parentheses are the nominal values.

| Layer    | Material                     | Thickness (nm)   |
|----------|------------------------------|------------------|
| metal M3 | AlSiCu                       | 2140 (2000)      |
| oxide 3  | SiO <sub>2</sub> (deposited) | 2100 (2200)      |
| metal M2 | AlSiCu + TiN                 | 1020 (1000 + 25) |
| oxide 2  | SiO <sub>2</sub> (deposited) | 2100 (2200)      |
| metal M1 | AlSiCu + TiN                 | 784 (750 + 25)   |
| oxide 1  | SiO <sub>2</sub> (thermal)   | 1310 (1300)      |

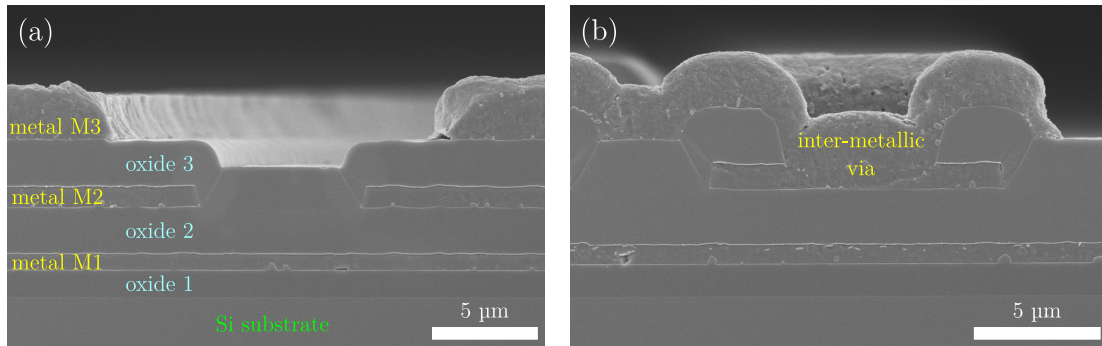


**Figure 8.19.** SEM images of a trap cross section. (a) Three metallic layers are separated from each other by oxide layers. The trap electrodes are realized on the top metal layer M3, the M2 layer is used for signal routing, the grounded M1 layer shields the Si substrate from laser light and reduces RF leakage into the substrate. (b) Inter-metallic vias connect the different metal layers. Figure courtesy of Infineon Austria.

<sup>12</sup> The Si in the Al bulk is in oversaturated solution (solubility limit 0.5 wt%) and is used to prevent diffusion of Al into the Si substrate when there is no thermal oxide. Cu migrates to the grain boundaries and reduces electromigration of the Al.

<sup>13</sup> The TiN layer is used as an anti-reflection coating in the optical lithography steps and is an adhesion promoter for the photoresist.

gaps between the trap electrodes on M3 are  $9\ \mu\text{m}$  wide<sup>14</sup>. On the lower-lying M2 and M1 layers, the smallest distance between different electrodes within each layer is  $5\ \mu\text{m}$ . The structured M1 and M2 layers lead to steps on the chip surface. These topological features are small compared to the electrode-ion separation  $d$  and are expected to have negligible influence on the trapping potentials. The multilayer structure in Tab. 8.5 is the default for the established fabrication process at Infineon, although up to 6 metal layers could be realized. For larger layer numbers, additional planarization steps would need to be added. Significant changes to the layer thicknesses would require a process optimization.

Fig. 8.20 shows microscope images of three trap samples. The  $80\ \mu\text{m}$  and  $120\ \mu\text{m}$  designs, described in the previous section, are shown in (a) and (b), respectively. The connection lines to the island-like trap electrodes have a maximal possible width and are routed on the thickest metal layer whenever possible to reduce their resistance. This helps to minimize RF-pickup on the DC electrodes. For the same reason, double vias are used to connect each of the periodic DC island electrodes to its signal line, such that the M2 and M3 layers are routed in parallel, (d). Additional shield electrodes connected to the RF GND minimize the parasitic coupling capacitance between the lines and the RF electrodes. Furthermore, connection lines don't cross below the RF rails with the exception of the leads connecting the individual DC islands at the center of the trap, Fig. 8.20 (e). Here, the routing is moved to the M1 layer to make room for a shield electrode on M2, that minimizes RF-pickup on the lines while maintaining the screening of the Si substrate from laser light. A minimal-instance version of the  $120\ \mu\text{m}$  design is shown in (c). For this version, the number of DC electrodes is drastically reduced to allow for connection lines with even lower resistance. The minimal-instance version is intended as a backup, in case the other designs show insufficient grounding of the DC electrodes.

For both the  $80\ \mu\text{m}$  and  $120\ \mu\text{m}$  designs shown in (a) and (b), an additional variation exists, where about 79% of the M1 layer below the RF rails is removed. This is referred to as “structured M1 layer” in the following section, as opposed to the “continuous M1 layer” of the other design variations. At cryogenic temperatures, where the charge carriers in the Si substrate freeze out, the design variations with structured M1 layer should have a significantly lower capacitance of the RF electrodes to GND, thereby increasing the voltage gain of a step-up resonator [119], should this be necessary. A disadvantage might arise from the limited shielding of the Si substrate from laser light and the penetration of the RF field into the substrate [183].

---

<sup>14</sup> The gaps are realized by decreasing the size of adjacent electrodes by half the gap width each, with reference to the gap-less geometry used for the trap simulation, Tab. 8.1.

8. 2D linear trap array “Bucket-brigade”

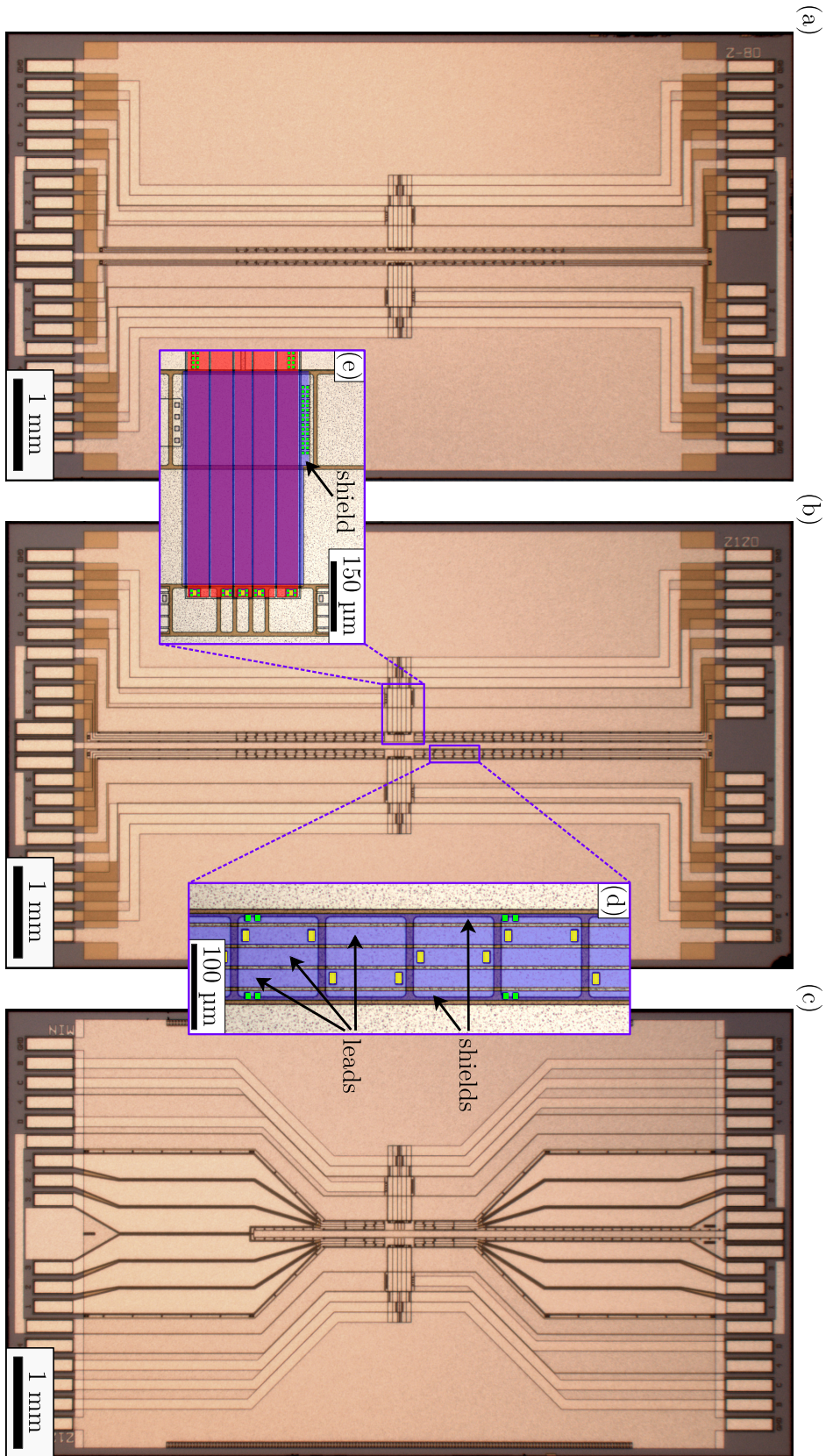


**Figure 8.20.** Microscope images of the BB traps. (a)  $d = 80 \mu\text{m}$  design, (b)  $d = 120 \mu\text{m}$  design, (c)  $d = 120 \mu\text{m}$  design with reduced number of island electrodes and fan-out for minimal lead resistance. (d), (e) False color views of the central region highlighting the electrode leads on the lower metal layers M2 (blue) and M1 (red). Inter-metallic vias are colored yellow between M3 and M2 and green between M2 and M1.

### 8.3.2. Electrical characterization

The trap structures were electrically characterized in terms of metal layer and via resistivity, dielectric strength and electrode capacitance. The resistance and dielectric strength measurements were performed at the facilities at Infineon<sup>15</sup>, using dedicated test structures<sup>16</sup>. These test structures were fabricated on the same wafer as the trap chips, undergoing identical fabrication steps. Additional breakdown tests on the actual trap chips were performed in Innsbruck. The electrode capacitances were determined directly on the trap chips at the facilities at Infineon<sup>17</sup>.

#### Resistance

Resistances of electrodes and leads in the three metal layers as well as the typical via resistances were determined with 4-wire measurements of test structures. The structure used to measure layer resistivities is a 65.5 mm long meander trace with 14  $\mu\text{m}$  width, realized on each of the metal layers. The resistivities are calculated from the measured trace resistances using the layer thicknesses in Tab. 8.5. The via resistances are determined from test structures with 30 identical vias connected in series. The results of the tests are listed in Tab. 8.6. The measured resistivity for the M3 layer is very close to the value  $\rho = 2.7 \times 10^{-8} \Omega \text{m}$  for pure Aluminum [184]. The other two layers have a slightly higher resistivity which can partly be attributed to the less conductive TiN layers, that add to the layer thickness. For cryogenic operation at  $T = 10 \text{ K}$ , the resistivity can be expected to drop by at least a factor 10, depending on the exact metal composition [185]. The vias between the different layers all have small resistance values of a few tens of  $\text{m}\Omega$ , indicating good electric connectivity. The resistance variation between the three via types stems from their different geometric realizations.

**Table 8.6.** Measured layer resistivities  $\rho$  and via resistances  $R_{\text{via}}$  at room temperature.

| Layer | $\rho$ ( $\Omega \text{m}$ ) | Via type | $R_{\text{via}}$ ( $\text{m}\Omega$ ) |
|-------|------------------------------|----------|---------------------------------------|
| M3    | $2.92(1) \times 10^{-8}$     | M3 to M2 | 29.9(3)                               |
| M2    | $3.11(5) \times 10^{-8}$     | M2 to M1 | 68.7(20)                              |
| M1    | $3.09(1) \times 10^{-8}$     | M3 to M1 | 49.7(10)                              |

From the measured resistivities, the maximal resistances of the individual electrode leads at room temperature can be calculated. The leads on the M1 layer, connecting

<sup>15</sup> The resistance measurements and DC breakdown tests were done by Christoph Bender, Infineon department for failure analysis (“Fehleranalyse”) in Villach, Austria.

<sup>16</sup> The geometry of the test structures was designed by Gerald Stocker.

<sup>17</sup> The capacitance measurements were done by Stephan Schönmann, Infineon department for failure analysis (“Fehleranalyse”) in München, Germany.

## 8. 2D linear trap array “Bucket-brigade”

to the DC island electrodes in the axial interaction zone, have a minimal width of  $w = 36 \mu\text{m}$  and maximal length  $l = 0.69 \text{ mm}$  (identical for all design in Fig. 8.20). This results in a maximal resistance of about  $R_{\text{lead}} \approx 0.8 \Omega$ . The leads for the periodically connected island electrode outside the axial interaction zone are on the M2 layer. In the  $80 \mu\text{m}$  design, these leads have a maximal length of about  $l = 3.56 \text{ mm}$  and a width of  $w = 10 \mu\text{m}$ , resulting in a maximal resistance of about  $R_{\text{lead}} \approx 11 \Omega$ . In the  $120 \mu\text{m}$  design, the lead width is  $w = 20 \mu\text{m}$  with a correspondingly smaller resistance  $R_{\text{lead}} \approx 5 \Omega$ . Vias add negligibly to the connection line resistance.

An upper bound for the expected ion heating rate  $\Gamma_{\text{h}}$  due to Johnson noise in the electrode leads can be given, using the maximal lead resistance  $R_{\text{lead}} \approx 11 \Omega$  of the periodically connected island electrodes. Noise on these electrodes has the largest impact on the ion heating rate, due to their close proximity to the trapping sites. The characteristic distance of these electrodes varies for different axial positions of the ions. For the electric field noise component along the axial direction, the maximal characteristic distance for the  $80 \mu\text{m}$  design is  $\delta_{c,z} = 1.1 \text{ mm}$ <sup>18</sup>. The amount of electric field noise is then  $S_E \sim 1.5 \times 10^{-13} \text{ V}^2\text{m}^{-2}\text{Hz}^{-1}$ , calculated at room-temperature  $T = 300 \text{ K}$  and with the lead resistance  $R_{\text{lead}} \approx 11 \Omega$  using Eq. (3.8). This corresponds to an axial ion heating rate of  $\Gamma_{\text{h}} = 22 \text{ phonons/s}$  at an axial frequency of  $\omega_z = 2\pi \times 1.0 \text{ MHz}$ , cf. Eq. (3.7). An analog calculation leads to a radial heating rate of  $\Gamma_{\text{h}} = 36 \text{ phonons/s}$ , using the maximal characteristic distance  $\delta_{c,r} = 0.5 \text{ mm}$  for the radial modes<sup>19</sup> and a radial frequency of  $\omega_r = 2\pi \times 3.0 \text{ MHz}$ . These estimates for the heating rates are significantly smaller than the expected motional coupling rate  $\Omega_c \approx 2\pi \times 1.0 \text{ kHz}$  between ions in adjacent trapping sites. At cryogenic temperatures, the estimates for the heating rates from Johnson noise are expected to be smaller by at least two orders of magnitude, due to the reduced temperature and lead resistance.

### DC breakdown

A conservative estimate of the dielectric strength of the deposited oxide is on the order of  $100 \text{ V}$  per  $\mu\text{m}$  dielectric thickness, based on empirical knowledge at Infineon. Experimentally, the electric strength of the  $2.1 \mu\text{m}$  thick  $\text{SiO}_2$  dielectric layer has been characterized by DC breakdown tests. For planar test structures, the dielectric breakdown voltage was found to be  $U_{\text{break}} > 1.2(2) \text{ kV}$ , much higher than the conservative estimate predicts. The measurements were carried out at atmospheric pressure and were limited by surface flash-over or arcing across the  $300 \mu\text{m}$  distance between the contact pads. Tests of actual trap samples yield a dielectric breakdown voltage  $U_{\text{break}} > 356(9) \text{ V}$

<sup>18</sup> In the  $120 \mu\text{m}$  design, it is  $\delta_{c,z} = 2.2 \text{ mm}$ .

<sup>19</sup> In the  $120 \mu\text{m}$  design, it is  $\delta_{c,r} = 0.9 \text{ mm}$ .

between the RF rails and the GND/DC electrodes. The tests were limited by surface flash-over across the  $9\ \mu\text{m}$  electrode gaps on the M3 layer. Since these tests were carried out at atmospheric pressure as well, the breakdown values in vacuum are expected to be even higher. Leakage currents were not detectable within the measurement resolution of approximately  $5\ \text{nA}$ .

### Capacitance

The capacitances  $C_i, C_o$  between the RF electrodes and the RF GND (represented by all other electrodes), as well as the direct coupling capacitance  $C_c$  between the inner and outer RF rails have been measured for the  $d = 80\ \mu\text{m}$  design. The results are listed in Tab. 8.7 along with estimates based on finite element electric field simulations of the multilayer trap structure. Details on these simulations are given in appendix B.4. The measured capacitances to GND for the design with continuous M1 GND layer are  $C_o = 39.5(5)\ \text{pF}$  for the outer RF rails and  $C_i = 7.2(2)\ \text{pF}$  for the inner RF rail. These values are comparable to capacitances of other multilayer traps [186]. The capacitance estimates (square brackets) are considerably smaller than the measured values, in particular for  $C_o$ . The discrepancy can mostly be explained by an additional capacitance contribution of the bonding pads and leads via the Si substrate, which can be treated as a floating conductor at room temperature. The substrate then acts as an RF GND because the impedance between substrate and GND layer on M1 is negligible in the RF domain due to the large extent of the GND layer, which covers almost the entire trap chip. The additional capacitance contribution is about  $1.7\ \text{pF}$  for  $C_i$  and  $6.8\ \text{pF}$  for  $C_o$  (see appendix B.4). At cryogenic temperatures, these additional contributions should vanish as the substrate becomes insulating<sup>20</sup>. For the design variation with structured M1 layer, where about 79% of the GND on M1 is removed below the RF rails, the capacitance estimates show a strong reduction of the capacitances  $C_o$  and  $C_i$ . The measured capacitances are, however, reduced by only about 10% compared to the design variations with continuous M1 layer. The discrepancy can again be explained by an additional capacitance contribution via the Si substrate. At room-temperature, the substrate acts as an RF GND and the additional contribution approximately compensates the capacitance reduction gained by the structuring of the M1 layer. At cryogenic temperatures, these contributions should vanish. The measured coupling capacitance  $C_c = 0.06(1)\ \text{pF}$  between the inner and outer RF rails is well below  $0.1\ \text{pF}$ . Phase-stabilized electric resonators driving the RF electrodes would hence need a capacitance tunability of below  $1\ \text{pF}$  to achieve the desired RF ratios  $\zeta \in [0.7, 1]$ , cf.

<sup>20</sup> A capacitance change of approximately the expected size has been observed in first experiments with the trap chips by a shift in the resonance frequency of the drive resonator at temperatures  $T \lesssim 40\ \text{K}$ .

## 8. 2D linear trap array “Bucket-brigade”

Fig. 6.6. Such a tunability was demonstrated with the resonator prototype, described in chapter 6.2. The extremely small value for  $C_c$  is explained by strong shielding effects from the GND / DC electrodes separating the RF rails. For the design with structured M1 layer, where the GND shield is removed below the RF rails, the coupling capacitance is increased by about a factor 3. For the  $d = 120 \mu\text{m}$  design, the capacitance estimates suggest values very close to those in the  $d = 80 \mu\text{m}$  design.

**Table 8.7.** Measured and simulated values of electrode capacitances.  $C_i, C_o$  are the capacitances between GND and the inner and outer RF rails, respectively.  $C_c$  is the direct coupling capacitance between inner and outer RF rails. The estimates are in square brackets. For the  $120 \mu\text{m}$  design, capacitances were not measured at Infineon (n. m.).

|                                         | $C_i$ (pF)   | $C_o$ (pF)     | $C_c$ (pF)     |
|-----------------------------------------|--------------|----------------|----------------|
| 80 $\mu\text{m}$ design                 | 7.2(2) [3.9] | 39.5(5) [26.2] | 0.06(1) [0.02] |
| 80 $\mu\text{m}$ design, M1 structured  | 6.5(2) [1.5] | 34.5(3) [10.0] | 0.19(1) [0.15] |
| 120 $\mu\text{m}$ design                | n. m. [3.7]  | n. m. [28.8]   | n. m. [0.01]   |
| 120 $\mu\text{m}$ design, M1 structured | n. m. [1.5]  | n. m. [10.7]   | n. m. [0.08]   |

Another important quantity is the amount of RF pickup on the DC island electrodes. RF pickup can lead to excess micromotion that cannot be compensated and even make the trap unstable. The estimate for the parasitic coupling capacitance between RF and adjacent DC island electrodes, calculated in the same way as the estimates in Tab. 8.7, gives  $C_c^{\text{DC}} \lesssim 0.1 \text{ pF}$  for all designs. Electrodes connected through a lead on M2 with  $R_{\text{lead}} = 11 \Omega$  at  $T = 300 \text{ K}$  would thus have a maximal RF pick up voltage  $U_p/U_{\text{RF}} = 2.1 \times 10^{-4}$ , cf. Eq. (7.1), where  $U_{\text{RF}}$  is the RF drive voltage at  $\Omega_{\text{RF}} = 2\pi \times 30 \text{ MHz}$ . This is a low level of RF pick up, around 10 times lower than the values measured in the YBCO trap for  $T < T_c$ , see chapter 7.3.1.

## 8.4. Future experiments

The Bucket-brigade traps presented in this chapter are a first generation of a new type of quantum simulator, based on parallel linear traps and well-to-well interactions. The primary goal of the trap design is to test the core operational principles of such a device. First measurements with the trap chips are ongoing while this thesis is being written. In fact, loading and storage of ions in multiple trapping sites have already been demonstrated. An image of a lattice of four ions, trapped simultaneously in the  $d = 120 \mu\text{m}$  design, is shown in Fig. 8.21<sup>21</sup>. Immediate next steps are the characterization

<sup>21</sup> The trap was operated in the cryogenic setup described in chapter 4.1. An RF voltage of about 180 V at 25.0 MHz was applied at both the inner and outer RF rails, using the RF resonator prototype described in chapter 6.2.1. For axial multiwell confinement, the DC voltages for the home configuration, Tab. B.1, were applied. The four ions were simultaneously illuminated using the laser sheet for

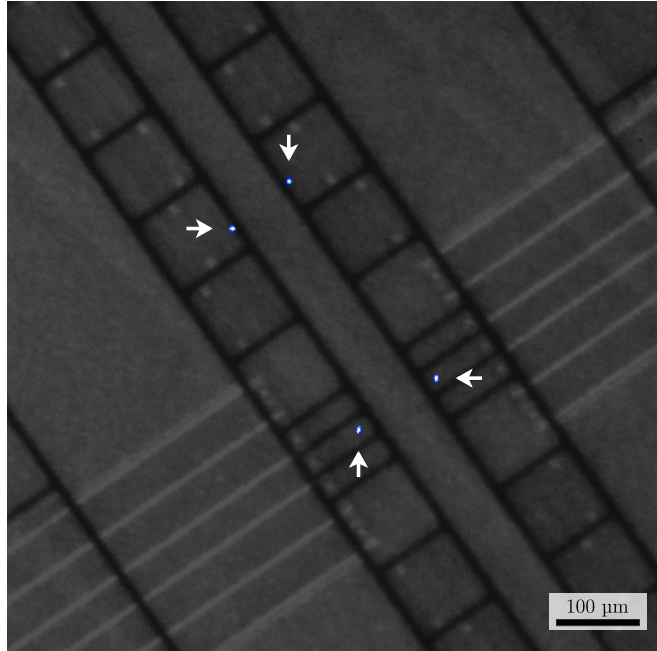


**Figure 8.21.** Photograph of four ions (white-blue, marked with arrows) trapped in a square lattice configuration in a BB trap with ion-surface separation  $d = 120 \mu\text{m}$ . The ion fluorescence image is superimposed onto a background image of the trap electrodes (gray scale).

of the traps in terms of ion-lifetime, electric stray fields and heating rate in order to assess and possibly improve the multilayer fabrication process and the trap design. The basic shuttling operations – reconfiguration of the ion lattice and reduction of inter-ion distance along two directions – need to be demonstrated as a prerequisite to observe motional coupling and eventually entanglement between ions in adjacent potential wells. In addition, general techniques relevant for large-scale trapped ion quantum processors can be studied. For instance, loading of trap arrays could be realized employing the bucket-brigade shuttling process: In an iterative scheme, ions would be loaded only at one trapping site at the trap edge by overlapping the ionization lasers at this location. Once the desired number of ions is loaded, the multiwell would be shifted by one period towards the trap center and the next site is loaded. This scheme could be further refined by fast loading from a reservoir zone on the trap chip, where a large number of ions is stored. To study such a process, a reservoir zone could be implemented in one half of the trap chip and the electrodes in the axial interaction zone could be used to control the ion transfer into the other half of the chip. In future designs, multiple reservoir zones could be integrated in the electrode geometry to quickly compensate for ion loss. Complementary to this scheme, reloading at arbitrary trapping sites could be

---

Doppler cooling described in chapter [4.2.2](#).

## 8. 2D linear trap array “Bucket-brigade”

implemented using crossed photo-ionization beams, as has been demonstrated recently [53]. Moreover, one could study the transition of the two RF nulls from the horizontal to the vertical orientation (regimes II and I in Fig. 8.5). This transition is controlled by the level of RF voltage on the inner RF rail and might be utilizable for a physical SWAP operation [187, 188]. Ions from the left and right RF null could be exchanged deterministically by adding suitable DC control fields to the RF potential.

Another prospect is the extension of the Bucket-brigade design to larger arrays with more than 100 trapping sites. The strategies developed to optimize the electrode geometry and the shuttling processes should be applicable to such designs. For instance, the algorithm to determine voltage sets for simultaneous confinement at two trapping sites can be readily extended to a larger number of sites. Also, the concept of bucket-brigade shuttling using a small number of control voltages to move entire multiwells should be immediately applicable. Another point is the choice of RF rail width. In the current design, the outer rails are much larger than the inner rail, which leads to relatively large trap depths. In a larger array, rails with smaller and larger widths can be arranged in an alternating fashion as depicted in Fig. 8.22 (a) to achieve a similar effect. An additional benefit of this configuration is a tilt of the radial modes towards the thinner RF rails when the axial DC confinement is added. A reduction of the distance between adjacent ions along  $x$  can be achieved by lowering the RF voltage on every second RF rail. Naturally, a stronger reduction would be required on the wider RF rails. Trap simulations of such an array geometry show the feasibility of the approach for an array with  $10 \times 10$  trapping sites, as described in appendix B.5. One could also imagine an approach with tapered RF rails, as shown in Fig. 8.22 (b). In such an array ions shuttled along the trap axes would follow a “zigzag” trajectory, alternately coming close to their neighbors on the left and right. This approach could further reduce the technical overhead, since it might work entirely without adjustable RF voltages. It requires, however, a careful design to minimize axial micromotion fields due to the rail taper.

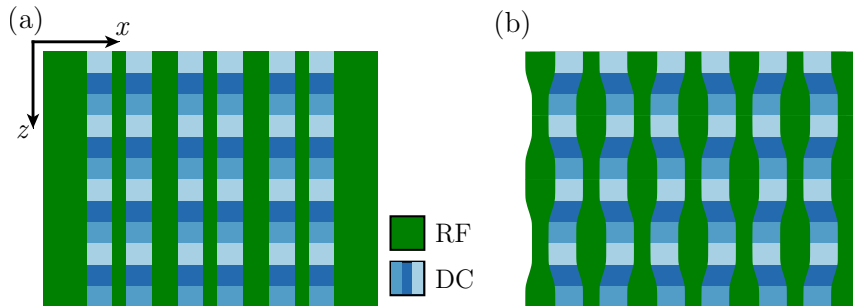


**Figure 8.22.** Illustration of possible future array geometries. (a) Alternating thinner and wider RF rails can increase the trap depth and lead to a tilt of the radial modes relative to the trap normal. (b) Tapered RF rails lead to a reduced distance between different pairs of adjacent linear traps at different axial positions.

## 9. Summary and outlook

In this thesis, contributions to the field of trapped-ion quantum computing have been presented. The described developments and experiments explore different technical elements of a novel ion-lattice quantum processor based on surface trap arrays. The investigated aspects comprise trap design and fabrication, novel trap materials and electronic means to control radio-frequency trapping fields in a cryogenic environment.

The electrical tests of the  $4 \times 4$  point trap array Ziegelstadl, described in chapter 5, proved to be a valuable tool for the assessment of basic electrical properties of trap chips and for electrical failure analysis. The tests revealed an insufficient dielectric strength that made the Ziegelstadl traps unusable. The electric failures occurred at specific locations on the chip, where the thickness of the dielectric layer between trap electrodes and signal lines is reduced. Apart from this issue, that may be fixed by an improved fabrication process, the Ziegelstadl traps suffer from an intrinsic weakness of the trap design, that was found by trap simulations. During RF-controlled shuttling operations, required for well-to-well entangling gates, the trap depth becomes extremely small. This effect was previously unnoticed, but appears to be a general feature of point-trap arrays. Despite the fact that no ions could be trapped in the Ziegelstadl array, it did provide important insights for future trap designs and fabrications, which led to the development of the Bucket-brigade trap array, described in chapter 8. The Bucket-brigade array is an advanced surface trap design with  $2 \times 9$  trapping sites, representing a minimal instance of a two-dimensional array of segmented linear traps. Using DC- and RF-controlled shuttling operations, the distance between adjacent lattice sites can be locally reduced to about  $40 \mu\text{m}$  to  $50 \mu\text{m}$ , for which a motional coupling rate of about  $1 \text{ kHz}$  between the sites can be expected. The relatively large ion-surface separation of  $80 \mu\text{m}$  and  $120 \mu\text{m}$  increases the likeliness of the motional heating rate to be lower than the coupling rate. The “bucket-brigade shuttling” procedure, developed for this design, adds the useful capability to shuttle an arbitrarily large multiwell of trapping sites using only four control voltages. This concept can be used to reconfigure the ion lattice from square to triangular and can be readily applied to other trap designs. The RF-controlled shuttling operations envisioned in the Bucket-brigade array require independent control of the RF fields on two different trap electrodes. This can be realized using a pair of phase-

## 9. Summary and outlook

stabilized RF resonators with electronically adjustable capacitance as tuning element. The basic functionality of such a circuit was demonstrated with a resonator prototype, as described in chapter 6. The prototype can be operated at cryogenic temperatures of  $T \approx 10$  K and shows excellent electrical properties with a capacitance tuning range  $\Delta C > 1$  pF and a quality factor  $Q \approx 1000$ . These characteristics are sufficient to guarantee phase-stability of the two RF fields during RF-controlled shuttling operations in the Bucket-brigade array. More generally, these results can be of value for a variety of other experiments, where cryo-compatible capacitance-tunability is required.

In an independent line of research, a high-temperature superconductor was explored as a new trap material for scalable ion trap designs, operated at or below liquid nitrogen temperatures. The experiments, described in chapter 7, show that the usage of the superconductor YBCO is a viable option to realize ultra-low resistance electrodes and electrode leads, without compromising the trap operability and performance. In particular, at a temperature  $T \approx 10$  K the ion heating rate above a YBCO surface was found to be comparable to that observed above a gold surface, with absolute values  $\Gamma_h < 1$  phonon/s at a secular frequency  $\omega_z = 2\pi \times 1.0$  MHz and an ion-surface separation  $d \approx 225$   $\mu\text{m}$ . Furthermore, no increase of the motional heating rate due to the superconducting YBCO leads could be detected. A simple estimation of the Johnson noise created by a copper lead of identical geometry shows that a superconducting lead can be advantageous already for lead lengths of a few cm. The heating rates observed with an ion exposed to a YBCO electrode surface exhibit an interesting temperature dependence with a plateau region. The plateau has a sudden onset coinciding with the superconducting transition temperature  $T_c$  and stretches for around 50 K. This finding strongly suggests a relation between the measured heating rate and the superconductivity within the YBCO film. While the nature of this relation remains unsettled, experiments are suggested to further investigate this behavior. Given the fact that a trapped ion is an excellent probe for electric field noise, it might even prove to become a valuable tool to study effects like superconductivity.

The results of this thesis can be seen as stepping stones towards an ion-lattice quantum processor that could perform useful calculations. As this thesis is being written, loading of an ion lattice has been demonstrated in the Bucket-brigade trap array. As of this, many experiments lie ahead. Immediate next steps would be a trap characterization across the different lattice sites, the implementation of the bucket-brigade shuttling process for lattice reconfiguration and the observation of coherent coupling between adjacent lattice sites. This would enable simple simulations, for instance of spin frustration with three ions in a triangular lattice configuration. On a medium-term perspective, the array design can be further optimized and extended, allowing for

a larger number of control electrodes, more trapping sites and more advanced simulations. Optics and electronics could be integrated on-chip; a digital-to-analog converter with multiplexed DC channels and operable at cryogenic temperatures is currently being developed in a collaboration between our group in Innsbruck and Infineon Austria. The main long-term goal is the realization of push-button entanglement in two spatial dimensions, which, together with addressed single qubit operations and state readout, would allow the implementation of quantum error correction. This would complete the vision of a scalable universal quantum processor based on surface trap arrays.



# A. Appendix to the superconducting traps

This section contains additional information on the experiments performed in the YBCO traps (chapter 7).

## A.1. Thermal insulation and temperature calibration

The trap chip is attached and thermally anchored to a heatable copper carrier, which is thermally isolated from the cryogenic environment, in particular from the DC filter and resonator PCBs. The thermal decoupling reduces the heat load on the cryostat, helps to maintain the cryogenically pumped vacuum and ensures that technical noise attenuated by the low-pass filters is independent of the trap chip temperature, cf. section A.4.3. The thermal insulation is characterized using two silicon temperature diodes<sup>1</sup>, attached at the backside of the copper carrier and next to the resonator PCB, respectively. The data for chip B are shown in Fig. A.1 (a). During heating of the copper carrier from the base temperature  $T_{\text{carrier}} = 10\text{ K}$  to  $T_{\text{carrier}} = 210\text{ K}$ , the electronics PCBs experience only a small temperature change within  $T_{\text{electronics}} \approx (8 - 10)\text{ K}$ . For chip A, a similar insulation was measured with  $T_{\text{electronics}} \approx (6 - 10)\text{ K}$ . During such local heating of the trap carrier, thermal gradients build up that result in a slightly lower temperature  $T_{\text{trap}}$  of the trap chip compared to the carrier temperature  $T_{\text{carrier}}$ , which is measured with the sensor. This effect can be calibrated out by means of the in situ 4-wire measurement of the on-chip YBCO meander resistors  $R_m$ . The temperature dependence  $R_m(T)$ , measured during a global warm-up of the entire cryogenic system, is used as a reference for the calibration. For the global warm-up, the temperature gradients are negligible and one can identify  $T_{\text{trap}} \approx T_{\text{carrier}}$ . This assumption is verified by the measured critical temperatures  $T_c$  in chips A and B, that agree with the values specified at ceraco ceramic coating GmbH within 1 K, which sets the accuracy of the temperature calibration. A temperature calibration curve is then established by comparing the temperature dependence  $R_m(T)$  measured when locally heating the trap carrier with the global warm-up reference. The blue data in Fig. A.1 (b) shows the temperature difference  $\Delta T = T_{\text{trap}} - T_{\text{carrier}}$  obtained in this way, as function of the carrier temperature  $T_{\text{carrier}}$  during local heating. For temperatures below  $T_c$  no data are available, since the

---

<sup>1</sup> Lakeshore, DT-670

## A. Appendix to the superconducting traps

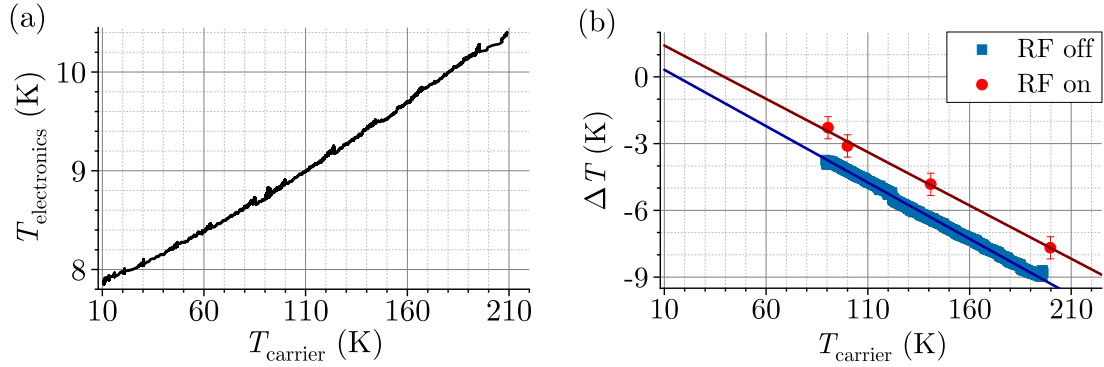


**Figure A.1.** (a) Characterization of the thermal decoupling showing the temperature  $T_{\text{electronics}}$  of the cryogenic electronics as function of the locally heated trap carrier temperature  $T_{\text{carrier}}$ . The uncertainty of the temperature measurements is about 0.01 K, determined from the root-mean-squared fluctuations of data without local heating over the course of 1 h. (b) Temperature calibration showing the temperature difference  $\Delta T$  between the temperature on the trap chip  $T_{\text{trap}}$  and the trap carrier  $T_{\text{carrier}}$  while locally heating the carrier. The blue and red data correspond to the trap’s RF drive being off and on, respectively. The solid lines are linear fits to the data.

meander resistance  $R_m$  vanishes. A linear fit is used to extrapolate  $\Delta T$  down to the base temperature around 10 K. The application of the RF drive leads to an additional heating of the trap chip and partially compensates the temperature gradient. This is shown by the red data in Fig. A.1 (b). RF pickup on the temperature sensor wires leads to a wrong reading, such that the calibration can only be done with the RF drive being off. The red data are obtained directly after switching off the drive, before relaxation of the system to the new steady state.

## A.2. DC voltage sets

A schematic overview of the 9 DC electrodes of the trap is shown in Fig. A.2. The DC voltage sets used for trap operation are derived from trap simulations<sup>2</sup> and are given in Tab. A.1. For the micromotion study described in chapter 7.3.1, the set  $\partial_{zz}\phi$  for axial confinement at the trap center  $z = 0$  is used. Different axial positions  $z \neq 0$  are obtained by application of the axial shim voltage set  $E_z$ . For the heating rate studies described in chapter 7.3.2, the confinement set  $\partial_{zz}\phi$  is scaled to realize different axial frequencies  $\omega_z$  for ions confined at the trap center.

<sup>2</sup> Unless stated otherwise, all trap simulations in this appendix were done with the electrode package for Python by R. Jördens (<https://github.com/nist-ionstorage/electrode>); see also [134, 135].

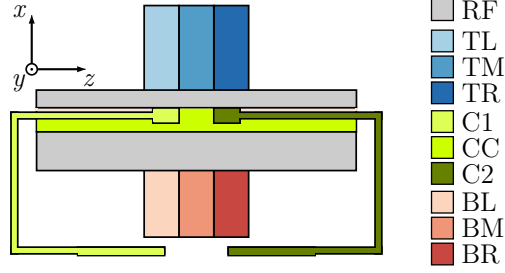


**Figure A.2.** Schematic view of the YBCO trap electrodes.

**Table A.1.** DC voltage sets for the measurements described in chapter 7.3. The labeling of the DC electrodes corresponds to the one in Fig. A.2. The set  $\partial_{zz}\phi$  is for axial confinement at the trap center with an axial frequency  $\omega_z = 2\pi \times 1.0$  MHz. The sets for micromotion compensation,  $E_i$ , are for a shift of about  $10\ \mu\text{m}$  in the respective direction at radial frequencies  $\omega_r \approx 2\pi \times 3$  MHz and axial frequency  $\omega_z = 2\pi \times 1.0$  MHz.

| voltage set         | electrode voltage (V) |         |        |        |        |        |        |         |        |
|---------------------|-----------------------|---------|--------|--------|--------|--------|--------|---------|--------|
|                     | TL                    | TM      | TR     | C1     | CC     | C2     | BL     | BM      | BR     |
| $\partial_{zz}\phi$ | 14.109                | -14.109 | 14.109 | 3.628  | 0.605  | 3.628  | 3.144  | -14.109 | 3.144  |
| $E_x$               | -1.966                | -5.105  | -1.966 | -0.484 | -0.484 | -0.484 | 1.215  | 1.718   | 1.215  |
| $E_y$               | 0.442                 | 1.275   | 0.442  | 1.342  | 1.342  | 1.342  | -0.371 | -0.514  | -0.371 |
| $E_z$               | 1.231                 | -0.000  | -1.231 | 0.000  | 0.000  | 0.000  | 0.272  | -0.000  | -0.272 |

### A.3. Details of the RF pickup model

In this section, the details of the RF pickup model are given, which is used in chapter 7.2 to derive quantitative estimates for the expected RF pickup fields in trap chip A for  $T < T_c$  and  $T > T_c$  (section 7.3.1). First, it will be argued that the excess micromotion measured in this study is indeed mainly caused by RF pickup fields from the DC electrodes, and not by an axial RF field  $E_z^{(\text{RF})}$ , generated directly by the RF electrodes. It will further be argued that the radial components of the RF pickup fields can be neglected compared to the axial component. Afterwards it will be shown that the dominant axial pickup fields are from electrodes C1, C2 and CC, in agreement with the estimates presented in Fig. 7.5. The electric parameters given in Tab. 7.2 are derived in the individual subsections at the end of this section.

The finite length of the RF rails leads to an RF field component  $E_z^{(\text{RF})}$  along the axis of the trap, causing excess micromotion. At the trap center,  $z = 0$ , the axial field  $E_z^{(\text{RF})}$  is zero due to the trap's mirror symmetry. With growing distance  $z$  from the center,  $E_z^{(\text{RF})}$  increases linearly within the investigated region  $z \in (-80, 80)\ \mu\text{m}$  as determined by trap simulation. At a position  $z = \pm 70\ \mu\text{m}$  and assuming an RF voltage  $U_{\text{RF}} = 219\ \text{V}$ , the simulations yield  $E_z^{(\text{RF})} \approx 14.2\ \text{V m}^{-1}$ , corresponding to a micromotion modulation

## A. Appendix to the superconducting traps

index  $\beta \approx 0.024$ . However, for the data set at  $T = 12$  K in Fig. 7.7, where this RF voltage was applied, the measured modulation index is  $\beta^{(\text{meas})} \approx 0.077$  at  $z \approx -71$   $\mu\text{m}$ . The contribution of  $E_z^{(\text{RF})}$  to this modulation index is only about 30%, the main contribution consequently stems from RF pickup fields on the DC electrodes. At  $T = 97$  K, the axial RF field  $E_z^{(\text{RF})}$  contributes only with 3%, as derived from the applied RF voltage  $U_{\text{RF}} = 238$  V and the value  $\beta^{(\text{meas})} \approx 0.85$  at  $z \approx -70$   $\mu\text{m}$  given by the linear fit to the measured data. The correct order of magnitude of the expected excess micromotion can hence be determined by considering only the contribution of RF pickup fields on the trap's DC electrodes, the contribution of  $E_z^{(\text{RF})}$  can be neglected for the estimate.

For the analysis of the RF pickup fields from the trap's DC electrodes, one needs to differentiate between the radial and axial field components. The net axial pickup field component  $E_z$  from all electrodes in sum fully contributes to micromotion that cannot be compensated, assuming a negligible axial RF field from the RF electrodes (see above). For the radial components  $E_x, E_y$ , the phase  $\phi_p$  of the pickup field relative to the RF drive voltage  $U_{\text{RF}}$  on the RF electrodes matters. If the pickup field is in phase with  $U_{\text{RF}}$ , i. e.  $\phi_p = 0$  or  $\phi_p = \pi$ , it merely shifts the position of the RF null, while for arbitrary phase angles there is also a contribution to the excess micromotion [72]. The analysis of the radial pickup field components can be simplified by noting that the RF pickup ratio  $\epsilon_p$  on electrode CC, listed in Tab. 7.2, is similar to that on all other electrodes in amplitude and phase, excluding electrodes C1 and C2. The pickup ratio depends on four quantities: the parasitic capacitances  $C_0$  and  $C_p$ , the connection line impedance  $Z_{\text{line}}$  and the filter capacitance  $C_f$ , which is identical for all electrodes. The capacitances  $C_0$  and  $C_p$  are of the same order of magnitude for all electrodes as evident from the trap geometry, and small variations in their exact values do not affect the pickup ratio as shown below. Furthermore, for all electrodes except C1 and C2, the wiring to the filter PCB is identical, yielding the same parameters for the connection line impedance  $Z_{\text{line}}$ . The electrodes C1 and C2 are special since their connection line impedance  $Z_{\text{line}}$  is dominated by the meander resistance  $R_m$  for  $T > T_c$ . The following discussion of the radial pickup field components is, therefore, limited to electrodes C1, C2 and CC (representative for all other electrodes). From the RF pickup model, Eq. (7.1), one can calculate the phase angle  $\phi_p$  of the RF pickup voltage  $U_p$ . Using the electrical parameters given in Tab. 7.2 for electrode CC (derived below) one calculates  $\phi_p^{(\text{CC})} \approx 179.4^\circ$  for  $T = 12$  K and  $\phi_p^{(\text{CC})} \approx 167.5^\circ$  for  $T = 97$  K. The phase angle at  $T = 12$  K is very close to  $\pi$ , such that the radial components  $E_x, E_y$  of the electrodes' pickup fields contribute negligibly to the excess micromotion. The reason for the phase angle to be close to  $\pi$  is that the inductive impedance  $\Omega_{\text{RF}} L_{\text{line}} \approx 4.7 \Omega \gg R_{\text{line}} = 48 \text{ m}\Omega$ , completely dominates the line impedance  $Z_{\text{line}}$  at the drive frequency  $\Omega_{\text{RF}} = 2\pi \times 17.58$  MHz. The phase angle is, therefore, not significantly affected by small

variations of the parasitic capacitances  $C_0$  and  $C_p$  between the different electrodes. At  $T = 97$  K, the estimated phase angle  $\phi_p^{(CC)}$  is larger. However, at this temperature the pickup fields from electrodes C1 and C2 dominate by two orders of magnitude, see Tab. 7.2. A larger phase angle is also expected for electrodes C1 and C2 at  $T > T_c$ , where  $Z_{\text{line}} \approx R_m$  resulting in a phase angle of  $\phi_p^{(C1, C2)} \approx 19.3^\circ$ . However, for these electrodes the horizontal component is approximately zero along the trap axes,  $E_x(z) \approx 0$ , due to the trap symmetry, and  $E_y$  is perpendicular to the laser beams such that micromotion in this direction does not add to the measured signal, see Eq. (7.4). In summary, the radial pickup field components can be neglected since they are either small or approximately in phase with the RF drive. This finding is corroborated by the measured position dependence of the excess micromotion shown in Fig. 7.7: the measured data show a clear minimum at the trap center,  $z = 0$ , in stark contrast to the radial pickup field components  $E_x, E_y$ , which have a basically constant dependence on the axial position over the entire measurement range  $z \in [-80, 80]$   $\mu\text{m}$  for all electrodes as derived by trap simulations.

The dominating axial pickup fields  $E_z(z)$  are those from the central electrodes C1, C2, and CC as is evident from the simulated fields shown in Fig. A.3. For a given RF pickup voltage  $U_p$ , the axial field components  $E_z$  from electrodes C1, C2 and CC are at least a factor ten larger than those from other electrodes. Neglecting the contributions of these electrodes to the excess micromotion, therefore, leads to an error of about 10% assuming similar RF pickup ratios  $\epsilon_p$ . In the remainder of this section, the electrical parameter of electrodes C1, C2 and CC, given in Tab. 7.2, are derived.

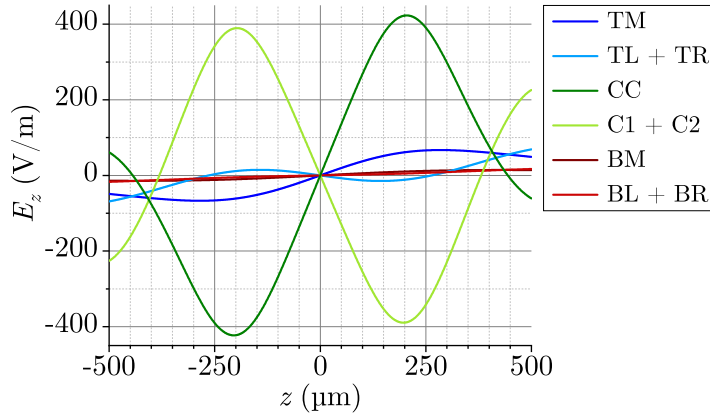


**Figure A.3.** Amplitude of the axial electric field component  $E_z$  for an RF pickup voltage  $U_p = 1$  V on either of the DC electrodes. The labeling of the electrodes is given in Fig. A.2. The “+” notation in the legend denotes the sum of individual electric fields from two electrodes at the same voltage  $U_p$ . The sum is used for electrodes, where identical pickup voltages  $U_p$  are expected due to the trap symmetry.

### A.3.1. Estimates for the parasitic capacitances $C_p$ , $C_0$

The parasitic capacitances between trap electrodes are determined by decomposing the trap into different cross sections  $i$  that stretch over a length  $l_i$ . Electric fields within the individual cross sections are calculated by means of a finite element simulation<sup>3</sup>. For each cross section, the parasitic capacitances  $C_p^{(i)}$  between electrodes C1, C2, CC and the RF electrode are determined by applying  $U = 1$  V DC to the RF electrode, calculating the resulting electric displacement field  $\mathbf{D}$  and evaluating the induced charge per length  $Q_{\text{ind}} = \oint_c \mathbf{D} \cdot d\mathbf{n}$  on the respective DC electrode. Here  $d\mathbf{n}$  represents the normal vector to each infinitesimal contour element and the integral runs over the entire contour  $c$  of the DC electrode. The parasitic capacitance is then given by  $C_p^{(i)} = l_i Q_{\text{ind}}/U$ . The total parasitic capacitance  $C_p = \sum_i C_p^{(i)}$  is the sum of the values of all cross sections. The parasitic capacitances to the ground electrode,  $C_0$ , are determined in an analogue fashion.

The sapphire substrate is modeled with a relative permittivity  $\epsilon_r^{(s)} = 10$ . The varnish between substrate and copper carrier is treated as an additional dielectric layer with unknown relative permittivity  $\epsilon_r^{(v)}$ . The copper carrier below the varnish is considered a grounded electrode. The coupling capacitances, Tab. 7.2, are given by the average of the results for the two extreme cases  $\epsilon_r^{(v)} = 1$  and  $\epsilon_r^{(v)} \rightarrow \infty$ ; uncertainties are given by the standard deviation.

### A.3.2. Estimates for the connection line impedance $Z_{\text{line}}$

Parts of this section are taken from Ref. [154], adapted for consistency with this thesis.

The impedance  $Z_{\text{line}} = R_{\text{line}} + i\omega L_{\text{line}}$  of the connection line between the trap's DC electrodes and the low-pass filters consists in general of a resistive part  $R_{\text{line}}$  and an inductive part  $L_{\text{line}}$ . First, the resistive part  $R_{\text{line}} = R_{\text{el}} + R_{\text{wb}} + R_{\text{tr}} + R_{\text{ct}}$  is calculated, which consists of the resistance  $R_{\text{el}}$  of the trap electrodes and meander leads, the resistance  $R_{\text{wb}}$  of the gold wire bonds, the resistance  $R_{\text{tr}}$  of the gold-plated copper trace on the filter PCB, and the sum of the contact resistances from wire bond to chip and from bond to PCB,  $R_{\text{ct}}$ . Bonds made by the bonding machine used to connect the electrodes have typical contact resistances of  $R_{\text{ct}} \approx 75$  m $\Omega$  at room-temperature. In the following, it is assumed that the contact resistances do not vary with temperature. The wire bonds have a diameter  $D_{\text{wb}} = 25$   $\mu\text{m}$  and a typical length  $l_{\text{wb}} \approx 1$  cm. The bond radius is larger than the skin depth  $\zeta_{\text{skin}}^{(\text{Au})}$  at  $\Omega_{\text{RF}} = 2\pi \times 17.58$  MHz, such that for the further calculation an outer ring with thickness  $\zeta_{\text{skin}}^{(\text{Au})}$  is considered instead of the

<sup>3</sup> COMSOL Multiphysics, version 5.3a.

full bond cross section. The skin depth  $\zeta_{\text{skin}}$  in a material is given by [106]

$$\zeta_{\text{skin}} = \sqrt{\frac{2\rho}{\omega\mu}}, \quad (\text{A.1})$$

where  $\rho$  is the resistivity of the material,  $\mu$  its permeability and  $\omega$  the frequency of the applied AC electric field. At  $T = 14\text{ K}$ , the skin depth in gold is  $\zeta_{\text{skin}}^{(\text{Au})} \approx 1.9\ \mu\text{m}$ , using  $\mu = \mu_0 = 4\pi \times 10^{-7}\ \text{H m}^{-1}$ ,  $\omega = \Omega_{\text{RF}}$  and a typical resistivity of  $\rho_{\text{Au}} \approx 0.026 \times 10^{-8}\ \Omega\ \text{m}$  [159]. A single wire bond's resistance at  $T = 14\text{ K}$  is then  $R_{\text{wb}} \approx 18.5\ \text{m}\Omega$ .

The traces have a width  $w_{\text{tr}} = 300\ \mu\text{m}$ , a thickness  $t_{\text{tr}} = 100\ \mu\text{m}$  and an approximate length  $l_{\text{tr}} \approx 3\ \text{cm}$  to the filter capacitor  $C_f = 330\ \text{nF}$ . The trace thickness is larger than the skin depth  $\zeta_{\text{skin}}^{(\text{Cu})}$  in copper at  $\Omega_{\text{RF}} = 2\pi \times 17.58\ \text{MHz}$ , therefore the trace thickness is replaced by twice the skin depth in the following. At  $T = 14\text{ K}$ , the skin depth in copper is  $\zeta_{\text{skin}}^{(\text{Cu})} \approx 0.56\ \mu\text{m}$ , using a typical resistivity  $\rho_{\text{Cu}} \approx 0.0022 \times 10^{-8}\ \Omega\ \text{m}$  [159]. The trace resistance is then  $R_{\text{tr}} \approx 2.0\ \text{m}\Omega$ . The electrode and lead resistances can be neglected below the superconducting transition,  $R_{\text{el}} \approx 0$  (see appendix A.4.1). In sum, one arrives at a connection line resistance to electrodes C1 and C2 of  $R_{\text{line}}^{(\text{C1,C2})} = R_{\text{el}} + R_{\text{ct}} + R_{\text{wb}} + R_{\text{tr}} \approx 95\ \text{m}\Omega$  at  $T = 14\text{ K}$ . The CC electrode is connected with a double bond, such that the wire bond and contact resistances need to be reduced by a factor two,  $R_{\text{line}}^{(\text{CC})} \approx 48\ \text{m}\Omega$  at  $T = 14\text{ K}$ .

At  $T = 97\text{ K}$ , the typical gold resistivity  $\rho_{\text{Au}} \approx 0.65 \times 10^{-8}\ \Omega\ \text{m}$  [159] with corresponding skin depth  $\zeta_{\text{skin}}^{(\text{Au})} \approx 9.7\ \mu\text{m}$  leads to a single bond resistance  $R_{\text{wb}} \approx 139.5\ \text{m}\Omega$ . The trace resistance is  $R_{\text{tr}} \approx 24.6\ \text{m}\Omega$ , using a typical copper resistivity  $\rho_{\text{Cu}} \approx 0.35 \times 10^{-8}\ \Omega\ \text{m}$  [159] with corresponding skin depth  $\zeta_{\text{skin}}^{(\text{Cu})} \approx 7.1\ \mu\text{m}$ . The electrode resistance is given by the gold top layer, which has a thickness of  $t_{\text{Au}} = 200\ \text{nm}$ . The length of the CC electrode from the trap center to the wire bond is  $l_{\text{CC}} = 3.65\ \text{mm}$  and the average width is  $w_{\text{CC}} = 130\ \mu\text{m}$ , leading to a resistance  $R_{\text{el}} = 913\ \text{m}\Omega$  using a resistivity  $\rho_{\text{Au}} \approx 0.65 \times 10^{-8}\ \Omega\ \text{m}$  [159]. The total connection line resistance for the CC electrode at  $T = 97\text{ K}$  is then  $R_{\text{line}}^{(\text{CC})} = R_{\text{ct}}/2 + R_{\text{wb}}/2 + R_{\text{tr}} + R_{\text{el}} \approx 1044\ \text{m}\Omega$ . For the electrodes C1 and C2 the connection line resistance at  $T = 97\text{ K}$  is completely dominated by the YBCO meander resistance,  $R_{\text{line}}^{(\text{C1,C2})} \approx R_{\text{m}} = 14.9(2)\ \text{k}\Omega$ .  $R_{\text{m}}$  is determined by a 4 point measurement.

The connection line inductance  $L_{\text{line}}$  is calculated as the sum of the inductances of the bonding wire and the PCB trace. For the electrodes C1 and C2 there is an additional contribution of the lead wires on the trap chip and of the meander line. The inductances for wire bonds and traces are calculated using [189, 190]

$$L_{\text{wire, single}} = \frac{\mu_0 l_{\text{wb}}}{2\pi} \left[ \ln \left( \frac{2l_{\text{wb}}}{r_{\text{wb}}} \right) - \frac{3}{4} \right], \quad (\text{A.2a})$$

## A. Appendix to the superconducting traps

$$L_{\text{wire, double}} = \frac{\mu_0 l_{\text{wb}}}{2\pi} \left[ \ln \left( \frac{2l_{\text{wb}}}{\sqrt{r_{\text{wb}} d_{\text{wires}}}} \right) - \frac{7}{8} \right], \quad (\text{A.2b})$$

$$L_{\text{trace}} = \frac{\mu_0 l_{\text{tr}}}{2\pi} \left[ \ln \left( \frac{2l_{\text{tr}}}{w_{\text{tr}} + t_{\text{tr}}} \right) + \frac{1}{2} \right], \quad (\text{A.2c})$$

where  $\mu_0 = 4\pi \times 10^{-7} \text{ H m}^{-1}$  is the vacuum permeability and  $r_{\text{wb}} = D_{\text{wb}}/2$  is the bond radius. The inductance  $L_{\text{wire, double}}$  takes into account the mutual inductance between the double wire bonds, which have a mean distance  $d_{\text{wires}} \approx 350 \mu\text{m}$ . Using the above values for the wire bond and trace geometry, one calculates a connection line inductance of  $L_{\text{line}}^{(\text{CC})} = L_{\text{wire, double}} + L_{\text{trace}} \approx 10 \text{ nH} + 33 \text{ nH} = 43 \text{ nH}$  for the CC electrode.

For the electrodes C1, C2 there is an additional contribution from the lead trace on the trap chip that connects the electrode with the YBCO meander and from the meander itself. The lead trace has a width  $w_{\text{le}} = 50 \mu\text{m}$ , a thickness  $t_{\text{le}} = 200 \text{ nm}$  and a length  $l_{\text{le}} = 5.6 \text{ mm}$ , resulting in an inductance  $L_{\text{lead}} \approx 7 \text{ nH}$ , using Eq. (A.2c). The inductance of the YBCO meander structure is calculated using the monomial expression [191]

$$L_{\text{meander}} = 0.00266 a_{\text{me}}^{0.0603} h_{\text{me}}^{0.4429} d_{\text{me}}^{0.606} w_{\text{me}}^{-0.173} N_{\text{me}}^{0.954}, \quad (\text{A.3})$$

where the geometrical parameters  $a_{\text{me}}, h_{\text{me}}, d_{\text{me}}, w_{\text{me}}$  are all in  $\mu\text{m}$  and the resulting inductance is in nH. The YBCO meander structures connected to electrodes C1, C2 have an approximate lead length  $a_{\text{me}} = 35 \mu\text{m}$ , segment length  $h_{\text{me}} = 420 \mu\text{m}$ , half pitch  $d_{\text{me}} = 20 \mu\text{m}$  and trace width  $w_{\text{me}} = 10 \mu\text{m}$ . The number of segments with full length  $h$  is  $N_{\text{me}} = 12$ . The corresponding inductance is  $L_{\text{meander}} \approx 2 \text{ nH}$ . The total inductance of the connection line to electrodes C1, C2 is then  $L_{\text{line}}^{\text{C1, C2}} = L_{\text{wire, single}} + L_{\text{trace}} + L_{\text{lead}} + L_{\text{meander}} \approx 13 \text{ nH} + 33 \text{ nH} + 7 \text{ nH} + 2 \text{ nH} = 55 \text{ nH}$ .

### A.3.3. Low pass filter components

The low pass filters used in the experiment are identical to those described in chapter 4.1.2. The values in Tab. 7.2 correspond to the components' specifications,  $R_{\text{f}} = 100 \Omega^4$  and  $C_{\text{f}} = 330 \text{ nF}^5$ . The actual filter circuit contains a second capacitor,  $C'_{\text{f}} = 470 \text{ pF}^6$  placed in parallel with  $C_{\text{f}}$ . Due to the much smaller capacitance of  $C'_{\text{f}}$ , this second capacitor was omitted in the calculation of the RF pick up ratio  $\epsilon$ , Eq. (7.1).

<sup>4</sup> Vishay, Y1625100R000Q9R

<sup>5</sup> Kemet, C2220C334J1GACTU

<sup>6</sup> Kemet, C0805C471J1GACTU

## A.4. Sources of electric field noise

This section is taken from Ref. [154], adapted for consistency with this thesis.

### A.4.1. Johnson noise from the YBCO meander leads

In this section, the estimates for a heating rate originating from JN in the YBCO meander leads in chip A, Tab. 7.3, are derived. Above the superconducting transition,  $T > T_c$ , the meander lead resistance  $R_m$  is determined by a 4-wire resistance measurement. The DC resistance equals to good approximation the resistance in the RF domain, since the YBCO film thickness  $t_{\text{YBCO}} = 50 \text{ nm}$  is much smaller than the skin depth: From the measured DC resistance  $R_m = 14.9(2) \text{ k}\Omega$  at  $T = 97(1) \text{ K}$ , one calculates the resistivity of the YBCO film in chip A,  $\rho_{\text{YBCO}}^{(100\text{K})} = R_m t_{\text{YBCO}} w_{\text{me}} / l_{\text{me}} \approx 1.44 \times 10^{-6} \Omega \text{ m}$ , using the length  $l_{\text{me}} = 5.18 \text{ mm}$  and the width  $w_{\text{me}} = 10 \mu\text{m}$  of the lead meander. This resistivity corresponds to a skin depth  $\zeta_{\text{skin}} \approx 604 \mu\text{m}$ , using Eq. (A.1) and assuming  $\mu = \mu_0 = 4\pi \times 10^{-7} \text{ H m}^{-1}$  [192] and  $\omega = 2\pi \times 1.0 \text{ MHz}$ . From the measured meander lead resistance  $R_m = 14.9(2) \text{ k}\Omega$  one then calculates the electric field noise  $S_E \approx 3.07(4) \times 10^{-12} \text{ V}^2 \text{ m}^{-2} \text{ Hz}^{-1}$  from a single meander lead, using Eqs. (3.8) and (3.9) with the characteristic distance  $\delta_c = 5.1 \text{ mm}$  of electrodes C1 and C2. The heating rate estimate,  $\Gamma_{\text{h}}^{\text{est.}} = 897(12) \text{ phonons/s}$  at  $\omega_z = 2\pi \times 1.0 \text{ MHz}$ , is calculated from Eq. (3.7) using the sum,  $2S_E$ , of the electric field noises from electrodes C1 and C2.

For temperatures  $T < T_c$ , the resistivity of YBCO in the RF domain is extremely small but finite [193]. The specified value for the resistivity of a YBCO film produced at ceraco is  $\rho_{\text{YBCO}} \approx 3.3 \times 10^{-11} \Omega \text{ m}$  at  $f = 10.9 \text{ GHz}$  and  $T = 10 \text{ K}$ <sup>7</sup>. Extrapolating the known quadratic scaling of the resistivity with frequency [194] down to the MHz regime, one calculates a resistivity  $\rho_{\text{YBCO}}^{(10\text{K})} = 2.8 \times 10^{-19} \Omega \text{ m}$  at  $f = 1.0 \text{ MHz}$  and  $T = 10 \text{ K}$ . For the 50 nm thick YBCO film used in chip A, the meander resistance at  $f = 1.0 \text{ MHz}$  and  $T = 10 \text{ K}$  is then  $R_m = \rho_{\text{YBCO}}^{(10\text{K})} l_{\text{me}} / (w_{\text{me}} t_{\text{YBCO}}) = 2.9 \text{ n}\Omega$ , with a corresponding electric field noise  $S_E = 6.1 \times 10^{-26} \text{ V}^2 \text{ m}^{-2} \text{ Hz}^{-1}$ . This leads to a heating rate estimate from both meanders of  $\Gamma_{\text{h}}^{\text{est.}} = 1.8 \times 10^{-11} \text{ phonons/s}$  at  $\omega_z = 2\pi \times 1.0 \text{ MHz}$  and  $T = 10 \text{ K}$ .

The meander lead resistance at  $T = 80 \text{ K}$  is calculated from  $\rho_{\text{YBCO}}^{(10\text{K})}$ , assuming a temperature scaling of the YBCO resistivity of  $\rho_{\text{YBCO}}(T) \propto (T/T_c)^2 (1 - (T/T_c)^2) / (1 - (T/T_c)^4)^2$  [195]. The resulting resistivity,  $\rho_{\text{YBCO}}^{(80\text{K})} = 4.4 \times 10^{-17} \Omega \text{ m}$  at  $f = 1.0 \text{ MHz}$  and  $T = 80 \text{ K}$ , corresponds to a meander resistance  $R_m = 460 \text{ n}\Omega$ . This resistance leads to an electric field noise  $S_E = 7.8 \times 10^{-23} \text{ V}^2 \text{ m}^{-2} \text{ Hz}^{-1}$  and a heating rate estimate  $\Gamma_{\text{h}}^{\text{est.}} = 2.3 \times 10^{-8} \text{ phonons/s}$  at  $\omega_z = 2\pi \times 1.0 \text{ MHz}$  and  $T = 80 \text{ K}$ .

<sup>7</sup> The specified sheet resistance of a 330 nm thick YBCO film produced by Ceraco ceramic coating GmbH, Ismaning, Germany is  $\rho_{\text{YBCO}} \approx 0.1 \text{ m}\Omega$  at  $f = 10.9 \text{ GHz}$  and  $T = 10 \text{ K}$ .

#### A.4.2. Exclusion of Johnson noise for the experiments in chip B

In this section it is shown that JN can be excluded as the dominant noise source of the measured heating rates in chip B (Figs. 7.9, 7.10 and 7.11). First, it is noted that JN from the trap electrodes, bonding wires and PCB traces, which are not filtered by the low-pass filters, should have a flat frequency dependence, see Eq. (3.8). This is in clear contrast to the approximate  $1/f$  scaling of the electric field noise corresponding to the measured heating rate data. JN from the low-pass filters is excluded by the temperature scaling. As the trap chip is heated to  $T = 200$  K, the filter temperature changes by only  $\Delta T_f \approx 2$  K or roughly a factor 0.2, due to the thermal insulation, see Fig. A.1 (a). Assuming a constant filter resistance in the range  $\Delta T_f$ , JN scales linearly with temperature, see Eq. (3.8). The electric field noise produced by the filters should therefore increase by about a factor 0.2 as well. In contrast, the measured noise level increases from  $c = 0.69(4)$  phonons/s at  $T = 14$  K to  $c = 19.7(6)$  phonons/s at  $T = 206$  K, see Fig. 7.11 (b). This corresponds to a change of about a factor 20, a hundredfold larger than the change expected from JN from the filters. Furthermore, the linear temperature dependence expected for JN from the filters does not correlate with the plateau-region measured for the heating rate for  $T > T_c$ .

In addition to the scaling arguments above, electric field noise estimates from JN are calculated for two temperature regimes,  $T < T_c$  and  $T > T_c$ . Electric field noise  $S_E^{(\text{JN})}$  from each electrode is caused by JN in three resistances: the electrode resistance  $R_{\text{el}}$ , the resistance  $R_{\text{line}}$  of the connection line to the low-pass filter, and the effective resistance  $R_{\text{filter}}$  of the filter itself. These resistances are calculated in the following subsections, for simplicity at only one temperature in each regime: for  $T < T_c$  at  $T = T_c \approx 90$  K, and for  $T > T_c$  at  $T = 200$  K, the highest temperature used in the experiments. All electrodes except CC are at distances larger than the ion-surface separation  $d$  from the trap center, where the ions are trapped in the heating rate measurements. The resistances  $R_{\text{el}}$  of these electrodes are, therefore, treated in the same fashion as  $R_{\text{line}}$  and  $R_{\text{filter}}$ , i. e., as common noise on the respective electrode. The electric field noise  $S_E^{(\text{JN})}$  produced by the total resistance  $R_{\text{tot}} = R_{\text{el}} + R_{\text{line}} + R_{\text{filter}}$  at the position of the ion is then calculated using Eqs. (3.8) and (3.9), with the individual electrodes' characteristic distances  $\delta_c$  derived from trap simulations. In particular for electrodes C1 and C2, which produce the largest JN as shown below, this is a reasonable approach: the vast majority of the resistances of electrodes C1 and C2 comes from the gold leads on the trap chip, whose impact on the electrodes' characteristic distance is negligible (cf. Fig. A.2). The same argument holds for the other electrodes, except CC. Electrode CC is directly below the trap center, such that JN within the electrode itself cannot be modeled as common noise. In the superconducting regime,  $T < T_c$ , the electrode resistivity is extremely

small and the corresponding JN can be neglected (see next subsection for details). For  $T > T_c$ , the resistance of the CC electrodes is dominated by the exposed YBCO area at the electrode center, which has a significantly larger resistivity than the gold covering the edges of the CC electrode. This fact is used to estimate the JN, as illustrated in Fig. A.4. The CC electrode is divided in three areas: the central area with high resistivity, where the YBCO is exposed, and the two leads on either side, which have a gold top layer. The left gold lead is connected to the low-pass filtered supply line and considered to be on RF ground. The exposed YBCO area is modeled as a resistor adding noise to the gold lead on the right side. The voltage fluctuations on this “noisy” lead are treated as common noise due to the high conductivity of the gold compared to the normal-state YBCO. The electric field noise at the trap center is then calculated from the characteristic distance  $\delta_c$  of the noisy lead. The details of this calculation are given in the next subsection. For geometric reasons, noise from the exposed YBCO on other trap electrodes should be smaller than the estimate for the CC electrode and is therefore neglected.

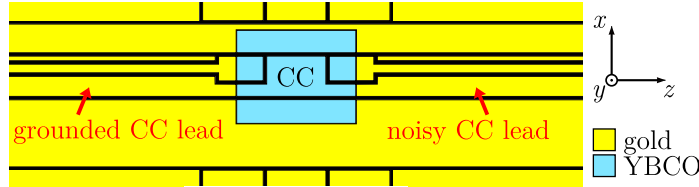


**Figure A.4.** Schematic view of the electrodes in the trap center illustrating the calculation of JN from electrode CC for  $T > T_c$ . The left lead of the CC electrode is connected to the RF ground on the filter board. The central area, where the YBCO is exposed, is modeled as a resistor adding JN to the “noisy” electrode lead on the right. The voltage fluctuations on the noisy lead induce electric field noise at the trap center.

Tab. A.2 lists the JN estimates for all trap electrodes. For  $T < T_c$ , the sum of the electric field noise contributions from all electrodes is  $S_{E,\text{tot}}^{(\text{JN})} = 9.6 \times 10^{-17} \text{ V}^2 \text{ m}^{-2} \text{ Hz}^{-1}$ . This is two orders of magnitude smaller than the value  $S_E = 2.3 \times 10^{-14} \text{ V}^2 \text{ m}^{-2} \text{ Hz}^{-1}$ , which corresponds to the smallest measured heating rate  $\Gamma_h \approx 2.1$  phonons/s at  $T = 83$  K and  $\omega_z = 2\pi \times 1.6$  MHz. The estimate  $S_{E,\text{tot}}^{(\text{JN})}$ , despite being calculated for  $T = 90$  K, is also still about a factor thirty smaller than the noise level  $S_E = 3.3 \times 10^{-15} \text{ V}^2 \text{ m}^{-2} \text{ Hz}^{-1}$ , which corresponds to the smallest measured heating rate  $\Gamma_h \approx 0.3$  phonons/s at  $T = 14$  K and  $\omega_z = 2\pi \times 1.6$  MHz. For  $T > T_c$ , the sum of the noise contributions from all electrodes gives an electric field noise  $S_{E,\text{tot}}^{(\text{JN}, 200 \text{ K})} = 1.3 \times 10^{-14} \text{ V}^2 \text{ m}^{-2} \text{ Hz}^{-1}$ . This is around a factor 7 smaller than the noise  $S_E = 9.3 \times 10^{-14} \text{ V}^2 \text{ m}^{-2} \text{ Hz}^{-1}$ , which corresponds to the smallest measured heating rate  $\Gamma_h \approx 8.5$  phonons/s at  $T = 206$  K and  $\omega_z = 2\pi \times 1.6$  MHz. For smaller temperatures, the estimate has to be adjusted in or-

## A. Appendix to the superconducting traps

der to make a meaningful statement. For  $T = 100$  K, a better estimate  $S_{E,\text{tot}}^{(\text{JN}, 100 \text{ K})} = S_{E,\text{tot}}^{(\text{JN}, 200\text{K})}/4.5 = 2.9 \times 10^{-15} \text{ V}^2\text{m}^{-2}\text{Hz}^{-1}$  is derived by taking into account the factor two smaller temperature and the factor 2.25 smaller resistivity of the gold top layer [159], which gives the dominant contribution to JN in this regime through the total resistance  $R_{\text{tot}} = 15.1 \Omega$  of electrodes C1 and C2.  $S_{E,\text{tot}}^{(\text{JN}, 100 \text{ K})}$  is around a factor 13 smaller than the noise level  $S_E = 3.6 \times 10^{-14} \text{ V}^2\text{m}^{-2}\text{Hz}^{-1}$ , that corresponds to the smallest measured heating rate  $\Gamma_{\text{h}} \approx 3.3$  phonons/s at  $T = 97$  K and  $\omega_z = 2\pi \times 1.6$  MHz.

**Table A.2.** Estimates for JN-induced electric field noise  $S_E^{(\text{JN})}$  from each trap electrode for  $T < T_c$  and  $T > T_c$ . The labeling of the electrodes is given in Fig. A.2. The estimates are calculated from the total effective resistances  $R_{\text{tot}}$  connected to the electrodes and their characteristic distance  $\delta_c$ , using Eqs. (3.8) and (3.9) at a temperature  $T = 90$  K ( $T < T_c$ ) and  $T = 200$  K ( $T > T_c$ ), respectively. Electrodes CC, TM and TB are mirror symmetric with respect to the trap center, such that common noise on either electrode does not induce electric field noise along the trap axis,  $S_E^{(\text{JN})} = 0$ , as reflected by the characteristic distance  $\delta_c = \infty$ . The estimate for electrode CC at  $T > T_c$  (marked with \*) is calculated from the resistance  $R^{\text{A}_{\text{YBCO}}} = 31.6 \Omega$  of the exposed YBCO area and the characteristic distance  $\delta_c = 24.3$  mm of the noisy gold lead.

| electrode | $\delta_c$ (mm)  | $T < T_c$                     |                                                              | $T > T_c$                     |                                                              |
|-----------|------------------|-------------------------------|--------------------------------------------------------------|-------------------------------|--------------------------------------------------------------|
|           |                  | $R_{\text{tot}}$ ( $\Omega$ ) | $S_E^{(\text{JN})} (\frac{\text{V}^2}{\text{m}^2\text{Hz}})$ | $R_{\text{tot}}$ ( $\Omega$ ) | $S_E^{(\text{JN})} (\frac{\text{V}^2}{\text{m}^2\text{Hz}})$ |
| C1, C2    | 5.10             | 0.235                         | $4.49 \times 10^{-17}$                                       | 15.1                          | $6.41 \times 10^{-15}$                                       |
| TL, TR    | 15.7             | 0.140                         | $2.83 \times 10^{-18}$                                       | 0.882                         | $3.96 \times 10^{-17}$                                       |
| BL, BR    | 71.5             | 0.140                         | $1.36 \times 10^{-19}$                                       | 0.882                         | $1.91 \times 10^{-18}$                                       |
| CC        | $\infty$ / *24.3 | 0.140                         | 0                                                            | *31.6                         | * $5.94 \times 10^{-16}$                                     |
| TM, BM    | $\infty$         | 0.140                         | 0                                                            | 0.882                         | 0                                                            |

In summary, JN from the considered sources is negligible compared to the measured noise for temperatures  $T < T_c$ . For  $T > T_c$ , the estimates are smaller than the measured noise, but are on the same order of magnitude. The largest amount of JN is expected for the data at  $T = 206$  K, where the JN noise estimate is only a factor 7 smaller than the smallest measured noise, corresponding to a JN contribution of about 14%. The details of the noise calculation are given in the following subsections.

### Trap electrodes

In the superconducting regime,  $T < T_c$ , the electrode resistivity is given by the extremely small resistivity  $\rho_{\text{YBCO}}$  of the YBCO film, such that JN from the trap electrodes, including CC, can be neglected. The resistivity  $\rho_{\text{YBCO}}^{(80\text{K})} = 4.4 \times 10^{-17} \Omega \text{ m}$  at  $f = 1.0$  MHz and  $T = 80$  K, calculated in section A.4.1, is seven orders of magnitude smaller than the resistivity  $\rho_{\text{Au}}^{(10\text{K})} = 2.3 \times 10^{-10} \Omega \text{ m}$  of gold at  $T = 10$  K [159].

For temperatures  $T > T_c$ , the resistances  $R_{\text{el}}$  of all trap electrodes except CC are given by the gold top layer, which has a thickness of  $t_{\text{Au}} = 200 \text{ nm}$ . Using a typical resistance  $\rho_{\text{Au}} = 1.46 \times 10^{-8} \Omega \text{ m}$  at  $T = 200 \text{ K}$  [159], gives a sheet resistance of  $\varrho_{\text{Au}}^{(200\text{K})} = \rho_{\text{Au}}/t_{\text{Au}} = 73.1 \text{ m}\Omega$ . From the gold sheet resistance one calculates the resistance of the trap electrodes from the trap geometry. The electrodes C1 and C2 have the largest resistance  $R_{\text{el}}^{(\text{C1, C2})} = 14.7 \Omega$  due to their elongated form stretching to the chip edge, with an average length of  $l_{\text{C1,C2}} = 10.0 \text{ mm}$  and a width of  $w_{\text{C1,C2}} = 50.0 \mu\text{m}$ . The electrodes TL, TM, TR, BL, BM and BR have identical geometries with lengths  $l_{\text{other}} = 3.00 \text{ mm}$  and widths  $w_{\text{other}} = 340 \mu\text{m}$ , giving rise to a resistance  $R_{\text{el}}^{(\text{other})} = 0.645 \Omega$ . The electrode resistances  $R_{\text{el}}$  are part of the value of the total resistance  $R_{\text{tot}}$  in Tab. A.2, which is used for the electric field noise estimate.

For electrode CC, the resistance  $R^{\text{A}_{\text{YBCO}}}$  of the exposed YBCO area, from the grounded gold lead to the noisy lead, needs to be calculated. First, the YBCO sheet resistance  $\varrho_{\text{YBCO}}^{(200\text{K})} = R_{\text{m}}w_{\text{me}}/l_{\text{me}} \approx 4.94 \Omega$  is determined from the measurement of the YBCO meander resistance  $R_{\text{m}} = 2.54 \text{ k}\Omega$  at  $T = 200 \text{ K}$ , using the meander dimensions given in section A.4.1. From the dimensions of the exposed YBCO area  $\mathcal{A}_{\text{YBCO}}$  within electrode CC one then finds a resistance  $R^{\text{A}_{\text{YBCO}}} = 31.6 \Omega$ . From this resistance, the electric field noise is calculated, using Eqs. (3.8) and (3.9) at a temperature  $T = 200 \text{ K}$  and the characteristic distance  $\delta_c = 24.3 \text{ mm}$  of the noisy gold lead of electrode CC.

## Cabling

Each of the trap's DC electrodes is connected to its first order RC filter via a gold wire bond and a gold-plated copper trace on the filter PCB. Electrodes C1 and C2 are singly bonded, all other electrodes are doubly bonded. The calculation of the total cabling resistance is identical to the one for the connection line resistance of electrodes C1, C2 and CC in appendix A.3.2, where all geometrical parameters are given.

At  $T = 90 \text{ K}$ , the typical gold resistivity  $\rho_{\text{Au}} \approx 0.566 \times 10^{-8} \Omega \text{ m}$  [159] leads to a single bond resistance  $R_{\text{wb}} \approx 115.3 \text{ m}\Omega$ . The trace resistance is  $R_{\text{tr}} \approx 6.66 \text{ m}\Omega$ , using a typical copper resistivity  $\rho_{\text{Cu}} \approx 0.281 \times 10^{-8} \Omega \text{ m}$  [159] with twice the corresponding skin depth  $\zeta_{\text{skin}}^{(\text{Cu})} \approx 21.1 \mu\text{m}$  at  $\omega = 2\pi \times 1.6 \text{ MHz}$  as effective trace thickness. The contact resistances of wire bond to trap chip and bond to PCB are assumed to be identical to the values measured at room temperature, in sum  $R_{\text{ct}} = 75 \text{ m}\Omega$ . The total connection line resistance for the electrodes C1 and C2 at  $T = 90 \text{ K}$  is then  $R_{\text{line}}^{(\text{C1,C2})} = R_{\text{ct}} + R_{\text{wb}} + R_{\text{tr}} = 197 \text{ m}\Omega$ . All other electrodes are doubly bonded, such that the contributions of  $R_{\text{ct}}$  and  $R_{\text{wb}}$  are reduced by a factor two,  $R_{\text{line}}^{(\text{other})} = R_{\text{ct}}/2 + R_{\text{wb}}/2 + R_{\text{tr}} = 102 \text{ m}\Omega$ .

At  $T = 200 \text{ K}$ , the typical gold resistivity  $\rho_{\text{Au}} \approx 1.46 \times 10^{-8} \Omega \text{ m}$  [159] leads to a single bond resistance  $R_{\text{wb}} \approx 297.8 \text{ m}\Omega$ . The trace resistance is  $R_{\text{tr}} \approx 12.9 \text{ m}\Omega$ , using

## A. Appendix to the superconducting traps

a typical copper resistivity  $\rho_{\text{Cu}} \approx 1.05 \times 10^{-8} \Omega \text{ m}$  [159] with corresponding skin depth  $\zeta_{\text{skin}}^{(\text{Cu})} \approx 40.7 \mu\text{m}$  as effective trace thickness. The total connection line resistance for the electrodes C1 and C2 at  $T = 200 \text{ K}$  is then  $R_{\text{line}}^{(\text{C1,C2})} = R_{\text{ct}} + R_{\text{wb}} + R_{\text{tr}} = 385 \text{ m}\Omega$ . For all other electrodes one gets  $R_{\text{line}}^{(\text{other})} = 199 \text{ m}\Omega$ .

### Low-pass filters

The resistances  $R_f$ ,  $R_a$ ,  $R_b$  within the RC filter circuit are another source of JN. The corresponding electric field noise is calculated by considering the effective real resistance  $R_{\text{filter}} = R_{\text{eff}}$  of the circuit from the perspective of the trap electrode [87]. For the filter circuit shown in Fig. A.5 (a) the effective real resistance is given by

$$R_{\text{eff}} = \text{Re} \left\{ \left( \frac{-i}{\omega C_{\text{el}}} \right) \parallel \left( R_b - \frac{i}{\omega C_b} \right) \parallel \left( R_a - \frac{i}{\omega C_a} \right) \parallel R_f \right\}, \quad (\text{A.4})$$

where  $a \parallel b$  denotes the impedance of two elements  $a$ ,  $b$  in parallel. The ESR of the filter capacitors is frequency dependent. Within the relevant frequency range  $\omega_z = 2\pi \times (0.4 - 1.8) \text{ MHz}$  the maximal ESRs are  $R_a = 24(1) \text{ m}\Omega$  and  $R_b = 1.3(1) \Omega$  according to the room temperature specification of the capacitors. This gives rise to a maximal effective real resistance  $R_{\text{filter}} = R_{\text{eff}} = 38(1) \text{ m}\Omega$ .

### A.4.3. Exclusion of external technical noise

External noise sources, in particular technical noise, are ruled out as cause of the measured temperature dependence of the heating rates. The measured data in Figs. 7.9, 7.10 and 7.11 show a clear increase of the heating rate with rising trap chip temperature  $T$ . External noise, in contrast, is not correlated with the trap chip temperature  $T$ , with exception of the supply for the local heater. This supply is excluded as origin of the measured noise: additional low-pass filtering of the output of this supply with a first order RC filter with a cut-off frequency around 1.6 kHz did not change the measured heating rates. An increase of a technical noise-limited heating rate with  $T$  through a variation in the cryogenic DC filter attenuation is excluded as well. The filter attenuation increases with rising  $T$ , as is shown in the following.

The thermal decoupling incorporated in the setup ensures that during local heating of the trap chip to temperatures  $T = (10 - 200) \text{ K}$ , the cryogenic environment, in particular the low-pass filters, stays at a nearly constant temperature  $T_f \approx (8 - 10) \text{ K}$ <sup>8</sup>, see Fig. A.1 (a). The change in  $T_f$  is small, but it might still lead to a variation in the attenuation of external technical noise by the low-pass filters. Therefore, the temperature dependence of the transfer function of the cryogenic low-pass filters is measured. The

<sup>8</sup> For chip A, a similar insulation was measured with  $T_f \approx (10 - 14) \text{ K}$ .

filters, all identical, are placed only a few centimeters away from the trap and suppress noise that might reach the trap electrodes through the DC lines. The equivalent circuit of these first order RC filters is shown in Fig. A.5 (a). The filter consists of a resis-

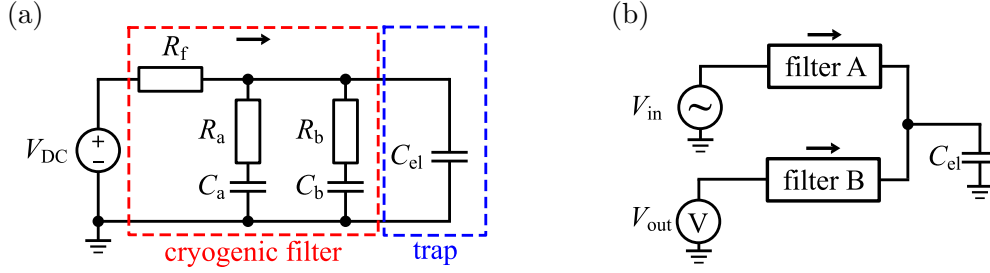


**Figure A.5.** (a) RC low-pass filter circuit used between the DC supplies and the trap electrodes. (b) Schematic layout of the circuit used for the measurement of the transfer function of the RC filters. The black arrows indicate the direction in which the filters act as low pass filters.

tor  $R_f = 100 \Omega$  (Vishay, Y1625100R000Q9R) and two capacitors  $C_a = 330 \text{ nF}$  (Kemet, C2220C334J1GACTU) and  $C_b = 470 \text{ pF}$  (Kemet, C0805C471J1GACTU) placed in parallel. Resistors  $R_a$ ,  $R_b$  model the equivalent series resistance (ESR) of the capacitors. The capacitance of the trap electrode to ground  $C_{el}$  is on the order of  $1 \text{ pF}$  and negligible compared to the filter capacitance. The electrical setup for the measurement of the filter's transfer function is shown in Fig. A.5 (b). Two filters, A and B, are wire bonded to the same trap electrode. An RF signal with amplitude  $V_{in}$  is injected into filter A, and the attenuated signal  $V_{out}$  is measured at the input of filter B. The transfer function measured in this configuration corresponds to that of the first order RC filter shown in Fig. A.5 (a), however with twice the filter capacitance  $C_{eff} \approx 2(C_a + C_b)$ . The additional capacitance reduces the cut-off frequency  $f_c \approx 4.8 \text{ kHz}$  by a factor of 2, which is irrelevant for the temperature scaling arguments used below. The resistance  $R_f$  of filter B can be neglected due to the high input impedance of  $1 \text{ M}\Omega$  of the oscilloscope used to measure the output signal  $V_{out}$ . Additional filter effects arising from  $R_f$  of filter B and the outgoing cabling capacitance  $C_{cab} \approx 300 \text{ pF}$  are negligible due to a high cut-off frequency  $f_c \approx 5 \text{ MHz}$ , well above the frequency range of interest.

Fig. A.6 shows the filter transfer function  $G = |V_{out}/V_{in}|^2$  for varying RC filter temperature  $T_f$  during cooling down and warming up of the entire cryogenic apparatus. The applied change in  $T_f$  strongly overestimates the variation in filter temperature  $T_f \approx (8 - 10) \text{ K}$  during the heating rate measurements. But even for stronger increase in  $T_f$ , the temperature scaling of the filter attenuation does not correlate with the heating rate data. Within the frequency range that is relevant for the experiment,  $\omega_z = 2\pi \times (0.4 - 1.8) \text{ MHz}$ , the low-pass filters show a slightly increasing attenuation for increasing temperature. This is likely due to an electric resonance caused by the

## A. Appendix to the superconducting traps

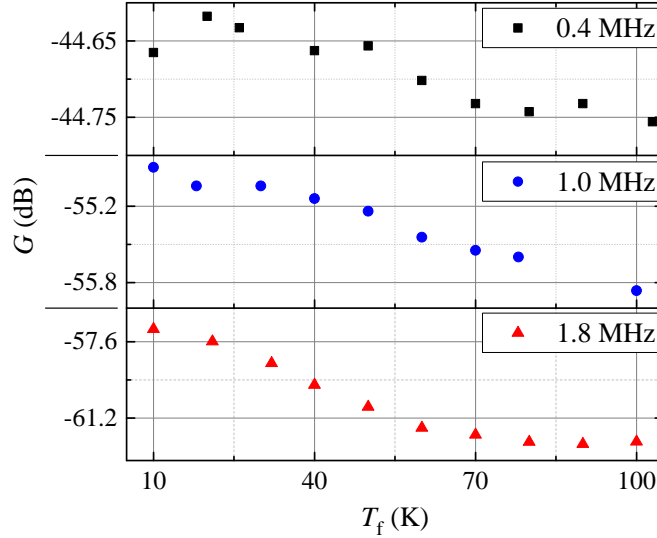


**Figure A.6.** Transfer function  $G$  of the cryogenic low-pass filters measured with the setup shown in Fig A.5 (b) as a function of the filter temperature  $T_f$  at three different frequencies  $\omega = 2\pi \times (0.4, 1.0, 1.8)$  MHz.

parasitic inductance of the wiring and the low-pass filter capacitance. A noise source outside the cryostat penetrating through the low-pass filter lines would therefore produce a heating rate that decreases with rising temperature, in stark contrast to the measured data in Fig. 7.11.

### A.4.4. Surface noise contribution from the exposed YBCO surface

Assuming surface noise as limiting noise source for the heating rate measurements in chip B (Fig. 7.11), the contribution of surface noise from the exposed YBCO surface to the electric field noise at the ion position  $\mathbf{r}_0$  is estimated in the following way. Surface noise  $S_{E,\mathcal{A}}^{\text{SN}}$  from an area  $\mathcal{A}$  on the chip surface is modeled as the sum of the noises from small patches that cover the entire area,  $S_{E,\mathcal{A}}^{\text{SN}} \propto \sum_{i \in \mathcal{A}} E_{z,i}^2$ , where  $E_{z,i}$  is the axial component of the field noise produced by patch  $i$  and the sum runs over all patches within  $\mathcal{A}$ . The noise fraction  $\chi$  caused by patches from within the exposed YBCO area  $\mathcal{A}_{\text{YBCO}} = 740 \times 580 \mu\text{m}^2$  is then given by  $\chi = S_{E,\mathcal{A}_{\text{YBCO}}}^{\text{SN}} / S_{E,\mathcal{A}_{\text{chip}}}^{\text{SN}}$ , where  $\mathcal{A}_{\text{chip}}$  is the total trap chip surface area and it is assumed that patches on the YBCO surface and the gold surface have identical fluctuation strengths.

The electric field noise contributions from the individual patches at the ion position  $\mathbf{r}_0$  are determined by calculating the axial electric field component  $E_{z,i}(\mathbf{r}_0)$  produced by a constant DC voltage on the respective patch using trap simulation. For the calculation, patch sizes of  $1 \times 1 \mu\text{m}^2$  are used. Convergence of the result is verified by varying the patch size between  $0.1 \times 0.1 \mu\text{m}^2$  and  $5 \times 5 \mu\text{m}^2$ . The chip area is approximated by an

area  $\mathcal{A}_{\text{chip}} = 10 \times 10 \text{ mm}^2$  placed centrally below the trapping position  $\mathbf{r}_0$ . The resulting noise fraction  $\chi = 0.939$  confirms that surface noise from the gold area can be neglected compared to the noise from the exposed YBCO area. The calculation is additionally validated by confirming the  $1/d^4$  scaling of the noise from the entire chip area  $S_{E, \mathcal{A}_{\text{chip}}}$  with the distance  $d$  from the trap chip, as expected from patch potential noise [87].



## B. Appendix to the 2 D linear trap array

This section contains additional information on the design of the linear trap array, described in chapter 8.

### B.1. Voltage sets

The DC voltage sets for axial confinement and micromotion compensation for the home configuration, the configuration with reduced RF and confinement in the axial interaction zone are compiled in Tabs. B.1, B.2 and B.3, respectively. The sets are calculated using the algorithm for simultaneous and independent confinement in two trapping sites, described in chapter 8.2.2.

**Table B.1.** Voltage sets for the home configuration with inter-trap distance  $s_t \approx 100 \mu\text{m}$ . The trap parameters for this configuration are in Tab. 8.2. The labeling of the DC electrodes is given in Fig. 8.10. All sets are for the central left minimum at  $x_0 = -s_t/2, z_0 = 0$ . The voltage sets for the central right minimum ( $x_0 = +s_t/2$ ) are identical upon swap of the electrode indices “l” and “r”. The set for confinement,  $\partial_{zz}\phi$ , is for 1.0 MHz axial frequency. The sets for micromotion compensation,  $E_i$ , are for a shift of about  $1 \mu\text{m}$  in the respective direction at the secular frequencies given in Tab. 8.2.

| $d$                                 | voltage set         | electrode voltage (V) |        |       |        |        |       |         |       |
|-------------------------------------|---------------------|-----------------------|--------|-------|--------|--------|-------|---------|-------|
|                                     |                     | DC1l                  | DC2l   | DC3l  | DC4l   | DC1r   | DC2r  | DC3r    | DC4r  |
| <b>120 <math>\mu\text{m}</math></b> | $\partial_{zz}\phi$ | 1.480                 | -0.068 | 1.480 | 0.815  | 0.383  | 0.673 | 0.383   | 2.292 |
|                                     | $E_x$               | 0.545                 | 0.545  | 0.545 | 2.000  | 0.523  | 0.523 | 0.523   | 1.552 |
|                                     | $E_y$               | 0.170                 | 0.170  | 0.170 | -0.145 | 0.074  | 0.074 | 0.074   | 0.500 |
|                                     | $E_z$               | -0.030                | 0.000  | 0.030 | 0.000  | 0.0066 | 0.000 | -0.0066 | 0.000 |
| <b>80 <math>\mu\text{m}</math></b>  | $\partial_{zz}\phi$ | 1.006                 | 0.297  | 1.006 | 0.737  | 0.396  | 0.473 | 0.396   | 1.352 |
|                                     | $E_x$               | 1.316                 | 1.316  | 1.316 | 4.000  | 1.250  | 1.250 | 1.250   | 2.984 |
|                                     | $E_y$               | 0.242                 | 0.242  | 0.242 | -0.015 | 0.127  | 0.127 | 0.127   | 0.500 |
|                                     | $E_z$               | -0.020                | 0.000  | 0.020 | 0.000  | 0.0033 | 0.000 | -0.0033 | 0.000 |

B. Appendix to the 2D linear trap array

**Table B.2.** Voltage sets for the configuration with reduced RF voltage,  $s_t \approx 40 \mu\text{m}$ . The trap parameters for this configuration are in Tab. 8.3. The labeling of the DC electrodes is given in Fig. 8.10. All sets are for the central left minimum at  $x_0 = -s_t/2, z_0 = 0$ . The voltage sets for the central right minimum ( $x_0 = +s_t/2$ ) are identical upon swap of the electrode indices “l” and “r”. The set for confinement,  $\partial_{zz}\phi$ , is for 1.0 MHz axial frequency. The sets for micromotion compensation,  $E_i$ , are for a shift of about  $1 \mu\text{m}$  in the respective direction at the secular frequencies given in Tab. 8.3.

| $d$                                 | voltage set         | electrode voltage (V) |        |       |        |        |        |        |       |
|-------------------------------------|---------------------|-----------------------|--------|-------|--------|--------|--------|--------|-------|
|                                     |                     | DC1l                  | DC2l   | DC3l  | DC4l   | DC1r   | DC2r   | DC3r   | DC4r  |
| <b>120 <math>\mu\text{m}</math></b> | $\partial_{zz}\phi$ | 2.021                 | -0.897 | 2.021 | -1.584 | -0.581 | 0.921  | -0.581 | 2.668 |
|                                     | $E_x$               | 0.722                 | 0.722  | 0.722 | 2.200  | 0.700  | 0.700  | 0.700  | 1.715 |
|                                     | $E_y$               | 0.120                 | 0.120  | 0.120 | -0.790 | -0.037 | -0.037 | -0.037 | 0.677 |
|                                     | $E_z$               | -0.050                | 0.000  | 0.050 | 0.000  | 0.028  | 0.000  | -0.028 | 0.000 |
| <b>80 <math>\mu\text{m}</math></b>  | $\partial_{zz}\phi$ | 1.082                 | -0.212 | 1.082 | -0.991 | -0.269 | 0.245  | -0.269 | 0.933 |
|                                     | $E_x$               | 0.697                 | 0.697  | 0.697 | 1.600  | 0.639  | 0.639  | 0.639  | 0.578 |
|                                     | $E_y$               | 0.157                 | 0.157  | 0.157 | -1.300 | -0.085 | -0.085 | -0.085 | 0.848 |
|                                     | $E_z$               | -0.029                | 0.000  | 0.029 | 0.000  | 0.014  | 0.000  | -0.014 | 0.000 |

**Table B.3.** Voltage sets for trapping in the axial interaction zone with axial distance  $s_t^{(\text{ax})} \approx 50 \mu\text{m}$ . The trap parameters for this configuration are in Tab. 8.4. The labeling of the DC electrodes is given in Fig. B.1. The set for confinement,  $\partial_{zz}\phi$ , is for simultaneous trapping at the two sites  $z_0^{(c)} = 25 \mu\text{m}$  and  $z_0^{(o)} = 459 \mu\text{m}$  with nominal axial frequency  $\omega_z = 2\pi \times 1.0 \text{ MHz}$ . The sets for micromotion compensation,  $E_i$ , are for a simultaneous shift of the central sites,  $z_0^{(c)} = \pm 25 \mu\text{m}$ , of about  $1 \mu\text{m}$  in the respective direction at the secular frequencies given in Tab. 8.4. The shim set  $\Delta\partial_{zz}\phi$  allows to change the secular frequency of the top central sites  $z_0^{(c)} = 25 \mu\text{m}$  by about 1 kHz, independently of the bottom central site  $z_0^{(c)} = -25 \mu\text{m}$ . Since the set uses only 6 electrodes, the axial position cannot be constrained and changes by  $\Delta z_0^{(c)} = 4 \mu\text{m}$  ( $2.5 \mu\text{m}$ ) for the 80  $\mu\text{m}$  (120  $\mu\text{m}$ ) design.

| $d$                                 | voltage set               | electrode voltage (V) |        |        |        |        |        |        |        |
|-------------------------------------|---------------------------|-----------------------|--------|--------|--------|--------|--------|--------|--------|
|                                     |                           | DCA                   | DCB    | DCC    | DCD    | DC1    | DC2    | DC3    | DC4    |
| <b>120 <math>\mu\text{m}</math></b> | $\partial_{zz}\phi$       | 34.30                 | -21.52 | 4.897  | 4.230  | 1.288  | 2.862  | 1.065  | 3.670  |
|                                     | $E_x$                     | 1.005                 | -0.207 | 0.588  | 5.000  | 0.348  | 0.125  | 0.041  | -0.064 |
|                                     | $E_y$                     | 0.300                 | -0.097 | 0.158  | 0.185  | 0.030  | 0.006  | 0.003  | 0.015  |
|                                     | $E_z$                     | -1.000                | 0.649  | -0.075 | -0.032 | -0.006 | -0.001 | -0.000 | -0.003 |
|                                     | $\Delta\partial_{zz}\phi$ | DCBt                  | DCCt   | DC4t   | DCBb   | DCCb   | DC4b   |        |        |
| <b>80 <math>\mu\text{m}</math></b>  | $\partial_{zz}\phi$       | 3.978                 | -1.159 | 1.904  | 2.048  | 1.177  | 2.708  | 1.198  | 2.857  |
|                                     | $E_x$                     | 0.912                 | 0.628  | 1.021  | 6.500  | 0.439  | 0.264  | 0.247  | 0.178  |
|                                     | $E_y$                     | 0.313                 | 0.209  | 0.342  | 0.450  | 0.046  | 0.023  | 0.025  | 0.031  |
|                                     | $E_z$                     | -0.100                | 0.066  | -0.006 | 0.003  | 0.000  | 0.000  | 0.000  | 0.000  |
|                                     | $\Delta\partial_{zz}\phi$ | DCBt                  | DCCt   | DC4t   | DCBb   | DCCb   | DC4b   |        |        |

## B.2. Bucket-brigade shuttling with meander-shaped DC electrodes

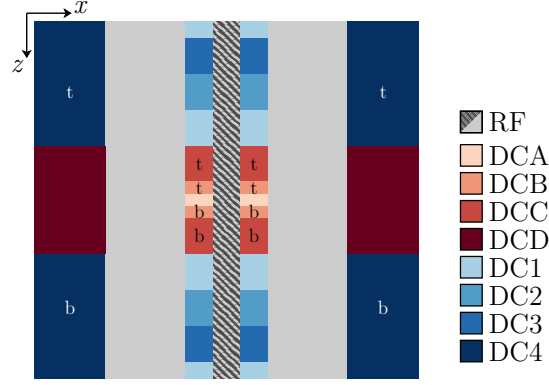


**Figure B.1.** Electrode set used for confinement and micromotion compensation in the axial interaction zone. The pattern of outer DC electrodes (blue) continues periodically to the top and bottom.

## B.2. Bucket-brigade shuttling with meander-shaped DC electrodes

The lattice reconfiguration processes characterized in chapter 8.2.3 can also be realized using meander-shaped DC electrodes instead of island-like electrodes. This approach has the advantage that all trap electrodes can be connected on a single metal layer, such that a multilayer fabrication process is not necessary. Fig. B.2 shows the set of DC electrodes for bucket-brigade shuttling in such a geometry. Six long electrodes with

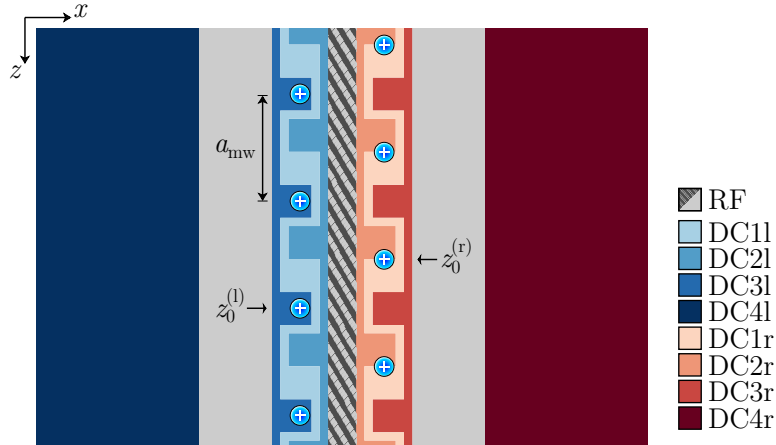


**Figure B.2.** Electrode set for bucket-brigade shuttling using a meander geometry for the central DC electrodes.

periodic variations in width along  $z$  form a meander structure along each of the two DC rails. This allows one to realize two independent multiwell potentials with spatial periodicity  $a_{mw}$  along each of the two RF nulls. Lattice reconfiguration processes are characterized by shifting the left and right multiwell positions  $z_0^{(l)}$ ,  $z_0^{(r)}$  independently

B. Appendix to the 2D linear trap array

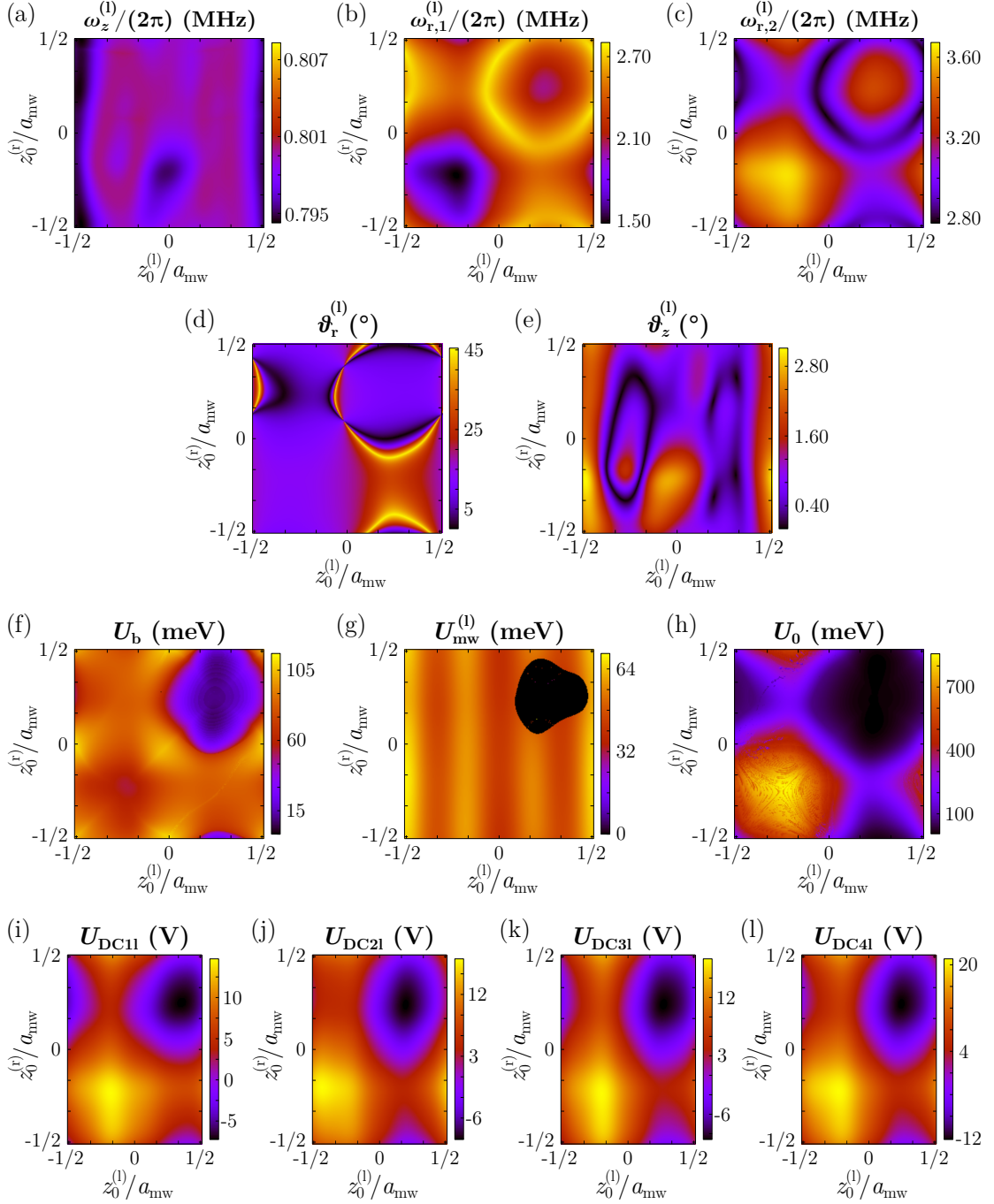


**Figure B.3.** Characterization of the bucket-brigade shuttling process using meander-shaped DC electrodes. The parameters varied are the positions  $z_0^{(l)}$ ,  $z_0^{(r)}$  of the left and right multiwell, respectively. Subplots (a)-(c) show the secular frequencies of the central left trapping site, (d) the tilt of the radial modes with respect to the vertical direction  $y$  and (e) the tilt of the axial mode with respect to the  $z$ -axis. Subplots (f) and (g) show the RF and multiwell potential barrier, respectively. At the black spot in (g) in the top right quadrant, the algorithm used to determine the multiwell barrier  $U_{mw}^{(l)}$  fails due to the low trap depth  $U_0$ , shown in (h). The applied DC voltages are shown ion (i)-(l).

### B.3. Shuttling out of the axial interaction configuration

in the range  $a_{\text{mw}}$  and evaluating the trapping parameters in each configuration. This has been done for an electrode geometry with rail widths  $w_1 = 85 \mu\text{m}$ ,  $w_o = 221 \mu\text{m}$ ,  $w_{\text{DC}} = 170 \mu\text{m}$  of the inner RF, outer RF and DC rails, respectively. The meander pitch is  $a_{\text{mw}} = 325 \mu\text{m}$ , the thinnest part of the meander structure in  $x$ -direction has a width of  $25 \mu\text{m}$ . The ion-surface separation for this geometry is  $d = 164 \mu\text{m}$ .

Fig. B.3 shows the characterization of lattice reconfiguration processes for an RF drive voltage  $U_{\text{RF}} = 186 \text{ V}$  at  $\Omega_{\text{RF}} = 2\pi \times 20 \text{ MHz}$ . All quantities except the trap depth  $U_0$  and RF barrier  $U_b$  are given for the left trapping site only. The corresponding data for the right site are identical upon mirroring the plots at the bottom left to top right diagonal due to the trap's mirror symmetry. Axial confinement is possible across the entire parameter space. However, the data has a more fine-grained structure compared to that in an island-like geometry, Fig. 8.12, due to the presence of the thin parts of the meander structure. The radial mode splitting, Fig. B.3 (b) and (c) is stronger in general, and regions of maximal and minimal splitting are closer together. The tilt  $\vartheta_z$  of the axial mode, (e), and even more the tilt  $\vartheta_r$  of the radial modes, (d), show drastic changes within small position variations of  $z_0^{(l)}, z_0^{(r)}$ . This can lead to mixing of mode populations during a shuttling process and will limit its speed. Another difficulty is the low trap depth  $U_0$ , (h), in the top right quadrant, where values below  $U_0 = 10 \text{ meV}$  are reached due to the negative DC voltages in that region. The black spot in (g) marks that region, since the algorithm used to determine  $U_{\text{mw}}^{(l)}$  fails for such low trap depths  $U_0$ . All these characteristics impose additional limitations on multiwell shuttling processes. Island-like electrodes were therefore favored for the BB trap design.

### B.3. Shuttling out of the axial interaction configuration

The shuttling sequence in Fig. 8.18, chapter 8.2.5, is realized by stitching together voltage sequences for three different electrode sets. For each set, the voltage sets for simultaneous confinement at the two positions  $z_0^{(c)}$  and  $z_0^{(o)}$  are calculated using the algorithm for multiwell confinement described in section 8.2.2. At the stitching points, some of the voltages have discontinuities, which are then linearly interpolated. For  $25 \mu\text{m} < z_0^{(c)} \lesssim 90 \mu\text{m}$ , all 8 DC electrodes listed in Figs. 8.18 (d) and (e) are treated independently to control the 6 electric field components and both axial curvatures at the two trapping sites  $z_0^{(c)}, z_0^{(o)}$ . While  $z_0^{(c)}$  is shifted away from the trap center, the outer site  $z_0^{(o)}$  is moved in the opposite direction to a position that yields identical voltages on the central electrodes DCA and DCB,  $U_{\text{DCA}} = U_{\text{DCB}}$ . For  $90 \mu\text{m} \lesssim z_0^{(c)} \lesssim 135 \mu\text{m}$ , the condition  $U_{\text{DCA}} = U_{\text{DCB}}$  is maintained by joining the central electrodes DCA and DCB. This reduces the number of control parameters by one and the axial position of the outer site is left as free parameter. The set point

## B. Appendix to the 2D linear trap array

for  $z_0^{(o)}$  in the algorithm is adjusted at the start and end point to avoid discontinuities in  $z_0^{(o)}$  at the stitching points. At  $z_0^{(c)} \approx 135 \mu\text{m}$ , the electrode voltages fulfill  $U_{\text{DC1}} = U_{\text{DC3}}$ , as needed for the final configuration where the trapping sites are directly above the edges between these electrodes. For  $z_0^{(c)} \gtrsim 135 \mu\text{m}$  the electrode set for bucket-brigade shuttling is used, i. e.,  $U_{\text{DC1}} = U_{\text{DC3}} = U_{\text{DCC}}$ ,  $U_{\text{DC2}} = U_{\text{DCA}} = U_{\text{DCB}}$ ,  $U_{\text{DC4}} = U_{\text{DCD}}$ . A local shim voltage set is added to the voltage set for confinement in the final configuration,  $z_0^{(c)} = a_{\text{mw}}/2$ ,  $z_0^{(o)} = 3a_{\text{mw}}/2$ , in order to realize a small shift to  $z_0^{(c)} < a_{\text{mw}}/2 = 153 \mu\text{m}$ . This local set is calculated only for position  $z_0^{(c)}$  using three control voltages  $U_{\text{DCA}} = U_{\text{DCB}}, U_{\text{DCC}}, U_{\text{DCD}}$ . As a side effect of this local set, also the outer site  $z_0^{(o)}$  is slightly shifted.

For completeness it should be added that it is not possible to realize the entire shuttling process, Fig. 8.18, using solely the algorithm for simultaneous confinement at sites  $z_0^{(c)}, z_0^{(o)}$  employed for  $25 \mu\text{m} < z_0^{(c)} \lesssim 90 \mu\text{m}$ . As  $z_0^{(c)}$  is shifted further away from the trap center, the algorithm produces diverging voltages on the central electrodes DCA, DCB at a critical distance  $z_0^{(c)} \approx 120 \mu\text{m}$ <sup>1</sup>. The singularity exists for arbitrary positions  $z_0^{(o)}$  of the outer site and produces in general different polarities on the two central electrodes,  $U_{\text{DCA}} \sim -U_{\text{DCB}}$ . However, for varying  $z_0^{(o)}$  the voltages  $U_{\text{DCA}}, U_{\text{DCB}}$  change polarity. Around  $z_0^{(o)} \approx 400 \mu\text{m}$ , a sweet spot exists where  $U_{\text{DCA}} = U_{\text{DCB}}$  as  $z_0^{(c)}$  approaches the critical distance. This behavior is used to realize the joining of electrodes DCA and DCB, required for the final bucket-brigade shuttling configuration.

### B.4. Finite element simulations of trap capacitances

The estimates for the trap electrode capacitances given in Tab. 8.7 are based on finite element simulations of a simplified trap cross section using COMSOL<sup>2</sup>. The parasitic coupling capacitance between RF and adjacent DC island electrodes, used to determine the expected amount of RF pickup on the DC electrodes, is estimated in the same way. A schematic view of the simulated geometry is shown in Fig. B.4. The dimensions of the RF and DC rail widths correspond to the trap geometry in Tab. 8.1. For the layer thicknesses, the measured values from Tab. 8.5 are used. The M2 layer and topology of the trap are not implemented in the simulation. For the Si substrate, a relative permittivity  $\epsilon_r = 11.45$  was used [196]. The dielectric constant  $\epsilon_r = 4.1$  of the SiO<sub>2</sub> layers is a known value at Infineon. In the simulation, individual electrodes are set in turn to  $U = 1 \text{V}$ , while all other electrodes are grounded. The electric displacement field  $\mathbf{D}$  is calculated and the induced charge per length  $Q_{\text{ind}} = \oint_c \mathbf{D} \cdot d\mathbf{n}$  is determined. The integral runs over the entire contour  $c$  of the electrode and  $d\mathbf{n}$  represents the

<sup>1</sup> In the  $d = 80 \mu\text{m}$  design the threshold is at  $z_0^{(c)} \approx 100 \mu\text{m}$ .

<sup>2</sup> COMSOL Multiphysics, Version 5.3a

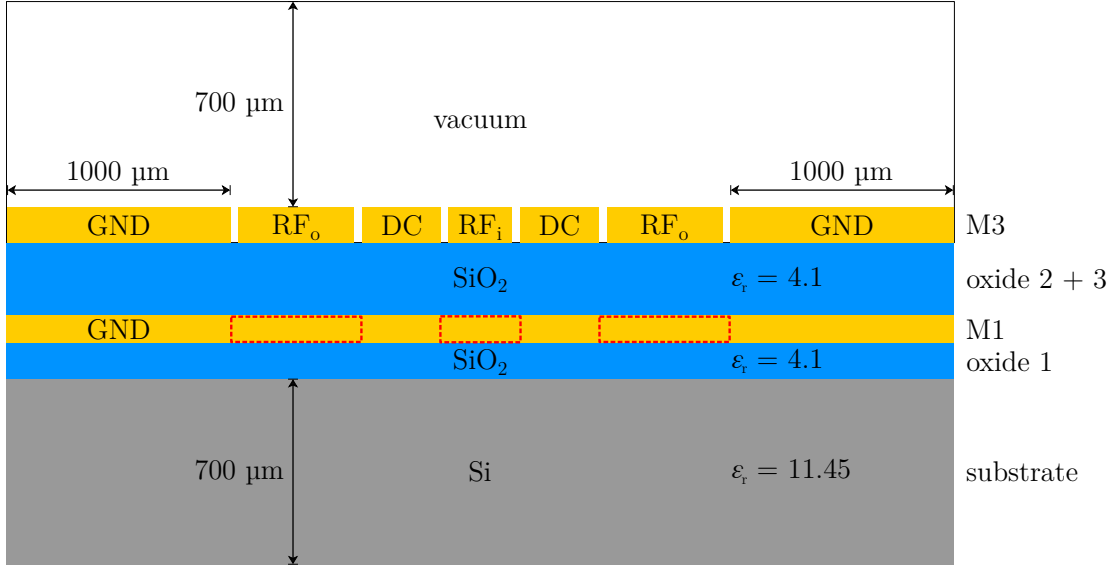


**Figure B.4.** Schematic view of the simplified trap structure simulated with COMSOL. The red dashed boxes mark, where the M1 GND electrode is cut out and replaced by SiO<sub>2</sub> to simulate the designs with structured M1 layer.

normal vector to each infinitesimal contour element. The capacitance is then given by  $C = l_{\text{el}}Q_{\text{ind}}/U$ , where  $l_{\text{el}}$  is the length of the electrode perpendicular to the plane of the cross section. For the design variations with structured M1 layer, the grounded M1 layer is removed below the RF rails over about 79% of their entire length (cf. chapter 8.3.1). To estimate the capacitances in these variations, a cross section with removed M1 GND is simulated. The capacitance estimates are then given by  $C = 0.21C_{\text{cont}} + 0.79C_{\text{struc}}$ , where  $C_{\text{cont}}$ ,  $C_{\text{struc}}$  are the simulated capacitance values for the geometry with continuous and structured M1 GND, respectively. The simulation results for the capacitances  $C_i$ ,  $C_o$  between RF rails and GND are compared with a simple parallel plate capacitor model,

$$C = \varepsilon_0 \varepsilon_r \frac{w_{\text{el}} l_{\text{el}}}{t}, \quad (\text{B.1})$$

where  $w_{\text{el}}$  is the width of the respective electrode,  $t$  is its separation from the GND layer and  $\varepsilon_r$  is the permittivity of the dielectric. For the design with continuous M1 layer,  $C_i$  and  $C_o$  match the parallel plate model within 3%. The estimates for  $C_o$ , given in Tab. 8.7, contain a parallel plate contribution of the RF leads on M3 connecting the RF rails to the bonding pads. This lead contribution is about 2.8 pF and is added to the estimates from the cross section simulation.

The capacitance contribution  $C_{\text{pad-GND}}$  of an RF bonding pad to GND via the Si substrate is estimated in the following way. First, it is assumed that the substrate is

## B. Appendix to the 2D linear trap array

a conductor at room-temperature (the substrate resistivity is  $\rho_{\text{sub}} = 3 \times 10^{-2} \Omega \text{ m}$  at  $T = 300 \text{ K}$ ). Further, it is assumed that the capacitance  $C_{\text{sub-GND}}$  between substrate and the GND electrode on M1 is much larger than the capacitance  $C_{\text{pad-sub}}$  between the pad and the substrate,  $C_{\text{sub-GND}} \gg C_{\text{pad-sub}}$ . This is a reasonable assumption, given that the surface area of a bonding pad is only around 0.2% of the surface area of the M1 GND layer. It follows, that  $C_{\text{pad-GND}} \approx C_{\text{pad-sub}}$ . The capacitance  $C_{\text{pad-sub}}$  is approximated by its parallel plate capacitance value using Eq. (B.1). The bonding pads use all three metallic layers and are separated from the substrate by the thickness  $t = 1.3 \mu\text{m}$  of the thermal oxide. Each bonding pad has a width of  $w = 129 \mu\text{m}$  and a length of  $l = 479 \mu\text{m}$ , leading to a capacitance of  $C_{\text{pad-GND}} = 1.71 \text{ pF}$  per bonding pad. The single bonding pad of the inner RF rail thus adds 1.7 pF to the capacitance  $C_i$ . The 4 bonding pads of the outer RF add 6.8 pF to  $C_o$ .

### B.5. Simulation of a trap array with $10 \times 10$ trapping sites

In this section, it is shown that the BB trap design can be extended to a larger number of parallel linear traps. For this, multiwell confinement and RF shuttling in a linear trap array with  $10 \times 10$  trapping sites are simulated. DC shuttling along the axial direction is not simulated since this aspect is already covered by the studies in the BB traps: confinement with reduced axial distance (cf. chapter 8.2.5) and bucket brigade shuttling of two adjacent, independent DC multiwells with 9 trapping sites each (cf. chapter 8.2.3). The geometry of the simulated  $10 \times 10$  trap array, shown in Fig. B.5, follows the approach introduced in Fig. 8.22 (a) in chapter 8.4. RF confinement in the radial ( $xy$ -) plane is produced by parallel RF rails with alternating widths  $w_e = 88 \mu\text{m}$  and  $w_o = 70.4 \mu\text{m}$ , referred to as even and odd RF rails, respectively, in what follows. A total of 15 RF rails leads to 14 parallel linear traps, out of which the innermost 10 linear traps are used for ion storage. The outermost pairs of linear traps on each side are dummy traps, introduced to make the trapping potential more homogeneous for the inner traps as discussed below. The widths of the even and odd RF rails differ by about 20%. This increases the trap depth in the home configuration, where the same RF voltage  $U_{\text{RF}}$  is applied to all RF rails. Furthermore, the difference in RF rail widths leads to a tilt of the radial modes with respect to the trap normal in the presence of DC confinement, allowing for simultaneous laser cooling of all secular modes with laser beams parallel to the trap surface. The segmented DC rails have a width  $w_{\text{DC}} = 79.2 \mu\text{m}$  and a segment length  $l_{\text{DC}} = 74.8 \mu\text{m}$ . Like in the BB trap design, the segments are periodically connected, with the same voltage being applied to every third segment. This allows one to create DC multiwell confinement with a well period of  $a_{\text{mw}} \approx 224 \mu\text{m}$ .

### B.5. Simulation of a trap array with $10 \times 10$ trapping sites

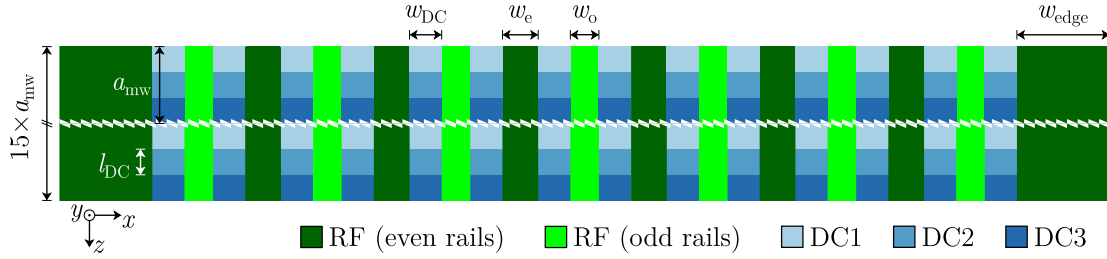


**Figure B.5.** Electrode geometry of the simulated linear trap array with  $10 \times 10$  trapping sites. The widths of the RF rails are  $w_e = 88 \mu\text{m}$  and  $w_o = 70.4 \mu\text{m}$  for the even and odd rails, respectively. The outermost RF rails have an increased width of  $w_{\text{edge}} = 228.8 \mu\text{m}$ . The DC rails have a width of  $w_{\text{DC}} = 79.2 \mu\text{m}$ . The DC segment length of  $l_{\text{DC}} = 74.8 \mu\text{m}$  gives rise to a DC multiwell periodicity of  $a_{\text{mw}} = 224.4 \mu\text{m}$ . Each DC rail consists of 45 segments, amounting to a total length of about 3.4 mm. The RF rails have a length of 8.0 mm. An additional ground electrode parallel to the trap surface (not shown) is located at a vertical distance of  $y = 1.0 \text{ mm}$ .

Inhomogeneities of the RF potential across the array can be a concern for simultaneous stable trapping in all lattice sites<sup>3</sup>. In the suggested geometry, Fig. B.5, inhomogeneities caused by edge effects are mitigated in three ways: First, an additional GND electrode at a distance  $y = 1.0 \text{ mm}$  above the trap surface is introduced. This top GND electrode is the dominating factor for the increased homogeneity of the RF (and DC) potential and also leads to an increased trap depth<sup>4</sup>. A top GND electrode could be realized for instance with a glass plate coated with indium tin oxide (ITO) and mounted rigidly above the trap chip. ITO remains conductive and optically transparent at cryogenic temperatures [197]. Second, an additional pair of linear dummy traps is added at either side of the array. The 10 central linear traps used for the quantum register are thereby increased to 14 linear traps. This is particularly helpful for keeping the trapping potentials of the central traps more homogeneous during RF shuttling operations. Ions loaded accidentally in the outer dummy traps could for instance be deterministically pushed out by suitable DC control fields on the outermost DC electrodes. Third, the width of the outermost RF rails is increased to  $w_{\text{edge}} = 228.8 \mu\text{m}$ . Adjusting this width mainly influences the homogeneity of the outermost traps used for the quantum register, relative to the central traps. This approach could be extended by additionally adjusting the widths of the outermost DC rails, then of the next RF rails, and so forth, going from the array edges towards the center.

The simplified geometry in Fig. B.5 shows the minimum of DC electrodes necessary

<sup>3</sup> For quantum operations between ions in adjacent sites, the usage of the axial mode for motional coupling gives some intrinsic robustness against inhomogeneities in the RF potential.

<sup>4</sup> For the same trap geometry but without GND top electrode, and scaled to yield the same ion-surface separation  $d$ , the trap depths  $U_0$ ,  $U_b$  and  $U_{\text{mw}}$  are decreased by roughly a factor 1.5. Furthermore, the stability  $q$ -factor shows a variations of 0.06 across the central 10 linear traps, ten times stronger as compared to the design with top GND layer.

## B. Appendix to the 2D linear trap array

for creating a 2D ion lattice. For a realistic operation as ion-lattice quantum processor, a further segmentation of the DC rails would be necessary. In particular, control electrodes for stray electric field compensation (micromotion compensation) and for fine control of secular frequencies (and potentially mode orientations) would be required.

### Multiwell confinement

To simulate multiwell confinement, a voltage set for axial confinement is calculated for a single trapping site at the center of the array. Upon applying this set, the periodicity of the RF and DC electrodes automatically creates a square array of trapping sites. DC voltages are applied to the DC segments as well as to the RF rails, in order to gain the required number of control parameters for axial confinement and micromotion compensation. Alternatively, one could use a finer segmentation of the DC rails. In the default trapping configuration, an equal RF voltage  $U_{\text{RF}}$  is applied to the even and odd RF rails and a DC voltage set for axial multiwell confinement is applied. The total confining potential  $\Phi$  in this home configuration is shown in Fig. B.6. The trap parameters for one of the central sites are listed in Tab. B.4. The cross sections (a), (b), (d) in Fig. B.6 show a square lattice of  $14 \times 12$  trapping sites out of which the central  $10 \times 10$  sites are to be used for ion storage. The additional sites at the trap edges are dummy sites, mitigating edge effects on the central sites. An RF voltage of  $U_{\text{RF}} = 172 \text{ V}$  at  $\Omega_{\text{RF}} = 2\pi \times 30 \text{ MHz}$  yields a stability  $q$ -factor of 0.4. The DC voltages for axial confinement are on the order of 1 V and give rise to an axial frequency

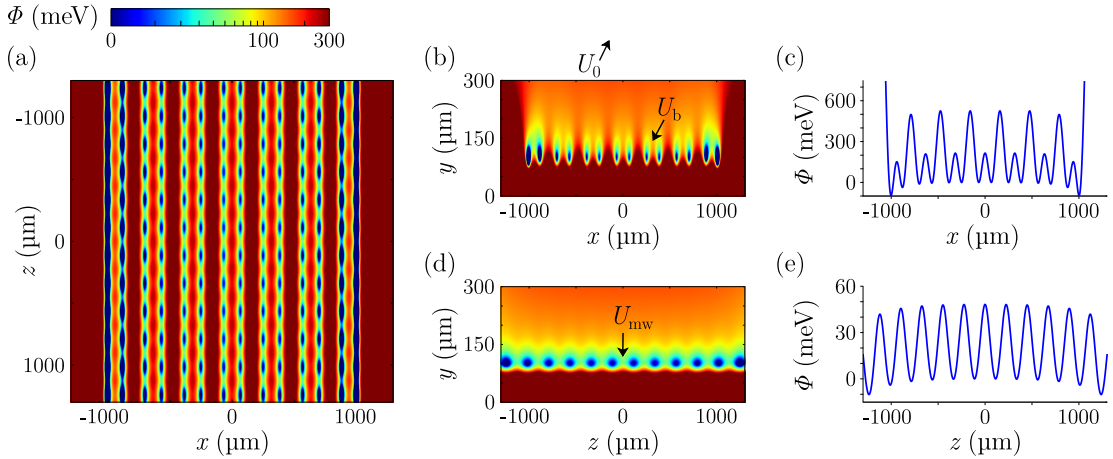


**Figure B.6.** Trap confinement in the home configuration of the array with  $10 \times 10$  trapping sites. Subplots (a), (b), (d) show cross sections of the total potential  $\Phi$  in the  $xz$ -,  $xy$ - and  $zy$ -plane, respectively, crossing the trapping site at  $r_0 = (-67, 102, -112) \mu\text{m}$ . The color scale is cut off at 300 meV and non-linear for better visibility of the minima. (c) Potential along the  $x$ -direction through the central trapping site at  $x_0, z_0 = (-67, -112) \mu\text{m}$ . (e) Axial multiwell potential through the same site. In all plots a DC offset field is subtracted from the data.

### B.5. Simulation of a trap array with $10 \times 10$ trapping sites

**Table B.4.** Trap parameters of the  $10 \times 10$  linear trap array in the home configuration, at the position of the central minimum at  $\mathbf{r}_0 = (-67, 102, -112) \mu\text{m}$ . The DC voltages are  $U_{\text{DC}1} = 0.292 \text{ V}$ ,  $U_{\text{DC}2} = 1.587 \text{ V}$ ,  $U_{\text{DC}3} = 0.292 \text{ V}$ ,  $U_{\text{RF}^{(e)}} = -1.557 \text{ V}$ ,  $U_{\text{RF}^{(o)}} = -1.578 \text{ V}$ .

| RF drive                    |        | secular freq.         |         | mode tilt     |             | trap depth      |         |
|-----------------------------|--------|-----------------------|---------|---------------|-------------|-----------------|---------|
| $U_{\text{RF}}^{(e)}$       | 172 V  | $\omega_z/(2\pi)$     | 1.0 MHz | $\vartheta_z$ | $0.0^\circ$ | $U_0$           | 330 meV |
| $U_{\text{RF}}^{(o)}$       | 172 V  | $\omega_{r,1}/(2\pi)$ | 4.0 MHz |               |             | $U_b$           | 116 meV |
| $\Omega_{\text{RF}}/(2\pi)$ | 30 MHz | $\omega_{r,2}/(2\pi)$ | 4.4 MHz | $\vartheta_r$ | $8.4^\circ$ | $U_{\text{mw}}$ | 45 meV  |
| $q$                         | 0.4    |                       |         |               |             |                 |         |

$\omega_z = 2\pi \times 1.0 \text{ MHz}$ . The DC confinement leads to a splitting of the radial frequencies,  $\omega_{r,1}, \omega_{r,2} = 2\pi \times (4.0, 4.4) \text{ MHz}$ , and causes a tilt  $\vartheta_r = 8.4^\circ$  of the radial modes with respect to the vertical direction  $y$ . The axial mode is aligned with the  $z$ -axis,  $\vartheta_z = 0$ . The axial multiwell barrier  $U_{\text{mw}} = 45 \text{ meV}$ , the RF barrier  $U_b = 116 \text{ meV}$  and the global trap depth  $U_0 = 330 \text{ meV}$  all have high values, well above the average kinetic energy  $E_{\text{th}} \approx 26 \text{ meV}$  of thermal gas molecules at room-temperature. The very high value of  $U_0$  is reached only at the position  $y = 1 \text{ mm}$  of the top GND layer.

The inner  $10 \times 10$  trapping sites show a very good homogeneity: The variation in ion-surface separation  $d$  is about  $1 \mu\text{m}$ . The stability  $q$ -factor varies within 0.404 and 0.409 for all sites. Variations in secular frequencies are about 4 kHz axially and 30 kHz radially. The radial mode tilt varies within  $8.0^\circ$  and  $13.1^\circ$ , the axial mode tilt stays below  $0.1^\circ$ . Radial shift of the sites off the RF null are below  $1 \mu\text{m}$ . Variations in the trap depths are negligible.

#### RF shuttling

Entanglement between ions in adjacent linear traps is facilitated by a reduction of the distance  $s_t$  between adjacent RF nulls. This is achieved by reducing the RF voltage  $U_{\text{RF}}$  on either the even or the odd RF rails. At a separation  $s_t = 40 \mu\text{m}$  one calculates a motional coupling rate  $\Omega_c = 2\pi \times 1.38 \text{ kHz}$ , using Eq. (3.4) and assuming an axial frequency  $\omega_z = 2\pi \times 1 \text{ MHz}$ . The trap confinement for such a reduced distance is shown in Fig. B.7. The cross sections (a) and (d) show how the  $14 \times 12$  trapping sites are rearranged upon attenuation of the RF voltage on the even and odd RF rails, respectively. In both configurations, the sites form pairs of columns such that for any trapping site a reduced distance  $s_t \approx 40 \mu\text{m}$  to either the adjacent site on the right or on the left can be realized<sup>5</sup>. The insets (b) and (e) show a magnified view of the marked pairs of trapping sites. The double-well potentials connecting the two sites of each pair

<sup>5</sup> In Fig. B.7 (a) and (d), a quartic potential  $\Phi_{\text{offset}}(x, z) = a_x x^4 + b_x x^2 + a_z z^4 + \text{const.}$  is subtracted from the data to increase the visibility of the minima. For the RF reduction on the even RF rails,  $a_x = 6.0 \times 10^{-15} \text{ eV}/\mu\text{m}^4$ ,  $b_x = 2.0 \times 10^{-9} \text{ eV}/\mu\text{m}^2$ ,  $a_z = 4.5 \times 10^{-15} \text{ eV}/\mu\text{m}^4$ . For the RF reduction on the odd RF rails,  $a_x = 4.0 \times 10^{-14} \text{ eV}/\mu\text{m}^4$ ,  $b_x = 1.5 \times 10^{-8} \text{ eV}/\mu\text{m}^2$ ,  $a_z = 4.5 \times 10^{-15} \text{ eV}/\mu\text{m}^4$ .

B. Appendix to the 2D linear trap array

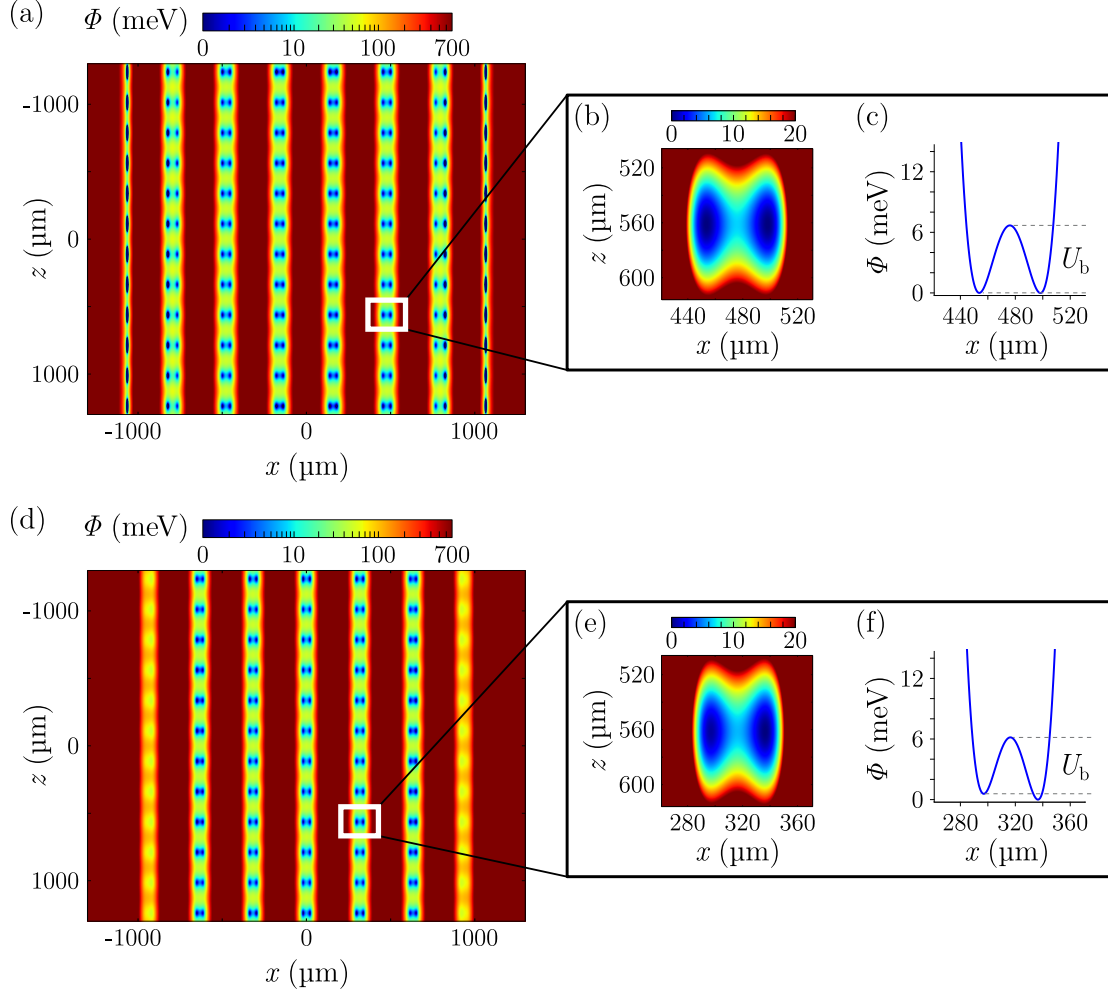


**Figure B.7.** Trap confinement in the reduced RF configuration with  $s_t \approx 40 \mu\text{m}$ , achieved by attenuating the RF voltage on the even RF rails, (a)-(c), and on the odd rails, (d)-(f). Subplots (a) and (d) show cross sections of the total potential  $\Phi$  in the  $xz$ -plane, crossing the trapping site at  $\mathbf{r}_0 = (139, 98, -112) \mu\text{m}$  and  $\mathbf{r}_0 = (20, 101, -112) \mu\text{m}$ , respectively. The color scale is non-linear and a quartic potential has been subtracted from the data for better visibility of the minima. The insets show a magnified view, (b) and (e), of the marked pair of trapping sites, and the line potential through them, (c) and (f).

### B.5. Simulation of a trap array with $10 \times 10$ trapping sites

**Table B.5.** Trap parameters of the  $10 \times 10$  linear trap array in the reduced RF configuration. For the attenuation on the even RF rails, the parameters are evaluated at the position of the central minimum at  $\mathbf{r}_0 = (139, 98, -112) \mu\text{m}$  and the DC voltages are  $U_{\text{DC}1} = 0.338 \text{ V}$ ,  $U_{\text{DC}2} = 1.970 \text{ V}$ ,  $U_{\text{DC}3} = 0.338 \text{ V}$ ,  $U_{\text{RF}^{(e)}} = -0.457 \text{ V}$ ,  $U_{\text{RF}^{(o)}} = -1.970 \text{ V}$ . For the attenuation on the odd RF rails, the parameters are evaluated at the position of the central minimum at  $\mathbf{r}_0 = (20, 101, -112) \mu\text{m}$  and the DC voltages are  $U_{\text{DC}1} = 0.320 \text{ V}$ ,  $U_{\text{DC}2} = 1.803 \text{ V}$ ,  $U_{\text{DC}3} = 0.320 \text{ V}$ ,  $U_{\text{RF}^{(e)}} = -1.803 \text{ V}$ ,  $U_{\text{RF}^{(o)}} = -0.870 \text{ V}$ .

| attenuation on | RF drive                    |        | secular freq.         |         | mode tilt     | trap depth  |                        |
|----------------|-----------------------------|--------|-----------------------|---------|---------------|-------------|------------------------|
| even RF rails  | $U_{\text{RF}}^{(e)}$       | 142 V  | $\omega_z/(2\pi)$     | 1.0 MHz | $\vartheta_z$ | $0.0^\circ$ | $U_0$ 192 meV          |
|                | $U_{\text{RF}}^{(o)}$       | 350 V  | $\omega_{r,1}/(2\pi)$ | 2.0 MHz |               |             | $U_b$ 3.9 meV          |
|                | $\Omega_{\text{RF}}/(2\pi)$ | 30 MHz | $\omega_{r,1}/(2\pi)$ | 2.0 MHz | $\vartheta_r$ | $33^\circ$  | $U_{\text{mw}}$ 33 meV |
|                | $q$                         | 0.21   | $\omega_{r,2}/(2\pi)$ | 2.3 MHz |               |             |                        |
| odd RF rails   | $U_{\text{RF}}^{(e)}$       | 350 V  | $\omega_z/(2\pi)$     | 1.0 MHz | $\vartheta_z$ | $0.0^\circ$ | $U_0$ 334 meV          |
|                | $U_{\text{RF}}^{(o)}$       | 205 V  | $\omega_{r,1}/(2\pi)$ | 2.5 MHz |               |             | $U_b$ 6.1 meV          |
|                | $\Omega_{\text{RF}}/(2\pi)$ | 30 MHz | $\omega_{r,1}/(2\pi)$ | 2.5 MHz | $\vartheta_r$ | $37^\circ$  | $U_{\text{mw}}$ 38 meV |
|                | $q$                         | 0.26   | $\omega_{r,2}/(2\pi)$ | 2.8 MHz |               |             |                        |

are shown in (c) and (f). The trap parameters for a site at the array center are listed in Tab. B.5. In the two configurations, the RF voltage is either attenuated by about 59.4% on the even RF rails, or by 41.4% on the odd rails, relative to the respective other rail which is at  $U_{\text{RF}} = 350 \text{ V}$ . The difference in required RF attenuation for the two configurations stems from the different RF rail widths. In either configuration, the axial multiwell confinement can be maintained using DC voltages on the order of 1 V with standard secular frequencies of  $\omega_z = 2\pi \times 1.0 \text{ MHz}$  axially and  $\omega_r = 2\pi \times (2.0 - 3.0) \text{ MHz}$  radially. The axial mode remains aligned with the  $z$ -axis,  $\vartheta_z = 0$ , the radial mode tilt is increased to about  $\vartheta_r \sim 35^\circ$ . The reason for the smaller radial frequencies in comparison to the home configuration is the decreased trap efficiency, just as in the case of the BB traps. For the simulations, a maximally applicable RF voltage  $U_{\text{RF}} = 350 \text{ V}$  was assumed, limiting the stability  $q$ -values to 0.21 and 0.26, respectively. Likewise, the double-well barrier is limited to  $U_b \approx 3.9 \text{ meV}$  and  $U_b \approx 6.1 \text{ meV}$ , in good agreement with the double-well model, Eq. (8.3). The multiwell barrier  $U_{\text{mw}} \sim 35 \text{ meV}$  and the trap depth  $U_0 = (192, 334) \text{ meV}$  remain at large values.

Concerning the homogeneity of the central  $10 \times 10$  trapping sites, the most notable variation exists in the reduced trap distance  $s_t$ . For attenuation on the even RF rails, this distance changes from  $s_t = 39 \mu\text{m}$  at the central linear traps,  $x \approx \pm 158 \mu\text{m}$ , to  $s_t = 44 \mu\text{m}$  at the next pair of traps,  $x \approx \pm 476 \mu\text{m}$ . At the outermost pair of traps,  $x \approx \pm 794 \mu\text{m}$ , the distance further increases to  $s_t = 56 \mu\text{m}$ , however, the outer site of this pair is not part of the central  $10 \times 10$  lattice anymore and thus not used to store an ion. For attenuation on the odd RF rails, the distance changes from  $s_t = 40 \mu\text{m}$

## B. Appendix to the 2D linear trap array

at the array center,  $x = 0 \mu\text{m}$ , to  $s_t = 39 \mu\text{m}$  at the next pair of traps,  $x \approx \pm 316 \mu\text{m}$ , and further to  $s_t = 35 \mu\text{m}$  at the outer pair of traps,  $x \approx \pm 632 \mu\text{m}$ . The variation in trap distance  $s_t$  is caused by the edge effects of the trap array along the  $x$ -direction and limits the possibility of parallelized entangling operations across the entire lattice due to the difference in expected coupling rate  $\Omega_c$ . Edge effects due to the finite number of RF rails also cause a variation in the stability  $q$ -factor and, therefore, in the radial frequencies. For attenuation on the even rails, the  $q$  values are between 0.21 and 0.35, allowing for simultaneous stable trapping, and the radial frequencies vary within  $\omega_r = 2\pi \times (2.0 - 3.6)$  MHz. For attenuation on the odd rails, the effect is weaker, with the  $q$ -factor ranging between 0.26 and 0.22 and a radial frequency variation of  $\omega_r = 2\pi \times (2.2 - 2.8)$  MHz. The differences in  $\omega_r$  and in trap distance  $s_t$  across the array cause a variation in the double-well barrier  $U_b$ , cf. Eq. (8.3). However,  $U_b$  does not fall below 2 meV across the entire array and in both configurations. For motional coupling between adjacent sites, the variation in radial frequencies is not a concern if the axial mode is employed. The finiteness of the array leads to additional inhomogeneities in conjunction with the fact that the voltage set for axial confinement is calculated only for a single site at the array center. This makes the axial multiwell potential non-ideal at the array edges. Due to this, the axial frequency  $\omega_z$  varies by 74 kHz for attenuation on the even RF rails. For attenuation on the odd rails, the effect is significantly smaller with a variation in  $\omega_z$  of 7 kHz. Lastly, edge effects lead to small shifts of the trapping sites off the RF null of about  $1 \mu\text{m}$  for both configurations, comparable to the home configuration.

In summary, the simulations show that the concepts of multiwell confinement and RF shuttling, introduced for the BB trap design, can be extended to large linear trap arrays with many parallel RF rails. It should be emphasized, that the simulations presented here are only a first study. Many of the limitations found could be mitigated in a further optimized trap geometry. In particular, edge effects of the lattice potential during RF shuttling operations causing for instance the variation in the reduced trap distance  $s_t$  could be drastically reduced by adjusting the RF and DC rail widths. A first step in this direction was made by increasing the width of the outermost RF rail, allowing for a match of the stability  $q$ -values of the outer linear traps with the central traps in the home configuration. Furthermore, a more advanced algorithm for the calculation of DC voltage sets could be employed, allowing one to individually control the potential at multiple trapping sites simultaneously. This would mitigate the variation in axial frequency and open up possibilities to improve the segmentation of the DC rails to further decrease edge effects. A stronger segmentation would also improve the control of the trapping potential across the lattice, enabling tuning of additional parameters such as the mode tilts and the trap distance  $s_t^{(\text{ax})}$  along the axial direction  $z$ .

# Bibliography

- [1] European Commission. Quantum flagship initiative. *online source*, Mar. 31, 2019. URL <https://qt.eu/>.
- [2] M. B. Plenio and V. Vitelli. [The physics of forgetting: Landauer’s erasure principle and information theory](#). *Contemporary Physics*, 42(1):25–60, 2001. doi: 10.1080/00107510010018916.
- [3] P. Shor. [Polynomial-Time Algorithms for Prime Factorization and Discrete Logarithms on a Quantum Computer](#). *SIAM Journal on Computing*, 26(5):1484–1509, 1997. doi: 10.1137/S0097539795293172.
- [4] L. K. Grover. [A Fast Quantum Mechanical Algorithm for Database Search](#). In *Proceedings of the Twenty-eighth Annual ACM Symposium on Theory of Computing*, STOC ’96, pages 212–219, New York, NY, USA, 1996. ACM. ISBN 0-89791-785-5. doi: 10.1145/237814.237866.
- [5] R. P. Feynman. [Simulating physics with computers](#). *International Journal of Theoretical Physics*, 21(6):467–488, Jun. 1982. ISSN 1572-9575. doi: 10.1007/BF02650179.
- [6] I. M. Georgescu, S. Ashhab, and F. Nori. [Quantum simulation](#). *Rev. Mod. Phys.*, 86:153–185, Mar. 2014. doi: 10.1103/RevModPhys.86.153.
- [7] M. Reiher, N. Wiebe, K. M. Svore, D. Wecker, and M. Troyer. [Elucidating reaction mechanisms on quantum computers](#). *Proceedings of the National Academy of Sciences*, 2017. ISSN 0027-8424. doi: 10.1073/pnas.1619152114.
- [8] B. Wang, M. Tao, Q. Ai, T. Xin, N. Lambert, D. Ruan, Y. Cheng, F. Nori, F. Deng, and G. Long. [Efficient quantum simulation of photosynthetic light harvesting](#). *npj Quantum Information*, 4(52):2056–6387, Oct. 2018. ISSN 1. doi: 10.1038/s41534-018-0102-2.
- [9] P. L. Knight, E. A. Hinds, M. B. Plenio, D. J. Wineland, M. Barrett, J. Britton, J. Chiaverini, B. DeMarco, W. M. Itano, B. Jelenković, C. Langer, D. Leibfried, V. Meyer, T. Rosenband, and T. Schätz. [Quantum information processing with](#)

- trapped ions. *Philosophical Transactions of the Royal Society of London. Series A: Mathematical, Physical and Engineering Sciences*, 361(1808):1349–1361, 2003. doi: 10.1098/rsta.2003.1205.
- [10] M. H. Devoret and R. J. Schoelkopf. [Superconducting Circuits for Quantum Information: An Outlook](#). *Science*, 339(6124):1169–1174, 2013. ISSN 0036-8075. doi: 10.1126/science.1231930.
- [11] D. Weiss and M. Saffman. [Quantum computing with neutral atoms](#). *Physics Today*, 70(7):44, 2017. doi: 10.1063/PT.3.3626.
- [12] X. Qiang, X. Zhou, J. Wang, C. M. Wilkes, T. Loke, S. O’Gara, L. Kling, G. D. Marshall, R. Santagati, T. C. Ralph, J. B. Wang, J. L. O’Brien, M. G. Thompson, and J. C. F. Matthews. [Large-scale silicon quantum photonics implementing arbitrary two-qubit processing](#). *Nature Photonics*, 12:534–539, 2018. ISSN 9. doi: 10.1038/s41566-018-0236-y.
- [13] L. M. K. Vandersypen and I. L. Chuang. [NMR techniques for quantum control and computation](#). *Rev. Mod. Phys.*, 76:1037–1069, Jan. 2005. doi: 10.1103/RevModPhys.76.1037.
- [14] A. Laucht, J. T. Muhonen, F. A. Mohiyaddin, R. Kalra, J. P. Dehollain, S. Freer, F. E. Hudson, M. Veldhorst, R. Rahman, G. Klimeck, K. M. Itoh, D. N. Jamieson, J. C. McCallum, A. S. Dzurak, and A. Morello. [Electrically controlling single-spin qubits in a continuous microwave field](#). *Science Advances*, 1(3), 2015. doi: 10.1126/sciadv.1500022.
- [15] D. P. DiVincenzo. [The Physical Implementation of Quantum Computation](#). *Fortschritte der Physik*, 48(9-11):771–783, 2000. doi: 10.1002/1521-3978(200009)48:9/11<771::AID-PROP771>3.0.CO;2-E.
- [16] H. Häffner, C. F. Roos, and R. Blatt. [Quantum computing with trapped ions](#). *Physics Reports*, 469(4):155 – 203, 2008. ISSN 0370-1573. doi: doi.org/10.1016/j.physrep.2008.09.003.
- [17] G. Werth, V. N. Gheorghie, and F. G. Major. *Charged Particle Traps II*. Springer-Verlag Berlin, 1 edition, 2009. doi: 10.1007/978-3-540-92261-2.
- [18] S. Olmschenk, K. C. Younge, D. L. Moehring, D. N. Matsukevich, P. Maunz, and C. Monroe. [Manipulation and detection of a trapped Yb<sup>+</sup> hyperfine qubit](#). *Phys. Rev. A*, 76:052314, Nov. 2007. doi: 10.1103/PhysRevA.76.052314.

- [19] K. Kim, S. Korenblit, R. Islam, E. E. Edwards, M.-S. Chang, C. Noh, H. Carmichael, G.-D. Lin, L.-M. Duan, C. C. J. Wang, J. K. Freericks, and C. Monroe. [Quantum simulation of the transverse Ising model with trapped ions](#). *New Journal of Physics*, 13(10):105003, Oct. 2011. doi: 10.1088/1367-2630/13/10/105003.
- [20] P. Schindler, D. Nigg, T. Monz, J. T. Barreiro, E. Martinez, S. X. Wang, S. Quint, M. F. Brandl, V. N., C. F. Roos, M. Chwalla, M. Hennrich, and R. Blatt. [A quantum information processor with trapped ions](#). *New Journal of Physics*, 15(12):123012, 2013.
- [21] T. P. Harty, D. T. C. Allcock, C. J. Ballance, L. Guidoni, H. A. Janacek, N. M. Linke, D. N. Stacey, and D. M. Lucas. [High-Fidelity Preparation, Gates, Memory, and Readout of a Trapped-Ion Quantum Bit](#). *Phys. Rev. Lett.*, 113:220501, Nov. 2014. doi: 10.1103/PhysRevLett.113.220501.
- [22] C. J. Ballance, T. P. Harty, N. M. Linke, M. A. Sepiol, and D. M. Lucas. [High-Fidelity Quantum Logic Gates Using Trapped-Ion Hyperfine Qubits](#). *Phys. Rev. Lett.*, 117:060504, Aug. 2016. doi: 10.1103/PhysRevLett.117.060504.
- [23] J. P. Gaebler, T. R. Tan, Y. Lin, Y. Wan, R. Bowler, A. C. Keith, S. Glancy, K. Coakley, E. Knill, D. Leibfried, and D. J. Wineland. [High-Fidelity Universal Gate Set for  \$^9\text{Be}^+\$  Ion Qubits](#). *Phys. Rev. Lett.*, 117:060505, Aug. 2016. doi: 10.1103/PhysRevLett.117.060505.
- [24] Y. Wang, M. Um, J. Zhang, S. An, M. Lyu, J.-N. Zhang, L.-M. Duan, D. Yum, and K. Kim. [Single-qubit quantum memory exceeding ten-minute coherence time](#). *Nature Photonics*, 11:646–650, Oct. 2017. doi: 10.1038/s41566-017-0007-1.
- [25] C. Figgatt, D. Maslov, K. A. Landsman, N. M. Linke, S. Debnath, and C. Monroe. [Complete 3-Qubit Grover search on a programmable quantum](#). *Nature Communications*, 8(1918), Dec. 2017. doi: 10.1038/s41467-017-01904-7.
- [26] T. Monz, D. Nigg, E. A. Martinez, M. F. Brandl, P. Schindler, R. Rines, S. X. Wang, I. L. Chuang, and R. Blatt. [Realization of a scalable Shor algorithm](#). *Science*, 351(6277):1068–1070, 2016. ISSN 0036-8075. doi: 10.1126/science.aad9480.
- [27] J. Chiaverini, D. Leibfried, T. Schaetz, M. D. Barrett, R. B. Blakestad, J. Britton, W. M. Itano, J. D. Jost, E. Knill, C. Langer, R. Ozeri, and D. J. Wineland. [Realization of quantum error correction](#). *Nature*, 432:602–605, Dec. 2004. doi: 10.1038/nature03074.

- [28] P. Schindler, J. T. Barreiro, T. Monz, V. Nebendahl, D. Nigg, M. Chwalla, M. Hennrich, and R. Blatt. [Experimental Repetitive Quantum Error Correction](#). *Science*, 332(6033):1059–1061, 2011. ISSN 0036-8075. doi: 10.1126/science.1203329.
- [29] D. Nigg, M. Müller, E. A. Martinez, P. Schindler, M. Hennrich, T. Monz, M. A. Martin-Delgado, and R. Blatt. [Quantum computations on a topologically encoded qubit](#). *Science*, 345(6194):302–305, 2014. ISSN 0036-8075. doi: 10.1126/science.1253742.
- [30] A. Bermudez, X. Xu, R. Nigmatullin, J. O’Gorman, V. Negnevitsky, P. Schindler, T. Monz, U. G. Poschinger, C. Hempel, J. Home, F. Schmidt-Kaler, M. Biercuk, R. Blatt, S. Benjamin, and M. Müller. [Assessing the Progress of Trapped-Ion Processors Towards Fault-Tolerant Quantum Computation](#). *Phys. Rev. X*, 7: 041061, Dec. 2017. doi: 10.1103/PhysRevX.7.041061.
- [31] J. Zhang, G. Pagano, P. W. Hess, A. Kyprianidis, P. Becker, H. Kaplan, A. V. Gorshkov, Z.-X. Gong, and C. Monroe. [Observation of a many-body dynamical phase transition with a 53-qubit quantum simulator](#). *Nature*, 551, Nov. 2017. doi: 10.1038/nature24654.
- [32] P. Jurcevic, H. Shen, P. Hauke, C. Maier, T. Brydges, C. Hempel, B. P. Lanyon, M. Heyl, R. Blatt, and C. F. Roos. [Direct Observation of Dynamical Quantum Phase Transitions in an Interacting Many-Body System](#). *Phys. Rev. Lett.*, 119: 080501, Aug. 2017. doi: 10.1103/PhysRevLett.119.080501.
- [33] E. A. Martinez, C. A. Muschik, P. Schindler, D. Nigg, A. Erhard, M. Heyl, P. Hauke, M. Dalmonte, T. Monz, P. Zoller, and R. Blatt. [Real-time dynamics of lattice gauge theories with a few-qubit quantum computer](#). *Nature*, 534: 516–519, Jun. 2016. doi: 10.1038/nature18318.
- [34] C. Hempel, C. Maier, J. Romero, J. McClean, T. Monz, H. Shen, P. Jurcevic, B. P. Lanyon, P. Love, R. Babbush, A. Aspuru-Guzik, R. Blatt, and C. F. Roos. [Quantum Chemistry Calculations on a Trapped-Ion Quantum Simulator](#). *Phys. Rev. X*, 8:031022, Jul. 2018. doi: 10.1103/PhysRevX.8.031022.
- [35] M. Müller, L. Liang, I. Lesanovsky, and P. Zoller. [Trapped Rydberg ions: from spin chains to fast quantum gates](#). *New Journal of Physics*, 10(9):093009, Sep. 2008. doi: 10.1088/1367-2630/10/9/093009.
- [36] A. M. Eltony, D. Gangloff, M. Shi, A. Bylinskii, V. Vuletić, and I. L. Chuang. [Technologies for trapped-ion quantum information systems](#). *Quantum Informa-*

- tion Processing*, 15(12):5351–5383, Dec. 2016. ISSN 1573-1332. doi: 10.1007/s11128-016-1298-8.
- [37] K. R. Brown, J. Kim, and C. Monroe. [Co-designing a scalable quantum computer with trapped atomic ions](#). *Npj Quantum Information*, 2(16034), Nov. 2016. doi: 10.1038/npjqi.2016.34.
- [38] B. Lekitsch, S. Weidt, A. G. Fowler, K. Mølmer, S. J. Devitt, C. Wunderlich, and W. K. Hensinger. [Blueprint for a microwave trapped ion quantum computer](#). *Science Advances*, 3(2), 2017. doi: 10.1126/sciadv.1601540.
- [39] D. Kielpinski, C. Monroe, and D. J. Wineland. [Architecture for a large-scale ion-trap quantum computer](#). *Nature*, 417:709–711, Jun. 2002. doi: 10.1038/nature00784.
- [40] R. Reichle, D. Leibfried, R. B. Blakestad, J. Britton, J. D. Jost, E. Knill, C. Langer, R. Ozeri, S. Seidelin, and D. J. Wineland. [Transport dynamics of single ions in segmented microstructured Paul trap arrays](#). *Fortschritte der Physik*, 54(8-10):666–685, 2006. doi: 10.1002/prop.200610326.
- [41] S. Schulz, U. Poschinger, K. Singer, and F. Schmidt-Kaler. [Optimization of segmented linear Paul traps and transport of stored particles](#). *Fortschritte der Physik*, 54(8-10):648–665, 2006. doi: 10.1002/prop.200610324.
- [42] R. Bowler, J. Gaebler, Y. Lin, T. R. Tan, D. Hanneke, J. D. Jost, J. P. Home, D. Leibfried, and D. J. Wineland. [Coherent Diabatic Ion Transport and Separation in a Multizone Trap Array](#). *Phys. Rev. Lett.*, 109:080502, Aug. 2012. doi: 10.1103/PhysRevLett.109.080502.
- [43] A. Walther, F. Ziesel, T. Ruster, S. T. Dawkins, K. Ott, M. Hettrich, K. Singer, F. Schmidt-Kaler, and U. Poschinger. [Controlling Fast Transport of Cold Trapped Ions](#). *Phys. Rev. Lett.*, 109:080501, Aug. 2012. doi: 10.1103/PhysRevLett.109.080501.
- [44] L. E. de Clercq, H.-Y. Lo, M. Marinelli, D. Nadlinger, R. Oswald, V. Negnevitsky, D. Kienzler, B. Keitch, and J. P. Home. [Parallel Transport Quantum Logic Gates with Trapped Ions](#). *Phys. Rev. Lett.*, 116:080502, Feb. 2016. doi: 10.1103/PhysRevLett.116.080502.
- [45] P. Kaufmann, T. F. Gloger, D. Kaufmann, M. Johanning, and C. Wunderlich. [High-Fidelity Preservation of Quantum Information During Trapped-Ion Transport](#). *Phys. Rev. Lett.*, 120:010501, Jan. 2018. doi: 10.1103/PhysRevLett.120.010501.

- [46] T. Ruster, C. Warschburger, H. Kaufmann, C. T. Schmiegelow, A. Walther, M. Hettrich, A. Pfister, V. Kaushal, F. Schmidt-Kaler, and U. G. Poschinger. [Experimental realization of fast ion separation in segmented Paul traps](#). *Phys. Rev. A*, 90:033410, Sep. 2014. doi: 10.1103/PhysRevA.90.033410.
- [47] W. K. Hensinger, S. Olmschenk, D. Stick, D. Hucul, M. Yeo, M. Acton, L. Deslauriers, C. Monroe, and J. Rabchuk. [T-junction ion trap array for two-dimensional ion shuttling, storage, and manipulation](#). *Applied Physics Letters*, 88(3):034101, 2006. doi: 10.1063/1.2164910.
- [48] K. Wright, J. M. Amini, D. L. Faircloth, C. Volin, S. C. Doret, H. H., C.-S. Pai, D. W. Landgren, D. Denison, T. Killian, R. E. Slusher, and A. W. Harter. [Reliable transport through a microfabricated X-junction surface-electrode ion trap](#). *New Journal of Physics*, 15(3):033004, Mar. 2013. doi: 10.1088/1367-2630/15/3/033004.
- [49] G. Shu, G. Vittorini, A. Buikema, C. S. Nichols, C. Volin, D. Stick, and Kenneth R. Brown. [Heating rates and ion-motion control in a Y-junction surface-electrode trap](#). *Phys. Rev. A*, 89:062308, Jun. 2014. doi: 10.1103/PhysRevA.89.062308.
- [50] H. J. Kimble. [The quantum internet](#). *Nature*, 453:1023, Jun. 2008. doi: 10.1038/nature07127.
- [51] C. Monroe, R. Raussendorf, A. Ruthven, K. R. Brown, P. Maunz, L.-M. Duan, and J. Kim. [Large-scale modular quantum-computer architecture with atomic memory and photonic interconnects](#). *Phys. Rev. A*, 89:022317, Feb. 2014. doi: 10.1103/PhysRevA.89.022317.
- [52] R. C. Sterling, H. Rattanasonti, S. Weidt, K. Lake, P. Srinivasan, S. C. Webster, M. Kraft, and W. K. Hensinger. [Fabrication and operation of a two-dimensional ion-trap lattice on a high-voltage microchip](#). *Nature Communications*, 5(3637), Apr. 2014. doi: 10.1038/ncomms4637.
- [53] C. D. Bruzewicz, R. McConnell, J. Chiaverini, and J. M. Sage. [Scalable loading of a two-dimensional trapped-ion array](#). *Nature Communications*, 7(13005), 2016. doi: 10.1038/ncomms13005.
- [54] M. Kumph, P. Holz, K. Langer, M. Meraner, M. Niedermayr, M. Brownnutt, and R. Blatt. [Operation of a planar-electrode ion-trap array with adjustable RF electrodes](#). *New Journal of Physics*, 18(2):023047, 2016.

- [55] M. Mielenz, H. Kalis, M. Wittmer, F. Hakelberg, U. Warring, R. Schmied, M. Blain, P. Maunz, D. L. Moehring, D. Leibfried, and T. Schaetz. [Arrays of individually controlled ions suitable for two-dimensional quantum simulations](#). *Nature Communications*, 7(11839), Jun. 2016. doi: 10.1038/ncomms11839.
- [56] K. R. Brown, C. Ospelkaus, Y. Colombe, A. C. Wilson, D. Leibfried, and D. J. Wineland. [Coupled quantized mechanical oscillators](#). *Nature*, 471:196, Feb. 2011. doi: 10.1038/nature09721.
- [57] M. Harlander, R. Lechner, M. Brownnutt, R. Blatt, and W. Hänsel. [Trapped-ion antennae for the transmission of quantum information](#). *Nature*, 471(200):200–203, Mar. 2011. doi: 10.1038/nature09800.
- [58] A. C. Wilson, Y. Colombe, K. R. Brown, E. Knill, D. Leibfried, and D. J. Wineland. [Tunable spin–spin interactions and entanglement of ions in separate potential wells](#). *Nature*, 512:57–60, 2014. doi: 10.1038/nature13565.
- [59] A. K. Ratcliffe, R. L. Taylor, J. J. Hope, and A. R. R. Carvalho. [Scaling Trapped Ion Quantum Computers Using Fast Gates and Microtraps](#). *Phys. Rev. Lett.*, 120:220501, May 2018. doi: 10.1103/PhysRevLett.120.220501.
- [60] H. Bombin and M. A. Martin-Delgado. [Topological Quantum Distillation](#). *Phys. Rev. Lett.*, 97:180501, Oct. 2006. doi: 10.1103/PhysRevLett.97.180501.
- [61] B. P. Lanyon, P. Jurcevic, M. Zwerger, C. Hempel, E. A. Martinez, W. Dür, H. J. Briegel, R. Blatt, and C. F. Roos. [Measurement-Based Quantum Computation with Trapped Ions](#). *Phys. Rev. Lett.*, 111:210501, Nov. 2013. doi: 10.1103/PhysRevLett.111.210501.
- [62] M. Johanning, A. F. Varón, and C. Wunderlich. [Quantum simulations with cold trapped ions](#). *Journal of Physics B: Atomic, Molecular and Optical Physics*, 42(15):154009, Jul. 2009. doi: 10.1088/0953-4075/42/15/154009.
- [63] A. Friedenauer, H. Schmitz, J. T. Glueckert, D. Porras, and T. Schaetz. [Simulating a quantum magnet with trapped ions](#). *Nature Physics*, 4:757, 07 2008. doi: 10.1038/nphys1032.
- [64] A. E. B. Nielsen, G. Sierra, and J. I. Cirac. [Local models of fractional quantum Hall states in lattices and physical implementation](#). *Nature Communications*, 4:2864, Nov. 2013. doi: 10.1038/ncomms3864.

## Bibliography

- [65] S. Earnshaw. On the Nature of the Molecular Forces which Regulate the Constitution of the Luminiferous Ether. *Transactions of the Cambridge Philosophical Society*, 7:97, 1848.
- [66] P. K. Ghosh. *Ion traps*. Clarendon Press, 1995.
- [67] J. H. Wesenberg. [Electrostatics of surface-electrode ion traps](#). *Phys. Rev. A*, 78:063410, Dec. 2008. doi: 10.1103/PhysRevA.78.063410.
- [68] M. G. House. [Analytic model for electrostatic fields in surface-electrode ion traps](#). *Phys. Rev. A*, 78:033402, Sep. 2008. doi: 10.1103/PhysRevA.78.033402.
- [69] D. Leibfried, R. Blatt, C. Monroe, and D. Wineland. [Quantum dynamics of single trapped ions](#). *Rev. Mod. Phys.*, 75:281–324, Mar. 2003. doi: 10.1103/RevModPhys.75.281.
- [70] F. A. Shaikh and A. Ozakin. [Stability analysis of ion motion in asymmetric planar ion traps](#). *Journal of Applied Physics*, 112(7):074904, 2012. doi: 10.1063/1.4752404.
- [71] F. G. Major, V. N. Gheorghie, and G. Werth. *Charged Particle Traps*. Springer-Verlag, 2005. doi: 10.1007/b137836.
- [72] D. J. Berkeland, J. D. Miller, J. C. Bergquist, W. M. Itano, and D. J. Wineland. [Minimization of ion micromotion in a Paul trap](#). *Journal of Applied Physics*, 83(10):5025–5033, 1998. doi: 10.1063/1.367318.
- [73] A. Steane. [The ion trap quantum information processor](#). *Applied Physics B*, 64(6):623–643, Jun. 1997. ISSN 1432-0649. doi: 10.1007/s003400050225.
- [74] A. Steane, C. F. Roos, D. Stevens, A. Mundt, D. Leibfried, F. Schmidt-Kaler, and R. Blatt. [Speed of ion-trap quantum-information processors](#). *Phys. Rev. A*, 62:042305, Sep. 2000. doi: 10.1103/PhysRevA.62.042305.
- [75] J. Jin and D. A. Church. [Precision lifetimes for the  \$\text{Ca}^+\$  4p  \$^2\text{P}\$  levels: Experiment challenges theory at the 1% level](#). *Phys. Rev. Lett.*, 70:3213–3216, May 1993. doi: 10.1103/PhysRevLett.70.3213.
- [76] A. Kreuter, C. Becher, G. P. T. Lancaster, A. B. Mundt, C. Russo, H. Häffner, C. Roos, W. Hänsel, F. Schmidt-Kaler, R. Blatt, and M. S. Safronova. [Experimental and theoretical study of the 3d  \$^2D\$ -level lifetimes of  \$^{40}\text{Ca}^+\$](#) . *Phys. Rev. A*, 71:032504, Mar. 2005. doi: 10.1103/PhysRevA.71.032504.

- [77] R. Gerritsma, G. Kirchmair, F. Zähringer, J. Benhelm, R. Blatt, and C. F. Roos. [Precision measurement of the branching fractions of the  \$4p\ ^2P\_{3/2}\$  decay of Ca II.](#) *The European Physical Journal D*, 50(1):13–19, Nov. 2008. ISSN 1434-6079. doi: 10.1140/epjd/e2008-00196-9.
- [78] M. Ramm, T. Pruttivarasin, M. Kokish, I. Talukdar, and H. Häffner. [Precision Measurement Method for Branching Fractions of Excited  \$P\_{1/2}\$  States Applied to  \$^{40}\text{Ca}^+\$ .](#) *Phys. Rev. Lett.*, 111:023004, Jul. 2013. doi: 10.1103/PhysRevLett.111.023004.
- [79] Michael Chwalla. *Precision spectroscopy with  $^{40}\text{Ca}^+$  ions in a Paul trap.* PhD thesis, Leopold-Franzens-Universität Innsbruck, Apr. 2009.
- [80] W. M. Itano, J. C. Bergquist, J. J. Bollinger, J. M. Gilligan, D. J. Heinzen, F. L. Moore, M. G. Raizen, and D. J. Wineland. [Quantum projection noise: Population fluctuations in two-level systems.](#) *Phys. Rev. A*, 47:3554–3570, May 1993. doi: 10.1103/PhysRevA.47.3554.
- [81] H. J. Metcalf and P. van der Straten. *Laser Cooling and Trapping.* Springer-Verlag, 1 edition, 1999. ISBN 978-1-4612-1470-0. doi: 10.1007/978-1-4612-1470-0.
- [82] J. I. Cirac and P. Zoller. [Quantum Computations with Cold Trapped Ions.](#) *Phys. Rev. Lett.*, 74:4091–4094, May 1995. doi: 10.1103/PhysRevLett.74.4091.
- [83] A. Sørensen and K. Mølmer. [Entanglement and quantum computation with ions in thermal motion.](#) *Phys. Rev. A*, 62:022311, Jul. 2000. doi: 10.1103/PhysRevA.62.022311.
- [84] T. R. Tan, J. P. Gaebler, R. Bowler, Y. Lin, J. D. Jost, D. Leibfried, and D. J. Wineland. [Demonstration of a Dressed-State Phase Gate for Trapped Ions.](#) *Phys. Rev. Lett.*, 110:263002, Jun. 2013. doi: 10.1103/PhysRevLett.110.263002.
- [85] S. Stenholm. [The semiclassical theory of laser cooling.](#) *Rev. Mod. Phys.*, 58:699–739, Jul. 1986. doi: 10.1103/RevModPhys.58.699.
- [86] I. Marzoli, J. I. Cirac, R. Blatt, and P. Zoller. [Laser cooling of trapped three-level ions: Designing two-level systems for sideband cooling.](#) *Phys. Rev. A*, 49:2771–2779, Apr. 1994. doi: 10.1103/PhysRevA.49.2771.
- [87] M. Brownnutt, M. Kumph, P. Rabl, and R. Blatt. [Ion-trap measurements of electric-field noise near surfaces.](#) *Rev. Mod. Phys.*, 87:1419–1482, Dec. 2015. doi: 10.1103/RevModPhys.87.1419.

## Bibliography

- [88] Christian F. Roos. *Controlling the quantum state of trapped ions*. PhD thesis, Leopold-Franzens-Universität Innsbruck, Feb. 2000.
- [89] M. J. Madou. *Fundamentals of Microfabrication*. CRC Press, 2nd edition edition, October 8, 2018. doi: 10.1201/9781482274004.
- [90] J. M. Amini, H. Uys, J. H. Wesenberg, S. Seidelin, J. Britton, J. J. Bollinger, D. Leibfried, C. Ospelkaus, A. P. VanDevender, and D. J. Wineland. [Toward scalable ion traps for quantum information processing](#). *New Journal of Physics*, 12(3):033031, Mar. 2010. doi: 10.1088/1367-2630/12/3/033031.
- [91] D.-I. “Dan” Cho, S. Hong, M. Lee, and T. Kim. [A review of silicon microfabricated ion traps for quantum information processing](#). *Micro and Nano Systems Letters*, 3(1):2, Apr. 2015. ISSN 2213-9621. doi: 10.1186/s40486-015-0013-3.
- [92] B. Tabakov, F. Benito, M. Blain, C. R. Clark, S. Clark, R. A. Haltli, P. Maunz, J. D. Sterk, C. Tigges, and D. Stick. [Assembling a Ring-Shaped Crystal in a Microfabricated Surface Ion Trap](#). *Phys. Rev. Applied*, 4:031001, Sep. 2015. doi: 10.1103/PhysRevApplied.4.031001.
- [93] A. Bautista-Salvador, G. Zarantonello, H. Hahn, A. Preciado-Grijalva, J. Morgner, M. Wahnschaffe, and C. Ospelkaus. [Multilayer ion trap technology for scalable quantum computing and quantum simulation](#). *New Journal of Physics*, 21(4):043011, Apr. 2019. doi: 10.1088/1367-2630/ab0e46.
- [94] Ion Quantum Technology Group, University of Sussex. 2D square array microchips. *unpublished*, online source, Oct. 29, 2019. URL <http://www.sussex.ac.uk/physics/iqt/research/researchers/microchip.html#hex>.
- [95] F. Hakelberg, P. Kiefer, M. Wittemer, U. Warring, and T. Schaetz. [Interference in a Prototype of a Two-Dimensional Ion Trap Array Quantum Simulator](#). *Phys. Rev. Lett.*, 123:100504, Sep. 2019. doi: 10.1103/PhysRevLett.123.100504.
- [96] M. Kumph, M. Brownnutt, and R. Blatt. [Two-dimensional arrays of radio-frequency ion traps with addressable interactions](#). *New Journal of Physics*, 13(7):073043, 2011.
- [97] M. Harlander, M. Brownnutt, W. Hänsel, and R. Blatt. [Trapped-ion probing of light-induced charging effects on dielectrics](#). *New Journal of Physics*, 12(9):093035, Sep. 2010. doi: 10.1088/1367-2630/12/9/093035.

- [98] S. X. Wang, G. Hao Low, N. S. Lachenmyer, Y. Ge, P. F. Herskind, and I. L. Chuang. [Laser-induced charging of microfabricated ion traps](#). *Journal of Applied Physics*, 110(10):104901, 2011. doi: 10.1063/1.3662118.
- [99] D. T. C. Allcock, T. P. Harty, H. A. Janacek, N. M. Linke, C. J. Ballance, A. M. Steane, D. M. Lucas, R. L. Jarecki, S. D. Habermehl, M. G. Blain, D. Stick, and D. L. Moehring. [Heating rate and electrode charging measurements in a scalable, microfabricated, surface-electrode ion trap](#). *Applied Physics B*, 107(4):913–919, Jun. 2012. ISSN 1432-0649. doi: 10.1007/s00340-011-4788-5.
- [100] K. K. Mehta, C. D. Bruzewicz, R. McConnell, R. J. Ram, J. M. Sage, and J. Chiaverini. [Integrated optical addressing of an ion qubit](#). *Nature Nanotechnology*, 11:1066–1070, Aug. 2016. doi: 10.1038/nnano.2016.139.
- [101] D. Kielpinski, C. Volin, E. W. Streed, F. Lenzini, and M. Lobino. [Integrated optics architecture for trapped-ion quantum information processing](#). *Quantum Information Processing*, 15(12):5315–5338, Dec. 2016. ISSN 1573-1332. doi: 10.1007/s11128-015-1162-2.
- [102] M. Ghadimi, V. Blüms, B. G. Norton, P. M. Fisher, S. C. Connell, J. M. Amini, C. Volin, H. Hayden, C.-S. Pai, D. Kielpinski, M. Lobino, and E. W. Streed. [Scalable ion–photon quantum interface based on integrated diffractive mirrors](#). *npj Quantum Information*, 3:1, Jan. 2017. doi: 10.1038/s41534-017-0006-6.
- [103] C. Piltz, T. Sriarunothai, A. F. Varón, and C. Wunderlich. [A trapped-ion-based quantum byte with  \$10^{-5}\$  next-neighbour cross-talk](#). *Nature Communications*, 5: 4679, Aug. 2014. doi: 10.1038/ncomms5679.
- [104] A. Seif, K. A. Landsman, N. M. Linke, C. Figgatt, C. Monroe, and M. Hafezi. [Machine learning assisted readout of trapped-ion qubits](#). *Journal of Physics B: Atomic, Molecular and Optical Physics*, 51(17):174006, Aug. 2018. doi: 10.1088/1361-6455/aad62b.
- [105] M. Diederich, H. Häffner, N. Hermanspahn, M. Immel, H.J. Kluge, R. Ley, R. Mann, W. Quint, S. Stahl, and G. Werth. [Observing a single hydrogen-like ion in a Penning trap at  \$T = 4\$  K](#). *Hyperfine Interactions*, 115(1):185–192, Nov. 1998. ISSN 1572-9540. doi: 10.1023/A:1012665109427.
- [106] J. D. Jackson. *Classical electrodynamics*. Wiley, 3 edition, 1999.
- [107] V. M. Schäfer, C. J. Ballance, K. Thirumalai, L. J. Stephenson, T. G. Ballance, A. M. Steane, and D. M. Lucas. [Fast quantum logic gates with trapped-ion qubits](#). *Nature*, 555:75–78, Feb. 2018. doi: 10.1038/nature25737.

## Bibliography

- [108] Q. A. Turchette, D. Kielpinski, B. E. King, D. Leibfried, D. M. Meekhof, C. J. Myatt, M. A. Rowe, C. A. Sackett, C. S. Wood, W. M. Itano, C. Monroe, and D. J. Wineland. [Heating of trapped ions from the quantum ground state](#). *Phys. Rev. A*, 61:063418, May 2000. doi: 10.1103/PhysRevA.61.063418.
- [109] C. J. Myatt, B. E. King, Q. A. Turchette, C. A. Sackett, D. Kielpinski, W. M. Itano, C. Monroe, and D. J. Wineland. [Decoherence of quantum superpositions through coupling to engineered reservoirs](#). *Nature*, 403:269–273, Jan. 2000. doi: 10.1038/35002001.
- [110] I. A. Boldin, A. Kraft, and C. Wunderlich. [Measuring Anomalous Heating in a Planar Ion Trap with Variable Ion-Surface Separation](#). *Phys. Rev. Lett.*, 120:023201, Jan. 2018. doi: 10.1103/PhysRevLett.120.023201.
- [111] J. A. Sedlacek, A. Greene, J. Stuart, R. McConnell, C. D. Bruzewicz, J. M. Sage, and J. Chiaverini. [Distance scaling of electric-field noise in a surface-electrode ion trap](#). *Phys. Rev. A*, 97:020302, Feb. 2018. doi: 10.1103/PhysRevA.97.020302.
- [112] J. B. Johnson. [Thermal Agitation of Electricity in Conductors](#). *Phys. Rev.*, 32:97–109, Jul. 1928. doi: 10.1103/PhysRev.32.97.
- [113] H. Nyquist. [Thermal Agitation of Electric Charge in Conductors](#). *Phys. Rev.*, 32:110–113, Jul. 1928. doi: 10.1103/PhysRev.32.110.
- [114] D. A. Hite, Y. Colombe, A. C. Wilson, K. R. Brown, U. Warring, R. Jördens, J. D. Jost, K. S. McKay, D. P. Pappas, D. Leibfried, and D. J. Wineland. [100-Fold Reduction of Electric-Field Noise in an Ion Trap Cleaned with In Situ Argon-Ion-Beam Bombardment](#). *Phys. Rev. Lett.*, 109:103001, Sep. 2012. doi: 10.1103/PhysRevLett.109.103001.
- [115] N. Daniilidis, S. Gerber, G. Bolloten, M. Ramm, A. Ransford, E. Ulin-Avila, I. Talukdar, and H. Häffner. [Surface noise analysis using a single-ion sensor](#). *Phys. Rev. B*, 89:245435, Jun. 2014. doi: 10.1103/PhysRevB.89.245435.
- [116] D. T. C. Allcock, L. Guidoni, T. P. Harty, C. J. Ballance, M. G. Blain, A. M. Steane, and D. M. Lucas. [Reduction of heating rate in a microfabricated ion trap by pulsed-laser cleaning](#). *New Journal of Physics*, 13(12):123023, Dec. 2011. doi: 10.1088/1367-2630/13/12/123023.
- [117] Michael Niedermayr. *Cryogenic surface ion traps*. PhD thesis, Leopold-Franzens-Universität Innsbruck, Jul. 2015. URL <https://resolver.obvsg.at/urn:nbn:at:at-ubi:1-2520>.

- [118] D. Gandolfi, M. Niedermayr, M. Kumph, M. Brownnutt, and R. Blatt. [Compact radio-frequency resonator for cryogenic ion traps](#). *Review of Scientific Instruments*, 83(8):084705, 2012. doi: 10.1063/1.4737889.
- [119] M. F. Brandl, P. Schindler, T. Monz, and R. Blatt. [Cryogenic resonator design for trapped ion experiments in Paul traps](#). *Applied Physics B*, 122(6):157, May 2016. ISSN 1432-0649. doi: 10.1007/s00340-016-6430-z.
- [120] Regina Lechner. *Photoionisation of  $^{40}\text{Ca}$  with a frequency-doubled 422 nm laser and a 377 nm laser diode*. Master's thesis, Leopold-Franzens-Universität Innsbruck, May 2010.
- [121] Muir Kumph. *2D Arrays of Ion Traps for Large Scale Integration of Quantum Information Processors*. PhD thesis, Leopold-Franzens-Universität Innsbruck, Jul. 2015. URL <https://resolver.obvsg.at/urn:nbn:at:at-ubi:1-2040>.
- [122] Roman Stricker. *Gatteroperationen hoher Güte in einem optischen Quantenbit*. Master's thesis, Leopold-Franzens-Universität Innsbruck, Mar. 2017.
- [123] T. W. Hänsch and B. Couillaud. [Laser frequency stabilization by polarization spectroscopy of a reflecting reference cavity](#). *Optics Communications*, 35(3):441 – 444, 980. ISSN 0030-4018. doi: [https://doi.org/10.1016/0030-4018\(80\)90069-3](https://doi.org/10.1016/0030-4018(80)90069-3).
- [124] R. W. P. Drever, J. L. Hall, F. V. Kowalski, J. Hough, G. M. Ford, A. J. Munley, and H. Ward. [Laser phase and frequency stabilization using an optical resonator](#). *Applied Physics B*, 31(2):97–105, Jun. 1983. ISSN 1432-0649. doi: 10.1007/BF00702605.
- [125] Y. Pang, J. J. Hamilton, and J.-P. Richard. [Frequency noise induced by fiber perturbations in a fiber-linked stabilized laser](#). *Appl. Opt.*, 31(36):7532–7534, Dec. 1992. doi: 10.1364/AO.31.007532.
- [126] Kirill Lakhmanskiy. *On heating rates in cryogenic surface ion traps*. PhD thesis, Leopold-Franzens-Universität Innsbruck, Oct. 2019.
- [127] Philipp Schindler. *Frequency synthesis and pulse shaping for quantum information processing with trapped ions*. Master's thesis, Leopold-Franzens-Universität Innsbruck, Sep. 2008.
- [128] Kirsten Langer. *Miniaturisierte zweidimensionale Ionenfallen mit segmentierter Radiofrequenzelektrode*. Master's thesis, Leopold-Franzens-Universität Innsbruck, Oct. 2013.

- [129] Martin Meraner. *Elektrische Ansteuerung einer Oberflächenfalle*. Master's thesis, Leopold-Franzens-Universität Innsbruck, Dec. 2016.
- [130] F. Lai, M. Li, H. Wang, Y. Jiang, and Y. Song. [Effect of oxygen flow rate on the properties of SiO<sub>x</sub> films deposited by reactive magnetron sputtering](#). *Chin. Opt. Lett.*, 3(8):490–493, Aug. 2005.
- [131] N. Tomozeiu. [Silicon Oxide \(SiO<sub>x</sub>, 0 < x < 2\): a Challenging Material for Optoelectronics](#). In Padmanabhan Predeep, editor, *Optoelectronics*, chapter 3. IntechOpen, Rijeka, 2011. doi: 10.5772/20156.
- [132] J. Santamaría, E. Iborra, F. Sánchez Quesada, G. González Díaaaz, and M. Rodríguez Vidal. [Sputtering of SiO<sub>2</sub> in O<sub>2</sub>–Ar atmospheres](#). *Thin Solid Films*, 139(2): 201 – 208, 1986. ISSN 0040-6090. doi: [https://doi.org/10.1016/0040-6090\(86\)90338-X](https://doi.org/10.1016/0040-6090(86)90338-X).
- [133] J. O. Carneiro, F. Machado, L. Rebouta, M. I. Vasilevskiy, S. Lanceros-Méndez, V. Teixeira, M. F. Costa, and A. P. Samantilleke. [Compositional, Optical and Electrical Characteristics of SiO<sub>x</sub> Thin Films Deposited by Reactive Pulsed DC Magnetron Sputtering](#). *Coatings*, 9(8), 2019. ISSN 2079-6412. doi: 10.3390/coatings9080468.
- [134] R. Schmied, J. H. Wesenberg, and D. Leibfried. [Optimal Surface-Electrode Trap Lattices for Quantum Simulation with Trapped Ions](#). *Phys. Rev. Lett.*, 102:233002, Jun. 2009. doi: 10.1103/PhysRevLett.102.233002.
- [135] R. Schmied. [Electrostatics of gapped and finite surface electrodes](#). *New J. Phys.*, 12:023038, Feb. 2010. doi: 10.1088/1367-2630/12/2/023038.
- [136] H. Bartzsch, D. Glöß, P. Frach, M. Gittner, E. Schultheiß, W. Brode, and J. Hartung. [Electrical insulation properties of sputter-deposited SiO<sub>2</sub>, Si<sub>3</sub>N<sub>4</sub> and Al<sub>2</sub>O<sub>3</sub> films at room temperature and 400°C](#). *physica status solidi (a)*, 206(3):514–519, 2009. doi: 10.1002/pssa.200880481.
- [137] E. A. Gulbransen, T. P. Copan, and K. F. Andrew. [Oxidation of Copper between 250° and 450°C and the Growth of CuO “Whiskers”](#). *Journal of The Electrochemical Society*, 108(2):119–123, 1961. doi: 10.1149/1.2428024.
- [138] K. Hinode, Y. Homma, and Y. Sasaki. [Whisker growth on aluminum thin films during heat treatment](#). *AIP Conference Proceedings*, 418(1):359–370, 1998. doi: 10.1063/1.54656.

- [139] S. C. Doret, J. M. Amini, K. Wright, C. Volin, T. Killian, A. Ozakin, D. Denison, H. Hayden, C.-S. Pai, R. E. Slusher, and A. W. Harter. [Controlling trapping potentials and stray electric fields in a microfabricated ion trap through design and compensation](#). *New Journal of Physics*, 14(7):073012, 2012.
- [140] M. Cetina, A. Grier, J. Campbell, I. Chuang, and V. Vuletic. [Bright source of cold ions for surface-electrode traps](#). *Phys. Rev. A*, 76:041401, Oct. 2007. doi: 10.1103/PhysRevA.76.041401.
- [141] A. P. VanDevender, Y. Colombe, J. Amini, D. Leibfried, and D. J. Wineland. [Efficient Fiber Optic Detection of Trapped Ion Fluorescence](#). *Phys. Rev. Lett.*, 105:023001, Jul. 2010. doi: 10.1103/PhysRevLett.105.023001.
- [142] T. H. Kim, P. F. Herskind, T. Kim, J. Kim, and I. L. Chuang. [Surface-electrode point Paul trap](#). *Phys. Rev. A*, 82:043412, Oct. 2010. doi: 10.1103/PhysRevA.82.043412.
- [143] P. F. Herskind, A. Dantan, M. Albert, J. P. Marler, and M. Drewsen. [Positioning of the rf potential minimum line of a linear Paul trap with micrometer precision](#). *Journal of Physics B: Atomic, Molecular and Optical Physics*, 42(15):154008, 2009. doi: 10.1088/0953-4075/42/15/154008.
- [144] T. H. Kim, P. F. Herskind, and I. L. Chuang. [Surface-electrode ion trap with integrated light source](#). *Applied Physics Letters*, 98(21):214103, 2011. doi: 10.1063/1.3593496.
- [145] Tony Hyun Kim. *An Optical-fiber Interface to a Trapped-ion Quantum Computer*. PhD thesis, Massachusetts Institute of Technology, Aug. 2011. URL <http://hdl.handle.net/1721.1/77089>.
- [146] B. Lengeler. [Semiconductor devices suitable for use in cryogenic environments](#). *Cryogenics*, 14(8):439 – 447, 1974. ISSN 0011-2275. doi: 10.1016/0011-2275(74)90206-9.
- [147] W. Schenk, F. Kremer, G. Beddies, T. Franke, P. Galvosas, and P. Rieger. *Physikalisches Praktikum*. Springer Spektrum, 14 edition, 2014.
- [148] T. W. Borneman and D. G. Cory. [Bandwidth-limited control and ringdown suppression in high-Q resonators](#). *Journal of Magnetic Resonance*, 225:120 – 129, 2012. ISSN 1090-7807. doi: 10.1016/j.jmr.2012.10.011.

- [149] A. Detti, M. De Pas, L. Duca, E. Perego, and C. Sias. [A compact radiofrequency drive based on interdependent resonant circuits for precise control of ion traps](#). *Review of Scientific Instruments*, 90(2):023201, 2019. doi: 10.1063/1.5063305.
- [150] S. X. Wang, Y. Ge, J. Labaziewicz, E. Dauler, K. Berggren, and I. L. Chuang. [Superconducting microfabricated ion traps](#). *Applied Physics Letters*, 97(24):244102, 2010. doi: 10.1063/1.3526733.
- [151] J. Chiaverini and J. M. Sage. [Insensitivity of the rate of ion motional heating to trap-electrode material over a large temperature range](#). *Phys. Rev. A*, 89:012318, Jan. 2014. doi: 10.1103/PhysRevA.89.012318.
- [152] M. K. Wu, J. R. Ashburn, C. J. Torng, P. H. Hor, R. L. Meng, L. Gao, Z. J. Huang, Y. Q. Wang, and C. W. Chu. [Superconductivity at 93 K in a new mixed-phase Y-Ba-Cu-O compound system at ambient pressure](#). *Phys. Rev. Lett.*, 58:908–910, Mar. 1987. doi: 10.1103/PhysRevLett.58.908.
- [153] R. Liang, D. A. Bonn, and W. N. Hardy. [Evaluation of CuO<sub>2</sub> plane hole doping in YBa<sub>2</sub>Cu<sub>3</sub>O<sub>6+x</sub> single crystals](#). *Phys. Rev. B*, 73:180505, May 2006. doi: 10.1103/PhysRevB.73.180505.
- [154] K. Lakhmanskii, P. C. Holz, D. Schärftl, B. Ames, R. Assouly, T. Monz, Y. Colombe, and R. Blatt. [Observation of superconductivity and surface noise using a single trapped ion as a field probe](#). *Phys. Rev. A*, 99:023405, Feb. 2019. doi: 10.1103/PhysRevA.99.023405.
- [155] P. L. W. Maunz. [High Optical Access Trap 2.0](#). Technical report, Sandia National Lab., 2016.
- [156] Dominic Schärftl. *High temperature superconducting ion traps*. Master’s thesis, Leopold-Franzens-Universität Innsbruck, May 2016.
- [157] N. Daniilidis, S. Narayanan, S. A. Möller, R. Clark, T. E. Lee, P. J. Leek, A. Wallraff, St. Schulz, F. Schmidt-Kaler, and H. Häffner. [Fabrication and heating rate study of microscopic surface electrode ion traps](#). *New Journal of Physics*, 13(1):013032, Jan. 2011. doi: 10.1088/1367-2630/13/1/013032.
- [158] M. Niedermayr, K. Lakhmanskii, M. Kumph, S. Partel, J. Edlinger, M. Brownnutt, and R. Blatt. [Cryogenic surface ion trap based on intrinsic silicon](#). *New Journal of Physics*, 16(11):113068, Nov. 2014. doi: 10.1088/1367-2630/16/11/113068.
- [159] R. A. Matula. [Electrical Resistivity of Copper, Gold, Palladium, and Silver](#). *J. Phys. Chem. Rev. Data*, 8:1147–1298, 1979. doi: 10.1063/1.555614.

- [160] V. L. Ginzburg and L. D. Landau. [On the theory of superconductivity](#). *Zh. Eksp. Teor. Fiz.*, 20(1064):English translation in: L. D. Landau, Collected papers (Oxford: Pergamon Press, 1965) p. 546, 1950. doi: 10.1016/B978-0-08-010586-4.50078-X.
- [161] N. Bhattacharya and C. Neogy. [Frequency and temperature dependence of ac loss and scaling study of a high-temperature cuprate superconductor](#). *Physica Scripta*, 85(5):055701, May 2012. doi: 10.1088/0031-8949/85/05/055701.
- [162] C. Barone, F. Romeo, S. Pagano, M. Adamo, C. Nappi, E. Sarnelli, F. Kurth, and K. Iida. [Probing transport mechanisms of BaFe<sub>2</sub>As<sub>2</sub> superconducting films and grain boundary junctions by noise spectroscopy](#). *Scientific Reports*, 4, Aug. 2014. ISSN 6163. doi: 10.1038/srep06163.
- [163] A. Chakrabarti and C. Neogy. [A generalized method of estimation of critical exponents through an indigenous susceptometry setup for YBCO materials](#). *Cryogenics*, 55-56:35 – 46, 2013. ISSN 0011-2275. doi: 10.1016/j.cryogenics.2013.02.003.
- [164] N. Driza, S. Blanco-Canosa, M. Bakr, S. Soltan, M. Khalid, L. Mustafa, K. Kawashima, G. Christiani, H-U. Habermeier, G. Khaliullin, C. Ulrich, M. Le Tacon, and B. Keimer. [Long-range transfer of electron–phonon coupling in oxide superlattices](#). *Nature Materials*, 11:675, Jul. 2012. doi: 10.1038/nmat3378.
- [165] R. Fermani, T. Müller, B. Zhang, M. J. Lim, and R. Dumke. [Heating rate and spin flip lifetime due to near-field noise in layered superconducting atom chips](#). *Journal of Physics B: Atomic, Molecular and Optical Physics*, 43(9):095002, Apr. 2010. doi: 10.1088/0953-4075/43/9/095002.
- [166] B. Kasch, H. Hattermann, D. Cano, T. E. Judd, S. Scheel, C. Zimmermann, R. Kleiner, D. Koelle, and J. Fortágh. [Cold atoms near superconductors: atomic spin coherence beyond the Johnson noise limit](#). *New Journal of Physics*, 12(6):065024, Jun. 2010. doi: 10.1088/1367-2630/12/6/065024.
- [167] C. Henkel, S. Pötting, and M. Wilkens. [Loss and heating of particles in small and noisy traps](#). *Applied Physics B*, 69(5):379–387, Dec. 1999. ISSN 1432-0649. doi: 10.1007/s003400050823.
- [168] I. M. Vishik. [Photoemission perspective on pseudogap, superconducting fluctuations, and charge order in cuprates: a review of recent progress](#). *Reports on Progress in Physics*, 81(6):062501, Apr. 2018. doi: 10.1088/1361-6633/aaba96.

- [169] D. Kielpinski, B. E. King, C. J. Myatt, C. A. Sackett, Q. A. Turchette, W. M. Itano, C. Monroe, D. J. Wineland, and W. H. Zurek. [Sympathetic cooling of trapped ions for quantum logic](#). *Phys. Rev. A*, 61:032310, Feb. 2000. doi: 10.1103/PhysRevA.61.032310.
- [170] J. P. Home, M. J. McDonnell, D. J. Szwer, B. C. Keitch, D. M. Lucas, D. N. Stacey, and A. M. Steane. [Memory coherence of a sympathetically cooled trapped-ion qubit](#). *Phys. Rev. A*, 79:050305, May 2009. doi: 10.1103/PhysRevA.79.050305.
- [171] J. P. Home, D. Hanneke, J. D. Jost, J. M. Amini, D. Leibfried, and D. J. Wineland. [Complete Methods Set for Scalable Ion Trap Quantum Information Processing](#). *Science*, 325(5945):1227–1230, 2009. ISSN 0036-8075. doi: 10.1126/science.1177077.
- [172] Gerald Stocker. *Development of novel micro-fabricated ion traps*. Master’s thesis, Leopold-Franzens-Universität Innsbruck, Nov. 2019.
- [173] H. J. Briegel, D. E. Browne, W. Dür, R. Raussendorf, and M. Van den Nest. [Measurement-based quantum computation](#). *Nature Physics*, 5:19–26, Jan. 2009. doi: 10.1038/nphys1157.
- [174] M. Mamaev, R. Blatt, J. Ye, and A. M. Rey. [Cluster State Generation with Spin-Orbit Coupled Fermionic Atoms in Optical Lattices](#). *Phys. Rev. Lett.*, 122:160402, Apr. 2019. doi: 10.1103/PhysRevLett.122.160402.
- [175] P. Jurcevic, B. P. Lanyon, P. Hauke, C. Hempel, P. Zoller, R. Blatt, and C. F. Roos. [Quasiparticle engineering and entanglement propagation in a quantum many-body system](#). *Nature*, 511:202, Jul. 2014. doi: 10.1038/nature13461.
- [176] F. L. J. Sangster and K. Teer. [Bucket-brigade electronics: new possibilities for delay, time-axis conversion, and scanning](#). *IEEE Journal of Solid-State Circuits*, 4(3):131–136, Jun. 1969. ISSN 0018-9200. doi: 10.1109/JSSC.1969.1049975.
- [177] M. H. Oliveira and J. A. Miranda. [Biot-Savart-like law in electrostatics](#). *European Journal of Physics*, 22(1):31, 2001. doi: 10.1088/0143-0807/22/1/304.
- [178] U. Tanaka, K. Suzuki, Y. Ibaraki, and S. Urabe. [Design of a surface electrode trap for parallel ion strings](#). *Journal of Physics B: Atomic, Molecular and Optical Physics*, 47(3):035301, 2014.
- [179] M. Cetina, A. Bylinskii, L. Karpa, D. Gangloff, K. M. Beck, Y. Ge, M. Scholz, A. T. Grier, I. Chuang, and V. Vuletić. [One-dimensional array of ion chains coupled to an optical cavity](#). *New Journal of Physics*, 15(5):053001, 2013.

- [180] M. A. Rowe, A. Ben-Kish, B. L. DeMarco, D. Leibfried, V. Meyer, J. Beall, J. Britton, J. Hughes, W. M. Itano, B. Jelenkovic, C. Langer, T. Rosenband, and D. Wineland. [Transport of quantum states and separation of ions in a dual RF ion trap](#). *Quantum Inf. Comput.*, 2:257, Jul. 2002. doi: 10.26421/QIC2.4.
- [181] R. B Blakestad, C. Ospelkaus, A. P VanDevender, J. H Wesenberg, M. J Biercuk, D. Leibfried, and D. J Wineland. [Near-ground-state transport of trapped-ion qubits through a multidimensional array](#). *Phys. Rev. A*, 84:032314, Sep. 2011. doi: 10.1103/PhysRevA.84.032314.
- [182] Robin Oswald. *Velocity Control of Trapped Ions for Transport Quantum Logic Gates*. Master's thesis, Eidgenössische Technische Hochschule Zürich, Nov. 2015.
- [183] K. K. Mehta, A. M. Eltony, C. D. Bruzewicz, I. L. Chuang, R. J. Ram, J. M. Sage, and J. Chiaverini. [Ion traps fabricated in a CMOS foundry](#). *Applied Physics Letters*, 105(4):044103, 2014. doi: 10.1063/1.4892061.
- [184] D. R. Lide. *CRC handbook of Chemistry and Physics*. CRC press, Inc., 75 edition, 1994.
- [185] J. W. Ekin. *Experimental Techniques for Low-Temperature Measurements: Cryostat Design, Material Properties and Superconductor Critical-Current Testing*. Oxford university press, 2006.
- [186] D. Stick, W. K. Hensinger, S. Olmschenk, M. J. Madsen, K. Schwab, and C. Monroe. [Ion trap in a semiconductor chip](#). *Nature Physics*, 2:36–39, 2006. doi: 10.1038/nphys171.
- [187] F. Splatt, M. Harlander, M. Brownmatt, F. Zähringer, R. Blatt, and W. Hänsel. [Deterministic reordering of  \$^{40}\text{Ca}^+\$  ions in a linear segmented Paul trap](#). *New Journal of Physics*, 11(10):103008, Oct. 2009. doi: 10.1088/1367-2630/11/10/103008.
- [188] H. Kaufmann, T. Ruster, C. T. Schmiegelow, M. A. Luda, V. Kaushal, J. Schulz, D. von Lindenfels, F. Schmidt-Kaler, and U. G. Poschinger. [Fast ion swapping for quantum-information processing](#). *Phys. Rev. A*, 95:052319, May 2017. doi: 10.1103/PhysRevA.95.052319.
- [189] C. R. Paul. *Inductance Loop and Partial*. Wiley, 1 edition, 2009.
- [190] C. Spartaco and M. Francescaromana. *Signal Integrity and Radiated Emission of High-Speed Digital Systems*. Wiley, 2008. ISBN 9780470511664. doi: 10.1002/9780470772874.

- [191] G. Stojanović, L. Živanov, and M. Damnjanović. [Novel efficient methods for inductance calculation of meander inductor](#). *COMPEL - The international journal for computation and mathematics in electrical and electronic engineering*, 25(4): 916–928, 2006. doi: 10.1108/03321640610684079.
- [192] H. Salamati and P. Kameli. [AC susceptibility of  \$\text{YBa}\_2\text{Cu}\_3\text{O}\_{7-\delta}\$  superconducting thin film in a perpendicular field](#). *Physica B: Condensed Matter*, 321(1):337 – 341, 2002. ISSN 0921-4526. doi: 10.1016/S0921-4526(02)01070-0.
- [193] W. J. Carr, Jr. *AC loss and macroscopic theory of superconductors*. CRC Press, 2 edition, 2001.
- [194] D. Miller, P. L. Richards, S. Etemad, A. Inam, T. Venkatesan, B. Dutta, X. D. Wu, C. B. Eom, T. H. Geballe, N. Newman, and B. F. Cole. [Residual losses in epitaxial thin films of  \$\text{YBa}\_2\text{Cu}\_3\text{O}\_7\$  from microwave to submillimeter wave frequencies](#). *Appl. Phys. Lett.*, 59(18):2326–2328, 1991. doi: 10.1063/1.106058.
- [195] D. Qu, D. Shi, A. Ferendeci, D. Mast, H. A. Blackstead, and I. Maartense. [Scaling behaviour of rf surface resistance in oxygen deficient single-domain YBCO](#). *Superconductor Science and Technology*, 13(6):902–907, May 2000. doi: 10.1088/0953-2048/13/6/356.
- [196] J. Krupka, J. Breeze, A. Centeno, N. Alford, T. Claussen, and L. Jensen. [Measurements of Permittivity, Dielectric Loss Tangent, and Resistivity of Float-Zone Silicon at Microwave Frequencies](#). *IEEE Transactions on Microwave Theory and Techniques*, 54(11):3995–4001, Nov. 2006. ISSN 0018-9480. doi: 10.1109/TMTT.2006.883655.
- [197] M. Wiesel, G. Birkl, M. S. Ebrahimi, A. Martin, W. Quint, N. Stallkamp, and M. Vogel. [Optically transparent solid electrodes for precision Penning traps](#). *Review of Scientific Instruments*, 88(12):123101, 2017. doi: 10.1063/1.5002180.